



**HAL**  
open science

# Characterization of the interface of high-k praseodymium oxide thin films on silicon surfaces

Laure Libralesso

► **To cite this version:**

Laure Libralesso. Characterization of the interface of high-k praseodymium oxide thin films on silicon surfaces. Condensed Matter [cond-mat]. Université Joseph-Fourier - Grenoble I, 2006. English. NNT : . tel-00121855v2

**HAL Id: tel-00121855**

**<https://theses.hal.science/tel-00121855v2>**

Submitted on 4 Apr 2007

**HAL** is a multi-disciplinary open access archive for the deposit and dissemination of scientific research documents, whether they are published or not. The documents may come from teaching and research institutions in France or abroad, or from public or private research centers.

L'archive ouverte pluridisciplinaire **HAL**, est destinée au dépôt et à la diffusion de documents scientifiques de niveau recherche, publiés ou non, émanant des établissements d'enseignement et de recherche français ou étrangers, des laboratoires publics ou privés.

**UNIVERSITE JOSEPH FOURIER – GRENOBLE 1**

**U.F.R. DE PHYSIQUE**

EUROPEAN SYNCHROTRON RADIATION FACILITY (E.S.R.F.)

**DOCTORAT**

Discipline : **Physique**

Spécialité : **Matériaux**

Présentée et soutenue publiquement par

**Laure LIBRALESSO**

**Caractérisation de l'interface de couches minces  
d'oxyde de praséodyme « high-k »  
sur surfaces de silicium**

*Directeur de thèse :*     **Jörg ZEGENHAGEN**

*Co-directrice :*       **Catherine DUBOURDIEU**

Soutenue le 28 septembre 2006

**Jury :**

<b>M. Joël CHEVRIER</b>	LEPES / CNRS - UJF, Grenoble	<i>Président du jury</i>
<b>M. Guy HOLLINGER</b>	LEOM / Ecole Centrale de Lyon	<i>Rapporteur</i>
<b>M. Wolfgang MORITZ</b>	LMU / Dept. of Earth & Environmental Sciences - Section Crystallography	<i>Rapporteur</i>
<b>M<sup>me</sup> Claudine NOGUERA</b>	LPS / INSP – Université Paris Sud	<i>Examineur</i>
<b>M. Jörg ZEGENHAGEN</b>	ESRF, Grenoble	<i>Directeur de thèse</i>
<b>M<sup>me</sup> Catherine DUBOURDIEU</b>	LMGP / CNRS-INPG	<i>Co-directrice de thèse</i>
<b>M. Daniel BENSAHEL</b>	STMICROELECTRONICS	<i>Invité</i>



Characterization of the interface of  
high-k praseodymium oxide  
thin films on silicon surfaces

by

Laure LIBRALESSO

A Thesis Submitted to  
the University Joseph Fourier (Grenoble, FRANCE)  
for the grade of Doctor of Philosophy  
in Physics

July, 2006



*“La science n’a pas de patrie,  
car la connaissance appartient  
à l’humanité et est le phare  
qui éclaire le monde”,*

*Louis PASTEUR*

*À mes parents.*



# Acknowledgments

*This work has been carried out within the Surface and Interface Science Group of the European Synchrotron Radiation Facility (E.S.R.F.) in Grenoble. I would like first to acknowledge Jörg Zegenhagen, responsible for the ID32 beamline, to have given me this great opportunity to carry out this Ph.D. project within his team. As my thesis supervisor, he was always available for discussions and provided me valuable advice throughout this research work.*

*I am grateful to Catherine Dubourdieu, my thesis co-supervisor, for her interest in the project, her help in presenting better my results (always asking relevant questions - not always so easy to answer). Catherine, your rigorous analysis and your pragmatic way to conduct research really helped me to progress.*

*Tien-Lin Lee, I express you my deep gratitude for your valuable collaboration and your constant interest in this work. Your passion and motivation in Science are inexhaustible and I have learnt so much from you. Thanks to have shared with me all these hours of work. You have helped me to get a better perspective on the collected results. Your knowledge is really precious. Thank you for your support and friendly encouragements.*

*I am also thankful to Thomas Schroeder to have been the one who initiated this project among the ID32 research subjects and for his guidance through the first months of the thesis. He introduced me to the gate oxide problematic and taught me a lot in the huge surface science world.*

*I am honored that Professors Guy Hollinger and Wolfgang Moritz have accepted to judge this thesis manuscript. I also wish to express deep thanks to the other committee members: Joël Chevrier, Claudine Noguera, and Daniel Bensahel.*

*I am happy to acknowledge Nicole Jeutter for the enthusiastic and fruitful discussions we had about silicon surfaces, thin film oxide growths and surface x-ray diffraction. It was really motivating to collaborate with you Nicole. I also thank Wolfgang Moritz to have received me in his group within a week in the framework of the PhD work and to have deepened my knowledge in surface x-ray diffraction. Thank you also to Dieter Schmeisser and Patrick Hoffmann for the collaborative work we had within the first year of the PhD project.*

*Special thanks to Isabelle Joumard, my office-mate, for all the discussions we had, not only scientific ones, for her wise advice and a constant serenity. I appreciated a lot to share the same office with you and I wish you all the best for your next position at the CNRS.*

*I also would like to thank the ESRF for having provided the financial support for this PhD work.*

*I am grateful to all the people who assisted and helped me during this project: Jean-Pierre Vassali, an expert in preparing excellent well-oriented silicon crystal surfaces; Igor Matko, a TEM expert who realized high resolution TEM cross section images of our samples; Frédérique Ducroquet, who carried out the electrical measurements on our samples (thank you very much Frédérique for your help and your explanations); Irina Snigireva who helped us to trace the source of nickel impurities in the UHV chamber thanks to her expertise in scanning electron microscopy; Harald Müller who assisted us in the ESRF Chemistry Lab. Thanks also to the ESRF mechanics service team for their support, in particular with the sample holders machining.*

*All my other colleagues from ID32 are also sincerely acknowledge: Frank and Yvonne, the electrochemists; Sebastian Thiess, the photoemission and x-ray standing waves PhD student expert; Lionel André, technician on ID32 (merci Lionel pour ton aide!); Helena Isern, our very well organized BLOM (thank you Helena for all your advice); Lucien Petit, our engineer (je me souviendrai toujours de ton délicieux gâteau aux trois chocolats!) Manuel Perez, our BLISS support (incredibly dynamic guy!).*

*And all the other members (past or present) of the Surface and Interface Science Group: in particular Ioana popa (chocolate addicted), Marcelo, Dina, Bärbel, Luciana, Oier, Cristian, Angelo, Tobias... and all the others: thank you for your kindness!*

*All my colleagues and friends from the ESRF/ILL photo club, in particular Jo (keep smiling :o) ), Chantal, Christophe and Franck: thank you for your help and advice!*

*Didier, camarade de formation (citons ici l'IUT Mesures Physiques de Grenoble), merci pour les quelques courses à pied qui m'ont permis de m'aérer l'esprit et lever la tête du guidon! c'est promis, on y retourne prochainement! ;o)*

*Fabrizio e Monica, grazie di tutto amici miei! Merci également à toutes les personnes qui ont contribué de près ou de loin à rendre ces trois années mémorables: Murielle & Co, Silvietta (cara amica mia ti auguro fortunà e felicità), Daniela (simpaticissima milanese), Viviana (mi ricordero del tuo dinamismo e la tua gioia di vivere!), Leide (peaceful Bresilian woman, when do we go back to yoga?), Lio (mouses, snails and turtles remind me of you), Fabio, Alessandro, Chiara,... et tous les autres: amicizzia a tutti!*

*I also thanks my brother for his kindness and wish him all the best in his studies. The words of thank at the end go to my parents, without whom this work would never have come into existence (literally): Merci pour tout!*

Laure Libralesso.



# Contents

<b>Acknowledgements</b>	<b>i</b>
<b>General Introduction</b>	<b>1</b>
<b>1 Pr-oxide/Silicon interface formation and Gate oxides</b>	<b>4</b>
1.1 Interest in “High-K” materials . . . . .	6
1.1.1 Worldwide efforts in search of alternative high-K dielectrics . . . . .	8
1.1.2 $\text{Pr}_2\text{O}_3$ as a gate oxide . . . . .	9
1.2 $\text{Pr}_2\text{O}_3$ bulk properties: a $\text{PrO}_2$ derived structure . . . . .	11
1.3 $\text{Pr}_2\text{O}_3$ thin films on Si(111) . . . . .	15
1.4 Present status about the Pr-oxide growth on Si(001) by MBE . . . . .	18
1.4.1 Differences in MBE growth . . . . .	18
1.4.2 The very initial stage - a $3\times 1$ phase . . . . .	20
1.4.3 An amorphous Pr-silicate layer next to the interface . . . . .	21
1.4.4 Thicker films - the $\text{Pr}_2\text{O}_3$ cubic phase . . . . .	23
1.5 Scientific motivation of this work: The Oxide/Si interfaces . . . . .	24
1.5.1 Why $\text{Pr}_2\text{O}_3$ ? . . . . .	24
1.5.2 Scientific issues . . . . .	26

<b>2</b>	<b>Experimental</b>	<b>29</b>
2.1	UHV sample preparation and sample transfer . . . . .	29
2.1.1	The small UHV system . . . . .	29
2.1.2	The big UHV chamber for sample transfer . . . . .	30
2.2	Scanning tunneling microscopy . . . . .	32
2.2.1	Principle and set up . . . . .	32
2.2.2	Use and limits of the STM . . . . .	34
2.3	Low energy electron diffraction (LEED): Principle and set-up . . . . .	34
2.4	Auger electron spectroscopy (AES) . . . . .	36
2.5	XRD experiments on the ID32 beamline . . . . .	38
2.5.1	Baby chamber transfers . . . . .	38
2.5.2	Diffraction set-up . . . . .	38
2.5.3	X-ray reflectivity . . . . .	41
2.5.4	Grazing incidence x-ray diffraction . . . . .	45
2.5.5	Patterson function . . . . .	54
2.6	X-ray photoelectron spectroscopy . . . . .	55
2.6.1	Sample transfer . . . . .	55
2.6.2	XPS set-up . . . . .	56
2.6.3	Principle . . . . .	57
2.6.4	Preliminaries before data collection . . . . .	60
<b>3</b>	<b>Pr<sub>2</sub>O<sub>3</sub> growth on Si(111)</b>	<b>63</b>
3.1	The Si(111)-7×7 reconstructed surface . . . . .	63
3.1.1	Surface preparation on wafers . . . . .	63
3.1.2	LEED and STM results . . . . .	64
3.2	Pr <sub>2</sub> O <sub>3</sub> on Si(111) . . . . .	66
3.2.1	Oxide growth . . . . .	66
3.2.2	Results . . . . .	67
3.2.3	Discussion . . . . .	71
3.2.4	Summary . . . . .	73

<b>4</b>	<b>UHV growth of Pr-oxide on Si(001)</b>	<b>75</b>
4.1	Si substrate surface preparation and characterization . . . . .	76
4.1.1	Cleaning of the hat shaped silicon substrates . . . . .	76
4.1.2	LEED and STM results . . . . .	77
4.2	The oxide growth conditions . . . . .	79
4.3	Thickness dependence of the Pr-O film growth . . . . .	80
4.3.1	<i>in-situ</i> study by LEED and STM . . . . .	80
4.3.2	Summary . . . . .	87
4.3.3	XRD study . . . . .	87
4.4	Phases identification . . . . .	90
4.4.1	XRD results and structural properties . . . . .	90
4.4.2	XPS results . . . . .	96
4.4.3	Summary . . . . .	99
4.5	Room temperature grown samples subsequently post-annealed in different (P,T) conditions . . . . .	100
4.5.1	XPS and Auger findings at the beamline . . . . .	100
4.5.2	Complementary AES results from the SCL . . . . .	104
4.5.3	Summary . . . . .	108
4.6	Discussion on the Pr-O film growth on Si(001) under UHV . . . . .	108
<b>5</b>	<b>Pr-oxide thin films on Si(001):</b>	
	<b>The 3×1 phase</b>	<b>112</b>
5.1	Growth at different oxygen partial pressure at fixed temperature . . . . .	113
5.1.1	X-ray structural characterization at ID32 . . . . .	113
5.1.2	XPS and Auger results obtained at ID32 . . . . .	115
5.1.3	Characterization by AES . . . . .	121
5.1.4	Summary . . . . .	122
5.2	Growth at different T with P <sub>O2</sub> fixed . . . . .	122
5.2.1	XRD results from the beamline . . . . .	123
5.2.2	Characterization by AES . . . . .	125

5.2.3	Summary . . . . .	127
5.3	Short summary on the growth optimization . . . . .	128
5.4	Characterization of films prepared by optimized growth conditions . . . . .	128
5.4.1	LEED, STM and AES results from the Lab . . . . .	129
5.4.2	XRD characterization at the beamline . . . . .	133
5.4.3	XPS results from the beamline . . . . .	145
5.4.4	Complementary analysis on the optimized films . . . . .	152
5.4.5	Summary . . . . .	156
5.4.6	Pr-oxide films on Si(001) : Discussions . . . . .	157
	<b>General conclusion and Outlook</b>	<b>160</b>
	<b>French summary of the thesis</b>	<b>166</b>
	<b>List of Acronyms</b>	<b>177</b>
	<b>Appendix A</b>	<b>179</b>
	<b>Appendix B</b>	<b>189</b>
	<b>Bibliography</b>	<b>190</b>





# General Introduction

The goal of this project has been to investigate, at the atomic scale and from the very early stage, the growth of praseodymium oxide on silicon (111) and (001) oriented substrates. This rare-earth oxide has been considered recently as a good “high-k” dielectric candidate to substitute  $\text{SiO}_2$  as a gate oxide in CMOS transistors for further down scaling of devices. The study reported here focuses on characterizing the film/substrate interfaces by combining several surface science techniques. On the technologically more important Si(001) substrate, the study of the influences of the growth parameters and the understanding of the phase formation at the interface has been an important aspect of our work.

Generally speaking, dielectric materials play an important role in a variety of technological applications, such as logic and memory devices, data storage and data transmission, sensors, and modern displays. Successful integration of new functional thin-film dielectrics in the conventional silicon processing technology would enable the manufacture of new devices of superior performance. The control of the oxide/silicon interface region and the understanding of the initial stages in the growth of thin films are key issues in these fields since the surface to volume ratio increases significantly in nanometer scale structures. These low dimensional structures are difficult to study, and thanks to synchrotron radiation based techniques, many unexplored aspects of these issues can be investigated.

The framework of the study presented here is based on the need, in the coming years, to replace  $\text{SiO}_2$  as a gate dielectric in microelectronic devices. To downscale further device dimensions, alternative high-k dielectrics are needed by 2008. While amorphous oxides will likely be employed in the first phase, the semiconductor industry requires solutions for crystalline oxides with an epitaxial interface to the silicon substrate by 2013 [1]. Besides perovskite oxides, films with fluorite-derived structures, such as  $\text{Pr}_2\text{O}_3$  [2], are considered promising candidates for epitaxial high-k oxides on silicon. No high resolution structural

investigations on the interface atomic structure of these gates oxides on Si(001) has been so far reported in the literature. As the interface plays a key role as the size of the devices decreases, its study motivated this project. To understand better the Pr-oxide/Si interfaces (prepared under a typical MBE growth condition), mainly three systems were studied within this project : The very early stages of the  $\text{Pr}_2\text{O}_3$  growth on Si(111) characterized by LEED and STM, the clean Si(001)- $2\times 1$  reconstructed surface, and the initial stages of  $\text{Pr}_2\text{O}_3$  growth on Si(001), as well as the phase formation at this film/substrate interface.

In this thesis work, prior to the growth of Pr-oxide on the technologically more important Si(001) surface, the  $\text{Pr}_2\text{O}_3$ /Si(111) system is examined as a model system as growth of high quality single crystalline  $\text{Pr}_2\text{O}_3$  on Si(111) surfaces occurs [3]. The initial stages of this oxide growth on Si(001) with film thicknesses up to 3–4 nm are then investigated. Our approach focuses on atomic scale studies of the Pr-oxide/Si(001) interface by several complementary *in situ* surface science techniques (LEED, AES, STM). LEED reveals whether the surface is ordered or not and gives information on the surface symmetry; AES provides chemical information on the sample surface and STM presents its morphology. These surface science techniques available in the surface characterization laboratory (SCL) of the insertion device beamline ID32 at the European Synchrotron Radiation Facility (ESRF) are complemented by synchrotron radiation grazing incidence x-ray diffraction that reveals the structure of the deposits. From this latter technique an experimental model of the  $\text{Pr}_2\text{O}_3$ /Si(001) interface is proposed and thanks to this quantitative information a valuable input on a controversially discussed  $3\times 1$  interfacial phase (silicide or Pr-oxide) is given. These results are also complemented by synchrotron based XPS measurements, which provide more chemical information on the oxide layers.

In addition, the influence of the  $\text{O}_2$  partial pressure, as well as of the growth temperature and post-annealing treatments, on the growth are also explored.

By investigating phenomena taking place on length-scales of a few nanometers we wanted to learn more about the interactions and modifications of a Si surface upon the formation of an interface with an oxide layer. For the X-ray techniques we used, in order to maximize the contribution from the interface to the total signals, a sample with an ultrathin ( $\approx 1$  nm) oxide layer is desirable. To ensure the cleanness of the substrate surfaces and the high quality of such thin layers, UHV conditions were maintained throughout the sample preparation and characterization. It should be noted that praseodymium oxides are unstable in air. Notice also that unwanted X-ray contributions and reactions with the oxide

layers, which can complicate the data analysis, can be introduced by the protection layers used in *ex-situ* measurements, i.e. a Si capping layer. Therefore, such capping layers were not considered in our experiments.

This thesis is organized as follow :

Chapter 1 presents the status in the field of “high-k” oxides, including the background for the choice of Pr-oxide, a summary of its bulk properties as well as the most recent and relevant findings of this oxide growth on both Si(111) and Si(001). The scientific motivation and goal of the work reported in this thesis is then specified.

Chapter 2 explains the experimental techniques used in this work and recalls the basic theoretical background used for analyzing the results presented in the next chapters.

Chapter 3 reports the initial stages of the Pr-oxide layer formation on the Si(111) substrate surface studied by LEED and STM. The findings are correlated with the results of Jeutter and Moritz who obtained an atomic scale structural model of the  $\text{Pr}_2\text{O}_3/\text{Si}(111)$  interface by using surface x-ray diffraction [4].

The growth of Pr-oxide on Si(001)- $2\times 1$  is reported in Chapters 4 and 5. Chapter 4 describes the results of the Pr-oxide growth on Si(001) under UHV conditions, after presenting some details on the Si(001)- $2\times 1$  substrate preparation. A phase separation is observed and Pr-silicide phase appears under UHV, beyond a certain oxide thickness. The influence of post-annealing treatments under various (P,T) conditions is also reported in this chapter.

Chapter 5 summarizes the main results of the attempts to optimize the growth parameters for  $3\times 1$  interfacial layer within a narrow (P,T) window. Furthermore, this chapter presents a comprehensive chemical and structural analysis of the optimized samples and describes the characterization results of a  $3\times 1$  interfacial phase.

The thesis closes with a summary and concludes with some suggestions for further studies of the system  $\text{Pr}_2\text{O}_3$  on silicon, which are motivated by the present findings.



## Chapter 1

# Pr-oxide/Silicon interface formation and Gate oxides

---

Our understanding of the basic physics and chemistry of oxides remains far behind that of metals and semiconductors despite their technological and scientific importance [5]. In particular, surface science studies of oxides surfaces and interfaces with metal or semiconductors present a number of critical challenges. The first major problem is the structural complexity of oxides. As an example the corundum structure ( $\alpha$ -Al<sub>2</sub>O<sub>3</sub>, V<sub>2</sub>O<sub>3</sub>, etc.) has ten atoms per unit cell. One of the first goals of a surface science study is to find out where the atoms are on a surface, but it is clear that the complexity of oxide structures can make this a formidable task [6]. A second major issue is a similarly complex combination of chemical and physical properties, such as wide ranges of possible oxidation states and hence series of oxides with different compositions. When studying surfaces and interfaces, which have reduced symmetry, all these difficulties are greatly enhanced. Another key issue is a limited number of suitable experimental techniques to study oxides. Indeed, many powerful surface science techniques like electron diffraction/spectroscopy or scanning tunneling microscopy require a conducting specimen, which is rarely the case for oxide materials. Our current understanding of insulating materials has benefited greatly from the use of X-ray scattering methods and modern synchrotron facilities in the hard X-ray regime [7]. In addition, to fully understand such complex systems as oxide surfaces and interfaces with other materials, the application of a wide range of experimental techniques (rather than the use of a single method) is necessary.

Metal oxide semiconductor field emission transistors (MOSFETs) are at the very heart of modern integrated circuits (IC's). A fundamental limit of the downscaling of these

devices is in view, concerning the exponential increase in the tunneling current with further decreasing the film thickness for the current SiO<sub>2</sub> gate oxide. Fig. 1.1 shows a schematic cross section of a field effect transistor.

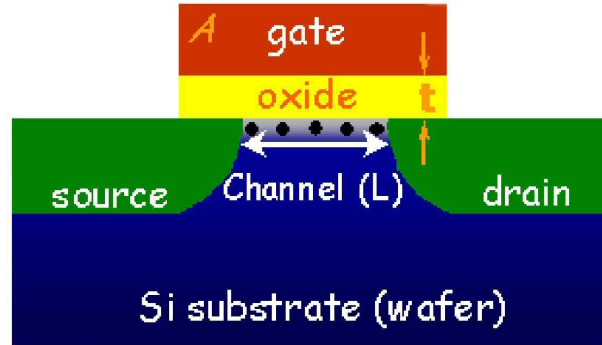


Figure 1.1: Schematic cross section of a field effect transistor.  $L$  is the channel length,  $A$  is the gate area and  $t$  is the gate oxide thickness.

The specific gate capacitance  $C$  of a field effect transistor is proportional to its area  $A$  and the dielectric constant  $K$  and inversely proportional to the thickness  $t$  of the gate dielectric. It is expressed as

$$C = \frac{K\varepsilon_0 A}{t} \quad (1.1)$$

where  $\varepsilon_0$  is the permittivity in vacuum, which is a constant ( $\varepsilon_0=8.854 \times 10^{-12}$  F.m<sup>-1</sup>).

The reduction of the leakage current while maintaining the same gate capacitance requires therefore a thicker film with a higher dielectric constant [8,9].

The need for an alternative (high-K) dielectrics has become urgent in order to replace the classical SiO<sub>2</sub> gate oxide in the next nodes when following Moore's law (45 and 32 nm) for complementary metal oxide semiconductor (CMOS) technology, which are coming up in only very few years from now [1]. Various candidates are currently studied. However, detailed knowledge of the oxide/Si(001) interface region as well as the oxide surface itself is still needed before these materials can be processed and the next step on the International Technology Roadmap for Semiconductors (ITRS) be reached in time [1].

In this chapter, once having presented the "High-K" materials interests, the choice of Pr<sub>2</sub>O<sub>3</sub> is justified. The results reported in the literature about the Pr<sub>2</sub>O<sub>3</sub>/Si(111) system are reviewed before presenting the current status about the Pr-oxide growth on Si(001) by MBE. Our scientific interest in this field is then explained. Some of the main bulk

properties of this material are recalled. Finally our objectives, together with the methods used, are explained.

## 1.1 Interest in “High-K” materials

Eq. (1.1) shows that the only way to avoid the reduction of the gate capacitance while shrinking the surface area of the transistor is to use a material with a higher dielectric constant  $K$  than  $\text{SiO}_2$ . These materials, called “high-K”, are characterized by their equivalent  $\text{SiO}_2$  thickness, called EOT (equivalent oxide thickness) and which is defined by

$$EOT = \frac{K_{\text{SiO}_2}}{K_{\text{high-K}}} \times t_{\text{high-K}} \quad (1.2)$$

where  $t_{\text{high-K}}$  is the physical thickness of the “High-K” material,  $K_{\text{high-K}}$  its dielectric constant and  $K_{\text{SiO}_2}$  the one of the silica, equal to 3.9.

Therefore the EOT corresponds to the necessary  $\text{SiO}_2$  thickness to obtain the same capacitance as the one given by a thickness  $t_{\text{high-K}}$ . The use of a “High-k” would avoid the tunneling conduction of the electrons through the gate simply by increasing the physical thickness of the gate dielectric, without decreasing of the transistor capacitance. Reciprocally the needed physical thickness of a “High-K” material as a function of the required EOT can be calculated from Eq. (1.2)

For further down-scaled devices “High-K” materials must not only have a high-K value (typically of the order of 10 to 30) but also satisfy other basic considerations. The insulators must have a **good lattice match** and a **compatible crystal structure** to Si. In addition, the oxide must satisfy various conditions such as being **stable** (thermodynamically and kinetically) in contact with Si [10] and having **high band gap** and sufficiently **large** ( $> 1$  eV) **conduction- and valence-band offsets**, with respect to the Si, to be a barrier for both electrons and holes, as recently reviewed by J. Robertson [11]. The oxide must also form a **high quality interface** with Si, with no interface states within the Si band gap. The current in the field effect transistor flows in the Si channel next to the interface, so the transistor performance depends fundamentally on the quality of this interface. The interface quality determines both carrier mobility and device stability. However, despite the intensive work on high-K oxides, the overall performances of the devices with high-K oxides

are still rather poor compared to those of  $\text{SiO}_2$  gate oxides, so that a deeper understanding of the interfaces is urgently needed. While the  $\text{SiO}_2/\text{Si}$  interface is understood in greater detail [12], partly because  $\text{SiO}_2$  is covalently bonded like Si so that simple atomic models can be constructed, in the case of high-K oxides ionic bonding without a fixed coordination creates the need for a new set of rules [13].

Fig. 1.2 presents the dielectric constant versus band gap for gate oxide candidates. It is shown that the band gap is roughly inversely proportional to the dielectric constant. As the dielectric constant increases, the band gap decreases. Thus this figure points out a problematic issue, i.e. even if it were possible to reduce the leakage current thanks to the increased thickness with increasing K, this may be nullified by the reduction of the barrier height. Since both the thickness and barrier height have an exponential influence upon the leakage current, one should find a trade-off between these two factors. For CMOS applications, most desirable candidates are dielectric materials with roughly equal valence and conduction band offsets to Si.

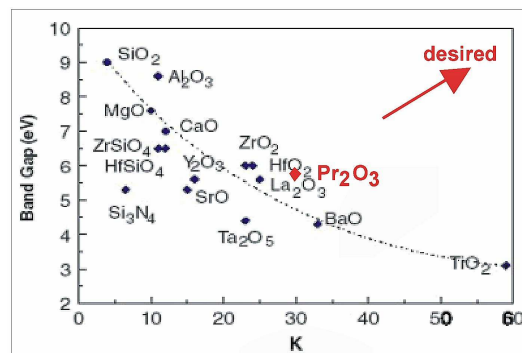


Figure 1.2: Static dielectric constant versus band gap for candidate gate oxides from [11].  $\text{Pr}_2\text{O}_3$  has been added according to the previously reported values in the literature [3]. An arrow indicates the desired trend.

The first “High-K” materials studied were the ones that were commonly used in micro-electronics and known to be compatible with the polysilicon gate electrode such as  $\text{Si}_3\text{N}_4$  ( $K=7.5$ ) [14] or  $\text{Al}_2\text{O}_3$  ( $K=11$ ) [15]. These materials exhibited high charge density and not sufficiently high K values. Therefore, studies on materials with higher K values started, such as  $\text{Ta}_2\text{O}_5$  ( $K=25$ ),  $\text{ZrO}_2$  ( $K=20-25$ ),  $\text{HfO}_2$  ( $K=20-25$ ) and  $\text{La}_2\text{O}_3$  ( $K=25$ ) [15]. On  $\text{Ta}_2\text{O}_5$ , studies revealed compatibility problems with the poly-Si gate electrode.  $\text{ZrO}_2$  and  $\text{HfO}_2$  had been considered as “Si-friendly”, i.e. thermodynamically stable on Si, and therefore are the subject of many publications but no successful integration is reported. In

addition, other potential candidates with a  $K$  value much higher, such as the  $\text{Ba}_x\text{Sr}_{1-x}\text{TiO}_3$  ( $K=200$ ) or other ferroelectric compounds, are investigated but their integration in a transistor still seems far away.

### 1.1.1 Worldwide efforts in search of alternative high- $K$ dielectrics

Amorphous Hf-oxide for high- $K$  application is a well documented subject in the literature. Hf-oxide technology is considered not good enough for the next technological nodes [11]. Indeed, this high- $K$  material has two major problems. The first drawback is the mobility degradation due to bad interface properties between Hf and Si, making necessary the use of either  $\text{SiO}_x$  or a Hf-oxide alloy interfacial layer, for instance, to increase the carrier mobility. The second problem is the Fermi level pinning (FLP) making difficult to obtain reasonably low voltage threshold in p-MOS devices [16].

In the post-Hf technology CMOS investigations, i.e. for the 32 nm node and beyond [1], many people are interested in rare-earth oxides, not only for high- $K$  gate application but also for MIM capacitors for instance. Some groups grow these rare-earth oxides by MBE (e.g. Osten's group in Germany [17–20], Kingon's group in The States (North Carolina) [21], and Iwai's group in Japan [16, 22]), other by sputtering (e.g. Gaboriaud's [23, 24] and Agius's [25] groups in France), MOCVD (e.g. Fragalà's group in Italy [26], Fröhlich's group in Slovakia [27], and Dubourdiu/Vallée in France [28]) or ALD (e.g. Scarel in Italy [29, 30], Jones in England and Ritala in Finland [31, 32]).

The common approach for alternative high- $K$  gate dielectrics has involved amorphous materials with higher dielectric constants, such as metal oxides and their silicates. The alternative is to use an epitaxial oxide, which would enable to obtain a higher interface quality with the substrate. MBE grown perovskite based oxides and rare-earth binary metal oxides are the two big oxide families under investigations.

The perovskite based oxides:  $\text{SrTiO}_3$  has been extensively studied as an epitaxial high- $K$  gate oxide candidate [33]. However, its band gap is too small ( $\approx 3$  eV) and too much asymmetric, giving rise to a conduction band offset below 1 eV. Other perovskite based oxides are currently under investigations, such as  $\text{LaAlO}_3$  for instance [34, 35].

Rare-earth binary metal oxides, like lanthanide oxide, have been reported to be among the most suitable candidates for CMOS application [18, 19, 36]. Regarding  $\text{Pr}_2\text{O}_3$ , its growth

on Si(001) has been accomplished by different growth techniques. MOCVD is used in Jones's group in England and in Finland by Ritala's and colleagues [31, 32]. Fragalà's group in Italy (Catania) also use this technique [37–40]. ALD grown Pr-oxide film are also reported from Jones's group in England and in Finland by Ritala [31, 32, 41] as well as by Päiväsäari in Finland [42]. PLD is also used for Pr-oxide deposition and Tarsa was the first one to report PLD grown Pr-oxide film in 1993 [43]; then more recently Kitai [44] and Sakai [45] in Japan presented their results obtained by using such a growth method, as well as Wolframm *et al.* [46]. MBE grown Pr-oxide films on Si(001) are reported from Müssig [47–49], Osten [2, 3, 50–53], and Schmeisser [54–59] mainly.

### 1.1.2 Pr<sub>2</sub>O<sub>3</sub> as a gate oxide

When the project started in 2003, the rare earth metal oxide Pr<sub>2</sub>O<sub>3</sub> was under investigations for microelectronic applications and the heteroepitaxial system Pr<sub>2</sub>O<sub>3</sub>/Si(001) was reported as having promising properties regarding the CMOS high-K requirements described in section 1.1.1. [3]. For instance, as displayed in Fig. 1.2, Pr<sub>2</sub>O<sub>3</sub> presents both a high K value ( $\approx 30$ ) and a relatively large band gap ( $\approx 6$  eV). These two properties made it considered for replacing SiO<sub>2</sub>.

In their previous studies, Osten *et al.* [2, 3, 53] have shown using MBE that crystalline Pr<sub>2</sub>O<sub>3</sub> grows as the cubic phase on Si(001), with a thin amorphous silicate layer separating the crystalline film from the Si substrate. Although this amorphous layer can possibly reduce the interface state density at the interface, it is likely to have a lower-K value than the crystalline Pr<sub>2</sub>O<sub>3</sub>. They also reported that rapid thermal annealing in dry N<sub>2</sub> up to 1050 °C for 20 sec. or 450 °C for 20 min did not cause any significant changes in the film properties, indicating that Pr<sub>2</sub>O<sub>3</sub> can survive thermal treatments typical for CMOS processing. Using gold as gate electrodes, they demonstrated leakage currents of  $J_g \approx 5.10^{-9}$  A/cm<sup>2</sup> at  $V_g = \pm 1.0$  V with film thickness of about 11 nm. The C-V measurements rendered EOTs of 1.4 nm and  $k \approx 30$  with no significant hysteresis for samples that have been post-annealed at 800 °C in UHV [60]. The oxide films were found to be unstable in air due to oxygen in-diffusion, which led to interfacial SiO<sub>2</sub> formation and electrical degradation.

As discussed in section 1.1, a large band gap is one of the criterions required for a gate oxide. For cubic Pr<sub>2</sub>O<sub>3</sub>, Osten *et al.* [51] have reported using valence band XPS and high

field tunneling a valence band offset of  $1.1 \pm 0.2$  eV and a conduction band offset of 0.5-1.5 eV, respectively for Pr<sub>2</sub>O<sub>3</sub> on Si(001). Knowing the band gap of Si to be 1.1 eV, their result suggests a band gap of 2.5-3.9 eV. Using O1s X-ray absorption spectroscopy (XAS) Schmeisser and Müssig [55] estimated the band gap of Pr<sub>2</sub>O<sub>3</sub> to be about 7 eV. By comparing the valence band XPS spectra of Si and Pr<sub>2</sub>O<sub>3</sub>/Si(001) and the onset of the Si2p and Pr4d XAS data, they measured the valence band and conduction band offsets to be both around 2 eV, which leads to a smaller band gap of 5.1 eV [56,61]. More recently Lupina *et al.* [62] have used valence band XPS and the energy loss feature in O1s core-level to determine the valence band offset and band gap to be 2.9 and 5.6 eV, respectively, for Pr-silicate on Si(001). This result suggests an asymmetric band alignment with a conduction band offset of 1.6 eV. A similar measurement was carried out by Sakai *et al.* [63] on Pr-silicate on Si(111) and they found a band gap of 6.5 eV and a more symmetric valence band offset of 2.75 eV.

Since the earlier work by Osten *et al.* [3], electrical characterizations of Pr<sub>2</sub>O<sub>3</sub> and Pr-silicate on Si have been reported by several other groups. Schwalke and Stefanov [64] have recently demonstrated fully functional MOSFETs using 17 nm thick MBE grown crystalline Pr<sub>2</sub>O<sub>3</sub> as the gate dielectric and polysilicon as the gate electrode. The MOS stacks showed an EOT of 1.8 nm with a leakage current below  $10^{-6}$  A/cm<sup>2</sup> for gate lengths < 10 μm. However, the Pr<sub>2</sub>O<sub>3</sub> gate stacks were found to suffer from severe charge trapping effects and become leaky for large gate lengths. Lupina *et al.* [62] reported electrical measurements of Pr-silicate films prepared by post-annealing Pr-metal layers on SiO<sub>2</sub>/Si(001). The 5 nm silicate films showed an EOT of 1.8 nm and a leakage current of  $5 \times 10^{-5}$  A/cm<sup>2</sup> at 1 V. The 10 nm thick Pr-silicate films grown on Si(111) by e-beam evaporation of Pr<sub>6</sub>O<sub>11</sub> by Sakai *et al.* [63] showed an EOT of 1.9 nm and leakage current of  $3 \times 10^{-9}$  A/cm<sup>2</sup> at 1 V. By adding Ti to the Pr-silicate layers, Schroeder *et al.* [64] reported an improved EOT of 1.2 nm but with a high leakage current of  $10^{-2}$  -  $10^{-3}$  A/cm<sup>2</sup>. The dielectric constants of 15 nm thick polycrystalline hexagonal-phase Pr<sub>2</sub>O<sub>3</sub> and 8 nm thick amorphous Pr-silicate films grown by MOCVD have been evaluated by Lo Nigro *et al.* [38] to be around 16 and 8, respectively. The dielectric constant of Pr-silicate films prepared by post-annealing amorphous PrO<sub>x</sub> layers grown by atomic layer epitaxy has been measured by Jones *et al.* [32] to be 21.

To summarize, the band gaps of both Pr<sub>2</sub>O<sub>3</sub> and Pr-silicate were measured to be around 6 eV with a valence band and a conduction band offsets of around 2 eV, which are high

enough to meet the requirements for gate oxide application. High-K values and low leakage currents have been demonstrated for these materials. However, large variations related to the growth conditions can be found in the results of the electrical characterizations, and fully functional transistors fabricated based on  $\text{Pr}_2\text{O}_3$  have revealed problems associated with the high interface states. More fundamental studies on interfacing Pr-oxide with Si would be therefore needed.

## 1.2 $\text{Pr}_2\text{O}_3$ bulk properties: a $\text{PrO}_2$ derived structure

The two Pr compounds of main interest in this study are  $\text{PrO}_2$  and  $\text{Pr}_2\text{O}_3$ . However, the oxides of praseodymium include not only  $\text{Pr}_2\text{O}_3$  and  $\text{PrO}_2$  but also a wide range of intermediate phases. Fig. 1.3 shows the complicate Pr-O binary compound phase diagram, as extracted from Ref. [65].  $\text{Pr}_2\text{O}_3$  is the most oxygen deficient phase while  $\text{PrO}_2$  is the richest one.

This very rich phase diagram has several stable stoichiometries with many  $\text{PrO}_x$  phases existing in the range  $1.5 < x < 2$ . All of them are described in Ref. [65]. With increasing oxygen content, the valence of the Pr ion changes from 3+ in  $\text{Pr}_2\text{O}_3$  to 4+ in  $\text{PrO}_2$ . For intermediate oxygen concentrations ( $1.5 < x < 2$ ), Pr sites have different oxygen coordination numbers. This allows for a stable trivalent or tetravalent Pr state.

Hyde *et al.* [66] have studied the temperature dependence of  $\text{PrO}_x$  composition under different oxygen pressure for  $1.5 \leq x \leq 1.833$ . They showed, for example, under 7.5 mbar of oxygen, that Pr-oxides lost oxygen continuously as temperature increased from below 300 °C and reduced to  $\text{Pr}_2\text{O}_3$  at around 1100 °C. When annealed in UHV, complete reduction of  $\text{Pr}_6\text{O}_{11}$  to  $\text{Pr}_2\text{O}_3$  is expected to occur at a much lower temperature.

Three basic structures are known for praseodymium oxide [65, 67].  $\text{PrO}_2$  exhibits the cubic calcium fluorite structure as shown in Fig. 1.4(a).  $\text{Pr}_2\text{O}_3$  crystallizes usually in the cubic manganese oxide (or bixbyite) structure (C-type), as presented in Fig. 1.4(b). This structure is based on the calcium fluorite structure, where 1/4 of the oxygen atoms have been removed from specific lattice sites, resulting in periodic oxygen vacancies. In addition, half of the Pr atoms are slightly displaced from the ideal cation sites. Figs. 1.4(c) and (d) display the  $\text{PrO}_2$  and cubic  $\text{Pr}_2\text{O}_3$  unit cells, respectively. For  $\text{Pr}_2\text{O}_3$ , there are also reports

of the hexagonal lanthanum oxide structure forming at high temperature (A-type), which is displayed in Fig. 1.5(b). Fig. 1.5(a) presents a hexagonal  $\text{Pr}_2\text{O}_3$  unit cell. The lattice parameters for these three structures are listed in Table 1.1.

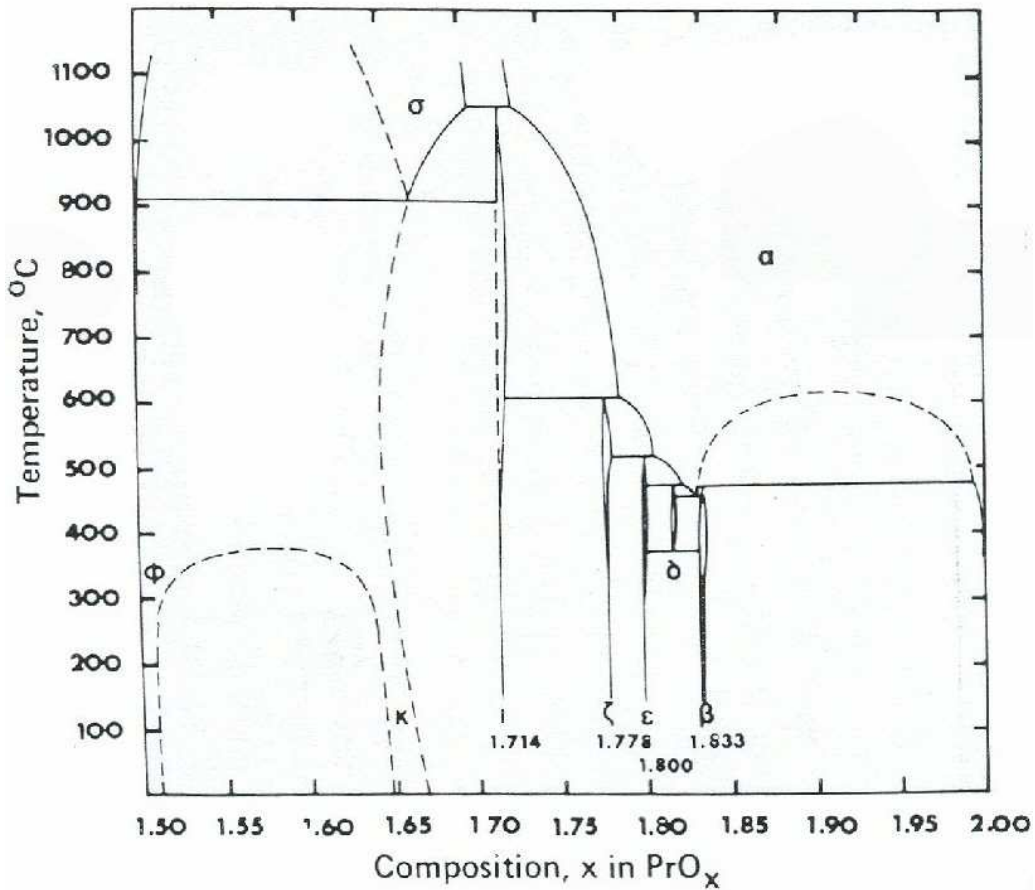


Figure 1.3: Pr-O binary compound phase diagram, as extracted from [65].

The cubic phases of  $\text{Pr}_2\text{O}_3$ ,  $\text{Y}_2\text{O}_3$ ,  $\text{Gd}_2\text{O}_3$ , etc, all share the bixbyite-type structure, which is also known as the C-type structure of the rare-earth sesquioxides and most of these oxides have many other possible phases. More detailed information on these binary oxides and other rare-earth oxides (thermodynamic and structural properties) can be found in Refs. [65, 67].

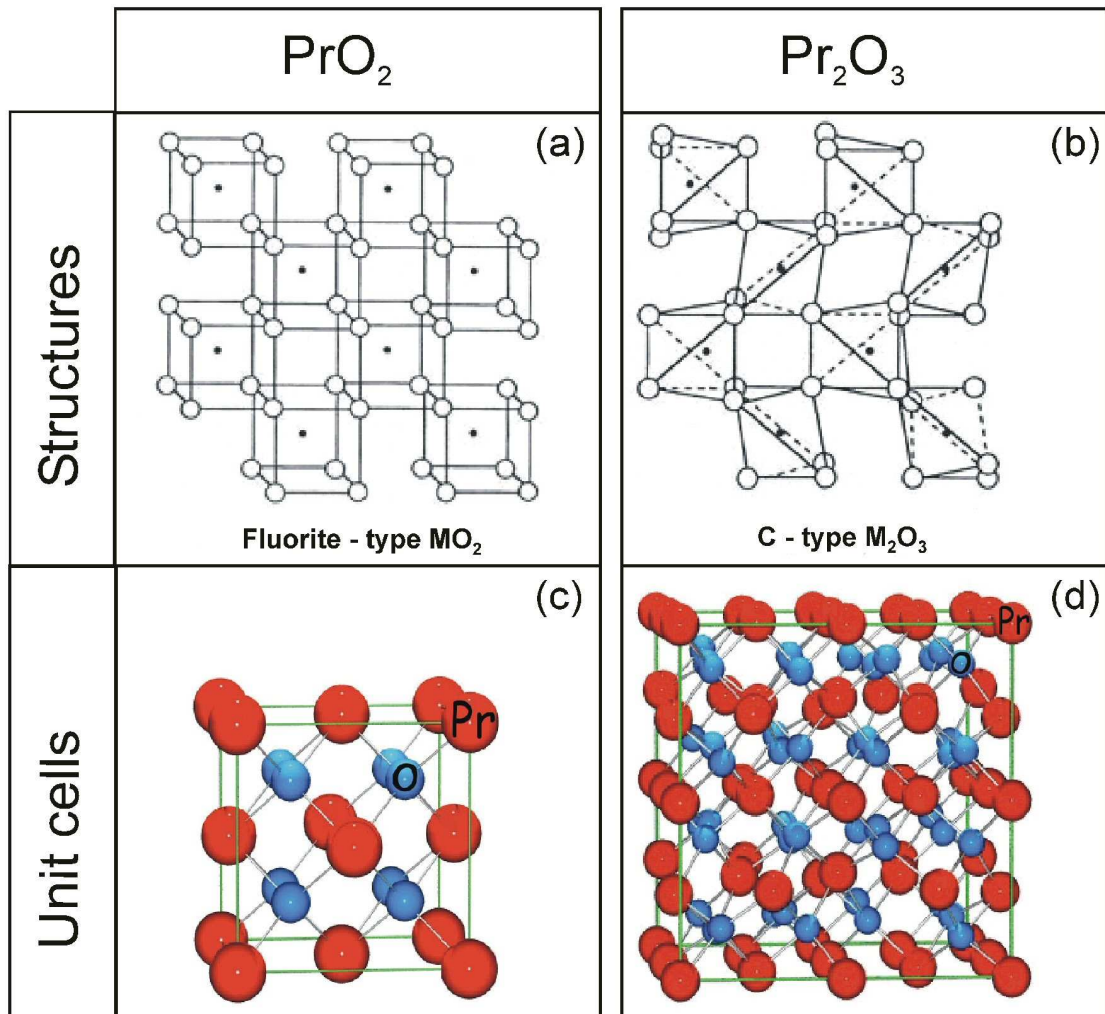


Figure 1.4:  $\text{PrO}_2$  and  $\text{Pr}_2\text{O}_3$  bulk structures (a) and (b) and unit cells (c) and (d). (a) For  $\text{PrO}_2$  fluorite each  $\text{Pr}^{4+}$  has eight equidistant  $\text{O}^{-2}$  neighbors. (b) Cubic  $\text{Pr}_2\text{O}_3$  can be obtained from the fluorite structure by removing every fourth atom in each (001) row of O atoms in such a way that the vacancy concentration is 25% in each row. Each  $\text{Pr}^{3+}$  has six equidistant  $\text{O}^{-2}$  neighbors. (c) one  $\text{PrO}_2$  unit cell contains 4 Pr atoms and 8 O atoms while (d) one  $\text{Pr}_2\text{O}_3$  unit cell contains 32 Pr atoms and 48 O atoms.

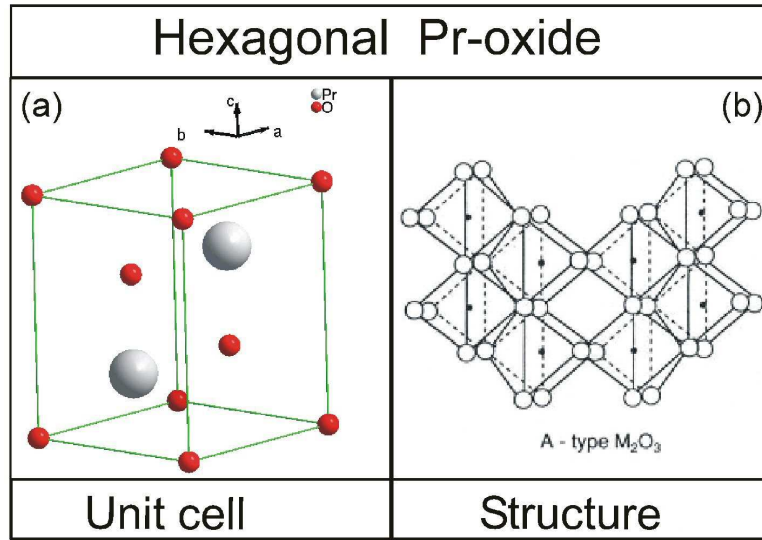


Figure 1.5: Hexagonal  $Pr_2O_3$ . Each  $Pr^{3+}$  has six equidistant  $O^{-2}$  neighbors and one  $O^{-2}$  neighbor at a slightly larger distance than cubic  $Pr_2O_3$ .

	Crystal system	Space group	a (nm) b (nm) c (nm)	No of Pr	No of O	Atom	X	Y	Z
PrO <sub>2</sub>	cubic	Fm $\bar{3}$ m (225)	0.5392	4	8	Pr	0.000	0.000	0.000
			0.5392			O	0.250	0.250	0.250
			0.5392						
Pr <sub>2</sub> O <sub>3</sub>	cubic	Ia $\bar{3}$ (206)	1.1152	32	48	Pr1	0.250	0.250	0.250
			1.1152			Pr2	0.970	0.000	0.250
			1.1152			O	0.386	0.145	0.380
Pr <sub>2</sub> O <sub>3</sub>	trigonal	P $\bar{3}$ m1 (164)	0.3857	2	3	Pr	0.333	0.667	0.235
			0.3857			O1	0.333	0.667	0.630
			0.6016			O2	0.000	0.000	0.000

Table 1.1: Crystal structures of PrO<sub>2</sub> and cubic and hexagonal phases of Pr<sub>2</sub>O<sub>3</sub>. The lattice parameters a, b and c and the atomic coordinates X, Y and Z are obtained from Ref. [68].

### 1.3 Pr<sub>2</sub>O<sub>3</sub> thin films on Si(111)

Praseodymium sesquioxide (Pr<sub>2</sub>O<sub>3</sub>) thin films have been found to grow on Si(111) in the trigonal phase [43, 52, 69], which is in the literature mostly referred to as hexagonal. Until now Si(001) is the substrate of choice for micro-electronic applications mostly because of the superior quality of SiO<sub>2</sub>. Replacing SiO<sub>2</sub> might also lead to reconsidering the use of the (001) orientation of the silicon substrate. This reconsideration has led to various growth studies of different “high-K” oxides on Si(111) [70] and other Si substrate orientations (e.g. Si(110) and Si(113)), as well as on other high mobility substrates such as Ge [71, 72]. In this context we have investigated the heteroepitaxial system Pr<sub>2</sub>O<sub>3</sub>/Si(111).

Tarsa *et al.* deposited Pr<sub>2</sub>O<sub>3</sub> on Si(111) by pulsed laser deposition in 1993 [43]. They found the Pr<sub>2</sub>O<sub>3</sub> “hexagonal” phase (A-type) growing with its (0001) surface on Si(111), as identified by RHEED and TEM. Similarly the azimuthal orientation of the Pr<sub>2</sub>O<sub>3</sub> deposits was determined such that the Pr<sub>2</sub>O<sub>3</sub> [2 $\bar{1}\bar{1}$ 0] direction is parallel to the [1 $\bar{1}$ 0] direction of Si(111). This epitaxy was also revealed for MBE grown films that exhibited high quality and a sharp Pr<sub>2</sub>O<sub>3</sub>/Si(111) interface, as demonstrated in Fig. 1.6 that presents the cross sectional TEM picture of MBE grown hexagonal Pr<sub>2</sub>O<sub>3</sub> on Si(111) from Liu *et al.* [69].

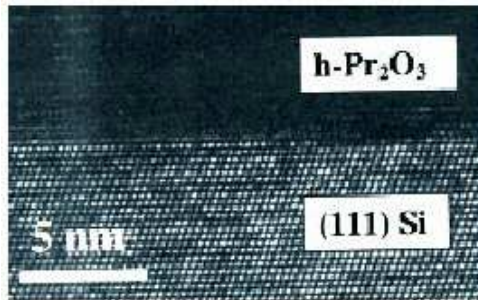


Figure 1.6: Cross sectional TEM picture from Liu *et al.* [69]. Sharp interface forms between the hexagonal Pr<sub>2</sub>O<sub>3</sub> film and the Si(111) substrate.

A very recent in situ surface X-ray diffraction (SXRD) study on ultra thin films confirmed this epitaxial relationship and revealed an interfacial structure consisting of a Si-O-Pr bond with Pr atoms above the T<sub>4</sub> sites and no indication for the presence of an intermediate oxide layer [4].

Table 1.2 shows the in-plane lattice constants and the lattice mismatch of the (0001) surface

unit cell of the hexagonal  $\text{Pr}_2\text{O}_3$  with the Si(111) surface unit cell. For comparison, similar information is given for the cubic  $\text{Pr}_2\text{O}_3$  (111) surface unit cell.

	Surface plane	Surface unit cell	Lattice constants $a = b$ (nm)	Mismatch with Si
Si	(111)	$1 \times 1$	0.384	
Hexagonal $\text{Pr}_2\text{O}_3$	(0001)	$1 \times 1$	0.386	-0.5%
Cubic $\text{Pr}_2\text{O}_3$	(111)	$4 \times 4$	1.577	-2.6%

Table 1.2: In-plane lattice constants of the hexagonal  $\text{Pr}_2\text{O}_3$ (0001) surface and cubic  $\text{Pr}_2\text{O}_3$ (111) surface and their mismatches with the Si(111) surface unit cell [73]. These three surfaces are plotted in Figs. 1.7 and 1.8.

The lattice mismatch between the “hexagonal” basal planes of  $\text{Pr}_2\text{O}_3$  and the Si(111) surface is only about -0.5% and both surface planes exhibit three-fold symmetry [73]. This small lattice mismatch is the key reason for the high quality epitaxial growth.

Using GIXRD, Schroeder *et al.* [74] have investigated the thickness dependent structural evolution of hexagonal  $\text{Pr}_2\text{O}_3$  layers on Si(111). They found that up to 3 nm the  $\text{Pr}_2\text{O}_3$  layers are pseudomorphic with a domain size about 50 nm, which reduces to 20 nm when the films are relaxed. For thicker as-grown films they observed the appearance of small fraction of cubic  $\text{Pr}_2\text{O}_3$ .

In addition to the (0001) plane of the hexagonal  $\text{Pr}_2\text{O}_3$ , the (111) plane of the cubic  $\text{Pr}_2\text{O}_3$  also has the same symmetry as the Si(111) surface with a -2.6% lattice mismatch. Liu *et al.* [69] have shown a hexagonal to cubic phase transition of  $\text{Pr}_2\text{O}_3$ /Si(111) films after being post-annealed in 1 bar of  $\text{N}_2$  at 600 °C. The cubic  $\text{Pr}_2\text{O}_3$  stacked along either the [111] or  $\overline{[111]}$  direction and exhibited two rotational domains. More recently it has been shown that by post-annealing hexagonal  $\text{Pr}_2\text{O}_3$ /Si(111) films in  $10^{-5}$  mbar of oxygen at 600 °C, 111-oriented cubic  $\text{Pr}_2\text{O}_3$  layers that follow a single stacking sequence can be achieved with  $\text{SiO}_2$  and Pr-silicate forming at the interface [75]. Interestingly, Sakai *et al.* [63] have reported the direct growth of cubic  $\text{Pr}_2\text{O}_3$  on Si(111) at 300 °C. Such films showed two rotational domains with an interfacial layer.

Fig. 1.7 depicts the  $1 \times 1$  unit cell of an idea-bulk terminated Si(111) surface. Fig. 1.8 shows the (111) and (0001) surface structures and unit cells of the cubic and hexagonal  $\text{Pr}_2\text{O}_3$ , respectively. The edge of the  $4 \times 4$  unit cell of the cubic  $\text{Pr}_2\text{O}_3$ (111) surface corresponds

to the diagonal of a cubic face of the bulk unit cell. The side views show that the two structures are fundamentally different in terms of their atomic layer stacking sequences and oxygen distributions.

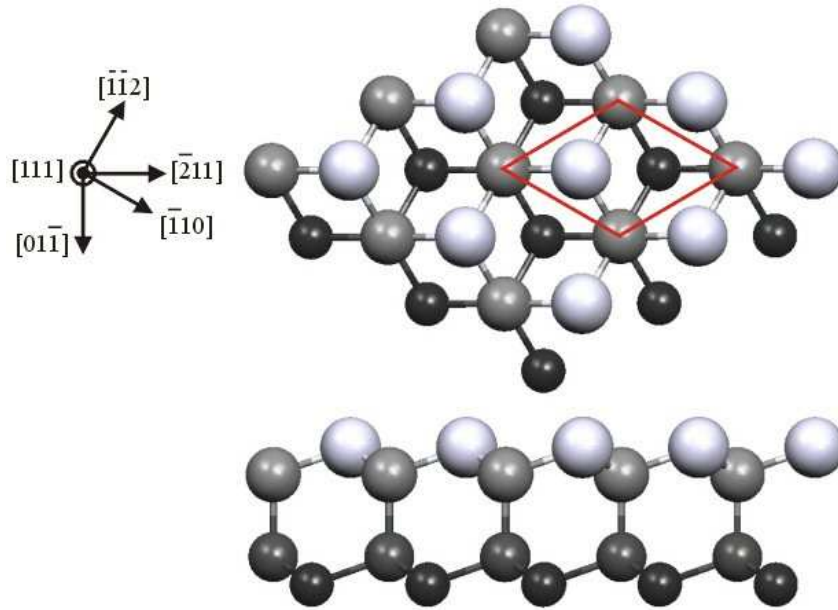


Figure 1.7: The  $1 \times 1$  unit cell of the Si(111) surface.

Unlike the case of cubic  $\text{Pr}_2\text{O}_3$  on Si(001), hexagonal  $\text{Pr}_2\text{O}_3$  on Si(111) can be overgrown with epitaxial Si with a smooth interface. This overgrowth of Si has been demonstrated by Tarsa *et al.* [43] and Osten *et al.* [51]. The Si epitaxial layer was found to grow along both the  $[111]$  and  $[\bar{1}\bar{1}\bar{1}]$  directions, leading to two rotational domains separated by  $180^\circ$  [76]. Such an epitaxial growth is considered to be interesting for developing Si/insulator or insulator/Si/insulator structure for applications in microelectronics and optoelectronics. The growth of  $\text{Gd}_2\text{O}_3/\text{Si}/\text{Gd}_2\text{O}_3/\text{Si}(111)$  has been recently reported by Fissel *et al.* [19].

It was noted in section 1.2 that the cubic  $\text{Pr}_2\text{O}_3$  has a  $\text{CaF}_2$  derived structure. It is known that  $\text{CaF}_2$  also grows along the  $[111]$  direction on Si(111) and the  $\text{CaF}_2/\text{Si}(111)$  system has been extensively studied in the past [77–81].

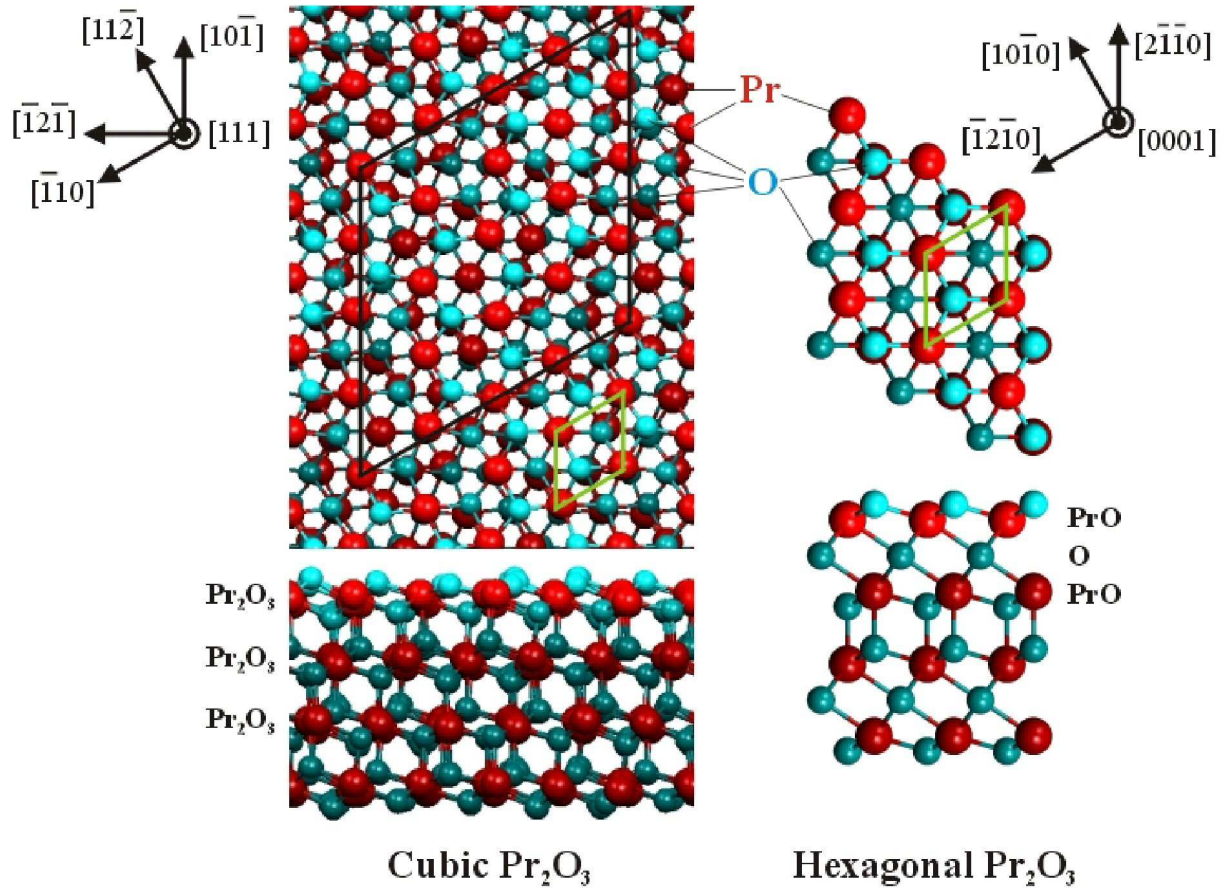


Figure 1.8: Cubic  $\text{Pr}_2\text{O}_3(111)$  and hexagonal  $\text{Pr}_2\text{O}_3(0001)$  surfaces (top) together with their respective side-views (bottom). The green rhombuses show the  $1 \times 1$  surface unit cells. The black rhombus on the cubic (111)  $\text{Pr}_2\text{O}_3$  plane represents the  $4 \times 4$  surface unit cell. .

## 1.4 Present status about the Pr-oxide growth on Si(001) by MBE

### 1.4.1 Differences in MBE growth

$\text{Pr}_2\text{O}_3$  has been found to grow in the cubic phase on Si(001) [52]. Experimental detail available in the literature regarding MBE grown  $\text{Pr}_2\text{O}_3$  films on Si(001) indicate some technical differences with respect to the substrate cleaning method, the deposition process and the source material, without emphasizing differences in the  $\text{Pr}_2\text{O}_3$  film quality.

For instance Fissel [60], Osten [50], and more recently Guo [82], reported results collected from hydrogen-terminated Si(001) substrates. Schmeisser [56,57] and Müssig [47] collected results for films grown on thermally cleaned Si(001) surfaces by flash annealing treatments as described in Ref. [83]. Osten, in Ref. [51], presented results obtained from these two kinds of surfaces: the initial stages of the  $\text{Pr}_2\text{O}_3$  growth were studied on thermally cleaned Si(001) surfaces, while for thicker layers growth experiments were performed on hydrogen-terminated surfaces. It is expected that the hydrogen-terminated Si(001) surface prepared by wet cleaning involving brief HF etching is atomically rough [84] with measurable amounts of carbon and oxygen [85]. In addition, the influence of surface miscut on the nucleation of Pr-oxide has not been addressed in the literature, although the miscut angles of the Si substrates vary widely among the different research groups.

Regarding the deposition process, electron beam evaporation is the commonly used technique for Pr-oxide. For growing films on commercial Si wafers a large diameter e-beam evaporator needs to be used. This type of source usually has a scanning electron beam striking directly the evaporant inside a crucible to reach the evaporation temperature. Due to the large volume of the crucible a thorough degassing of the evaporant is usually difficult to achieve. This leads to a higher oxygen background pressure during the deposition. For samples for academic research, typically a few millimeters wide, an Omicron-type e-beam evaporator is often employed. In this case energetic electrons bombard the crucible and the evaporant can be heated more uniformly due to the smaller volume. When  $\text{Pr}_6\text{O}_{11}$  powder, for example, is used with this type of evaporator, evaporation of Pr-oxide only occurs after a full reduction of  $\text{Pr}_6\text{O}_{11}$  to  $\text{Pr}_2\text{O}_3$  (the temperature for  $\text{Pr}_6\text{O}_{11}$  to lose oxygen is much lower than that for evaporating Pr-oxide). This allows the growth of Pr-oxide under UHV. In the previously cited work,  $\text{Pr}_6\text{O}_{11}$  has been the source material of choice, except in the case of Fissel [60], Guo [82] and Osten in Ref. [50], who have used granular  $\text{Pr}_2\text{O}_3$ . Notice that the growth rate, which should play also an important role in determining the surface morphology and crystallinity of the films, depends also on the type of evaporator. The deposition rate of an industrial type e-beam evaporator can be more than one order of magnitude higher than ones used in academic research.

Finally, an interfacial  $\text{SiO}_2$  layer may form, depending on the preparation procedure: (i) the starting surface is covered with native oxide or a regrown  $\text{SiO}_2$  layer or (ii) a high oxygen partial pressure is used during the growth or during post-annealing treatments [48, 54, 58, 86]. The presence of a  $\text{SiO}_2$  layer can promote the formation of Pr-silicate. One

should notice that MBE grown Pr-silicate on  $\text{SiO}_2/\text{Si}(001)$  surfaces were also obtained by e-beam evaporation of Pr metal [48, 62, 87–89].

In the next few paragraphs the structural and chemical properties of MBE grown Pr-oxide on  $\text{Si}(001)$  will be briefly reviewed. The typical growth condition for the results presented below involves evaporation of  $\text{Pr}_6\text{O}_{11}$  powders or  $\text{Pr}_2\text{O}_3$  granules from an electron-beam evaporator, an oxygen partial pressure in the  $10^{-8}$  mbar range and a sample temperature around  $550^\circ\text{C}$ . Three different stages will be introduced according to the sequence of their occurrence during the growth.

### 1.4.2 The very initial stage - a $3\times 1$ phase

The initial MBE growth of Pr-oxide on  $\text{Si}(001)$  has been monitored *in-situ* by RHEED. It was observed [3, 90] that in addition to the  $2\times 1$  pattern due to the reconstruction of the  $\text{Si}(001)$  clean surface, new RHEED spots appeared at the  $1/3$  positions between the  $1\times 1$  peaks during the first 0.5 nm of the growth, indicating the development of a superstructure with a three-fold lateral periodicity. Guo *et al.* [82] have reported recently a similar RHEED observation. A previous STM study of sub-monolayers of Pr-oxide on  $\text{Si}(001)$  by Müssig *et al.* [47] observed the nucleation of small clusters that appeared to have a  $3\times 1$  periodicity. However, photoelectron spectroscopy and cross sectional TEM have not detected so far any ordered thin layer at the interface.

Fig. 1.9 shows the detailed (101) projections of the bulk atomic structures of  $\text{Pr}_2\text{O}_3$  and  $\text{PrO}_2$ . The brighter Pr and O atoms are those on the top surfaces. The black rectangular boxes correspond to the unit cells matching the  $\text{Si}(001)$  surface structure: a  $3\times 1$  and a  $3\times 4$  unit cells for the  $\text{PrO}_2(101)/\text{Si}(001)$  and  $\text{Pr}_2\text{O}_3(101)/\text{Si}(001)$  interfaces, respectively. For the latter case a “pseudo”  $3\times 1$  unit cell can also be defined (the yellow dashed box). Notice that at the interfaces each  $3\times 1$  unit cell contains 2 Pr and 4 O atoms for  $\text{PrO}_2$  but 2 Pr and 3 O atoms (i.e. one oxygen vacancy per  $3\times 1$  unit cell) for  $\text{Pr}_2\text{O}_3$ . Thus, based on the bulk structures of  $\text{PrO}_2$  and  $\text{Pr}_2\text{O}_3$  a commensurate  $3\times 1$  (or pseudo  $3\times 1$ ) unit cell is possible to form on the  $\text{Si}(001)$  surface, defined in § 2.5.4, when the oxides grow along their [101] direction.

Such a  $3\times 1$  unit cell has been used as the fundamental structure by Dabrowski and Zavadinsky [3, 91] in their *ab initio* pseudopotential density functional theory calculations

for evaluating the properties of the Pr-oxide/Si(001) interfaces. However, quantitative information regarding the nature of this initial phase is still largely missing from the experimental side. For instance, Fissel *et al.* [18] have recently reported a  $3 \times 1$  superstructure observed by RHEED during the initial growth of  $\text{Nd}_2\text{O}_3$  on Si(001) under a similar growth condition to that used for  $\text{Pr}_2\text{O}_3$  growth on Si(001), and they attributed this structure to the formation of Nd-silicide, instead of ordered  $\text{Nd}_2\text{O}_3$ , at the interface.

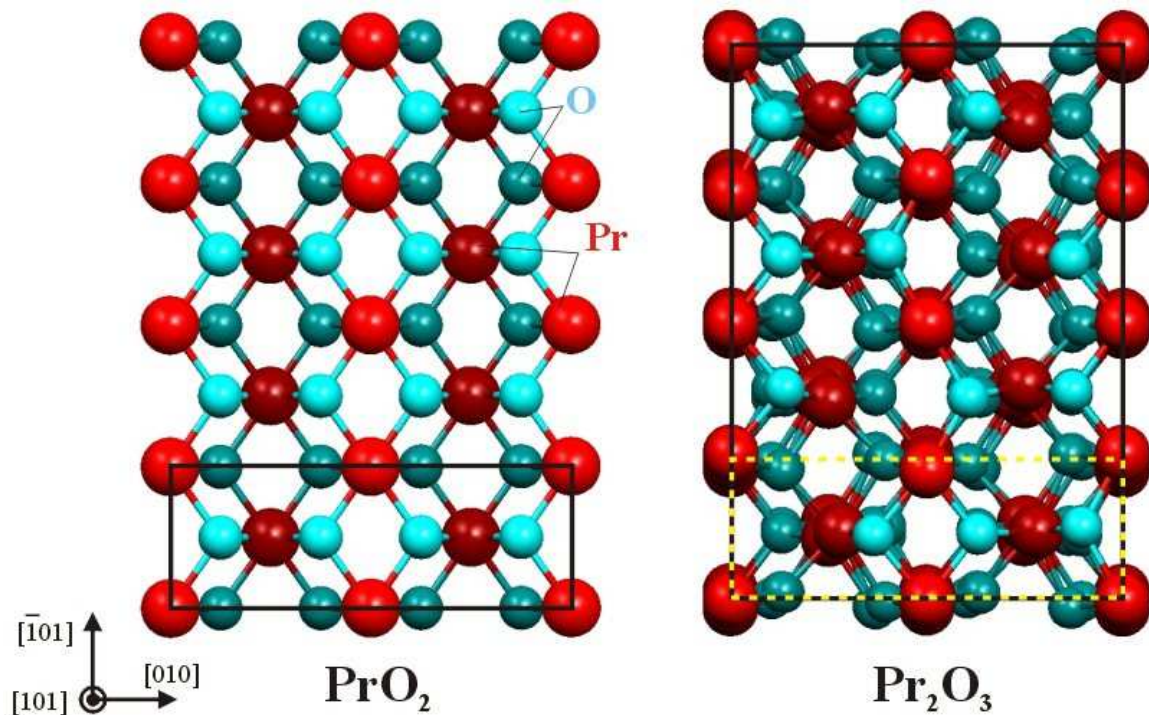


Figure 1.9: (101) projections of  $\text{PrO}_2$  and  $\text{Pr}_2\text{O}_3$  cubic structures. The brighter Pr and O atoms are those on the top surfaces. The black rectangular boxes correspond to the unit cells matching the Si(001) surface structure: a  $3 \times 1$  and a  $3 \times 4$  unit cells for the  $\text{PrO}_2(101)/\text{Si}(001)$  and  $\text{Pr}_2\text{O}_3(101)/\text{Si}(001)$  interfaces, respectively. For the latter case a “pseudo”  $3 \times 1$  unit cell can also be defined (the yellow dashed box). Notice that at the interfaces each  $3 \times 1$  unit cell contains 2 Pr and 4 O atoms for  $\text{PrO}_2$  but 2 Pr and 3 O atoms (i.e. one oxygen vacancy per  $3 \times 1$  unit cell) for  $\text{Pr}_2\text{O}_3$ . All the (101) atomic layers are stoichiometric.

### 1.4.3 An amorphous Pr-silicate layer next to the interface

Fig. 1.10 shows a cross sectional TEM picture of a  $\text{Pr}_2\text{O}_3$  film capped with a layer of polycrystalline Si from Osten *et al.* [51, 52]. A featureless layer, which appears to be a few nanometers thick, can be observed between the crystalline  $\text{Pr}_2\text{O}_3$  and the Si(001) substrate.

Such a featureless layer has been also seen in other cross sectional TEM pictures published more recently for MBE grown  $\text{Pr}_2\text{O}_3/\text{Si}(001)$  films [50,90]. *In-situ* RHEED investigation [3, 90] has reported the observation of no diffraction pattern after the growth of the first 0.5 nm and before the appearance of crystalline  $\text{Pr}_2\text{O}_3$ , indicating that a disordered layer forms at the initial stage. A similar RHEED pattern evolution has been also reported by Guo *et al.* [82]. To characterize the chemical composition of the Pr-oxide films, Fissel *et al.* [60] carried out a thickness dependent photoemission study, where they showed Si2p and O1s core-level spectra that support the presence of a silicate-like Si-O-Pr bonding configuration for 2 nm and thinner films. Using synchrotron-based photoelectron spectroscopy, Schmeisser *et al.* [54, 57, 58] studied the depth dependence of the Si2p and O1s line shapes. Based on the electronegativities of Pr, Si and O they also identified the formation of a Pr-silicate layer at the interface. In addition, Schmeisser *et al.* [55, 56, 59] have characterized the electronic properties of this silicate layer using resonant photoelectron spectroscopy and x-ray absorption spectroscopy. Theoretically the energetics of silicate formation at the Pr-oxide/Si(001) interface has been evaluated by Dabrowski and his co-workers [3, 58, 91]. They showed that with sufficient oxygen around, Pr-silicate is energetically more stable than  $\text{Pr}_2\text{O}_3$  when the Pr-oxide layer is in contact with  $\text{SiO}_2$ . Such silicate formation implies reaction of the arriving Pr-oxide molecules with the Si substrate and requires diffusion of Si through the film.

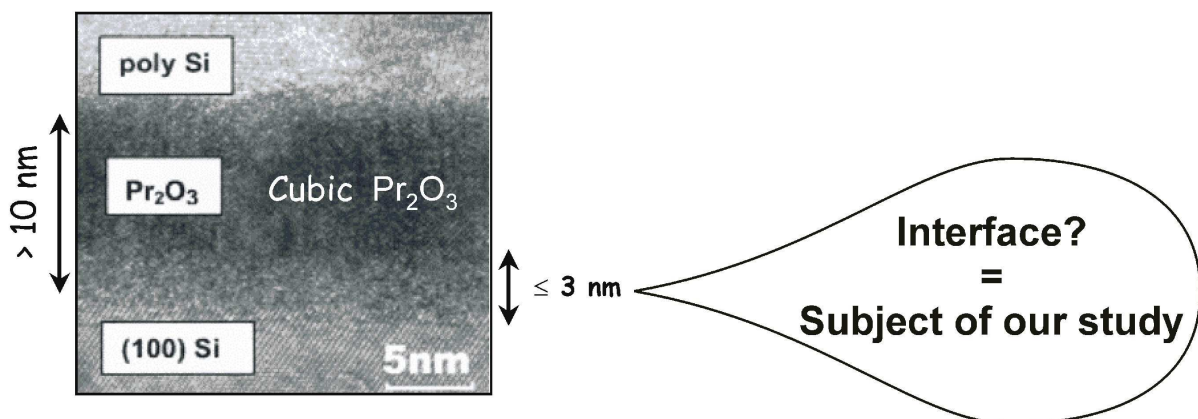


Figure 1.10: Cross sectional TEM picture from Osten *et al.* [51]. Film thickness comparison between previous studies ( $\geq 10$  nm) and the thickest one for our samples (about 3 nm).

#### 1.4.4 Thicker films - the $\text{Pr}_2\text{O}_3$ cubic phase

Earlier studies of thick Pr-oxide films grown by MBE on Si(001) were carried out by Osten *et al.* [51,52]. Based on XRD ( $\theta$ - $2\theta$  scans) they found that the oxide film grows into the cubic phase of  $\text{Pr}_2\text{O}_3$  with its (101) plane attached to the Si(001) surface. Fig. 1.11 shows the orientation of a  $\text{Pr}_2\text{O}_3$ (101) plane with respect to its bulk structure.

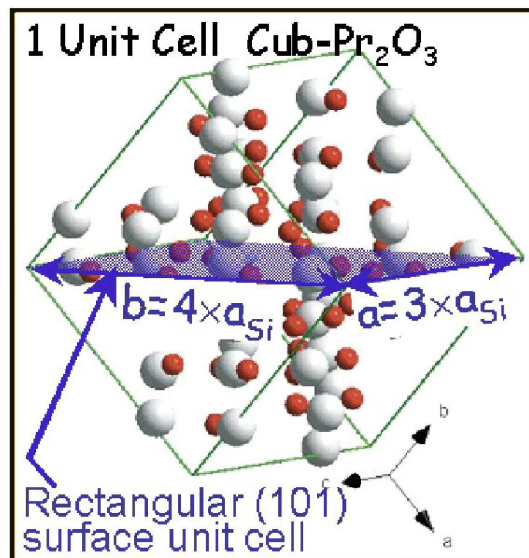


Figure 1.11: (101) plane of a  $\text{Pr}_2\text{O}_3$  cubic unit cell and its lattice parameters  $a$  and  $b$  compared with those of Si(001) surface unit cell (see section 2.5.4 for the definition).

Their *in-situ* RHEED studies and plan-view TEM images indicated that the  $\text{Pr}_2\text{O}_3$  layer is oriented laterally with its  $[010]$  and  $[\bar{1}01]$  parallel to the in-plane  $\langle 110 \rangle$  directions of the Si substrate. Such orientation leads to two equivalent domains that are related by a  $90^\circ$  rotation. The domain boundaries can be clearly seen in the plan-view TEM images. Photoelectron spectroscopy study by Fissel *et al.* [60] showed that upon the formation of the cubic  $\text{Pr}_2\text{O}_3$  phase a new O1s component appeared at a binding energy about 2 eV below the Pr-silicate peak. More recently Schroeder *et al.* [92] followed further the thickness dependence of the  $\text{Pr}_2\text{O}_3$  lattice constants using GIXRD, which suggests relaxation of the oxide layer at an early stage due to the lattice mismatch. Table 1.3 shows the in-plane lattice constants of the (101) surface unit cells of  $\text{Pr}_2\text{O}_3$  and  $\text{PrO}_2$  that can be commensurate to the Si(001) surface unit cell, as well as the corresponding lattice mismatches.

	Surface plane	Surface unit cell	Lattice constant a (nm)	Mismatch with Si	Lattice constant b (nm)	Mismatch with Si
Si	(001)	1×1	0.384		0.384	
Cubic Pr <sub>2</sub> O <sub>3</sub>	(101)	3×4	1.129	2.0%	1.596	-3.8%
PrO <sub>2</sub>	(101)	3×1	1.080	6.7%	0.382	0.5%

Table 1.3: In-plane lattice constants of the cubic Pr<sub>2</sub>O<sub>3</sub>(101) and PrO<sub>2</sub>(101) surfaces and their mismatches with the Si(001) surface unit cell (see § 2.5.4 for the definition). The surface unit cells of Pr<sub>2</sub>O<sub>3</sub> and PrO<sub>2</sub> (Fig. 1.9) are chosen to be the smallest ones that can be commensurate to the Si(001) surface unit cell.

In Ref. [92] the lateral domain size of the cubic Pr<sub>2</sub>O<sub>3</sub> phase has been also characterized. It was measured to be 5-10 nm for films below 10 nm, much smaller than the 20-60 nm domain size reported for the hexagonal phase Pr<sub>2</sub>O<sub>3</sub> grown on Si(111) [74]. Such small domain size, which leads to a poorer crystalline quality of the film, may be attributed to the formation of two rotational domains, as well as the presence of an amorphous Pr-silicate layer next to the interface that was discussed in the previous paragraph.

To close this section, it is worth mentioning that for the past two years Osten's and Fissel's groups have been reporting new studies on MBE growth of other rare-earth oxides, such as Gd<sub>2</sub>O<sub>3</sub> and Nd<sub>2</sub>O<sub>3</sub>, on Si(001) [17, 18], while Müssig *et al.* at IHP have moved toward the growth of Pr-silicate compounds on SiO<sub>2</sub> [48, 62, 64, 86, 89].

## 1.5 Scientific motivation of this work: The Oxide/Si interfaces

### 1.5.1 Why Pr<sub>2</sub>O<sub>3</sub>?

As reviewed in the previous sections, rare-earth oxides have been considered to be possible candidates as alternative gate oxides for replacing SiO<sub>2</sub> because of their high dielectric constants and still relatively large band gaps. Among these, many research groups have been highly interested for the past few years in Pr<sub>2</sub>O<sub>3</sub> and working towards device realization of this oxide material.

Despite the strong efforts in materials science research aiming at the integration of  $\text{Pr}_2\text{O}_3$  in Si devices, due to the complexity of the system, the growth mechanism is still not well understood and many growth parameters have not been fully explored, as mentioned in § 1.4. For the present work, we have identified particularly an unsolved scientific problem that is associated with the Pr-oxide/Si interface, which will be discussed in greater detail in section 1.5.2.

On the Si(001) surface  $\text{Pr}_2\text{O}_3$  grows as the cubic phase, which exhibits a  $\text{CaF}_2$  derived structure. Several other gate oxide candidates ( $\text{Nd}_2\text{O}_3$ ,  $\text{Gd}_2\text{O}_3$ ,  $\text{Y}_2\text{O}_3$ ,  $\text{ZrO}_2$ ,  $\text{CeO}_2$ ) that are being investigated have similar crystal structures in their bulk phases. General trends regarding the growth and properties among these materials may be obtained from the study of  $\text{Pr}_2\text{O}_3/\text{Si}(001)$  interface.

A number of gate oxide/Si interfaces have been evaluated theoretically by first-principles calculations [11,91,93,94]. Experimentally the quality of an interface is often characterized by cross sectional TEM. To determine more quantitatively the interfacial structures on an atomic scale, one would need to combine both studies. Such an approach has been applied mainly to epitaxial perovskite oxides on Si(001) [33,94]. However, the structure of the  $\text{SrTiO}_3/\text{Si}(001)$  interface, for example, whose growth was first demonstrated by McKee *et al.* back in 1998 [33], is still under debate [93]. The family of oxides that exhibits the  $\text{CaF}_2$  or the derived structures has received much less attention so far.

In the course of the present study, we discovered an ultrathin crystalline layer at the Pr-oxide/Si(001) interface. Surface x-ray diffraction (SXRD), which is one of the main x-ray methods available at our beamline, is well suited for characterizing such a buried, ordered structure and can potentially provide atomic-scale structural information about the interface.

Growing  $\text{Pr}_2\text{O}_3$  is technically less demanding than, for example, some of the perovskite oxides such as  $\text{SrTiO}_3$ . The former requires only the evaporation of either  $\text{Pr}_2\text{O}_3$  or  $\text{Pr}_6\text{O}_{11}$  from a single source, while for the latter co-evaporation from multiple elemental sources is needed and a rather sophisticated growth sequence developed by McKee *et al.* [33] has to be followed and monitored with RHEED in order to form a stable interface.

Another practical reason for choosing  $\text{Pr}_2\text{O}_3$  rather than other rare-earth oxides is that the knowledge about the MBE deposition on both the Si(001) and (111) surfaces was already available from other groups (IHP, Schmeisser's group at BTU Cottbus and Moritz's group

at the University of Munich) when the present project started. For example, MBE growth of  $\text{Nd}_2\text{O}_3$  and  $\text{Gd}_2\text{O}_3$  was much less studied than  $\text{Pr}_2\text{O}_3$  back in 2003.

### 1.5.2 Scientific issues

Interfacing a new oxide with silicon is one of the major challenges in finding alternative high-K materials. The matching of lattice parameters and chemistry across the oxide/Si interface determines mostly the orientation and phase of an oxide film. As the thickness of the gate stack is continuously scaled down, the quality of the interface plays a more and more important role in controlling the electrical characteristics of the device. In particular, the presence of a transition layer at the interface may set a lower limit on the EOT value that can be reached when the gate oxide layer thickness is further reduced.

A more fundamental effect that the detailed atomic structure and bonding at the oxide/Si interface can have is on the band offset as well as the formation of unwanted interface states. First-principles calculations by Först *et al.* [93] have shown that for the case of the  $\text{SrTiO}_3/\text{Si}(001)$  interface, the first layer of Sr, which has a coverage of 0.5 ML, eliminates the interface states associated with the dangling bonds of the Si dimers by saturating all the dangling bonds with two electrons from each Sr. They also demonstrated that by oxidizing the Si dimers one could raise the injection barrier to above the technologically required minimum. Later they suggested [94], based on comparisons of calculated and measured TEM images, that  $\text{LaAlO}_3$  may not be a good candidate as gate dielectric because of its electrically unsaturated interface resulting from the structure. Theoretical calculations by Peacock and Robertson [13] also showed how the valence band offset of  $\text{ZrO}_2$  on  $\text{Si}(001)$  depends on the atomic configuration of the interface. Fissel *et al.* [60] have observed, after annealing their as-grown  $\text{Pr}_2\text{O}_3/\text{Si}(001)$  samples in UHV, an increase of the valence band offset, which was explained by *ab initio* calculations to be due to oxygen depletion at the interface.

For  $\text{Pr}_2\text{O}_3$  on  $\text{Si}(001)$ , as discussed in the previous section for the current research status of the MBE growth, there is always a featureless layer of a few nanometers thick at the film/substrate interface in the cross sectional TEM pictures. Many results are consistent with the formation of an interfacial layer of disordered Pr-silicate. Obviously the presence of this low-K layer, as compared with  $\text{Pr}_2\text{O}_3$ , will influence and degrade the performances of the final devices. More importantly, this interfacial layer can block further downscaling of

devices. However, so far no quantitative study of the Pr-oxide/Si interface has been carried out on the atomic scale. Recently fully functional MOSFETs have been demonstrated by Schwalke and Stefanov [76] using crystalline  $\text{Pr}_2\text{O}_3$  as the gate dielectric. They showed that the  $\text{Pr}_2\text{O}_3$  gate stack suffers from structural defects and severe charge trapping effects, which may link to problems at the oxide/Si interface. It is therefore necessary to have a closer look at this interface for a better understanding of the structure and bonding configuration.

Experience with  $\text{SiO}_2$  on Si(001) has shown quite a lot of evidence that there is a transition region of altered structure between the crystalline silicon and the amorphous  $\text{SiO}_2$ . An ordered crystalline interfacial oxide layer around 5 Å thick between the crystalline Si substrate and the amorphous  $\text{SiO}_2$  layer have been reported by Ourmazd *et al.* who have established by high-resolution TEM that this crystalline oxide corresponds to tridymite, a stable, bulk form of  $\text{SiO}_2$  [95]. Pioneering photoemission studies of Himpsel *et al.* revealed that the silicon interface with thermally grown oxide is not abrupt but with a few layers of sub-stoichiometric oxide ( $\text{SiO}_x$ ) forming in the transition region between the two materials [96]. More recently X-ray diffraction analysis revealed that the thermally grown  $\text{SiO}_2$  film possesses some structural order throughout the oxide film [97–99]. Many first principle calculations have been motivated by such experimental results to characterize the  $\text{SiO}_2/\text{Si}(001)$  interface structure [100,101] and investigate the oxidation process on the atomic scale [102]. In addition, interfacing high-K oxides considered thus far for an alternative gate dielectric on  $\text{SiO}_2$  is also being extensively discussed [9,103]. The importance of the interface atomic arrangement has been recognized early on and strategies have been developed to quench interface states resulting from ill-defined structures [104].

Such a transition layer as the one found between  $\text{SiO}_2$  and Si, instead of an abrupt interface, may exist more regularly than is expected between amorphous metal oxides and crystalline Si. This layer could be highly ordered and even commensurate to the Si lattice. Since it is situated right above the gate channel, a detailed characterization of this layer may provide useful information that leads to better performance of the gate stack. For our study of  $\text{Pr}_2\text{O}_3$  on Si(001), the presence of a crystalline interface will allow a quantitative structural analysis on the atomic scale using SXRD. Our results can be directly compared with the first-principles calculations performed by Dabrowski and Zavodinsky [91], where several possible interfacial structures, such as crystalline  $\text{Pr}_2\text{O}_3$  and Pr-silicate layers with Si surfaces oxidized to different extents, have been considered.

To close this section, I would like to emphasize that synchrotron radiation based techniques can bring unique contributions to answering these technically challenging scientific questions and the subject of this study is believed to be closely related to other oxides having similar bulk structures, such as  $Y_2O_3$ ,  $Gd_2O_3$ ,  $HfO_2$ ,  $CeO_2$ ,  $ZrO_2$ , etc, when they are deposited as thin films on Si.



## Chapter 2

# Experimental

---

This chapter presents the experimental techniques used in this project. Sample preparation in the ultra high vacuum (UHV) systems at the ID32 surface characterization laboratory (SCL) and sample transfers in UHV to the beamline set-ups are described in section 2.1. The characterization techniques available in the SCL (STM, LEED, and AES) are presented and briefly discussed in sections 2.2 to 2.4.

In sections 2.5 and 2.6, the ID32 beamline is presented and in particular the two techniques available in the two experimental hutches of the beamline, i.e. surface X-ray diffraction (SXRD) and X-ray photoelectron spectroscopy (XPS), are explained. All the characterization techniques used in this study are non-destructive and can be applied *in situ*.

## 2.1 UHV sample preparation and sample transfer

### 2.1.1 The small UHV system

Fig. 2.1 presents the small UHV system of the SCL, which is based on an Omicron STM system. Its base pressure is typically below  $10^{-10}$  mbar. It is equipped with a residual gaz analyzer, an ion sputter gun, a number of ports for the connection of Knudsen cells and e-beam evaporators, a film thickness monitor, and a sample heater capable of both radiative and direct current heating. LEED and room temperature STM are the two characterization techniques available on this chamber.

The direct heating set-up enables substrate heating and cleaning at high temperature. Typically  $10 \times 3 \text{ mm}^2$  Si wafer samples, about  $350 \mu\text{m}$  thick, are mounted on direct heating sample plates, as shown in Fig. 2.2. Because of such a small sample cross section temperatures above  $1000^\circ\text{C}$  can be reached with a power close to about  $30 \text{ W}$  (current  $\leq 6 \text{ A}$ ). The sample temperature is measured with an optical pyrometer.

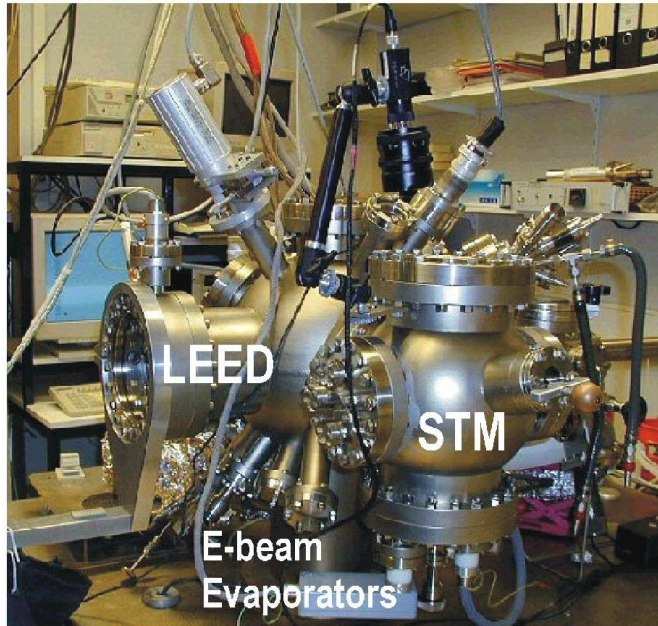


Figure 2.1: Small UHV system in the SCL.

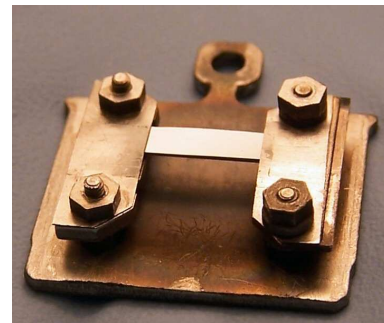


Figure 2.2:  $10 \times 3 \text{ mm}^2$  Si wafer mounted on a direct heating sample holder used for the small UHV system.

### 2.1.2 The big UHV chamber for sample transfer

The second UHV system of the SCL, so-called R2P2, is about four times bigger than the previously presented chamber. Its base pressure is in the range of  $10^{-11}$  mbar. Fig. 2.3 shows a picture of this UHV system. A central rotating arm enables the sample transfer from the e-beam heater (used for substrate cleaning) to the MBE growth chamber and STM, LEED and AES characterization tools.

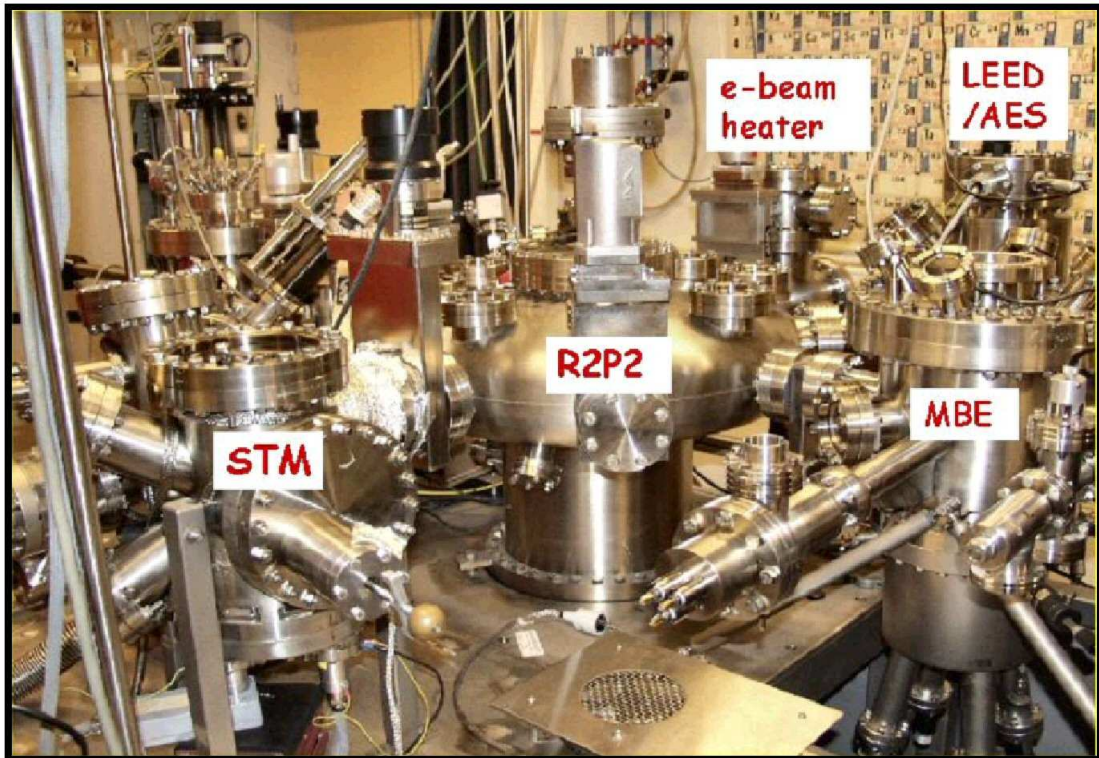


Figure 2.3: Big UHV system, so-called R2P2, located in the SCL. A central rotating arm enables the sample transfer from the e-beam heater to the MBE growth chamber and STM, LEED and AES characterization tools.

More detail on the e-beam heater can be found in section 4.1.1. Regarding the MBE chamber, it is equipped with an omicron e-beam evaporator, a molecular oxygen source with a leak valve to precisely adjusted the oxygen flux in the MBE chamber, a turbo pump to pump away the oxygen, a residual gas analyzer (RGA) and a quartz crystal microbalance (QCM), as well as a radiative heater enabling substrate heating up to  $900^{\circ}\text{C}$ . For the calibration of our growth rate via the QCM, a bulk density of  $6.88\text{ g/cm}^3$  was used for  $\text{Pr}_2\text{O}_3$ , as indicated in Ref. [105].

Fig. 2.4 shows a  $7\times 5\times 2\text{ mm}^3$  Si hat-shaped sample prior to the loading in the UHV system. The sample is mounted on a Mo plate with four Ta screws and two Ta wires. The plate has a  $5\times 5\text{ mm}^2$  window behind the Si crystal to allow direct electron bombardment of the back side of the crystal. The hat shaped samples are needed to perform SXRD experiments in order not to block the grazing incident X-ray beam. They have a  $5\times 5\text{ mm}^2$  active area (top surface).

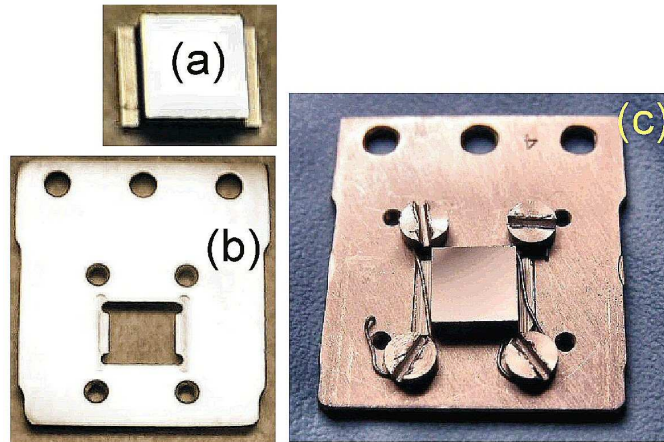


Figure 2.4: (a)  $7 \times 5 \times 2 \text{ mm}^3$  Si hat-shaped crystal. (b) Mo sample plate. (c) Si hat-shaped crystal fixed on a sample plate via Ta screws and wires.

## 2.2 Scanning tunneling microscopy

### 2.2.1 Principle and set up

The scanning tunneling microscope (STM) was invented by Binnig and Rohrer in 1982 and has revolutionized the field of surface science, as real-space atomic-resolution images of a sample surface become routinely available nowadays [106]. STM provides high-spatially resolved topographic and spectroscopic information of surfaces and adsorbate systems. Many of the electronic, magnetic, or structural properties of materials can be in this way investigated with atomic resolution. The information collected from a STM apparatus gives in favorable case directly a map of the local surface morphology. This is done either by measuring the charge transfer (current) or the excursion of the z-piezo while keeping the current constant. The latter mode, called constant current topography (CCT), is the more common one and was used in the following studies.

Fig. 2.5(b) presents the principle of scanning tunneling microscopy. A fine pointed tip is brought extremely close to a surface. A voltage is applied between the tip and the sample surface. When the probe tip is very close to the sample surface, a tunneling current flows between the tip and surface. The current is very sensitive to the distance between the tip and surface, as indicated in Fig. 2.5(c). The tip can be scanned across the surface

with the aid of piezo-electric actuators. The current between the sample and tip is sensed and the tip is moved towards and away from the sample surface to keep the current flow constant. The tunneling current is also proportional to the local density of state of the surface. Depending on the sign of the bias voltage, STM can probe either the filled or empty states of the surface. Therefore features observed in a STM topograph may contain also electronic effects.

Obviously, the sample needs to be electrically conducting, and to achieve atomic resolution for most samples the STM needs to operate in UHV conditions.

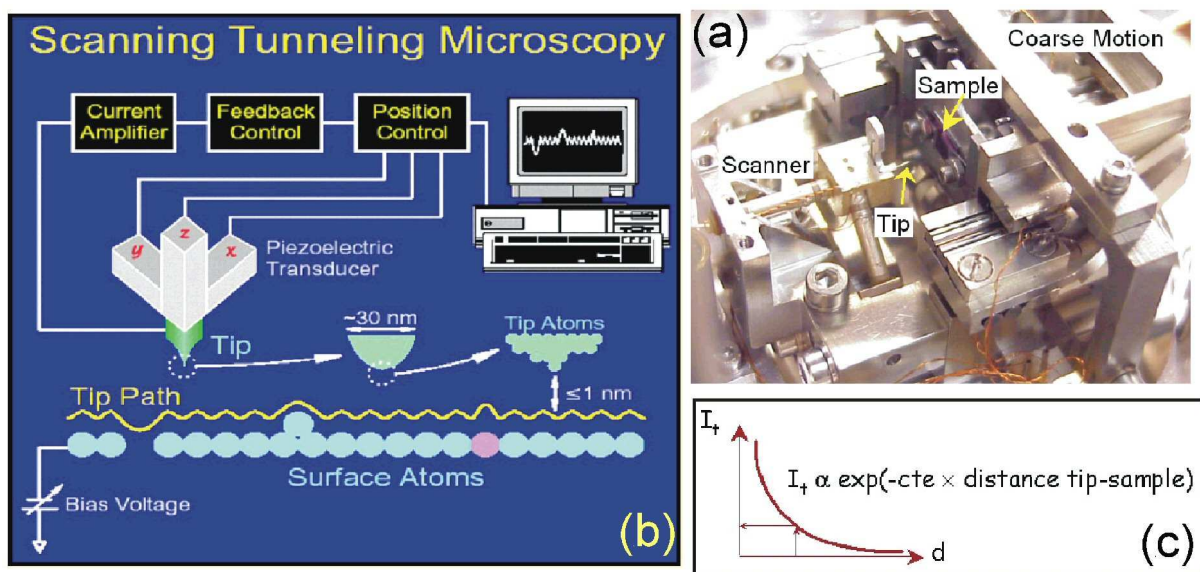


Figure 2.5: (a) Tripod scanner in the small UHV system. (b) Principle of scanning tunneling microscopy. Sketch made by R. P. Feynman. (c) Tunneling current  $I_t$  dependence on the tip-sample distance  $d$ . “cte” stands for “constant”.

In the small UHV chamber of the SCL, STM measurements are carried out with an Omicron tripod scanner (see Fig. 2.5 (a)) and in the big R2P2 system a conventional Omicron single tube scanner (microSTM) was used. The tips were home made from polycrystalline tungsten wires ( $\varnothing$  0.38 mm) by electrochemical etching, as described in Ref [107].

Constant current topography was carried out after the freshly prepared sample had reached room temperature. All reported biases refer to the applied sample potential. The shown STM topographs represent unfiltered raw data and only brightness and contrast were

adjusted in order to enhance the surface topography. For more detail on the tunneling theory and other considerations regarding scanning tunneling devices the reader is referred to Chen and Wiesendanger's books [108, 109].

### 2.2.2 Use and limits of the STM

The STM provides a real space image at the atomic scale. It locally probes the surface morphology (substrate and film). No chemical information is obtained. Different electronic properties of different species may give rise to a variation in contrast.

Therefore STM is an excellent technique for revealing growth morphology at atomic or near-atomic resolution, but it is limited in determining which chemical species is being imaged. It is therefore important to complement the STM data with chemical and electronic characterization of the surface. Another limitation is that STM cannot be used to study a buried structure.

In this study we have used the STM apparatus in CCT mode under UHV conditions to control the preparation of the surfaces.

The resolution of the instrument is  $\approx 2 \text{ \AA}$  lateral and  $0.01 \text{ \AA}$  vertical. The lateral accuracy depends on the piezo calibration and drift. The same is true for the height measured with the additional complication that this information may be dominated by electronic contrast.

## 2.3 Low energy electron diffraction (LEED):

### Principle and set-up

If a crystal is cut along a certain plane, then the atoms near the surface may well be disturbed from their equilibrium positions in the bulk. This leads to changes in the relative positions of the near surface atoms (surface reconstruction). Such changes can be explored with LEED. Due to the short mean free path, low energy electrons are diffracted only by a few atomic layers of the surface, which lead to Bragg rods perpendicular to the surface in the reciprocal space. As shown in Fig. 2.6, the scattering vector  $\mathbf{Q}$  and consequently

the wave vector for the diffracted electrons  $\mathbf{k}_f$  are selected by the intersection of the Bragg rods with the Ewald sphere, whose size varies as a function of the electron beam energy.

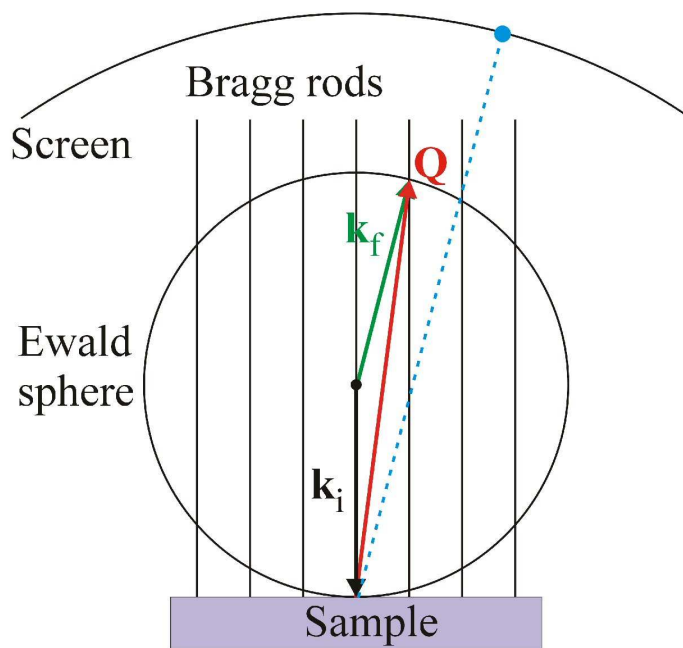


Figure 2.6: Principle of low energy electron diffraction.

Therefore, the surface crystallographic structure can be determined by bombarding the surface with monochromatic low energy electrons (approx. 10-200 eV) and observing diffracted electrons as spots on a phosphorescent screen (see Fig. 2.7). The relative positions of the spots on the screen reveal the symmetry and dimensions of the surface unit cell. The average intensity and sharpness of the spots reveal the degree of ordering of the surface.

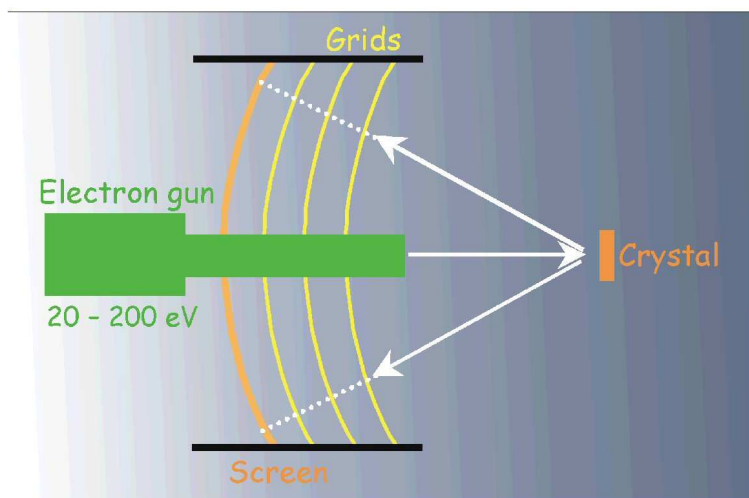


Figure 2.7: Schematic of a LEED set-up.

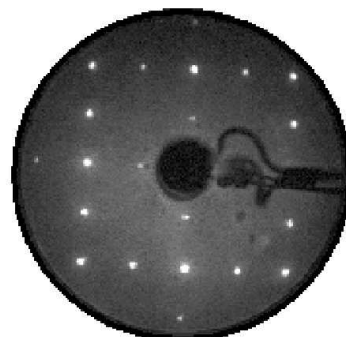


Figure 2.8: Typical LEED pattern of a Si(001)- $2\times 1$  reconstructed surface.

In this study, LEED measurements were performed with an Omicron reverse view optic (Fig. 2.7) and images were recorded via CCD cameras in the case of the small UHV chamber and the big system. The LEED patterns presented in this report were collected for an electron beam energy of around 50 eV. Fig. 2.8 displays a typical LEED pattern recorded from a clean Si(001) surface  $2\times 1$  reconstructed.

## 2.4 Auger electron spectroscopy (AES)

An Auger process involves two steps. In the first step, an atom is ionized by a photon or electron, resulting in an atom with a core hole. The typical energies of electron beams used in AES are 3-20 keV. In the second step, the excited atom relaxes through filling of the core hole with an outer shell electron. The energy thus released can be either directly detected as a photon (fluorescence) or used to eject another electron. This electron is called an Auger electron, named after Pierre Auger who observed this relaxation process in 1920's. After the emission of the Auger electron, the atom is left in a doubly ionized state.

Fig. 2.9 presents a schematic example of an Auger process that shows an atom ionized in the K orbital, an  $L_{2,3}$  electron filling the hole and an electron emitted from the same shell. The whole process is then denoted a  $KL_{2,3}L_{2,3}$  Auger process. As AES process involves

three electrons, the kinetic energy of an AES electron is characterized by the binding energies of three atomic levels (e.g. KLL, LMM, ...).

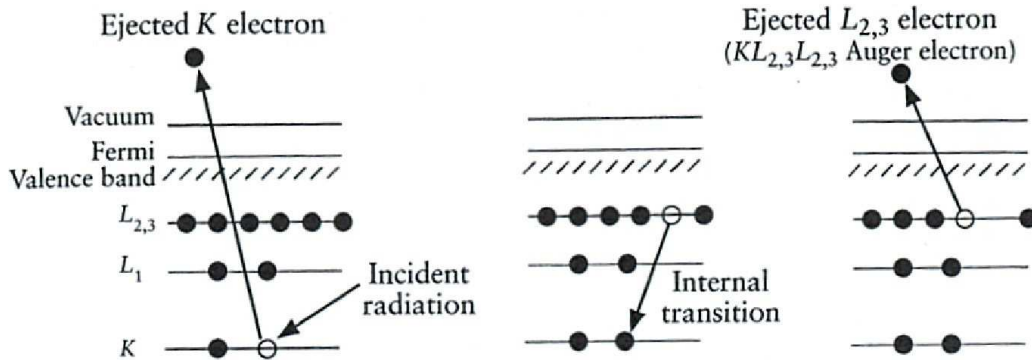


Figure 2.9: Schematic diagram of an AES process, showing photoionization of an atom by the ejection of a 1s electron, as extracted from [110].

AES measurements need to be performed in vacuum environment, as the electrons are absorbed if the pressure is too high ( $> 10^{-5}$  mbar), and also to preserve the surface cleanness of the studied samples. The basic advantages of this technique are its high sensitivity for chemical analysis in the 5 to 20 Å region below the surface, a rapid data acquisition speed, its ability to detect all elements above helium, and its capability of high-spatial resolution, if the specimen is excited by an electron beam that can be focused into a fine probe. AES is often used to check the surface purity after a sample surface preparation.

Fig. 2.10 gives an example with the O KLL AES spectrum. The plot presents the  $dI/dE$  function versus the kinetic energy  $E$ . All AES results will be presented similarly and the minimum of the AES wiggle will be addressed as “peak”.

In this study, AES has been mainly used to observe the Si LMM, Pr NOO, and O KLL lines. No quantitative analysis from these measurements were performed.

A retarding field analyser was used to detect the electrons and the energy of the incident electrons was 3 KeV. According to tabulated data [111], at this incident electron energy the escape depth of O KLL AES electrons is about 10-20 Å while the one of Pr NOO and Si LMM AES is around 5-10 Å.

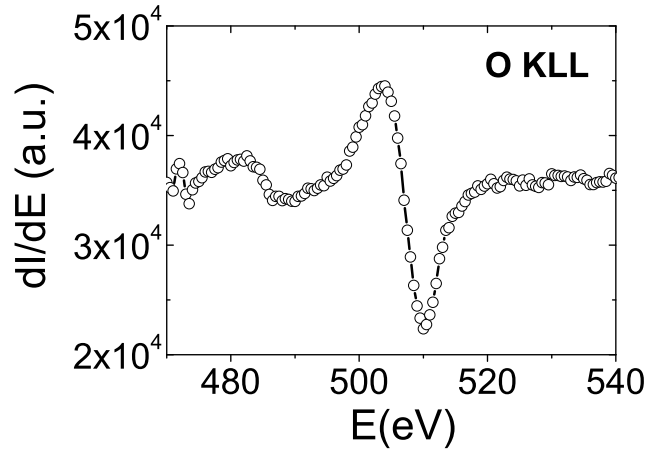


Figure 2.10: Example of AES spectrum.

## 2.5 XRD experiments on the ID32 beamline

X-ray diffraction experiments were performed in the first experimental hutch of the insertion device beamline ID32 at the ESRF. In particular, SXRD, also called GIXRD, was used to characterize the ordered Si / Pr-oxide interfaces.

### 2.5.1 Baby chamber transfers

After sample preparations and first series of characterizations in the SCL the samples are transferred individually inside the UHV suitcase, so called *baby chamber*, presented in Fig. 2.11. The pressure is kept in the  $10^{-10}$  mbar range by a 20 l/sec ion-pump. It is in this clean environment that the sample is carried onto the 6-circle diffractometer at the beamline.

### 2.5.2 Diffraction set-up

The sample is mounted onto the six-circle diffractometer of the ID32 beamline. Fig. 2.12 shows a picture of this diffractometer, at the center of which the baby chamber has been mounted. The arrow in the picture indicates the direction of the incident synchrotron beam.

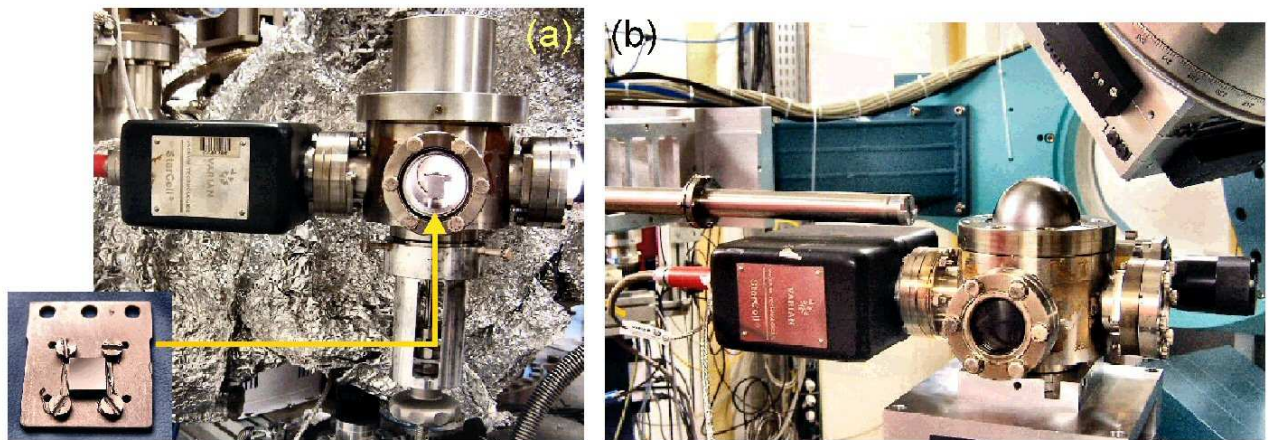


Figure 2.11: Baby chamber (UHV transfer suitcase) for diffraction experiments. (a) Chamber mounted on the R2P2 in the lab. (b) Chamber mounted onto the diffractometer at the beamline



Figure 2.12: ID32 experimental hutch 1. Six-circle diffractometer. UHV baby chamber at the center of the diffractometer. The synchrotron beam is indicated by the arrow.

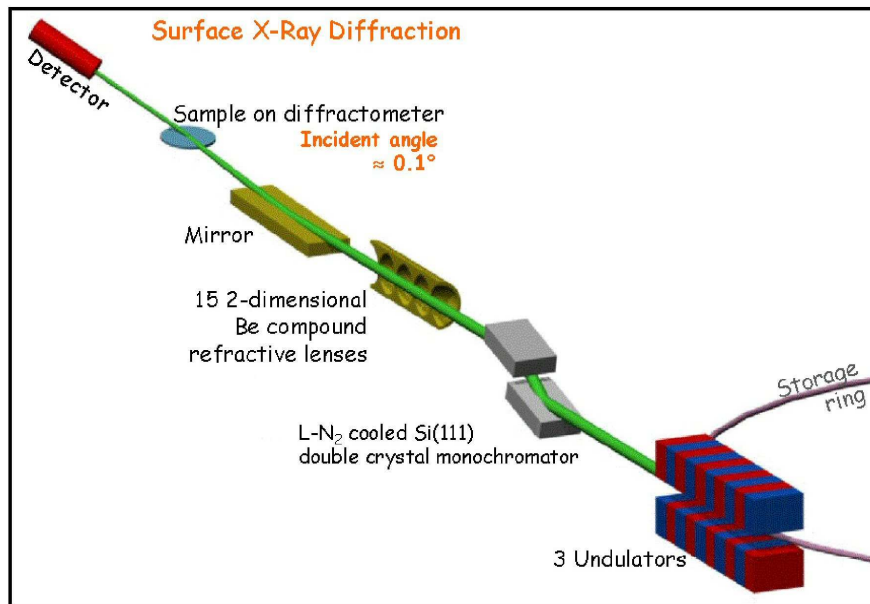


Figure 2.13: Schematic of the optics setup used for the diffraction experiments.

Fig. 2.13 shows a schematic set-up of the beamline optics for the diffraction experiments. The undulator radiation is first monochromized by a pair of Si(111) crystals with the first one held at liquid nitrogen temperature. The monochromator beam is then focused by up to fifteen 2-dimensional Be compound refractive lenses (CRLs). Afterwards this focused beam is reflected by an x-ray mirror coated with three stripes (Ru, Ni or SiO<sub>2</sub>) for rejecting the higher order harmonics generated by the undulators and transmitted by the higher order reflections of the Si(111) crystals. The final beam size, typically  $15(\text{V}) \times 500(\text{H}) \mu\text{m}^2$ , is defined by an entrance slit 70 cm before the sample. An ionization chamber filled with air is placed behind the slit for monitoring the incident beam intensity. Except for reflectivity measurements, the impinging beam arrives at the sample surface with a fixed grazing incident angle, typically  $0.1 \sim 0.12^\circ$  to enhance the signal to noise ratio for surface diffraction [112]. The penetration depth of the X-rays depends on the incident angle, the beam energy and the material of the sample (its electron density).

In the experiments presented in this report incident beam energies of about  $17 \sim 18 \text{ KeV}$  were used. For Si substrates, the penetration depth is estimated to be  $10 - 600 \text{ nm}$  for the impinging x-rays, as shown in Fig. 2.14 [113].

To collect the scattered intensity from the samples, a point detector (Cyberstar) was used. On the detector arm, a fixed aperture of  $3(\text{H}) \times 6(\text{V}) \text{ mm}^2$ , placed about 10 cm after the sample, is used to define the sample surface area that contributes diffracted beam

intensities to the point detector. A second aperture, typically  $3\times 3$  or  $2\times 2$  mm<sup>2</sup> in size, is placed approximately 95 cm after the sample for defining the in-plane and out-of-plane angular resolutions in the reciprocal space.

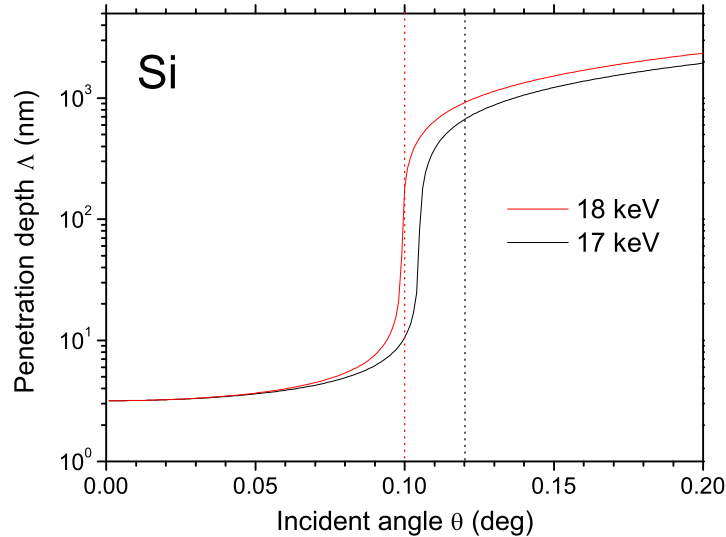


Figure 2.14: Si penetration depth at 17 and 18 KeV.

Fig. 2.15 shows a schematic map of the different X-ray scattering methods in reciprocal space.

### 2.5.3 X-ray reflectivity

X-ray reflectivity (XRR) is a technic sensitive to the electron density variation  $d\rho(z)/dz$  perpendicular to the sample surface, independent of the sample being crystalline or amorphous. Reflectivity scans consist in collecting the scattered intensity along the (00L) specular direction in the reciprocal space, as shown in Figs. 2.15 and 2.16 (a). In a specular reflectivity scan the surface normal, the incident and the scattered wave vectors are all in the same plane, with the incident angle  $\theta$  being equal to the exit angle. The scans start with  $\theta$  close to the critical angle  $\theta_c$  of the Si surface up to slightly before the first Bragg peak of the substrate.  $\theta_c \approx 0.11^\circ$  in the case of Si substrate and a beam energy of 16.75 eV.

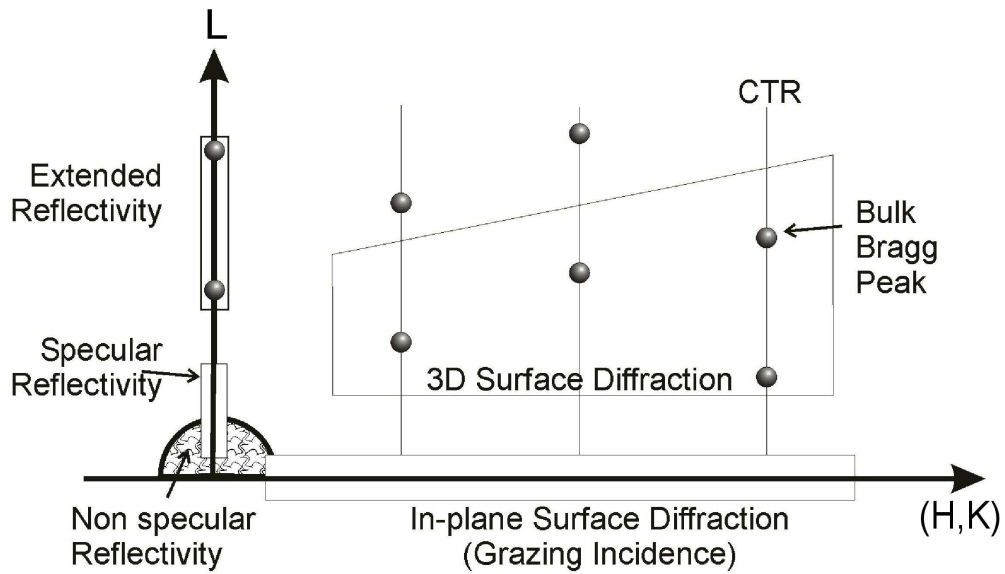


Figure 2.15: Schematic map of X-ray scattering methods in reciprocal space.

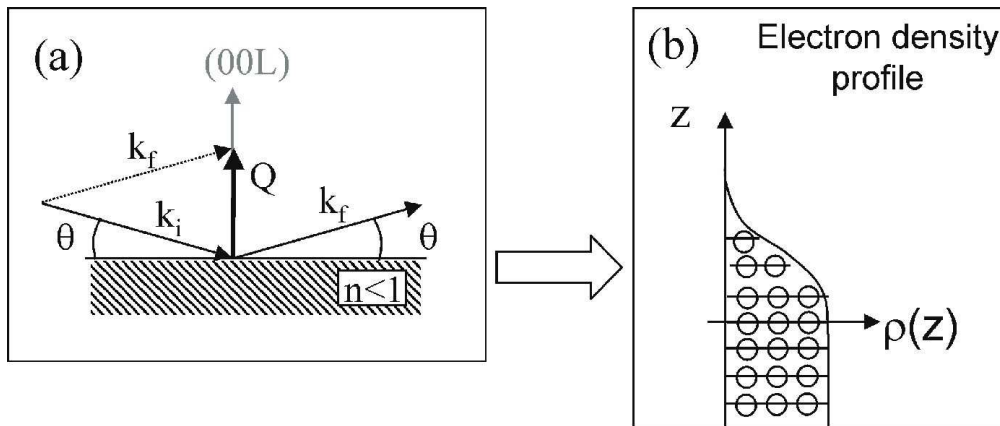


Figure 2.16: (a) Specular reflection geometry.  $Q$  is the momentum transfer vector,  $k_i$  and  $k_f$  the incident and the scattered wave vectors.  $Q = k_i - k_f$  and is along the  $(00L)$  rod, parallel to the surface normal.  $n$  is the index of refraction of the sample, which is less than unity for x-rays. (b) Electron density profile in the case of one bare substrate.

Since the momentum transfer  $Q$  is very small when  $\theta$  is close to  $\theta_c$ , specular reflectivity allows characterization of the electron density profile perpendicular to a surface on the length scale beyond 100 nm (cf. Fig. 2.16 (b)). From these measurements, layer thicknesses, roughnesses and electron densities of thin films, multilayer structures, and buried interfaces can be studied [112, 114].

In the case of a bare silicon substrate (Fig. 2.23) the reflectivity profile corresponds to the so-called Fresnel reflectivity  $R_F$ , which describes the reflectivity curve from a thick mirror (substrate surface) and can be expressed by:

$$R_F = \frac{16\pi^2 r_e^2}{Q^4} \rho_{si}^2 \quad (2.1)$$

with  $r_e$  is the classical electron radius ( $r_e = 2.818 \times 10^{-5} \text{Å}$ ),  $\rho_{si}$  the electron density of the silicon substrate and  $Q$  the momentum transfer that has been conventionally defined for reflectivity measurements as

$$Q = \frac{4\pi \sin\theta}{\lambda} \quad (2.2)$$

where  $\lambda$  is the wavelength of the beam energy used for the experiment.  $Q$  can be converted to the reciprocal lattice unit of the substrate used in SXRD by the relationship  $L = \frac{cQ}{2\pi}$ , where  $c$  is the lattice constant defining  $L$ .

When a film is present on top of the substrate, regularly spaced oscillations, also called Kiessig fringes can be observed in the reflectivity profile, no matter the new layer is ordered or disordered (cf. Figs. 2.23) [115]. These oscillations are related to the Fourier transform of the first derivative of the electron density with respect to the depth. The higher the oscillation frequency the thicker the film. A specular reflectivity curve can generally be described by

$$R = \frac{16\pi^2 r_e^2}{Q^4} \left| \int_{-\infty}^{\infty} \frac{d\rho(z)}{dz} e^{iQz} dz \right|^2 \quad (2.3)$$

where  $z$  is the depth below the surface. Eq. 2.3 is the so-called Master equation [112, 114]. One can notice that the prefactor in this formula is related to the Fresnel reflectivity (Eq. 2.1).

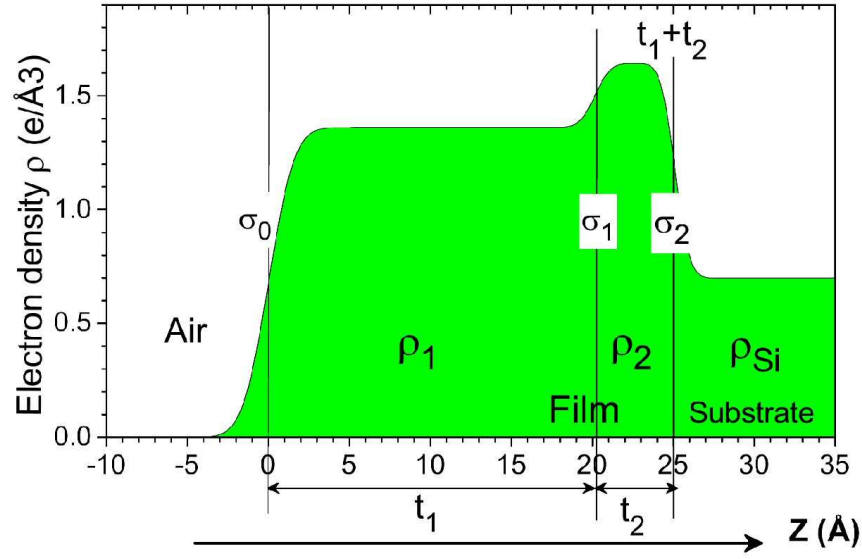


Figure 2.17: Electron density profile corresponding to the bilayer model used to explain our data.

Experimentally, reflectivity can be determined by dividing the background-subtracted scattered intensity by the intensity of the direct X-ray beam. The background intensity can be estimated by repeating the reflectivity measurement on both sides of the specular rod with a small in-plane  $Q$  vector.

In this study a bilayer model has been considered to explain our data. Fig. 2.17 shows the electron density profile  $\rho_z$  with respect to the depth  $z$  for such a model, where  $z$  is defined to be zero at the surface. The broadening at each interface, due to roughness, is described by an error function (erf). Therefore  $\rho(z)$  can be expressed as

$$\begin{aligned} \rho(z) = & \frac{1}{2}\rho_1 \left( \operatorname{erf} \frac{z}{\sqrt{2}\sigma_0} + 1 \right) \\ & + \frac{1}{2}(\rho_2 - \rho_1) \left( \operatorname{erf} \frac{z - t_1}{\sqrt{2}\sigma_1} + 1 \right) \\ & + \frac{1}{2}(\rho_{Si} - \rho_2) \left( \operatorname{erf} \frac{z - t_1 - t_2}{\sqrt{2}\sigma_2} + 1 \right) \end{aligned} \quad (2.4)$$

where  $\rho_1$ ,  $\rho_2$  and  $\rho_{Si}$  are the electron densities of the two layers and bulk Si,  $t_1$  and  $t_2$  the layer thicknesses, and  $\sigma_0$ ,  $\sigma_1$  and  $\sigma_2$  are the roughnesses of the three interfaces, as indicated

in Fig. 2.17. Applying Eq. 2.3 to 2.4 we have

$$R / \left( \frac{16\pi^2 r_e^2}{Q^4} \right) = \left| \rho_1 e^{-Q^2 \sigma_0^2 / 2} + (\rho_2 - \rho_1) e^{-Q^2 \sigma_1^2 / 2} e^{-iQ t_1} + (\rho_{Si} - \rho_2) e^{-Q^2 \sigma_2^2 / 2} e^{-iQ(t_1 + t_2)} \right|^2 \quad (2.5)$$

Using this equation the reflectivity experimental curves can be fitted and the parameters of Eq. 2.5, i.e. the electronic densities of the layers, their individual thicknesses, and the roughness of the interfaces, can be retrieved. Note that Eq. 2.3 and Eq. 2.5 describe the absolute reflectivity and therefore no scale factor should be included when they are used to fit reflectivity data.

As a remark, a quick way to estimate the film thickness  $t_{film}$  from the reflectivity profile is to use the following formula, assuming the data are plotted as functions of  $L$  :

$$\frac{t_{film}}{c} = \frac{N}{\Delta L_{tot}} \quad (2.6)$$

where  $N$  is the number of oscillations taken into account and  $\Delta L_{tot}$  the  $L$  periodicity of the  $N$  oscillations.

## 2.5.4 Grazing incidence x-ray diffraction

In a surface X-ray diffraction measurement the sample usually contains a surface layer due to surface reconstruction, relaxation or the presence of adsorbates, thin films or nano-clusters. The structure of this surface layer is unknown and therefore is the subject of the SXRD study. Below the surface layer an ideal bulk structure of the substrate is assumed.

Unfortunately, the volume of the surface region is much less than that of the bulk crystal, resulting in much lower diffraction intensities. Hence a synchrotron X-ray source is needed in order to acquire data over a large volume in reciprocal space. Using a third generation source like the ESRF can further reduce the data acquisition time and improve the data quality.

This technique is undifferentially called surface x-ray diffraction (SXRD) or grazing incidence X-ray diffraction (GIXRD), although SXRD is not always carried out at grazing

incident geometry. Due to the truncation of a bulk crystal at the surface, or the presence of a surface layer, the scattering intensities in the reciprocal space in a SXRD experiment are extended along the surface normal direction to form Bragg rods, which are discrete in HK plane but continuous along L.

Those Bragg rods that have contributions from the bulk are called crystal truncation rods (CTRs). They extend from the bulk Bragg peaks and are most sensitive to the structure of the surface layer near the so-called anti-Bragg regions, as indicated in Fig. 2.18. There are also rods that do not pass through any bulk Bragg peaks. These rods arise from the presence of superstructures, or relaxation of the surface layer. Note that the surface layer can also contribute to the CTRs if it is commensurate to the substrate lattice (see Fig. 2.23).

By measuring the intensity distribution in all three dimensions, one can determine the symmetries, unit cell dimensions, mosaicity, domain sizes, and possibly detailed atomic structures of the ordered parts of the surface layer.

One fast way to measure the intensity distribution is to perform line scans in the reciprocal space. The commonly used line scans include (i) in-plane radial scans, (ii) in-plane H/K scans at a constant K/H and (iii) L scans. For well polished surfaces with large domains the Bragg rods can be very sharp and missed by the fast line scans. A more accurate way to measure the intensities is to integrate the rods at each HKL position by a rocking (or  $\theta$ ) scan, where the sample is scanned about its surface normal with the detector arm fixed. Such rocking scans also allow proper background subtraction.

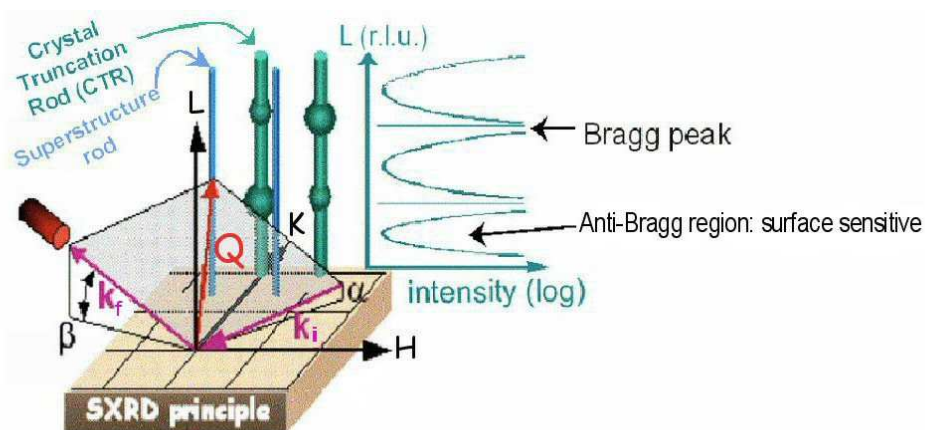


Figure 2.18: Grazing incidence X-ray diffraction : (H, K, L) reciprocal space and information collected along the out of plane directions.

## Notations

The incident and scattered wave vectors are expressed as  $\mathbf{k}_i$  and  $\mathbf{k}_f$ . The momentum transfer  $\mathbf{Q}$  is defined by  $\mathbf{Q}=\mathbf{k}_f-\mathbf{k}_i$ . The diffracted intensity can be expressed as a function of  $\mathbf{Q}$ . The norm of the wave vector is  $\frac{2\pi}{\lambda}$ , where  $\lambda$  is the wavelength of the incident beam.

$\alpha_i$  and  $\alpha_f$  are the incident and scattering angles, respectively, with respect to the sample surface. In the case of reflectivity measurements  $\alpha_i = \alpha_f = \theta$ .

## Scattered intensity from a surface

Since the scattered intensity from a surface is typically several orders of magnitude weaker compared to the incident beam, SXRD data can be well analyzed using the kinematical theory for x-ray diffraction. It shows that, for a small 3D single crystal that contains  $N_a \times N_b \times N_c$  unit cells defined by lattice vectors  $\mathbf{a}$ ,  $\mathbf{b}$  and  $\mathbf{c}$ , the scattered intensity can be described by [116]

$$I(\mathbf{Q}) \propto |F(\mathbf{Q})|^2 \frac{\sin^2(\pi N_a H)}{\sin^2(\pi H)} \frac{\sin^2(\pi N_b K)}{\sin^2(\pi K)} \frac{\sin^2(\pi N_c L)}{\sin^2(\pi L)} \quad (2.7)$$

where  $\mathbf{Q} = H\mathbf{a}^* + K\mathbf{b}^* + L\mathbf{c}^*$  is the momentum transfer, and  $F(\mathbf{Q})$  the structure factor of the unit cell, which can be expressed as

$$F(\mathbf{Q}) = \sum_j^{unit\ cell} f_j(Q) e^{-B_j Q^2/4} e^{2\pi i \mathbf{Q} \cdot \mathbf{r}_j} \quad (2.8)$$

where  $f_j$ ,  $B_j$  and  $\mathbf{r}_j$  are the atomic scattering factor, Debye-Waller B factor and position vector, respectively, for atom  $j$  in the unit cell. The atomic scattering factor for each element is tabulated as a function of  $\sin\theta/\lambda$ , or  $1/(2d_Q)$ , in Ref. [117], where  $\theta$ ,  $\lambda$  and  $d_Q$  are the incident angle, x-ray wavelength and lattice spacing of reflection  $\mathbf{Q}$ , respectively. The Debye-Waller factor  $\exp(-BQ^2/4)$  accounts for thermal vibrations of the lattice. For bulk Si the Debye-Waller B factor is  $0.47 \text{ \AA}^2$  at room temperature [118]. Eq. 2.8 shows that the structure factor  $F(\mathbf{Q})$  is the coherent sum of the scattered amplitudes from all atoms within a unit cell.

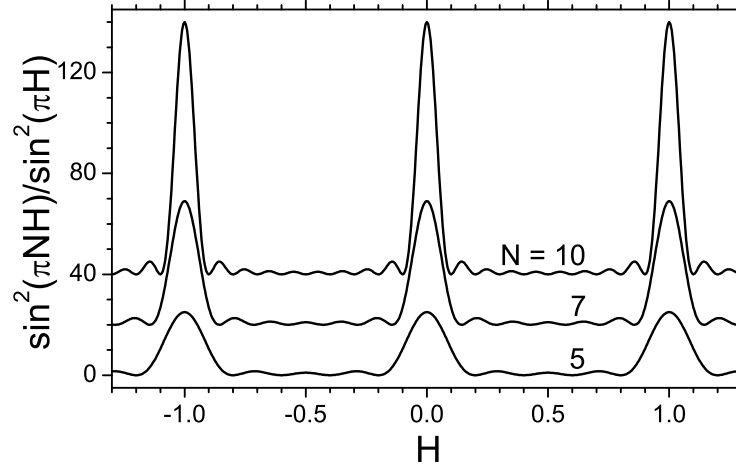


Figure 2.19: Plots of interference function for  $N = 5, 7,$  and  $10$ .

In Eq. 2.7 the three factors composed of sinusoidal functions are called interference functions. As demonstrated in Fig. 2.19 for 1D cases along  $H$ , the functions describe the width and height of the main peaks as well as the intensity modulations between them due to the finite size of the crystal. It can be shown from Eq. 2.7 that the peak height is proportional to the volume square of the crystal and the peak width is inversely proportional to the dimension of the crystal. For example, if  $\Delta H$  is the peak width or modulation periodicity measured in the reciprocal space, the corresponding real-space dimension  $\Delta$  along the  $\mathbf{a}$ -axis (e.g., domain size) would be

$$\Delta = a/\Delta H \quad (2.9)$$

In SXRD we are interested in determining the atomic structure of a surface layer, which is usually periodic parallel to the surface (up to the domain boundary) but non-periodic in the direction normal to the surface. This means  $N_c = 1$  and thus the interference function of  $L$  in Eq. 2.7 drops out. The in-plane domain size given by  $N_a$  and  $N_b$  determines the thickness of the Bragg rods through the interference functions of  $H$  and  $K$  in Eq. 2.7. However, the thickness of the rods as well as the values of the two in-plane interference functions at each rod do not depend on  $H$  and  $K$ , as evident in Fig. 2.19. Therefore, Eq. 2.7 shows that the scattered intensity modulations along the rods arise directly from the structure factor of

the surface layer  $F_{surface}(\mathbf{Q})$ . For superstructure (or fractional order) rods, we simply have

$$I(\mathbf{Q}) \propto |F_{surface}(\mathbf{Q})|^2 \quad (2.10)$$

For CTRs, the contribution from the ideal bulk of the substrate has to be included

$$I(\mathbf{Q}) \propto |F_{surface}(\mathbf{Q}) + F_{bulk}(\mathbf{Q})|^2 \quad (2.11)$$

Since we are only interested in the intensity distributions between the strong substrate Bragg peaks,  $F_{bulk}(\mathbf{Q})$  can be calculated from the kinematical theory, as described in Ref. [113, 119].

### Integrated intensity

In a real SXRD measurement one always integrates the scattered intensity over a finite volume in reciprocal space. Such integration introduces additional factors that have specific dependencies on  $\mathbf{Q}$  depending on the diffraction geometry and type of scan. These factors must be carefully removed to retrieve the structure factors for further analysis.

In the present work, all the SXRD experiments were performed on a six-circle diffractometer in a z-axis mode with a fixed incident angle  $\alpha_i$  and sample surface parallel to the floor. The large data set that will be presented in Chapter 5 was measured by the so-called rocking ( $\theta$ ) scans described previously. Following the pioneering work by Vlieg [120], the integrated intensity obtained by a rocking scan can be expressed as

$$I_{int} \propto PLC_{rod}C_{area}|F(\mathbf{Q})|^2 \quad (2.12)$$

where  $P$ ,  $L$ ,  $C_{rod}$  and  $C_{area}$  are the polarization factor, Lorentz factor, rod interception correction and area correction. They are described in detail in Ref. [120]. For each rocking scan the peak intensity is first integrated numerically after background subtraction. The four correction factors in Eq. 2.7(6) are then calculated and removed from the integrated intensity to obtain the structure factor. The errors of such experimentally determined structure factors are estimated following the procedure discussed in Ref. [121].

### Transformation matrix between coordinate systems

In SXRD it is more convenient to work with so called surface coordinates. Fig. 2.20 shows the relationship between a bulk and a surface unit cell for the Si(001) surface. The latter is 45° rotated away from the bulk coordinate system.

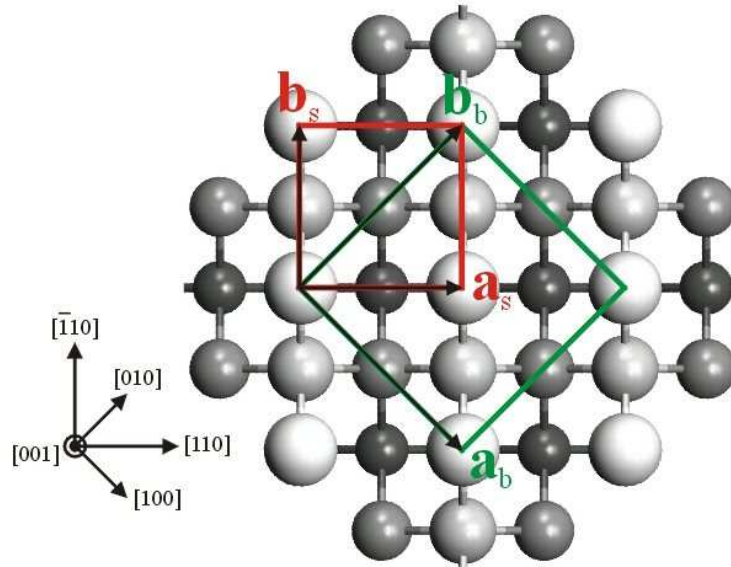


Figure 2.20: Si crystal structure. A bulk ( $\mathbf{a}_b, \mathbf{b}_b$ ) and a surface ( $\mathbf{a}_s, \mathbf{b}_s$ ) unit cell are displayed. The corresponding based vectors are indicated in the figure. The darker the atoms, the deeper the atomic plane is.

In the case of the bulk Si unit cell  $a = b = c = 5.43 \text{ \AA}$ . In the case of the Si(001) surface unit cell  $a = b = 3.84 \text{ \AA}$  while  $c = 5.43 \text{ \AA}$ . If  $X$  and  $Y$  are the coordinates of an atom, the transformation matrix from the surface to bulk coordinates in the real space is given by:

$$\begin{pmatrix} X \\ Y \end{pmatrix}_{bulk} = \begin{pmatrix} \frac{1}{2} & -\frac{1}{2} \\ \frac{1}{2} & \frac{1}{2} \end{pmatrix} \times \begin{pmatrix} X \\ Y \end{pmatrix}_{surface}$$

and the inverse transformation matrix is

$$\begin{pmatrix} X \\ Y \end{pmatrix}_{surface} = \begin{pmatrix} 1 & 1 \\ -1 & 1 \end{pmatrix} \times \begin{pmatrix} X \\ Y \end{pmatrix}_{bulk}$$

The transformation matrix from the surface to bulk coordinates in the reciprocal space is

given by

$$\begin{pmatrix} H \\ K \end{pmatrix}_{bulk} = \begin{pmatrix} 1 & -1 \\ 1 & 1 \end{pmatrix} \times \begin{pmatrix} H \\ K \end{pmatrix}_{surface}$$

and the inverse matrix is

$$\begin{pmatrix} H \\ K \end{pmatrix}_{surface} = \begin{pmatrix} \frac{1}{2} & \frac{1}{2} \\ -\frac{1}{2} & \frac{1}{2} \end{pmatrix} \times \begin{pmatrix} H \\ K \end{pmatrix}_{bulk}$$

All the scans presented in this report, along H, K or L directions, are plotted in surface Si reciprocal lattice unit (r.l.u.).

### In-plane scans, rod scans and domain size

In-plane scans contain in-plane information in the (H,K) plane. They are usually collected along high symmetry directions while the L value is kept around 0.1.

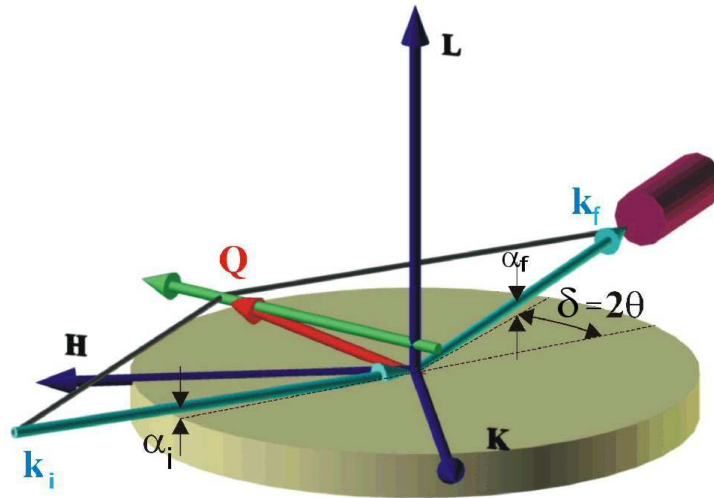


Figure 2.21: Scan along in-plane directions.  $Q$  is the momentum transfer vector,  $k_i$  and  $k_f$  the incident and the scattered wave vectors.  $\alpha_i$  is the incident angle and (H,K,L) are the reciprocal space base vectors.  $\delta$  is the angle between the incident and the scattered wave vectors.

Fig. 2.21 describes the in-plane radial scan geometry and displays the H, K, and L reciprocal space base vectors. The incident angle  $\alpha_i$  stays constant and both the sample and the detector are moving such that the  $Q$  vector scans along an in-plane (H,K) direction (the

green arrow in Fig. 2.21). In-plane scans are also commonly performed along a direction not pointing at the origin of the reciprocal space. Assuming an isotropic domain and using the Si(001) surface coordinate system previously defined, the in-plane domain size  $\Delta_{xy}$  can be retrieved from the FWHM ( $\Delta Q$ ) of an in-plane peak using (see Eq. 2.9)

$$\Delta_{xy} = \frac{3.84}{\Delta Q} \quad (2.13)$$

$\Delta Q$  can be most conveniently measured by a rocking scan around an in-plane peak on the H (or K) axis near the origin. Such a rocking scan is equivalent to a K (or H) scan and measures  $\Delta Q = \Delta K$  (or  $\Delta Q = \Delta H$ ). Measuring  $\Delta Q$  this way provides the highest Q resolution because the detector slit is nearly perpendicular to the scan direction. To estimate the contribution of in-plane mosaicity to  $\Delta Q$  one can compare the values of  $\Delta Q$  measured at several higher orders of reflections.

Fig. 2.22 describes the geometry of a rod scan. Similar to the in-plane scan, the FWHM  $\Delta L$  of a peak measured in a rod scan can be used to determine the thickness of the surface layer as  $\Delta_z = \frac{5.43}{\Delta L}$ .

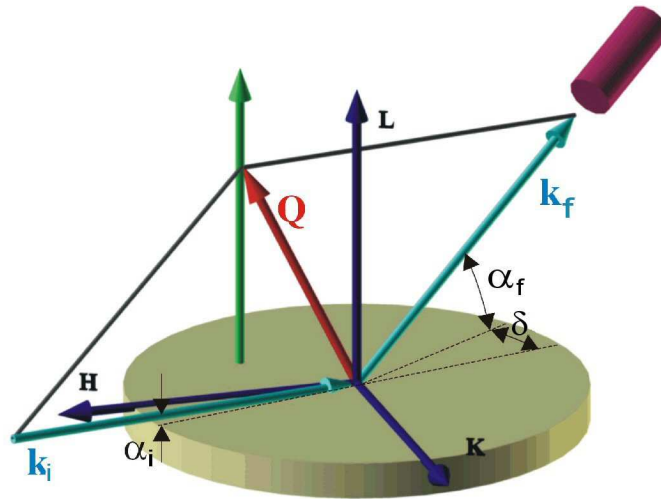


Figure 2.22: Scan along off-specular directions. The vectors are defined similarly than in Fig. 2.21.

From in-plane and rod scans the lattice constants  $a$ ,  $b$ , and  $c$  of the surface layer can be evaluated. In general, if a peak appears at (H,K,L) in the Si(001) surface coordinate

system, the lattice spacing  $d_{HKL}$  corresponding to this peak is

$$d_{HKL} = \left( \frac{H^2 + K^2}{3.84^2} + \frac{L^2}{5.43^2} \right)^{-\frac{1}{2}} \quad (2.14)$$

Fig. 2.23 summarizes the sensitivities of different kind of scans that can be performed in reciprocal space, i.e. reflectivity scans, in-plane scans and off-specular scans, to the different surface structures.

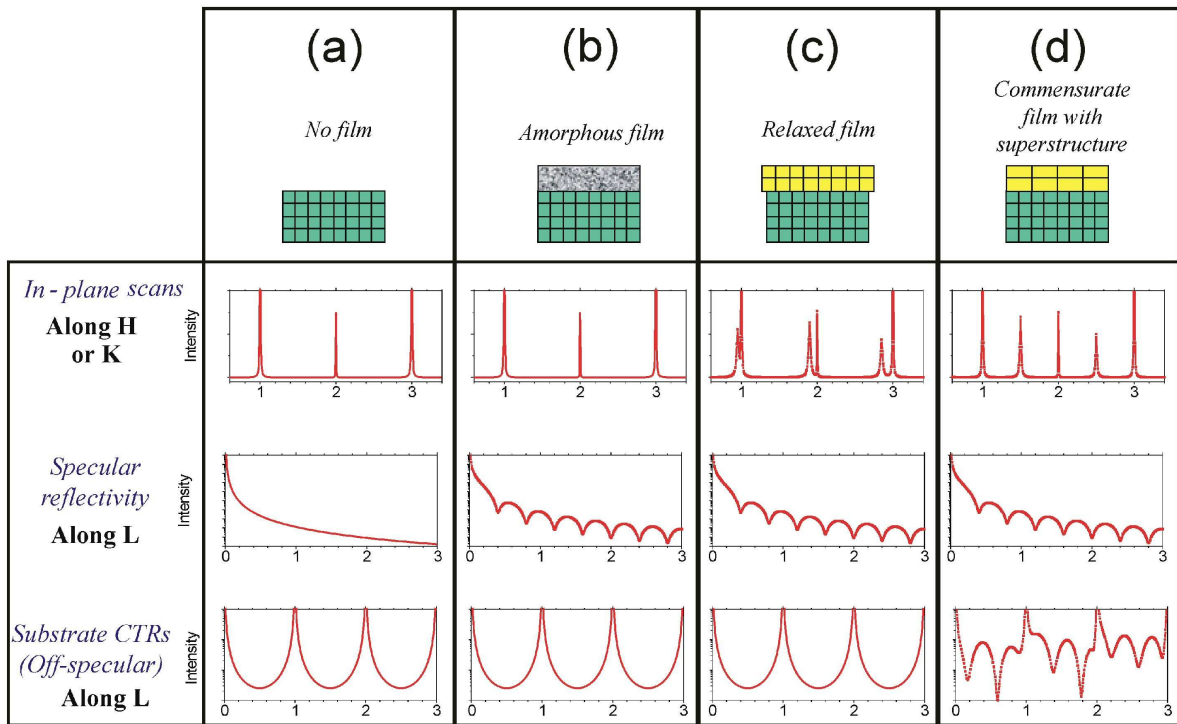


Figure 2.23: Specular reflectivity profiles in different cases: (a) A bare substrate ; (b) Substrate + Disordered / Amorphous film ; (c) Substrate + ordered film with its own lattice parameters ; (d) Substrate + ordered film with at least one in-plane lattice parameter commensurated with the one of the substrate.

Four different cases are considered: (a) a bare substrate ; (b) substrate + disordered / amorphous film ; (c) substrate + ordered film with its own lattice parameters ; (d) substrate + ordered film with at least one in-plane lattice parameter commensurated with the one of the substrate.

In the case of a bare silicon substrate (Fig. 2.23 (a)) the reflectivity profile corresponds to the so-called Fresnel reflectivity  $R_F$ , which describes the reflectivity curve from a thick

mirror (substrate surface). The in-plane and off-specular scans show the intensity maxima corresponding to the bulk Bragg peak of the substrate. The weaker peak appearing at  $H/K=2$  represents the tail of a CTR.

Fig. 2.23 (b) corresponds to the case of an amorphous film added on top of the crystalline substrate. The in-plane and off-specular scans remain unchanged compared with the one in Fig. 2.23 (a) because they are only sensitive to the ordered part of the surface layer. However in the case of the specular reflectivity scan the presence of an electron density variation due to the introduction of the film gives rise to Kiessig fringes. These regularly spaced oscillations remain unchanged in Figs. 2.23 (c) and (d), which correspond to a relaxed and a commensurate film, respectively. For these two cases the in-plane scans show additional sets of Bragg peaks corresponding to the in-plane lattice constants of the relaxed film (c) and the commensurate superstructure (d). In the case of the relaxed film (c), the off-specular scan still appears identical to the ones of a bare substrate and of an amorphous film. This is simply because the diffracted intensities from the ordered film and substrate are totally separated in reciprocal space. Finally, the off-specular scan with a commensurate film in (d) shows oscillations in the anti-bragg peak regions due to the interference of the diffracted X-rays from the film and the substrate. Note that only the surface layer ordered in all three dimensions will participate in this intensity modulation.

### 2.5.5 Patterson function

For a 3D structure that has an electron density  $\rho(x, y, z)$ , the 2D Patterson map projected along the z-axis can be defined by

$$P(x, y) = \int_{2D \text{ unit cell}} \rho(x', y') \rho(x + x', y + y') dx' dy' \quad (2.15)$$

where  $\rho(x, y) = \int_{-\infty}^{\infty} \rho(x, y, z) dz$  is the electron density projected along the z-axis. Since  $\rho(x, y)$  is also the Fourier sum of the structure factors in the HK plane  $F_{HK}(L=0)$ , i.e.,

$$\rho(x, y) = \frac{1}{A} \sum_{HK} F_{HK}(L=0) e^{-2\pi i(Hx+Ky)} \quad (2.16)$$

it can be shown that  $P(x,y)$  can be also expressed as

$$P(x,y) = \frac{1}{A} \sum_{HK} |F_{HK}(L=0)|^2 \cos(2\pi(Hx + Ky)) \quad (2.17)$$

where  $A$  is the area of the 2D unit cell projected on to the  $xy$  plane.

Eq. 2.15 shows that the Patterson function is the convolution of an electron density with its own inversion, i.e.  $P(x,y) = \rho(x,y) \otimes \rho(-x,-y)$ . In this convolution  $\rho(x',y')$  and  $\rho(x+x',y+y')$  will both have large values when  $(x',y')$  and  $(x+x',y+y')$  are vectors each pointing at an atom. This requires  $(x,y)$  to be an interatomic vector. Therefore the locations of the high intensity peaks in a Patterson map provide the interatomic vectors of a structure, which are often very valuable in identifying suitable models for structure determination.

In a SXRD experiment, if one chooses the  $z$ -axis to be perpendicular to the sample surface, Eq. 2.17 shows that an in-plane Patterson map can be constructed directly from the Fourier sum of the measured peak intensities of an in-plane data set. Note that since such a Patterson map corresponds to a projected structure, if one includes in the data set also the integer reflections, which have a major contribution from the substrate, the resulting Patterson map will be dominated by the bulk structure of the substrate. Therefore, this method is usually applied only to in-plane fractional-order reflections in SXRD for studying the unknown surface layer. Note also that no structural information along the surface normal direction is available in an in-plane Patterson map due to the projection.

## 2.6 X-ray photoelectron spectroscopy

The second experimental hutch of ID32 is dedicated to XPS and XSW experiments. For the purpose of this project only the XPS activity will be described.

### 2.6.1 Sample transfer

For the use of XPS experiments two new UHV transfer chambers have been developed, with the specificity of being able to carry up to 12 samples prepared in the SCL and transfer them to the XPS system at the beamline. Figs. 2.24(a) and (b) show pictures of such a XPS transfer chamber.

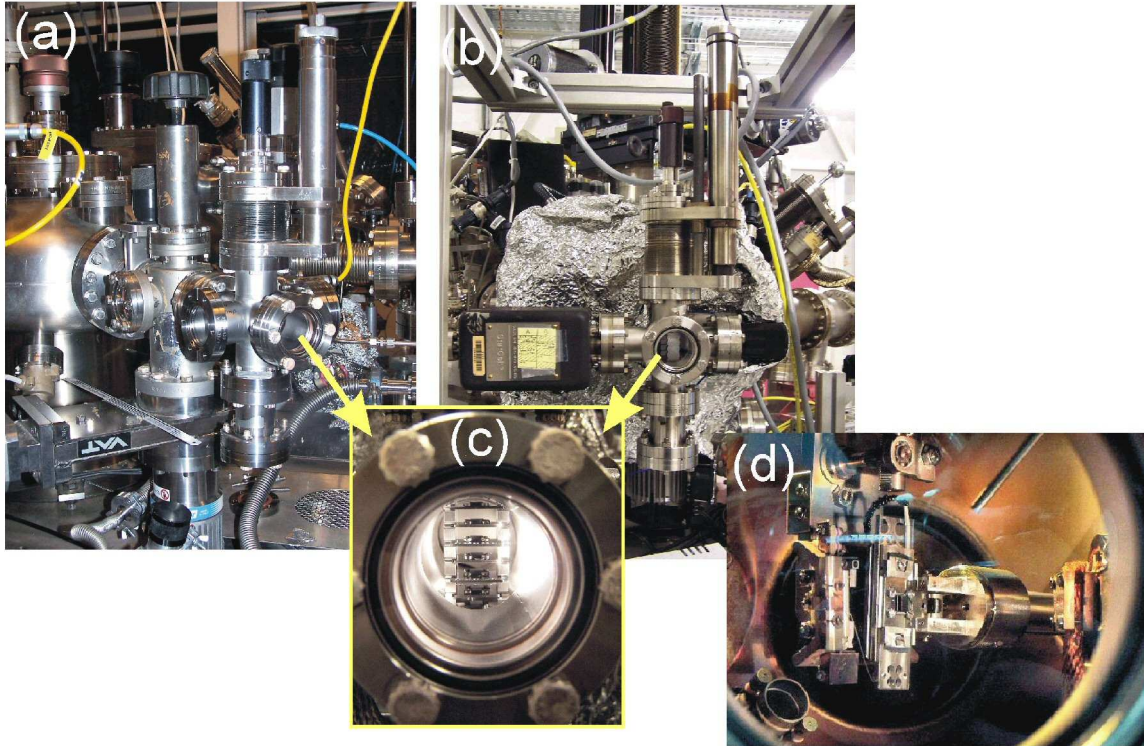


Figure 2.24: Transfer chamber for photoemission experiments. (a) Chamber connected to the R2P2 system in the SCL. (b) Chamber connected to the XPS system at the beamline. (c) View through the chamber port of the different samples loaded inside. (d) Transfer of one sample on the XPS chamber manipulator.

### 2.6.2 XPS set-up

The XPS experiments were carried out using a home designed UHV XPS system at ID32. The base pressure of the XPS chamber is  $1 \times 10^{-10}$  mbar. The sample was illuminated with undulator radiation, monochromatized by a pair of Si(111) crystals, which have an energy resolution  $\Delta E/E \approx 10^{-4}$ . The X-ray energy used to collect the XPS data was kept fixed at 2.6 KeV. The beam size defined by a pair of fixed apertures three meters before the sample was  $1.0(\text{H}) \times 0.8(\text{V}) \text{ mm}^2$ . The incident photon flux was monitored by the drain current measured from a  $0.8 \mu\text{m}$  thick Al mylar foil that was constantly in the beam and situated about 1.5 meters before the sample. The energy spectra of the emitted electrons were recorded by a commercial hemispherical electron analyzer (PHI360) equipped with a 16 channel detection system. All the presented data have been collected with a pass energy of 11.75 eV. Fig. 2.26 shows a schematic of the setup for XPS experiments and Fig. 2.25 a

photograph of the experimental setup at the beamline.

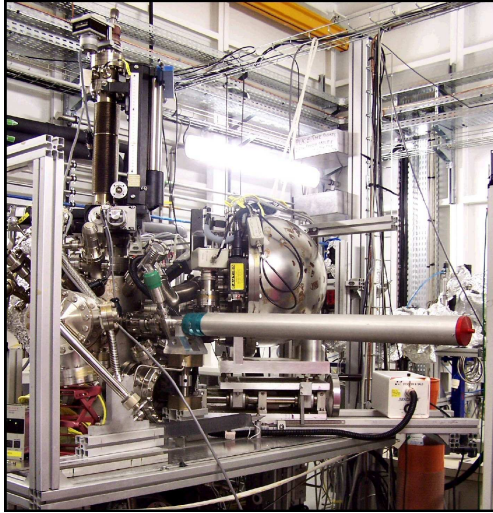


Figure 2.25: ID32 experimental hutch 2. XPS chamber.

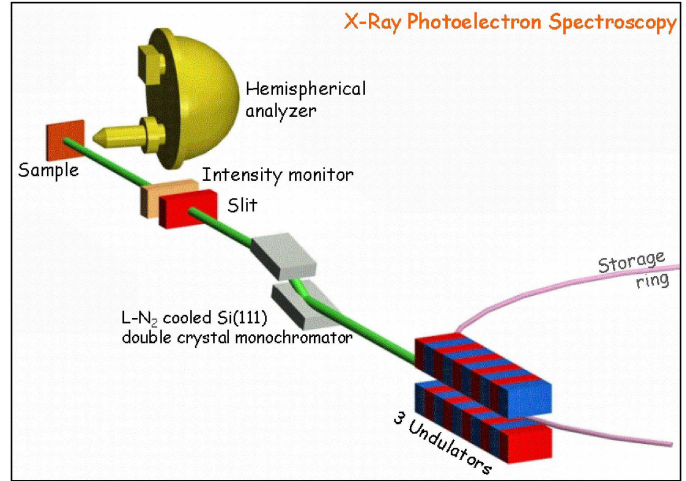


Figure 2.26: Schematic of the optics setup for XPS experiments.

The samples were electrically grounded to eliminate charging effects during the measurements. To minimize experimental uncertainties associated with long-term energy variations caused by spectrometer and monochromator instabilities and to improve the signal to noise ratio, the XPS data were collected over repeated scans. For quantitative analysis of the XPS spectra, a Shirley background function was assumed for background subtraction and a multipeak Gaussian deconvolution procedure was used to extract the exact line positions and intensities.

### 2.6.3 Principle

X-ray Photoelectron Spectroscopy (XPS), also known as Electron Spectroscopy for Chemical Analysis (ESCA), measures the kinetic energy  $E_K$  of the photoexcited electrons emitted from a sample to derive the binding energy  $E_B$  of the initial electronic state, which can be related to  $E_K$  by:

$$E_B = h\nu - E_K - \phi_A \quad (2.18)$$

where  $h\nu$  is the incident beam energy (photon energy), and  $\phi_A$  is the work function of the analyser, as illustrated in Fig. 2.28.

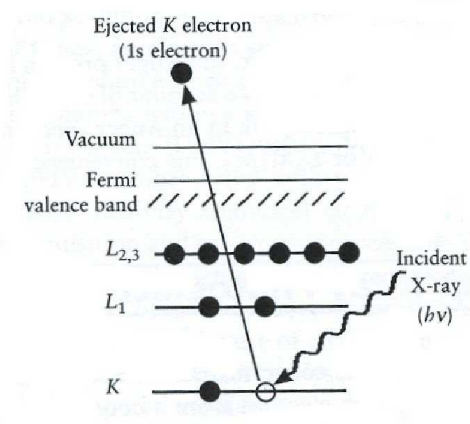


Figure 2.27: Schematic diagram of the XPS process, showing photoionization of an atom by the ejection of a 1s electron, as extracted from [110].

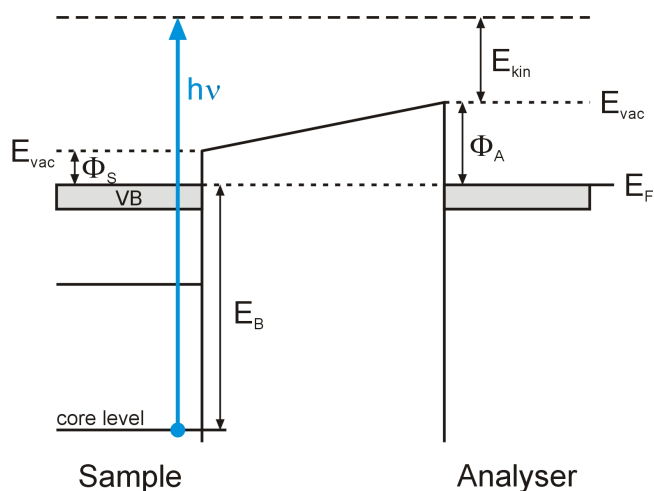


Figure 2.28: Schematic diagram of the energetics of the photoemission process.

Since the values of  $E_B$  are characteristic for each element and depend very often on the chemical bonds that the photoionized atom forms with its neighbors, XPS has been widely used to study the composition of a sample and the chemical states of the constituent atoms.

(i) **Chemical composition:** Due to the unique electronic configuration each element exhibits different ionizable energy levels, which are reflected as element-specific peaks in the x-ray photoelectron spectrum. The positions of the peaks correspond to the binding energies of the photoelectrons emitted from different atomic orbitals. XPS measurements thus allow the identification of participating elements by identifying their atomic core level lines. If additional information concerning the cross sections of the electronic transitions, the mean free paths of the electrons and the spectrometer efficiency is provided, even a quantitative determination of the chemical stoichiometry is possible [122].

(ii) **Chemical states:** The exact peak positions of core level emissions in XPS spectra are governed by the oxidation levels of the emitting atoms [123]. Generally, in case of a coordination with more electronegative ligands the core level electrons of the central atom appear at higher binding energy because charge transfers to the ligands make the central atom more positively charged and thus more difficult to emit an electron. This so-called chemical shift may influence the binding energy of the emitted electron up to 10 eV [122], which enables the identification of the chemical state of the emitting atom.

XPS has been considered as a surface sensitive technique due to the limited escape depths of the electrons. Fig. 2.29 depicts the universal curve for the electron mean free path, reproduced from [111]. XPS using conventional lab source works in the kinetic energy

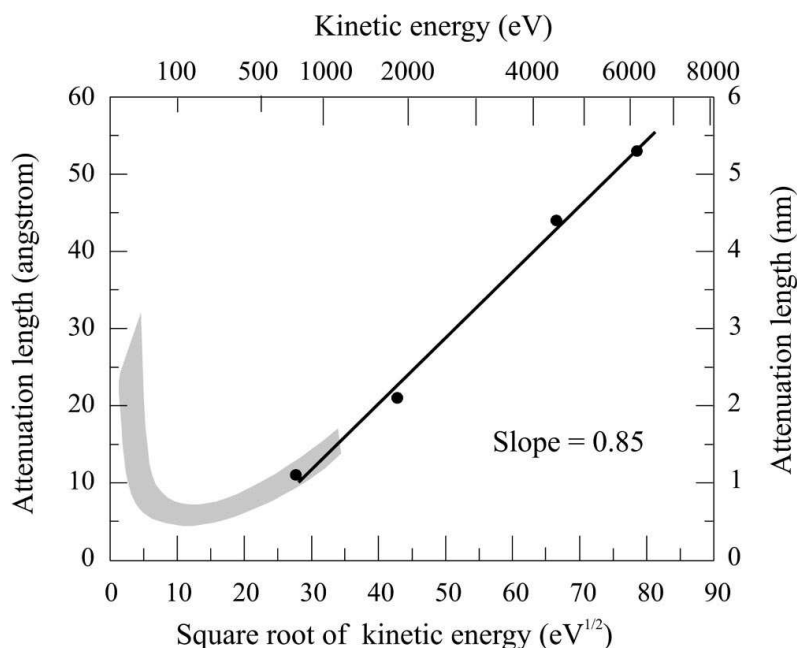


Figure 2.29: Electron mean free path universal curve extracted from [111].

range below 1500 eV and thus can provide a maximum probing depth of about 2 nm, which can be extended to beyond 5 nm when highly intense hard x-rays ( $> 5$  KeV) generated by a third generation synchrotron source are used.

In addition to changing the excitation energy, the information depth  $\Lambda$  of XPS can also be tuned by varying the emission angle  $\alpha$  of a photoelectron with respect to the sample surface, as defined in Fig. 2.30. This method is called angle-resolved XPS (ARXPS) and utilizes the fact that  $\Lambda \propto \sin\alpha$ . In a typical ARXPS measurement core level intensity ratios among different elements are recorded as functions of  $\alpha$  and the relative depth profiles of the atomic densities may be resolved with a reasonable accuracy. A suitable electron energy ensures a sufficient variation of the escape depth for different emission angles.

In addition to photoemission in a photoionization process, Auger electrons may also be emitted because of relaxation of the excited ions remaining after photoemission. This Auger process occurs roughly  $10^{-14}$  seconds after the photoelectric event. An outer electron falls into the inner orbital vacancy, and a second electron is simultaneously emitted, carrying off the excess energy, as discussed in section 2.4.

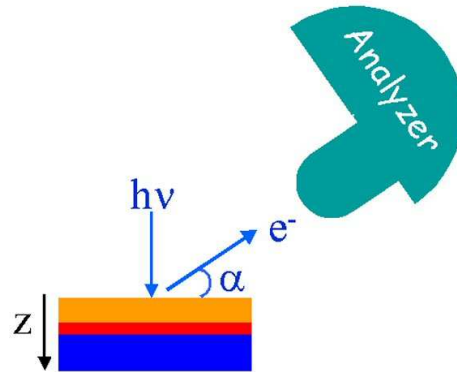


Figure 2.30: Drawing indicating how is the emission angle defined.

In this study we have worked at fixed  $h\nu$  and studied the Si2p, Si1s, O1s, Pr4d and Pr3d core levels as well as the valence band and Si KLL Auger.

## 2.6.4 Preliminaries before data collection

### Binding energy scale calibration

The calibration of the energy scale of the spectra was performed by measuring the Fermi edge of gold (Au) foils, since Au is a noble metal, so that no surface cleaning prior to an XPS measurement is required and its high density of states at the Fermi edge makes the Fermi edge easily identifiable. The position of the Au Fermi edge marks the zero of the binding energy for the spectra measured from all the other samples (see Fig. 2.28) and provides a calibration of the incident photon energy  $h\nu$ . To account for energy drift due to instabilities of the monochromator and electron analyzer, we have measured the Au Fermi edge at the beginning and the end of the XPS beamtime. We found an energy drift of about 100 meV over four days. The average  $h\nu$  is found equal to 2603.84 eV.

### Resolution of the measurements

The measured Au Fermi edge was compared with the convolution of a Gaussian function and a Fermi function  $f(E_K)$ :

$$f(E_K) = \frac{1}{e^{-(E_K - E_F)/k_B T} + 1} \quad (2.19)$$

where  $k_B$  is Boltzmann's constant ( $=8.617 \times 10^{-5}$  eV/K) and  $T$  the temperature of the experiment (room temperature). The best agreement was reached when the FWHM of the Gaussian function was  $\approx 440$  meV, as shown in Fig. 2.31, which corresponds to the overall resolution of the experiment. The major contributions to this width are the band width of the x-ray beam, which is about 350 meV for Si(111) at 2.6 KeV, and the energy resolution of the electron analyzer (i.e.  $\Delta E_{all}^2 = \Delta E_{beam}^2 + \Delta E_{analyzer}^2$ ). Subtracting quadratically the band width of the beam from the overall width, we estimate that the energy resolution of the analyzer is about 270 meV for the pass energy we used.

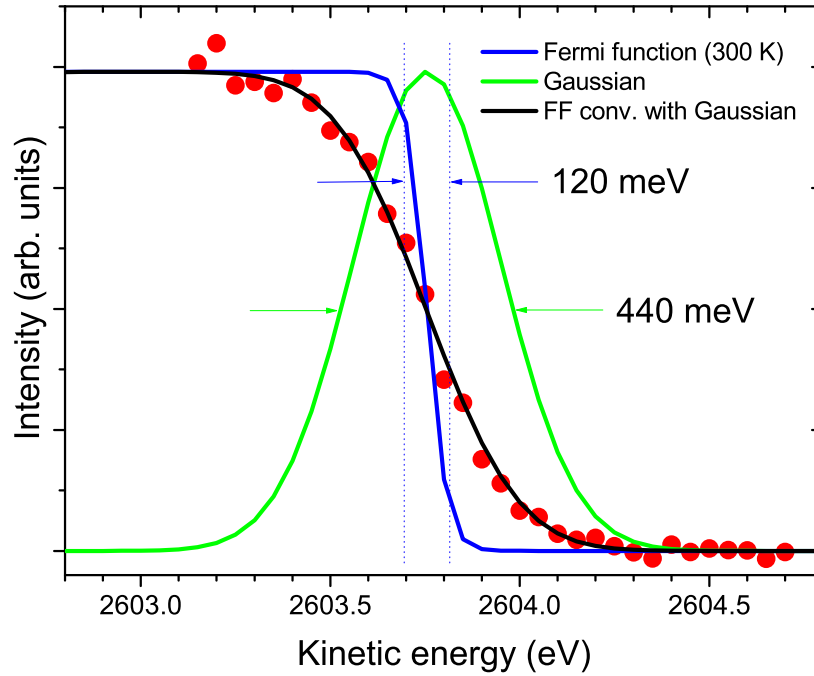


Figure 2.31: Au Fermi edge measurement compared with the convolution of a Gaussian function and a Fermi function.

### Determination of the electron absorption coefficient of the oxide film $\mu$

The absorption coefficient of the oxide film  $\mu_{Film}$  was assumed equal to the one of the Si substrate  $\mu_{sub}$  and denoted as  $\mu$ . It was determined experimentally for  $\approx 2.5$  KeV electrons

using one sample with a 2.5 nm thick film by monitoring the Si2p signal from the bulk substrate at different emission angles  $\alpha$  (see Fig. 2.30).  $\mu$  was found equal to  $0.4 \text{ \AA}^{-1}$ . Therefore, the mean free path (mfp) of the outgoing electrons with this energy, which can be described by  $1/\mu$ , is about 2.5 nm. This value is in agreement with the one found in Fig. 2.29.

## Chapter 3

# Pr<sub>2</sub>O<sub>3</sub> growth on Si(111)

---

The initial stages of the molecular beam epitaxy (MBE) growth of Pr<sub>2</sub>O<sub>3</sub> on atomically clean Si(111) commercially available 350  $\mu\text{m}$  thick wafers have been studied under UHV conditions ( $\leq 10^{-9}$  mbar) by low energy electron diffraction (LEED) and scanning tunneling microscopy (STM) from the nucleation to the coalescence of the first layers. At very low coverages, the oxide nuclei decorate the dimer rows of the silicon surface as line structure forming open triangles. At higher coverages, two-dimensional, equilateral, triangular islands with a fairly narrow size distribution and a well defined thickness are observed. Island nucleation occurs both at step edges and on the terraces. Upon coalescence at coverages beyond one monolayer, the surface is covered by a flat and pseudomorphic oxide film with a (1 $\times$ 1) surface unit cell. The observed (1 $\times$ 1) LEED patterns are in agreement with the epitaxial growth of the trigonal Pr<sub>2</sub>O<sub>3</sub> on Si(111) with one specific orientation. These findings are correlated with the results of Jeutter and Moritz who obtained an atomic scale structural model of the Pr<sub>2</sub>O<sub>3</sub>/Si(111) interface by using surface x-ray diffraction [4].

### 3.1 The Si(111)-7 $\times$ 7 reconstructed surface

#### 3.1.1 Surface preparation on wafers

The Si(111) substrates were cleaved from As-doped wafers with a resistivity  $< 0.01 \Omega\cdot\text{cm}$  and a maximum miscut angle of  $\pm 0.1^\circ$ , as indicated by the supplier. These 350  $\mu\text{m}$  thick substrates were slowly outgassed at 650  $^\circ\text{C}$  and then cleaned by repeated flash annealing for

a few seconds at  $1250^\circ\text{C}$ , as described in the literature [83]. Temperatures were measured using an optical pyrometer.

### 3.1.2 LEED and STM results

Before  $\text{Pr}_2\text{O}_3$  deposition, the quality of the  $(7\times 7)$  reconstructed surface of the  $\text{Si}(111)$  substrate was characterized by LEED and STM. Fig. 3.1 presents the LEED and STM results collected on the clean  $\text{Si}(111)$ - $7\times 7$  reconstructed surface.

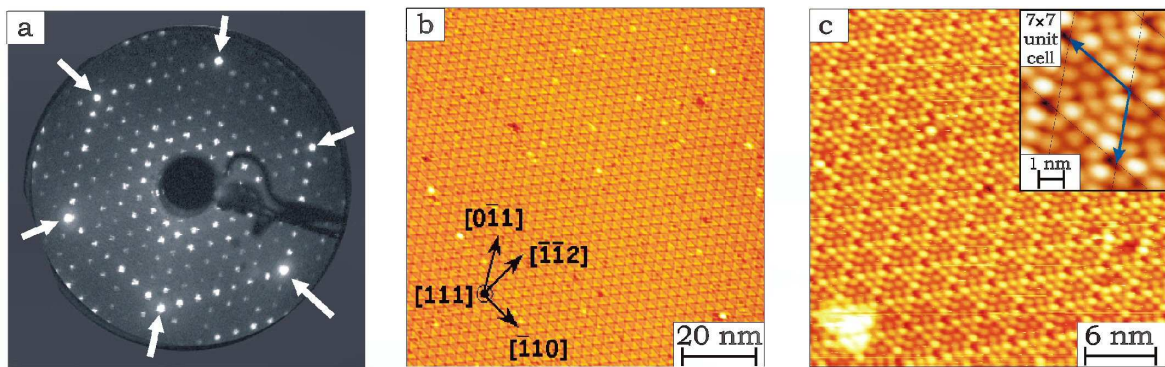


Figure 3.1: LEED and STM results of the clean  $\text{Si}(111)$ - $7\times 7$  reconstructed surface. (a) LEED pattern recorded at 40 eV. The  $1\times 1$  spots are marked by arrows. The specular beam is covered by the electron gun in the middle. Extra spots are due to the  $7\times 7$  reconstruction. (b) Large scale STM topograph.  $100\times 100\text{nm}^2$ ,  $U_s = -1.93\text{ V}$ ,  $I = 1.14\text{ nA}$ .  $\text{Si}(111)$  bulk crystallographic coordinates apply for all images. (c) High resolution STM topograph of a clean  $\text{Si}(111)$  surface,  $30\times 30\text{ nm}^2$ ,  $U_s = -1.90\text{ V}$ ,  $I = 0.05\text{ nA}$ . Inset showing in greater details a  $7\times 7$  unit cell with its characteristic 12 adatoms.

Fig. 3.1(a) depicts its LEED pattern recorded at 40 eV. The specular beam is covered by the electron gun in the middle. The  $1\times 1$  spots are marked by arrows and extra spots in between are due to the  $7\times 7$  reconstruction and testify towards a well ordered and clean surface.

Figs. 3.1(b) and (c) show the corresponding STM results, at two different scale, of this  $\text{Si}(111)$ - $7\times 7$  reconstructed surface. Fig. 3.1(b) displays a  $100\times 100\text{ nm}^2$  flat terrace with a small amount of surface defects ( $< 2\%$ ) appearing as depressions or protrusions. The bulk lattice directions mark the crystallographic orientation of the surface and is valid for all the STM images presented in this chapter.

Fig. 3.1(c) correspond to a  $30 \times 30 \text{ nm}^2$  zoom in on the same surface and resolves the  $7 \times 7$  unit cell meshes of the reconstructed silicon surface. The inset in the top right corner shows in greater details a  $7 \times 7$  unit cell. It consists of two triangular subunits. Each of them contains six protrusions, corresponding to the adatoms of the dimer-adatoms-stacking fault (DAS) model proposed by Takayanagi *et al.* in Ref. [124]. This model explains in detail the  $7 \times 7$  reconstruction and is depicted in Fig. 3.2.

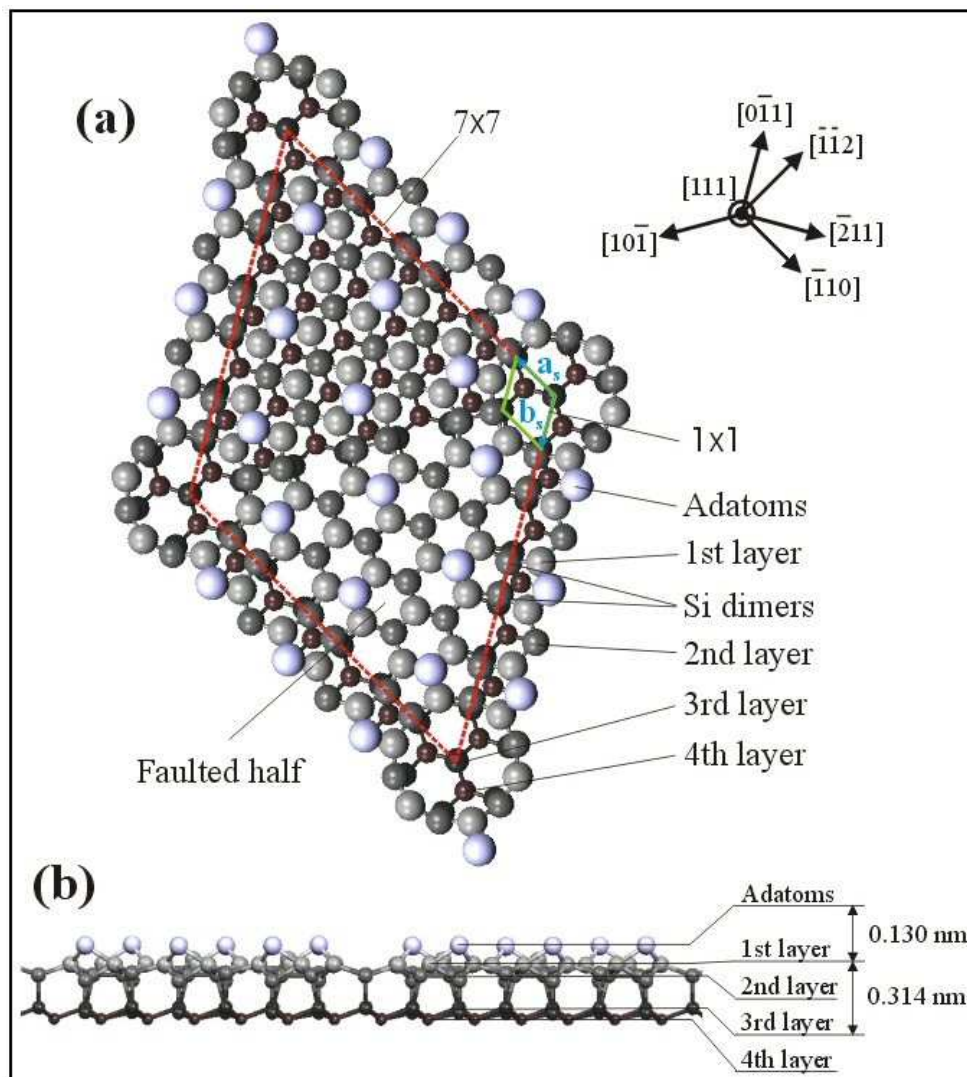


Figure 3.2: (a) Dimer-adatom-stacking-fault (DAS) model of Takayanagi *et al.* [124]. The darker the atoms the deeper they are. (b) Side view of the  $Si(111)$  structure, from a  $1 \times 1$  bulk-like layer to the  $7 \times 7$  reconstructed surface, that is projected along the  $[10\bar{1}]$  direction. This is thus a projection of the long diagonal of the  $7 \times 7$  unit cell. Note the opposite stacking sequences at the left and right sides of this side view. The right-hand side has a stacking fault.

Fig. 3.2(a) shows a top view of the  $7\times 7$  reconstructed surface. The bulk lattice directions indicate the crystallographic orientation of the top view, which corresponds to the one of the STM images. The Takayanagi *et al.* structural model features (i) different stacking in the two halves of the  $7\times 7$  unit cell, (ii) nine atom pairs (dimers) per unit cell and (iii) 12 adatoms over the cell. Fig. 3.2(b) presents a side view of the  $\text{Si}(111)$  structure, from a  $1\times 1$  bulk-like structure at the bottom to the  $7\times 7$  reconstructed surface, that is projected along the  $[10\bar{1}]$  direction.

## 3.2 $\text{Pr}_2\text{O}_3$ on $\text{Si}(111)$

### 3.2.1 Oxide growth

The Pr-oxide deposition was carried out with an Omicron e-beam evaporator initially filled with  $\text{Pr}_6\text{O}_{11}$  powder (five nines purity) and extensively outgassed (more than 15 hours in a row) in UHV conditions, above  $600^\circ\text{C}$ , until the background pressure reached the low  $10^{-10}$  mbar range, in order to get the reduction to the  $\text{Pr}_2\text{O}_3$  stoichiometry [125]. The powder is contained in a Mo crucible on which 1000 V volts are applied for the e-beam evaporation. The deposition rate of  $\text{Pr}_2\text{O}_3$  was measured by a quartz balance and adjusted to a rate of about 1/30 ML/min, where one ML of  $\text{Pr}_2\text{O}_3$  is defined as one  $\text{Pr}_2\text{O}_3$  unit cell per  $\text{Si}(111)$  surface unit cell, which corresponds to a  $\text{Pr}_2\text{O}_3$  thickness of 0.6 nm. During deposition, the temperature of the Si substrate was kept at  $550^\circ\text{C}$  and the background pressure remained in the  $10^{-10}$  mbar range with no  $\text{O}_2$  detected by the residual gas analyzer. Once the growth was completed, each sample was kept at the deposition temperature for three minutes, and then cooled down slowly at a rate of about  $2^\circ\text{C}/\text{sec}$ . Films with seven different coverages, ranging from submonolayer (sub-ML) up to 2 ML, were prepared and studied *in situ*. For each coverage, a fresh substrate was used. The results from five of the seven samples are presented here in detail.

## 3.2.2 Results

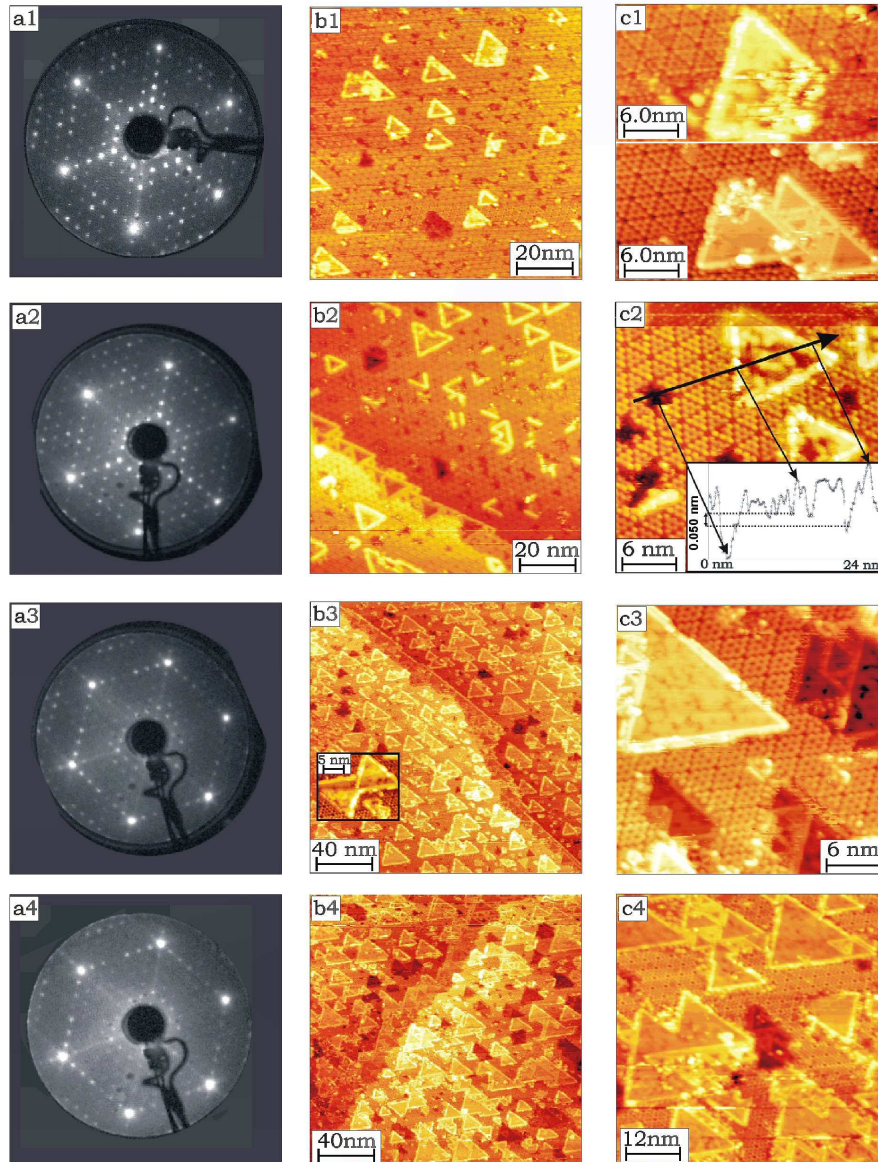


Figure 3.3: LEED and STM topographs of sub-ML  $\text{Pr}_2\text{O}_3$  on  $\text{Si}(111)$ . All the “a” images are the LEED patterns recorded at 40 eV. The “b” images correspond to large scale STM topographs and “c” images are the corresponding high resolution STM topographs of the initial growth coverages of  $\text{Pr}_2\text{O}_3$  on  $\text{Si}(111)$ . (a1), (b1) and (c1) correspond to 0.1 ML  $\text{Pr}_2\text{O}_3$ . (b1) and (c1) were recorded at  $U_s = -2.04$  V,  $I = 1.08$  nA. (b1) size is  $100 \times 100$  nm<sup>2</sup> and (c1) corresponds to 2 STM topographs of  $30 \times 15$  nm<sup>2</sup>. (a2), (b2) and (c2) correspond to 0.2 ML  $\text{Pr}_2\text{O}_3$ . (b2) and (c2) parameters are  $U_s = -2.04$  V,  $I = 1.08$  nA. (b2) size is  $100 \times 100$  nm<sup>2</sup> and (c2) area is  $30 \times 30$  nm<sup>2</sup>. (a3), (b3) and (c3) correspond to 0.7 ML  $\text{Pr}_2\text{O}_3$ . (b3) and (c3) were recorded at  $U_s = -2.32$  V,  $I = 0.58$  nA. (b3) size is  $200 \times 200$  nm<sup>2</sup> and (c3) is  $30 \times 30$  nm<sup>2</sup>. (a4), (b4) and (c4) correspond to 0.8 ML  $\text{Pr}_2\text{O}_3$ . (b4) and (c4) were recorded at  $U_s = -2.36$  V,  $I = 1.58$  nA. (b4) size is  $200 \times 200$  nm<sup>2</sup> and (c4) area is  $60 \times 60$  nm<sup>2</sup>.

LEED patterns of the growth of  $\text{Pr}_2\text{O}_3$  films on  $\text{Si}(111)$  are recorded for increasing coverages ranging from sub-ML to 2 ML. The ones for sub-ML coverages are reported in Figs. 3.3(a1-a4). They reveal (i) a diffuse background that increases with the oxide coverage, indicating a decrease of coherently diffracting scatterers, and (ii) the appearance of diffuse scattering intensity connecting the silicon substrate  $1\times 1$  spots, and (iii) that the LEED spots characteristic of the  $7\times 7$  reconstruction become weaker.

The corresponding STM topographs for the subML  $\text{Pr}_2\text{O}_3$  coverages are reported in Figs. 3.3 (b1-b4) for the large scale images and Figs. 3.3(c1-c4) for the high resolution ones. The results for four different deposition steps (0.1 ML, 0.2 ML, 0.7 ML and 0.8 ML) are presented. The image in Figs. 3.3 (b1) and (b2) reveal 2D, equilateral triangular islands with a narrow size distribution. Smaller oxide nuclei, forming lines along the dimer rows of the Si surface, are also visible. The rims of the triangular islands are aligned with the surface unit cell edges of the  $7\times 7$  reconstruction. Fig. 3.3(b2) shows that the nucleation has occurred both on the terraces and at the step edges. The image shown in Figs. 3.3 (b3) and (b4) reveal that the growth proceeds layer-by-layer with 2D islands covering the terraces and decorating the steps of the silicon surface. The majority of the triangular islands respects the three-fold symmetry of the substrate surface and thus is oriented in the same direction. The inset in Fig. 3.3(b3) shows the rare case of an equilateral island rotated by  $180^\circ$ . Fig. 3.3(c4), corresponding to a 0.1 ML higher coverage, exhibits a few more islands with such a rotation.

Higher resolution STM topographs for the same coverages are presented in Figs. 3.3(c1-c4). The STM images shown in Figs. 3.3(c1) -in particular the bottom part- and (b2) (0.1 ML and 0.2 ML coverage) reveals that the rims of the 2D triangular oxide islands roughly coincide with the lines where the dimers of the  $7\times 7$  structure are located. Adjacent to the boundaries (rims) of the triangular  $\text{Pr}_2\text{O}_3$  islands are the “faulted” halves of the  $\text{Si}(111)$ - $7\times 7$  reconstruction, which can be distinguished from the other halves with regular stacking upon closer inspection by their slightly “brighter” appearance. These islands are predominant. Triangular  $\text{Pr}_2\text{O}_3$  islands that are rotated by  $180^\circ$  around the  $\text{Si}(111)$  surface normal and bordered with the “unfaulted” halves can also be found on the surface (inset in Figs. 3.3(b3) and Fig. 3.3(c4)), but very rarely. The morphology of the surface at such low coverages (0.1-0.2 MLs) is characterized by coexistence of the oxide islands and the  $\text{Si}(111)$ - $7\times 7$  reconstruction remaining intact between the islands. Within the 2D oxide islands no ordered structure can be distinguished. Line scans performed through several

islands for the 0.2 ML coverage, such as the one presented in the inset of Fig. 3.3(c2), show that in the deepest inner parts the STM tips drops by about 0.05 nm into the corner-holes of the clean  $7\times 7$  surface. The length of the edges of the 2D oxide islands varies between 9 and 12 nm, while for the 0.1 ML coverage these edge lengths varie between 4 and 7 nm. Figs. 3.3(b3) (0.7 ML coverage) and (b4) (0.8 ML coverage) reveal that the average island size increases with the oxide coverage. A relatively narrow size distribution of equilateral triangular islands with edge lengths of about 15-20 nm is found in Fig. 3.3(b3) and in Fig. 3.3(c4) these edge lengths is distributed between 12 and 23 nm while small second layer islands appear on the larger islands in the first layer.

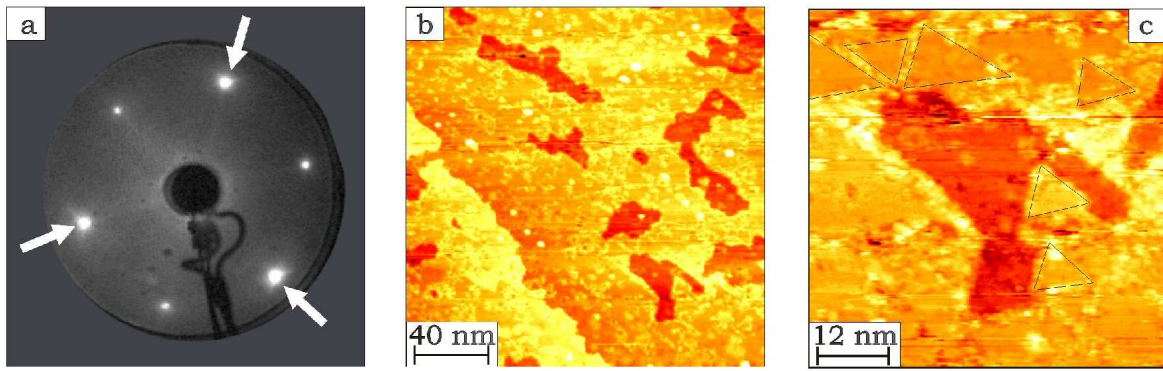


Figure 3.4: LEED and STM topographs of a 2ML thick  $\text{Pr}_2\text{O}_3$  on  $\text{Si}(111)$ . (a) LEED pattern at 40 eV. The stronger  $1\times 1$  spots are marked by arrows and prove the threefold symmetry of the overlayer. (b) Large scale STM topograph.  $200\times 200\text{ nm}^2$ ,  $U_s = -2.50\text{ V}$ ,  $I = 1.58\text{ nA}$ . (c) High resolution STM topograph.  $60\times 60\text{ nm}^2$ ,  $U_s = -2.50\text{ V}$ ,  $I = 1.58\text{ nA}$ . Dashed lines enhance some of the visible 2D triangle edges.

The LEED and STM results for a 2 ML thick  $\text{Pr}_2\text{O}_3$  layer are reported in Fig. 3.4. Fig. 3.4(a) shows the LEED pattern from such a 2 ML thick  $\text{Pr}_2\text{O}_3$  overlayer. Only spots in the positions of the  $1\times 1$  spots of the clean  $\text{Si}(111)$  surface are visible, and no superstructure spots are observed. The  $1\times 1$  diffraction spots exhibit now a pronounced 3-fold symmetry that is expected for a “hexagonal” (0001) surface with trigonal symmetry. Fig. 3.4(b) presents the corresponding large scale STM topograph. The surface is now completely covered by a  $\text{Pr}_2\text{O}_3$  film. The film morphology appears flat, except for the steps originating from the  $\text{Si}(111)$  surface and for some still visible boundaries of the coalesced 2D triangular islands. Thus, Fig. 3.4(b) demonstrates a layer-by-layer growth with a completed first oxide layer while the second one is commencing to spread. Fig. 3.4(c) displays a higher resolution STM topograph on such a sample. The patchwork pattern, highlighted by the triangles, shows 2D islands that have coalesced to a flat film.

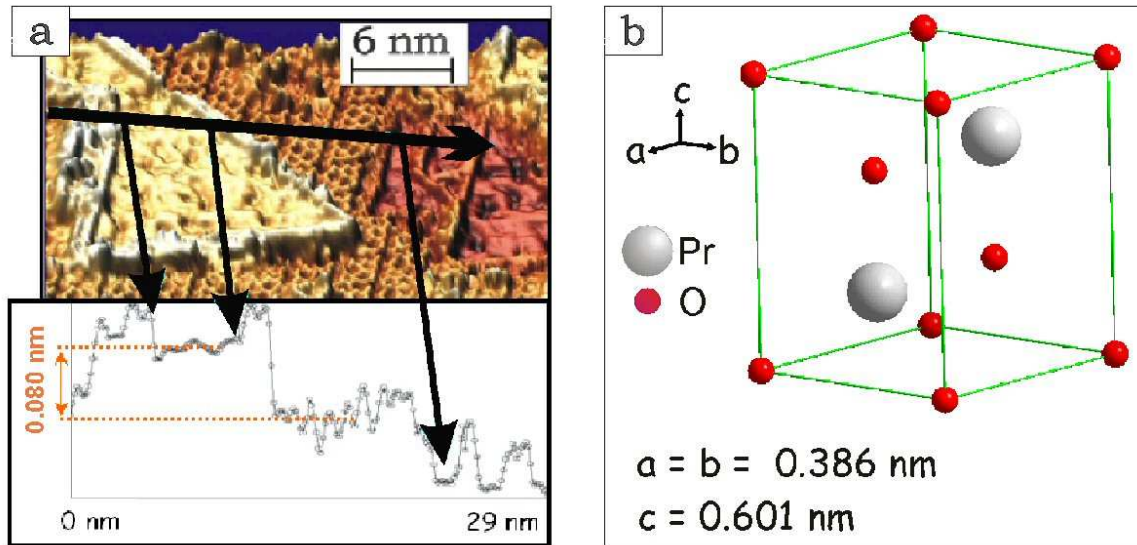


Figure 3.5: (a) Top: 3D STM topograph of Fig. 3.3(c3), bottom: line profile across Fig. 3.3(c3), as indicated in the above 3D STM topograph. (b) Bulk structure of a hexagonal  $\text{Pr}_2\text{O}_3$  unit cell as a reminder. The  $c$  lattice constant of the unit cell corresponds to 1 ML.

In Fig. 3.5(a) the 3D rendering of the STM topograph in Fig. 3.3(c3) and a cross section are shown. Analysis of several such cross sections revealed that the height of the interior of the islands with respect to the adatoms of the  $7\times 7$  reconstruction is about 0.08 nm. The rims of these 2D islands appear “brighter” and about 0.05 nm higher than the inner part. The silicon adatoms of the clean reconstructed substrate surface are still visible between the 2D islands.

In Fig. 3.5(b) a “hexagonal”  $\text{Pr}_2\text{O}_3$  unit cell is shown. The primitive unit cell belongs to the trigonal crystal system. The three-fold axis corresponds to the  $[0001]$  direction.

Fig. 3.6 presents the atomic structural model of the  $\text{Pr}_2\text{O}_3/\text{Si}(111)$  interface established by Jeutter *et al.* [4]. They found an interface structure formed by Pr-O-Si bonds. The first Pr atoms are above the Si  $T_4$  sites, i.e. the Si in the second atomic layer below the Si surface (Si2). In addition their analysis shows that the oxide starts growing with a thickness of 0.6 nm, corresponding to one bulk unit cell from the hexagonal phase of  $\text{Pr}_2\text{O}_3$ , which is in agreement with our results.

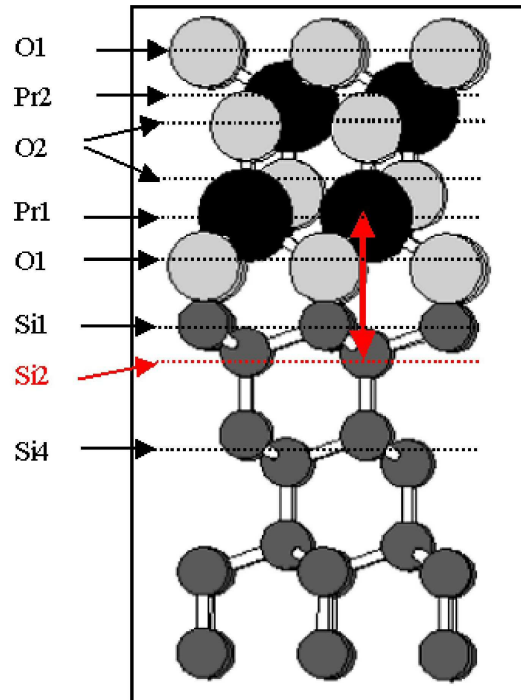


Figure 3.6: Atomic structural model of the  $\text{Pr}_2\text{O}_3/\text{Si}(111)$  interface established by Jeutter *et al.* from the analysis of SXRD data [4]. Atom Pr1 is above the Si  $T_4$  sites (Si2), i.e. the Si in the second atomic layer below the Si surface, using the atom labels used for the data refinement analysis. The interface is formed by Pr-O-Si bonds.

### 3.2.3 Discussion

Both, the LEED and STM results support the conclusion that  $\text{Pr}_2\text{O}_3$  grows epitaxially on  $\text{Si}(111)$ . The LEED results further suggest the pseudomorphic growth of a “hexagonal” (0001) oxide layer. While the (111) face of a cubic  $\text{Pr}_2\text{O}_3$  film would exhibit also a three-fold symmetry, its surface unit cell would be 4-times larger [74] (see Fig. 1.8), which is not in agreement with the observed  $1 \times 1$  LEED pattern. The STM images of  $\text{Pr}_2\text{O}_3$  on  $\text{Si}(111)$  reveal a nucleation process involving the formation of 2D triangular islands, respecting the three-fold symmetry of both the film and the substrate. Below 1 ML, the size of the islands increases with oxide coverage. Their length can always be expressed in terms of multiples of the silicon  $7 \times 7$  unit cell length. Energetically favored nucleation sites seem to be mainly the step edges of the silicon surface and the dimer rows of the  $7 \times 7$  unit cell on the terraces (Figs. 3.3(b1), (b2), (c1) and (c2)). The latter is revealed by the formation of the small one-dimensional nuclei at the very first stages of the growth, as visible for

instance in Figs. 3.3(b2) and (c2). The former can be concluded from the fact that the step edges are fully decorated with 2D islands, whereas the regions close to the step edges on the lower terraces are depleted of islands (Fig. 3.3(b2)).  $\text{Pr}_2\text{O}_3$  molecules arriving at distances from the step edges exceeding the diffusion length for the given temperature form nucleates on the terraces. All triangular islands are oriented with their edges (rims) next and parallel to the dimer rows of the silicon  $7\times 7$  reconstruction. The lateral size of the islands at this stage (0.2 ML) ranges from two to four  $7\times 7$  silicon unit cells. At this stage the STM clearly shows that the  $7\times 7$  reconstruction is destroyed where the oxide film forms. The adatoms, which are weakly bonded to the surface, are most likely the first to be affected by the arriving oxide molecules. The height of the interior of the 2D islands appears irregular at this coverage. The highest inner parts are about 0.05 nm above the adatoms of the clean  $\text{Si}(111)$ - $7\times 7$  reconstructed surface and the deepest inner parts are about 0.05 nm lower than the depressions (corner holes) of the clean re-constructed silicon surface, as shown in the line scan in Fig. 3.3(c2).

The STM image presented in Fig. 3.3(b2) shows preferred nucleation of islands at a lower step edge with a region depleted of islands in front, whereas the upper step edge has an island density similar to that observed away from the step edge on the lower terrace. Such an island density distribution indicates the presence of a diffusion barrier (Schwöbel barrier [126]) at the upper step edges and identifies the lower step edges as preferred nucleation sites. From these results we estimate a diffusion length of 30 nm for  $\text{Pr}_2\text{O}_3$  for the given growth parameters. The average terrace width was found to be 100 nm (STM images not shown here), due to a miscut of about  $0.1^\circ$  toward the  $\langle 110 \rangle$  direction. Thus the terrace width is three times larger than the diffusion length. This ratio explains why the  $\text{Pr}_2\text{O}_3$  islands nucleate both at the step edges and on the free terraces. At higher coverage (0.7 ML), the average lateral size of the 2D islands increases to five to seven  $7\times 7$  silicon unit cells.

The apparent 2D islands height of 0.08 nm can be explained by assuming that the epitaxial oxide film grows directly on an unreconstructed  $1\times 1$  silicon surface. Taking into account the heights of the different atomic layers of the  $7\times 7$  reconstructed surface (Fig. 3.2), which in total constitute a thickness of 0.44 nm [127], and adding the 0.08 nm height of the oxide above the adatoms, a total thickness of 0.52 nm for the oxide layer can be deduced. Because of the different densities of states between the insulating oxide and the Si substrate, STM is not expected to determine the height of the oxide accurately. Thus, this thickness agrees

well with the 0.60 nm c-axis length of the “hexagonal”  $\text{Pr}_2\text{O}_3$  unit cell (Fig. 3.5(b)). Our result is in qualitative agreement with the recent SXRD study of Jeutter *et al.* [4], revealing that  $\text{Pr}_2\text{O}_3$  forms bonds with an unreconstructed  $\text{Si}(111)$  layer at the interface. Once the first 0.60 nm “hexagonal” layer is completed, the second 0.60 nm thick layer grows on top.

A question remains regarding the apparently elevated rims of the 2D islands in the STM topographs. This observation may be explained by a higher density of electronic states, with a structure similar to the interior. However, the rims represent the interface between the  $\text{Pr}_2\text{O}_3$  islands and the reconstructed  $\text{Si}(111)$  surface and thus it is very likely that they exhibit a particular structure, which we cannot resolve in this study. Previous studies on the  $\text{CaF}_2/\text{Si}(111)$  system explained similar bright island features as being due to an excess of Si atoms produced in the transition from  $7\times 7$  structure to a bulk like structure during growth of a monolayer of CaF [128]. The smooth coalescence of the 2D islands at higher growth coverage (Figs. 3.4(b) and (c)) proves that the growth proceeds in a 2D pseudomorphic way, in agreement with the observation of smooth films by a recent *ex-situ* XRD investigation [74].

### 3.2.4 Summary

We have studied the initial stages of the epitaxy of  $\text{Pr}_2\text{O}_3$  on  $\text{Si}(111)$  under UHV condition. Combining STM and LEED, We found a layer-by-layer oxide growth of two-dimensional, equilateral, triangular islands on unreconstructed  $\text{Si}(111)$  surface. The observed  $(1\times 1)$  LEED patterns indicate pseudomorphic oxide films and are in agreement with the epitaxial growth of the trigonal  $\text{Pr}_2\text{O}_3$  on  $\text{Si}(111)$  with one specific orientation. Domains, rotated by  $180^\circ$  around the  $(111)$  surface normal are very rarely observed by STM. Therefore, we have shown that single-crystal  $\text{Pr}_2\text{O}_3$  of good crystalline quality can be grown epitaxially on  $\text{Si}(111)$  surfaces. The pseudomorphic oxide film grows on the atomically clean  $\text{Si}(111)$  surface lifting the  $7\times 7$  reconstruction away. The 2D equilateral triangular islands were found to have a fairly narrow size distribution and to grow on terraces with preferential nucleation observed at step edges of the  $\text{Si}(111)$  surface. Determined by STM, the thickness of one complete layer is about 0.52 nm, which agrees well with the 0.6 nm height of the “hexagonal”  $\text{Pr}_2\text{O}_3$  unit cell. Our findings are in agreement with the structural analysis by SXRD of Jeutter *et al.* [4] revealing an epitaxial “hexagonal”  $\text{Pr}_2\text{O}_3$  layer that has a thickness corresponding to the c-lattice constant of this phase, i.e. 0.6013 nm, as first

growing on Si(111). In this study Jeutter *et al.* have also identified the interface atomic structure of  $Pr_2O_3/Si(111)$  as consisting of a Si-O-Pr bond with Pr atoms above the  $T_4$  sites of the Si atomic structure (i.e. Si in the second atomic layer below the Si surface).

## Chapter 4

# UHV growth of Pr-oxide on Si(001)

---

Pr-oxide films were deposited on very low miscut ( $0.01^\circ$ ) hat shaped Si(001) substrates in the R2P2 chamber under UHV conditions. The initial growth stages were studied *in-situ* by LEED, STM, and AES to obtain information on structural ordering, surface morphology and chemical composition of the oxide films. The LEED and STM characterization focused on the nucleation stages of the oxide growth. Further characterizations by XRD and XPS were carried out at the beamline after transferring the samples under UHV conditions. This study was performed for samples grown at  $550^\circ\text{C}$ , typical temperature used in previous studies [3,129]. The effect of the surface miscut will be also discussed. For that purpose, a few samples were grown on a vicinal Si(001) surface, in the small UHV chamber, presented in section 2.1.1, at  $550^\circ\text{C}$  under UHV conditions.

During the initial growth stage, Pr-oxide and silicate nucleate on the surface and form a 2D layer, followed by a transition from 2D to 3D growth of the film. This transition is accompanied by a phase separation with the appearance of  $\text{PrSi}_2$  islands. Since Pr-silicide is not desirable we have then investigated the effect of temperature by growing films at room temperature under UHV and subsequently post-anneal them under different (P,T) conditions.

## 4.1 Si substrate surface preparation and characterization

### 4.1.1 Cleaning of the hat shaped silicon substrates

We typically used n-type Si(001) hat shaped sample crystals presented in Fig. 2.4, which were phosphorus doped and had a resistivity of 0.7480  $\Omega\cdot\text{cm}$ . This particular sample shape was needed for the SXRD technique, in order to have a surface that can be rotated azimuthally by  $360^\circ$  when mounted on the diffractometer without blocking the grazing incidence synchrotron beam by the sample fixation (screws, wires, or spot-welded foils). The used sample area (top surface) was  $5\times 5\text{ mm}^2$ . These sample crystals were prepared in the ESRF crystal-shop with the requirement of having a minimum miscut as desired for the present studies. It is also convenient for SXRD experiments to have a low-miscut surface, which allows the optical axis of the surface to be parallel to a crystallographic axis of the substrate lattice.

A critical step in the sample preparation was the substrate surface cleaning in order to obtain the  $2\times 1$  reconstruction without any metal contamination (Nickel contaminations had turned out to be the most critical), with low defect density and long dimer rows. To get such a Si surface, which is a pre-request for the project and more generally for collecting a high quality SXRD data set on the surface under investigation, a considerable amount of time had been invested. In total, eight months were needed.

For performing STM on the Si(001) surface, high temperature flash annealing has been the well established and the only reliable way for obtaining atomic resolution images [83, 84]. The critical issue in this procedure is to be able to anneal the sample surface to  $\approx 1200^\circ\text{C}$  while maintaining the chamber pressure in the UHV range. For thin Si(001) wafer samples, direct current heating has been widely used for achieving such a condition. For the hat shaped crystals used in the present studies, which are needed for SXRD measurements, to reach such a high temperature with direct current heating would require unpractically high current due to the large cross section of the crystals.

To solve the above sample heating problems an e-beam heater was developed, with careful choice of materials to fulfill the above described requirements. A design of this heater is shown in Fig. 4.1(a). Fig. 4.1(b) focusses on the tungsten (W) filament fixed on the bottom

part of the e-beam heater stage and Fig. 4.1(c) displays a top view of the e-beam heater with a hat-shaped sample mounted on it.

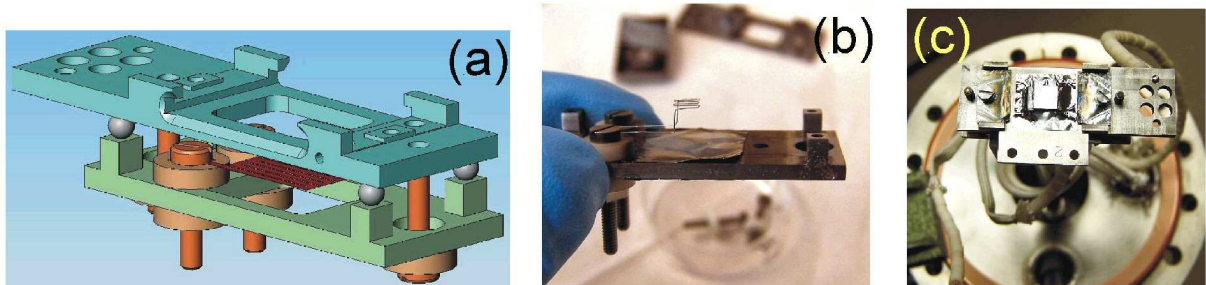


Figure 4.1: (a) Design of the e-beam heater for Si(001) cleaning by flash annealing treatments above  $1000^{\circ}\text{C}$ . (b) Construction of the e-beam heater W filament. (c) Sample on its sample plate mounted on the e-beam heater stage.

The cleaning procedure consists of slowly outgassing the samples at  $650^{\circ}\text{C}$  for around eight hours, subsequently flash annealing them at a temperature above  $950^{\circ}\text{C}$  until the pressure reaches  $2 \times 10^{-9}$  mbar and then decreasing the temperature to  $850^{\circ}\text{C}$  for the pressure to recover. The same procedure is repeated until the sample is possible to stay more than 15 sec. at the flashing temperature. The flashing temperature is then increased. Such cycles are repeated until the pressure can remain below  $2 \times 10^{-9}$  mbar a few tens of seconds when the sample is flashed annealed at  $1250^{\circ}\text{C}$ , as described in the literature [83]. Temperatures were measured using an optical pyrometer. The quality of the  $(2 \times 1)$  reconstruction of the Si(001) surface was first characterized by LEED and STM. We have analyzed the atomic structure of the Si(001)- $2 \times 1$  reconstructed clean surface using SXRD. The results are summarized in Appendix A.

#### 4.1.2 LEED and STM results

Before  $\text{Pr}_2\text{O}_3$  deposition, the quality of the  $(2 \times 1)$  reconstructed surface of the Si(001) substrate was systematically characterized by LEED and STM.

Fig. 4.2 presents a large scale STM topograph of a clean Si(001) dimerized surface. An average terrace width of about 120 nm can be estimated. Adjacent terraces are separated by a single atomic step. Two types of steps, alternating with each other, are visible on the

topograph: (i)  $S_A$  type, which has straight step edges with dimer rows parallel to the step edges and (ii)  $S_B$  type, which has rough, wavy step edges, with dimer rows perpendicular to the step edges [130]. These dimer rows originate from the pairing of the surface atoms, leading to a double sized surface unit cell, as compared with the ideal-bulk terminated one, and the occurrence of  $2\times 1$  and  $1\times 2$  reconstructions, as revealed by the LEED pattern in the inset, recorded at 53 eV.

Fig. 4.3 shows the dimerized Si(001) surface in greater detail and enables us to associate the two different domains ( $2\times 1$  and  $1\times 2$ ) with different heights in the cell so that one terrace will have one domain orientation. The line profile in Fig. 4.3 indicates that two terraces are separated by a step height of 0.13 nm, matching with  $1/4^{th}$  of the Si bulk lattice constant, i.e. 0.543 nm.

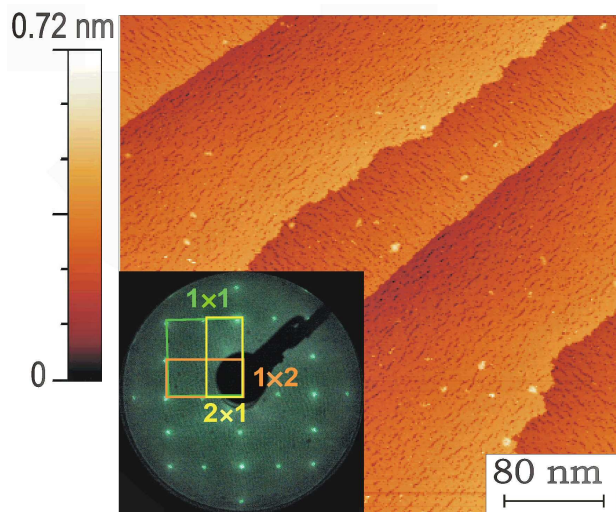


Figure 4.2: Large scale STM topograph of the clean Si(001)- $2\times 1$  reconstructed surface. Parameters :  $400\times 400$  nm<sup>2</sup>,  $U_s=-1.50$  V,  $I=0.20$  nA. Inset: the corresponding LEED pattern recorded at 53 eV.

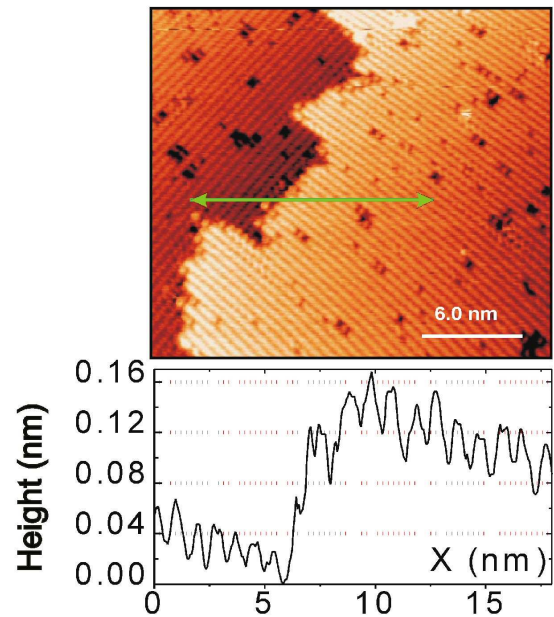


Figure 4.3: Small scale STM topograph of the clean Si(001) -  $2\times 1$  reconstructed surface complemented by a line profile across the green arrow on the topograph.

Therefore, from one terrace to the other the surface dimerization rotates by  $90^\circ$ , due to the silicon bonding geometry, giving rise to the  $2\times 1$  reconstruction [106]. It is important to underline that dimerization is a key factor in the dynamical behavior and the chemical activity of Si(001), e.g. atoms and molecules diffusing on the surface use dimer rows as

convenient “rails”.

It can be noticed that the STM topographs reveal still the presence of some defects on the surface (white spots and missing dimer rows). These defects can be further decreased by additional flash annealing treatments following the previously described recipe in § 4.1.1.

## 4.2 The oxide growth conditions

The oxide evaporation was mainly conducted in the UHV cluster-chamber system called R2P2, which has been described in § 2.1.2 (Chapter 2). The silicon substrates used are the hat-shaped ones presented in the previous section. The cleaning recipe to get the  $2\times 1$  reconstruction on the Si(001) surface consists of repeated flash annealings for a few seconds at  $1250^\circ\text{C}$ , as described previously and following a classical recipe [83].

The Pr-oxide deposition was carried out with an Omicron e-beam evaporator (EFM 3T from Omicron). The deposition features are similar to the ones described in Chapter 3. The Mo crucible of this e-beam evaporator was initially filled with  $\text{Pr}_6\text{O}_{11}$  powder (five nines purity) and extensively outgassed for about 24 hours at  $P_{\text{O}_2} \approx 5 \times 10^{-7}$  mbar until the background pressure reached the low  $10^{-10}$  mbar range. In this process of outgassing,  $\text{Pr}_6\text{O}_{11}$  is reduced to  $\text{Pr}_2\text{O}_3$  [125]. The deposition rate of  $\text{Pr}_2\text{O}_3$  was measured by a quartz crystal monitor (QCM) and adjusted to a rate of about  $0.2 \text{ \AA}/\text{min}$  of  $\text{Pr}_2\text{O}_3$  molecules. During deposition, the temperature of the Si substrate was typically kept at  $550^\circ\text{C}$ , as measured from an optical pyrometer, and the partial pressure of the residual  $\text{O}_2$  from the Pr-oxide evaporation source was below  $1 \times 10^{-10}$  mbar, while the total pressure was around  $5 \times 10^{-10}$  mbar, as indicated by a residual gas analyzer and an ion gauge, respectively. No additional  $\text{O}_2$  was supplied. Once the growth was completed, each sample was kept at the deposition temperature for three minutes, and then cooled down slowly at a rate of about  $2^\circ\text{C}/\text{sec}$ , under UHV conditions.

## 4.3 Thickness dependence of the Pr-O film growth

### 4.3.1 *in-situ* study by LEED and STM

#### Results on hat shaped samples

We first performed a combined LEED and STM study on a series of samples while increasing progressively the oxide coverages. Totally, ten different coverages were studied *in situ*, with film thicknesses ranging from 0.08 nm to about 2 nm, as estimated from the growth rate calibrated by our QCM. The results of six different coverages are presented in this subsection. Table 4.1 summarizes the main growth parameters of these samples.

The images shown in Figs. 4.4(a, b, d) and Figs. 4.5(e) were collected from the same sample, on which subsequent growths were performed, while Fig. 4.4(c) and Figs. 4.5(f) represent films grown on two other different substrates.

<i>Samples</i>	<i>a</i>	<i>b</i>	<i>d</i>	<i>e</i>	<i>c</i>	<i>f</i>
Thickness (nm)	0.16	0.2	0.4	1	0.28	2
<i>Comments : a, b, d, and e correspond to subsequent growths on a same sample while c and f are two different samples.</i>						
Pressure (mbar)	UHV : $\leq 10^{-10}$					
T ( $^{\circ}$ C)	550 $^{\circ}$ C					

Table 4.1: List of samples presented for the LEED and STM study.

The STM and LEED results of the four lowest coverage films (0.16 to 0.40 nm) are presented in Fig. 4.4. The image in Fig. 4.4(a1) reveals the formation of stripes elongated along two perpendicular directions, namely the bulk Si [110] and  $[1\bar{1}0]$  directions, after the Si(001) clean surface is covered by 0.16 nm of film. These directions are indicated in the image of Fig. 4.4(d1) and are valid for all the STM images in this figure. The top inset in Fig. 4.4(a1) shows a higher resolution image of the stripes and reveals an average length of 20 nm for the stripes along the [110] direction and 40 nm for those along  $[1\bar{1}0]$ . The corresponding LEED pattern in the bottom left inset still shows the  $1\times 1$  and  $2\times 1$  spots arising from the silicon substrate surface. However this pattern indicates (i) a higher diffuse background compared with the one in Fig. 4.2, revealing an increase of structural disorder of the surface, and (ii)

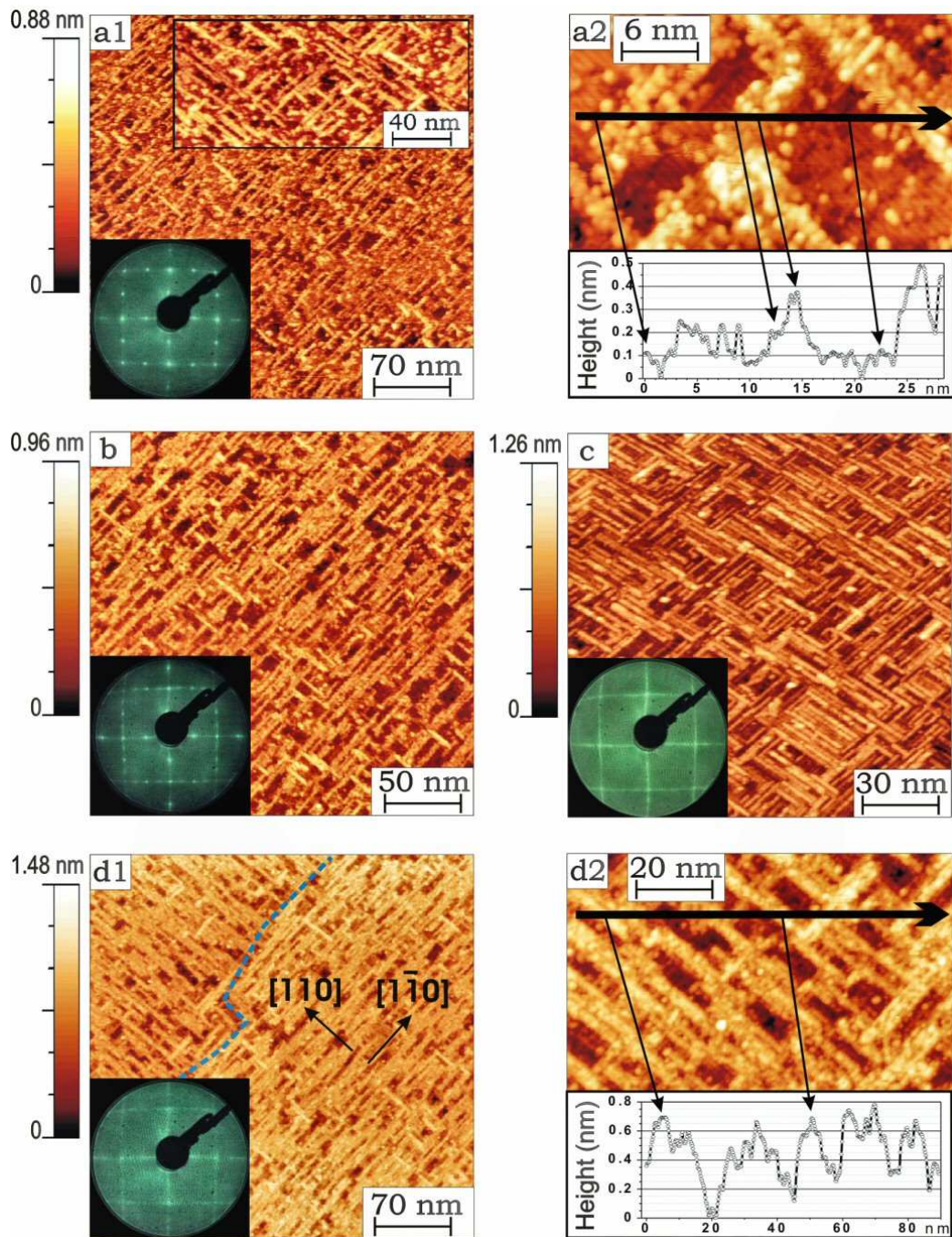


Figure 4.4: High resolution STM topographs of the initial growth coverages of  $\text{Pr}_2\text{O}_3$  on Si(001) complemented by LEED patterns at 53 eV and line profiles. (a1) Deposited thickness: 0.16 nm.  $350 \times 350 \text{ nm}^2$ ,  $U_s = 2.00 \text{ V}$ ,  $I = 0.10 \text{ nA}$ . Top insert : Zoom in on the same surface.  $200 \times 100 \text{ nm}^2$ ,  $U_s = 2.00 \text{ V}$ ,  $I = 0.18 \text{ nA}$ . Bottom insert: LEED pattern at 53 eV; (a2) Same coverage as (a1).  $30 \times 20 \text{ nm}^2$ ,  $U_s = 2.00 \text{ V}$ ,  $I = 0.50 \text{ nA}$ . Bottom: line profile across (a2); (b) Deposited thickness: 0.20 nm.  $250 \times 250 \text{ nm}^2$ ,  $U_s = 2.00 \text{ V}$ ,  $I = 0.50 \text{ nA}$ ; (c) Deposited thickness: 0.28 nm.  $150 \times 150 \text{ nm}^2$ ,  $U_s = 2.50 \text{ V}$ ,  $I = 0.10 \text{ nA}$ ; (d1) Deposited thickness: 0.40 nm.  $350 \times 350 \text{ nm}^2$ ,  $U_s = 2.00 \text{ V}$ ,  $I = 0.50 \text{ nA}$ . A dashed line enhances a step edge; (d2) Same coverage as (d1).  $100 \times 60 \text{ nm}^2$ ,  $U_s = 2.00 \text{ V}$ ,  $I = 0.50 \text{ nA}$ . Bottom: line profile across (d2). The LEED patterns are rotated by  $45^\circ$  with respect to the STM images.

the appearance of diffuse scattering intensity between the silicon substrate ( $1\times 1$ ) spots. The higher resolution STM topograph presented in Fig. 4.4(a2) shows in greater detail the surface morphology of the Si surface after the growth and resolves the dimer rows of the  $2\times 1$  reconstruction of the Si(001) surface between the elongated oxide stripes, which appear brighter in the topograph.

A typical line profile of such a surface is presented in the inset of Fig. 4.4(a2). The areas marked by the left- and right-most arrows share the same height that corresponds to the silicon dimer rows along the  $[110]$  direction. The height difference between these arrows and the second-left one corresponds to a Si atomic step ( $\approx 0.14$  nm). The dimer rows visible under the second-left arrow are indeed aligned along the  $[1\bar{1}0]$  direction. Since the STM images for the Si(001) clean surface showed previously in section 4.1. (Fig. 4.2) a typical terrace width of 500 nm, the presence of small domains in Fig. 4.4(a2) containing dimer rows aligned in two perpendicular directions indicates that silicon reacts with Pr-oxide. This reaction removes some of the silicon atoms in the topmost layer and leads to small patches of holes separated by atomic steps. The third-left arrow indicates the height of the oxide species on top of the  $[1\bar{1}0]$  oriented Si dimer rows. Fig. 4.4(a2) shows clearly that the oxide stripes prefer to grow perpendicularly to the Si dimer rows with a width of about 2-4 nm. The LEED pattern at this coverage is still dominated by the Si(001)- $2\times 1$  dimer structure and thus does not give very much information about the oxide film.

Fig. 4.4(b) shows both the STM topograph and the LEED pattern characterizing a surface covered with a 0.2 nm film. Longer bright features can be observed in the  $[1\bar{1}0]$  direction. The corresponding LEED pattern in the inset suggests the formation of a  $4\times 1$  superstructure, developed along the  $[110]$  and  $[1\bar{1}0]$  directions of the silicon substrate. This superstructure corresponds to a unit cell with 4 times the size of Si surface unit cell in one direction. This last value is in agreement with the width of the oxide stripes, as estimated from the corresponding STM topograph. At a slightly higher coverage the  $4\times 1$  like LEED pattern turns into continuous streaks along the  $[110]$  and  $[1\bar{1}0]$  directions, as the ones shown in the inset of Fig. 4.4(c). These streaks can be denoted as a  $n\times 1$  reconstruction, where  $n$  is an unspecified number. This reconstruction may be explained by a broader width distribution of the oxide stripes, compared with the previous lower coverages, as suggested from the corresponding STM topograph. From the STM topograph the bright oxide features are estimated to be around 30 nm long in the  $[110]$  direction and 15 nm in the  $[1\bar{1}0]$ , while the width is estimated to be between 1 and 3 nm. This STM image also

suggests coalescence of adjacent stripes.

Fig. 4.4(d1) shows the surface morphology after 0.4 nm of Pr-oxide has been evaporated on the silicon surface. A dashed line highlights a step edge that was present before any Pr-oxide deposition. The image shows that each terrace promotes the growth predominantly in one direction. The corresponding LEED pattern looks like the one in Fig. 4.4(c) but the diffracted intensity becomes rather weak. A closer look at this surface in Fig. 4.4(d2) reveals a narrow height distribution of the elongated oxide line features. Comparison between Figs. 4.4(d) and 4.4(c) shows that longer deposition mainly increases the density of the elongated oxide line features rather than changing their shape, size or height.

Fig. 4.5 presents the STM and LEED results of two samples with coverages  $\geq 1$  nm. Fig. 4.5(e1) shows the surface morphology of two adjacent terraces covered with a 1 nm film. The blue dashed line highlights a step edge. The elongated bright features cannot be clearly identified anymore at this stage and only much shorter rectangular domains can be distinguished. The corresponding LEED pattern in the inset reveals still the presence of a  $n \times 1$  superstructure but its intensity is further weakened by a high background. In addition weak  $2 \times 1$  spots can be distinguished. A smaller scale image of this surface is shown in Fig. 4.5(e2), where new rectangular islands, about  $10 \times 7$  nm<sup>2</sup> in lateral dimensions appear. They are about 0.4 nm higher than the rest of the film, as estimated from the line profile in the inset. In addition, a depletion zone can be observed around each island. With even higher coverage (2 nm) these 3D islands become larger while the oxide stripes vanish completely, as shown in Fig. 4.5(f1). Square islands, with a lateral size ranging from  $20 \times 20$  nm<sup>2</sup> to  $70 \times 70$  nm<sup>2</sup>, and rectangular ones, with a lateral size ranging from  $8 \times 20$  nm<sup>2</sup> to  $10 \times 60$  nm<sup>2</sup>, can be found on the surface. The height distribution of these islands can be seen from the typical line profile in Fig. 4.5(f2), which shows the presence of  $\approx 5$  and 10 nm high islands with large depletion zones (the corresponding line profile shows a height  $\leq 1$  nm) around them. A 2D layer is also visible between these islands and appears to be  $\approx 2$  nm thick. This latter thickness is in good agreement with the value estimated from the calibrated growth rate. The presence of these depletion areas around the islands suggests that the material that forms the islands may be partially supplied by the 2D layer. The LEED pattern at this stage shows that the  $n \times 1$  streaks have almost disappeared while the  $1 \times 1$  spots are still visible with a high background. The presence of the  $1 \times 1$  spots from the silicon substrate may result from electrons penetrating the reduced film thickness in the depletion areas. In addition, very weak  $2 \times 1$  intensity modulation can

be observed and might also arise from the silicon substrate surface in these areas.

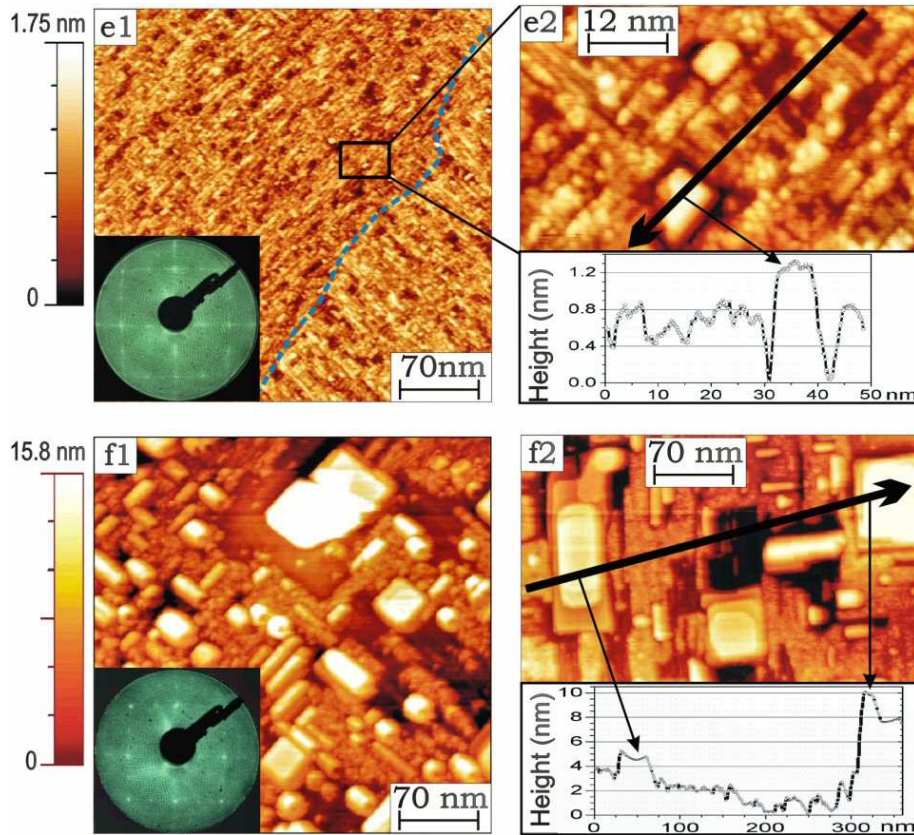


Figure 4.5: High resolution STM topographs of the  $\text{Pr}_2\text{O}_3$  growth on Si(001) complemented by corresponding LEED patterns at 53 eV and line profiles. (e1) Deposited thickness: 1 nm.  $350 \times 350 \text{ nm}^2$ ,  $U_s = 2.00 \text{ V}$ ,  $I = 0.10 \text{ nA}$ . A dashed line enhances a step edge; (e2) Zoom in on the same local area shown on image (e1).  $60 \times 40 \text{ nm}^2$ ,  $U_s = 3.00 \text{ V}$ ,  $I = 0.50 \text{ nA}$ . Bottom: line profile across (e2); (f1) Deposited thickness: 2 nm.  $350 \times 350 \text{ nm}^2$ ,  $U_s = -2.50 \text{ V}$ ,  $I = 0.10 \text{ nA}$ ; (f2) Same coverage as (f1). (f2) is rotated by  $45^\circ$  compared with (f1).  $350 \times 250 \text{ nm}^2$ ,  $U_s = 3.50 \text{ V}$ ,  $I = 0.10 \text{ nA}$ . Bottom: line profile across (f2). The LEED patterns are rotated by  $45^\circ$  with respect to the STM images.

### Influence of the substrate miscut on the film morphology

The  $\text{Pr}_2\text{O}_3$  growth has also been investigated on Si(001) wafers with an overall miscut angle of  $\pm 0.1^\circ$ , as given by the supplier. The study was carried out in the small UHV chamber described in § 2.1.1 and followed the same sample preparation procedure that the hat shaped samples prepared in the R2P2 chamber, as described in section 4.1. The main results are presented in Fig. 4.6. The local miscut estimated from the average terrace width

on the STM topograph presented in Fig. 4.6(a) is about  $0.17^\circ$ . This image shows a typical

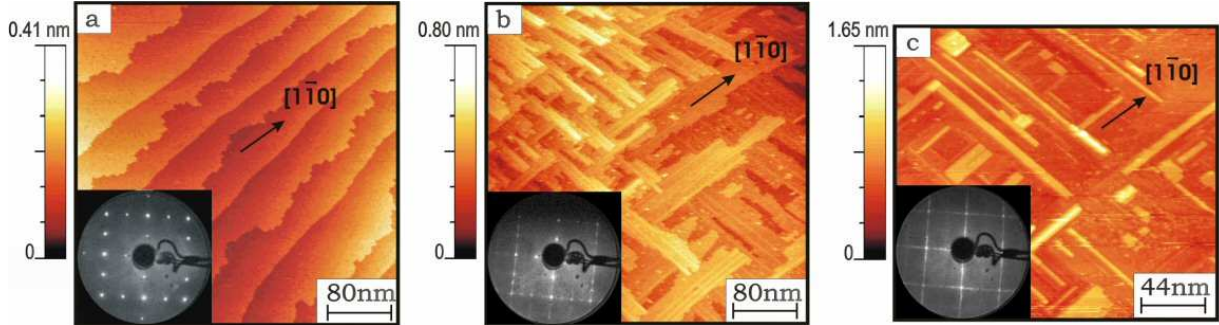


Figure 4.6: High resolution STM topographs of the  $\text{Pr}_2\text{O}_3$  growth on Si(001) n-type wafers with a miscut angle of  $\pm 0.1^\circ$ . Inserts: LEED patterns at  $\simeq 50$  eV. (a) Clean Si(001)- $2\times 1$  reconstructed surface.  $400\times 400$  nm<sup>2</sup>,  $U_s = -2.00$  V,  $I = 0.60$  nA; (b) Deposited thickness: 0.24 nm.  $400\times 400$  nm<sup>2</sup>,  $U_s = -2.23$  V,  $I = 0.07$  nA; (c) Deposited thickness: 1 nm.  $220\times 200$  nm<sup>2</sup>,  $U_s = -3.59$  V,  $I = 0.09$  nA. The LEED patterns are rotated by  $45^\circ$  with respect to the STM images.

STM topograph of the cleaned Si(001)- $2\times 1$  reconstructed surface for these commercially available wafers. The terrace width is about 40 to 60 nm, which corresponds to a step density at least 3 times higher than that of the hat-shaped crystals (cf. Fig. 4.2). Fig. 4.6(b) shows the STM and LEED results of a surface covered with a 0.24 nm  $\text{Pr}_2\text{O}_3$  film, similar to the one presented in Fig. 4.4(b). The oxide adsorption modifies the morphology of the step edges, which become rougher. It is apparent in Fig. 4.6(b) that when Pr-oxide adsorbs on small terraces (the upper-left corner) the elongated bright features develop along the  $[1\bar{1}0]$  direction that means perpendicularly to the step edge of A-type terraces (flat edge), which have their dimer rows parallel to the step edge (see section 4.1). Since we know from Fig. 4.4(a2) that the elongated bright features grow perpendicular to the dimer rows, Fig. 4.6(b) suggests that when step density is high, Pr-oxide grows preferentially on A-type steps, while B-type steps are etched away. On larger terraces (the lower right corner in Fig. 4.6(b)), the growth of Pr-oxide causes small patches of holes to develop in the middle of terraces for both type of steps. The corresponding LEED pattern shown in the inset reveals the formation of a  $4\times 1$  superstructure at this stage as previously reported in the case of the hat shaped samples. Fig. 4.6(c) shows the results for a coverage similar to Fig. 4.5(e), i.e.  $\approx 1$  nm. The LEED pattern in inset evolved in  $n\times 1$  streaks. The STM topograph shows rectangular islands are about 50 to 60 nm long in the  $[1\bar{1}0]$  direction, i.e. the step edges direction, while in the perpendicular direction their lengths reach about 100 nm. These observations suggest that the increase of step density may promote the formation of larger domains. The effects of surface miscut were not investigated further in

the framework of this project.

### AES results on hat shaped crystals

An AES study was carried out *in-situ* to monitor the evolution of the AES spectra for Pr, Si, and O with increasing oxide film thickness. Fig. 4.7 presents a summary of these data. The derivatives of the intensities are plotted for better reading. Fig. 4.7(a) shows

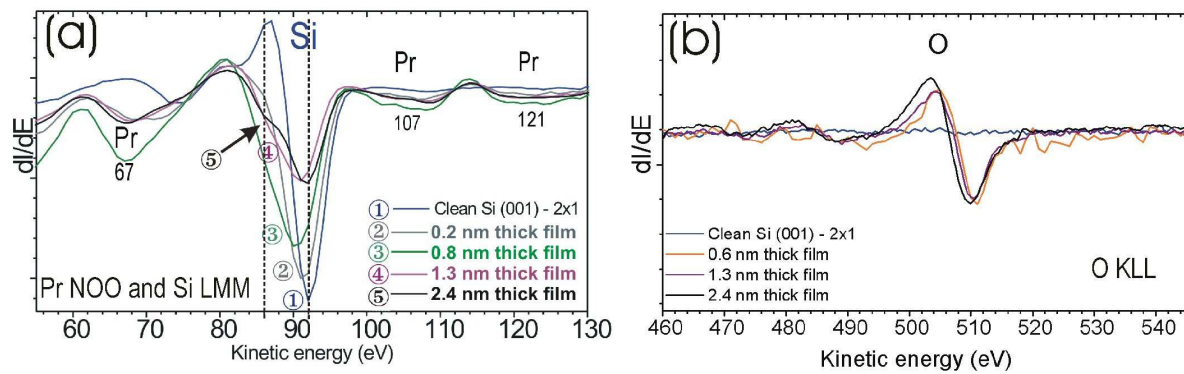


Figure 4.7: AES spectra evolution for Pr, Si, and O from clean Si to 2.4 nm thick oxide film on Si recorded at 3 KeV. (a) AES spectra of Pr NOO and Si LMM recorded with a lock-in sensitivity of  $300 \mu\text{V}$ . (b) O KLL Auger spectra with a ten times higher sensitivity ( $30 \mu\text{V}$ ).

the evolution of the Pr NOO and Si LMM Auger spectra. The main features visible in this figure are the main Si component at 92 eV (position marked with a dashed line) and 3 Pr components at 67 eV, 107 eV and 121 eV, not evolving very much with the oxide coverage (except spectrum 3, whose large  $\frac{dI}{dE}$  amplitude in the 67 eV energy range is most likely due to a premature acquisition of the spectrum while the system was not stable). The Pr-oxide growth on the silicon substrate shows the following two effects on the AES spectra: (i) the shift of the 92 eV Si peak toward lower electron energy, associated with an intensity decrease and broadening of this peak (from spectrum 1 to 4), (ii) for oxide films above 1 nm the main Si component shifts back to 92 eV with a shoulder appearing at around 87 eV (spectra 4 and 5), the energy of the main Pr Auger component (position marked with a dashed line). Therefore, effect (i) means that within the probing depth of the experiment less and less Si substrate (92 eV) is detected while more Pr and possibly oxidized silicon species - as compared with AES spectra of native  $\text{SiO}_2$  films - (87 eV) are progressively probed with increasing oxide coverage. Effect (ii) may be associated with

the formation of the 3D islands and large depletion areas. The 3D islands may contain silicon species with Auger electron energies around 92 eV. The reduced film thickness of the depletion areas also allows more contribution of the silicon substrate to the 92 eV peak.

Fig. 4.7(b) shows the O KLL Auger spectra evolution, recorded with a sensitivity ten times the one used for Fig. 4.7(a). The O peak position as well as its intensity basically does not change while the film thickness increases beyond 0.6 nm. These results suggest that the 3D islands observed in Fig. 4.5 for film thicknesses  $\geq 1$  nm may contain much less oxygen than the thinner films.

### 4.3.2 Summary

Our STM studies show that the Pr-oxide growth under UHV conditions leads (i) at the initial stages, to the formation of stripes elongated in the  $[110]$  and  $[1\bar{1}0]$  directions, which give rise to streaky  $n \times 1$  LEED pattern, where the  $n$ -fold is attributed to the width of the stripes and is not very well defined due to their broad distribution ; (ii) as the film coverage increases beyond 1 nm 3D rectangular (occasionally square) islands form in the film.

### 4.3.3 XRD study

#### Evolution of in-plane scans

Fig. 4.8 shows two types of in-plane radial scans performed along the K and  $H = K$  directions for samples with different film thicknesses from 0.2 to 2.5 nm. In addition, an in-plane radial K scan for a clean Si substrate is plotted as a reference scan. The peaks marked with arrows arise from a tetragonal  $\text{PrSi}_2$  phase while the ones appearing at multiples of  $\frac{1}{3}$  correspond to a  $3 \times 1$  superstructure. Detailed explanations of this structure identification are given in section 4.3.1. Fig. 4.8(a) suggests that the tetragonal  $\text{PrSi}_2$  phase starts to appear at a film thickness between 0.2 and 0.6 nm, as Bragg peaks from this structure are not observed for the 0.2 nm thick film and are visible only for films  $\geq 0.6$  nm. Fig. 4.8(a) indicates that the peaks of the  $3 \times 1$  superstructure ( $K=1.33$  and  $2.67$ ) are already present for the film with thickness of 0.2 nm, with the half-order peaks from the Si dimers still visible at  $K = 1.5$  and  $2.5$ . The intensity contribution visible at  $K \approx 0.88$  on this scan could

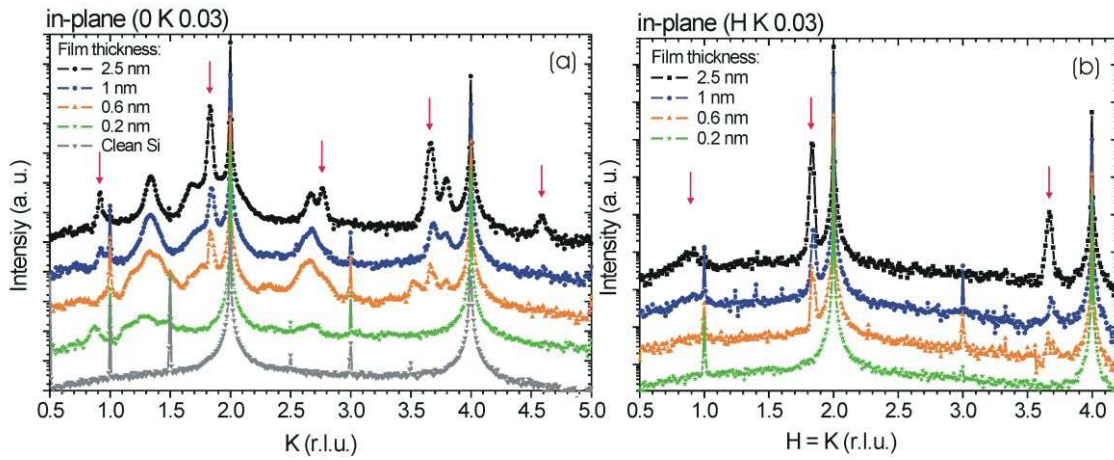


Figure 4.8: In-plane scans for different samples with different film thicknesses. Peak intensities are presented in Log scale. The scans are plotted in Si reciprocal lattice unit (r.l.u.). The arrows indicate the peaks from the  $\text{PrSi}_2$  phase. (a) Scans along the  $[0K0]$  direction for 5 samples: from clean Si substrates to around 2.5 nm thick films. (b) Scans along the  $[HK0]$  direction for 4 samples: from 0.2 nm to around 2.5 nm thick films.

originate from the  $4 \times 1$  intermediate phase observed in Fig. 4.4(b). The  $3 \times 1$  superstructure peaks at this coverage are much broader than those of the films thicker than 1 nm, suggesting that when the film thickness is below 1 nm the  $3 \times 1$  phase is not fully developed. Fig. 4.8(b) shows additional in-plane Bragg peaks from the  $\text{PrSi}_2$  phase along the  $H=K$  direction appearing after the film thickness reaches 0.6 nm.

### Evolution of specular reflectivity and Si CTRs

Fig. 4.9 shows the specular reflectivities and Si (10L) and (20L) CTRs, for samples with different film thicknesses from 0.2 nm to 2.5 nm.

For the 2.5 nm film, the specular reflectivity intensity in Fig. 4.9(a) oscillates with a periodicity corresponding to a real space dimension of 2.4 nm, which is in agreement with the thickness of the 2D layer discussed previously in section 4.3.1. For film thicknesses  $\leq 1$  nm the periodicity of the intensity oscillations in the specular reflectivities cannot be clearly identified due to the small modulation amplitudes, which suggest that the elongated bright features observed in STM (Figs. 4.4 and 4.5(e)) for the thinner films may have an electron density lower than that of the 2D layer developed for the thicker films. In addition to the average electron density, off-specular rods are also sensitive to the structural ordering of the interfaces and overlayers. The strong intensity modulations observed in the (10L) and

(20L) CTRs in Figs. 4.9(b) and (c) indicate that an atomically ordered layer, commensurate to the Si substrate, is developing as the total film thickness increases. For film thicknesses  $\leq 0.6$  nm, the changing shape of the intensity modulations in the (10L) and (20L) rods can be mostly attributed to the increase of the thickness of this commensurate layer. Beyond 0.6 nm, the shapes of the two CTRs remain essentially unchanged up to 2.5 nm, suggesting that this commensurate layer is confined to the interface with a maximum thickness  $\leq 0.6$  nm. Comparing these results to the in-plane data this commensurate layer is expected to have a  $3 \times 1$  in-plane superstructure. This superstructure is discussed in greater detail in Chapter 5.

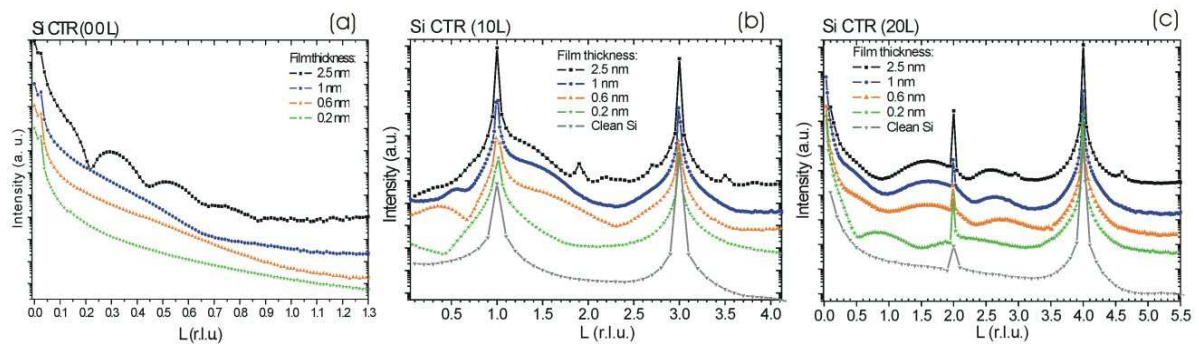


Figure 4.9: Intensity distribution along three Si rods for different film thicknesses. Peak intensities are presented in Log scale. The scans are plotted in Si reciprocal lattice unit (r.l.u.). (a) (00L) Specular reflectivity results for 4 different samples, from 0.2 nm to 2.5 nm thick films. (b) (10L) Si CTRs for 5 different samples, the 4 top ones are the same than in (a) and a last one corresponds to a clean Si(001) surface. (c) (20L) Si CTRs for the same samples than (b).

In the next section a 2.5 nm thick film grown in UHV at 550 °C is examined using XRD and XPS. The different film phases are identified, with a particular focus on the 3D islands.

## 4.4 Phases identification

### 4.4.1 XRD results and structural properties

#### Specular reflectivity measurement

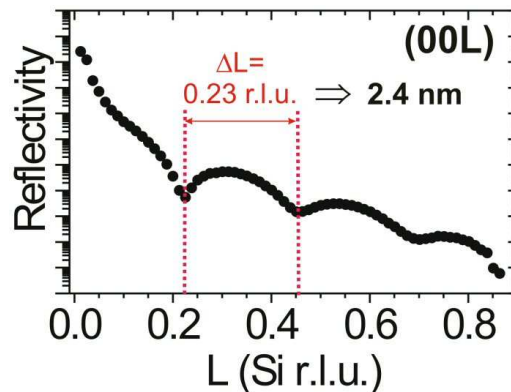


Figure 4.10: Film thickness estimation from a specular reflectivity measurement using x-rays energy of 16.75 KeV. The intensity is in Log scale and the L values are presented in silicon reciprocal lattice unit (r.l.u.).

Fig. 4.10 shows the measured specular reflectivity collected from a sample with a deposited thickness of about 2.5 nm, approximately the same film thickness as the sample presented in Figs. 4.5(f). From the periodicity of the oscillations an average film thickness of 2.4 nm is estimated for this sample (cf. Eq. 2.14). This good agreement with the deposited thickness attests the proper growth calibration with the QCM.

#### Reciprocal space map and in-plane information

The reciprocal space map (RSM) in Fig. 4.11 is based on one mesh scan measured over the area  $0.75 \leq H \leq 4.75$  and  $-0.2 \leq K \leq 2.2$  with  $L = 0.03$ . It was collected from the same sample represented in Fig. 4.10. The diffraction data exhibited mirror symmetry along the  $H = K$  directions. The mirror image of this mesh with respect to the mirror plane along the  $H = K$  direction was produced and placed in the region  $-0.2 \leq H \leq 2.2$  and  $0.75 \leq K \leq 4.75$ . The presence of this mirror plane in the reciprocal space can be seen from the two in-plane scans in Fig. 4.12, since these scans along the H- and K- directions appear to be virtually

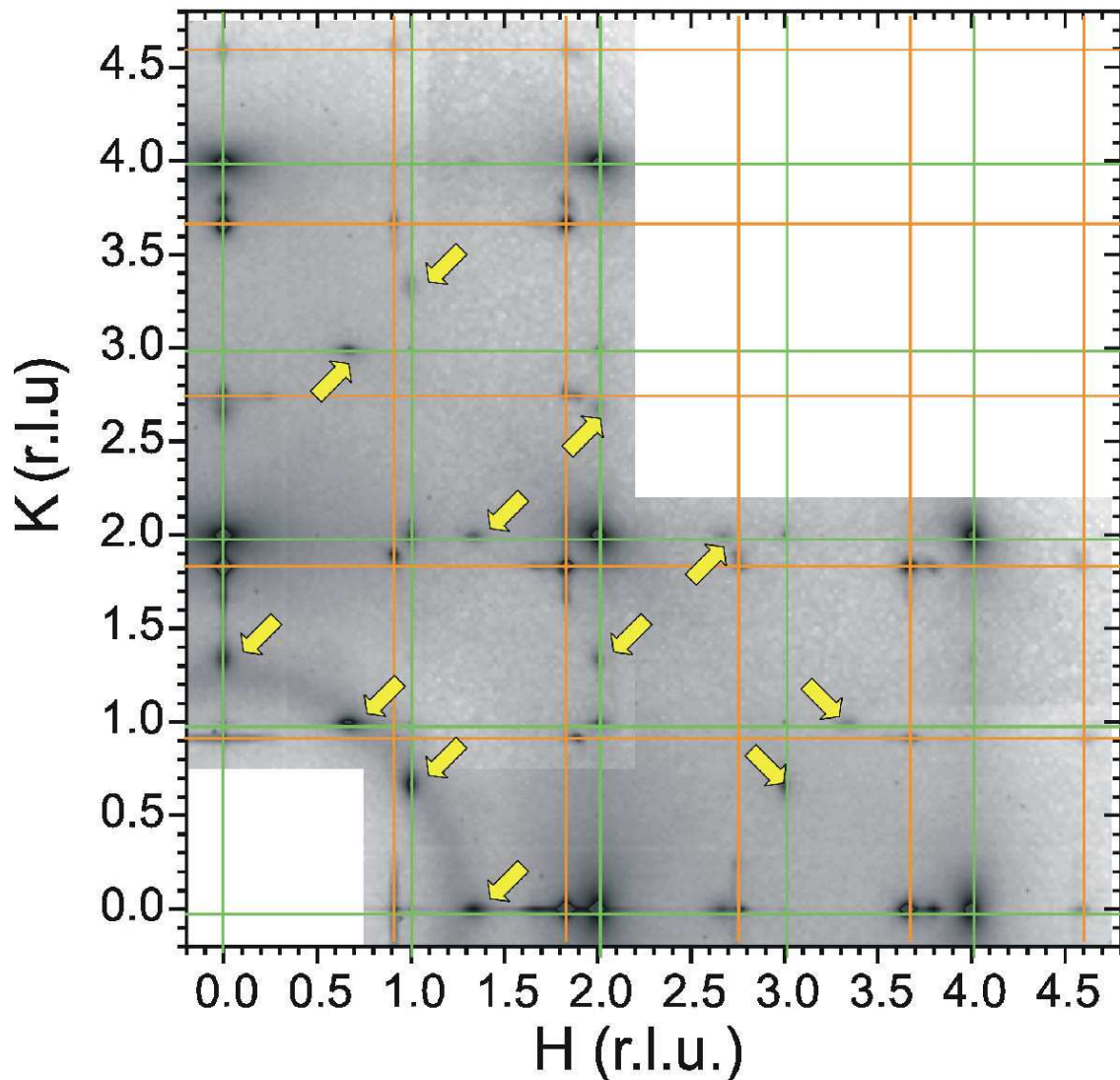


Figure 4.11: Mesh scan in the (H,K) reciprocal space plane for a 2.5 nm thick Pr-oxide film grown under UHV conditions on Si(001). Peak intensities are presented in Log scale. H and K values are in Si reciprocal lattice unit (r.l.u.). X-ray energy was 16.75 KeV.

identical. A number of spots with different intensities can be observed and organized along two sets of lines. The first series appears at integer H and K values (intersections between two green lines). The most intense spots correspond to the silicon in-plane Bragg reflections while the weaker ones can be associated with silicon CTRs. Along each integer H or K line additional spots can be observed, as marked by the arrows. They arise from a superstructure commensurate with the Si substrate that can be identified to have a  $3 \times 1$  unit cell with two equivalent domains rotated by  $90^\circ$  from each other. The peaks corresponding to this  $3 \times 1$  (or  $1 \times 3$ ) superstructure appear between the substrate in-plane peaks with H or

K equal to multiples of  $\frac{1}{3}$ . Some of these fractional order spots are missing, indicating that certain reflections are forbidden by the superstructure. Further detail about the structural identification of this  $3 \times 1$  phase are reported in Chapter 5.

The second series of spots appear at non-integer H and K values (intersections between two orange lines) and thus correspond to an incommensurate structure. The aim of the next paragraph is to identify this incommensurated phase.

### Incommensurate phase identification

In-plane radial scans along the H and K directions have been performed to determine the lattice constants  $a$  and  $b$ , respectively, of this incommensurate phase. The results are presented in Fig. 4.12.

The two most intense peaks in Figs. 4.12(a) and (b) arise from the silicon in-plane Bragg reflections. The peaks corresponding to the incommensurate phase are marked with arrows. The other ones are due to the  $3 \times 1$  superstructure and will be discussed in Chapter 5.

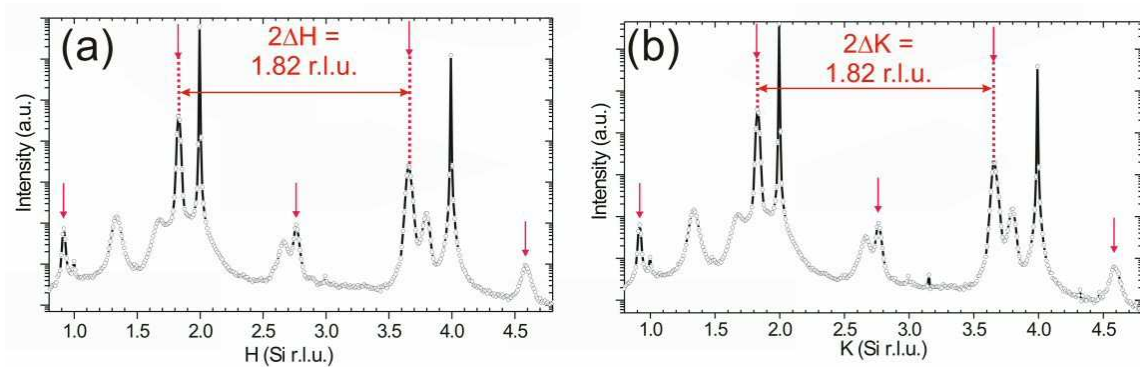


Figure 4.12: (a) in-plane radial scan along the H direction, at  $K = 0$  and  $L = 0.03$ . For more detail see the text. (b) in-plane radial scan along the K direction, at  $H = 0$  and  $L = 0.03$ . For more detail see the text.

The first observation is that the position and the peak intensities along the H direction appears identical to the ones along the K direction. In addition, only one set of peaks appears with a constant periodicity along both H and K directions, suggesting that the in-plane incommensurate peaks form a cubic sublattice in reciprocal space. From these

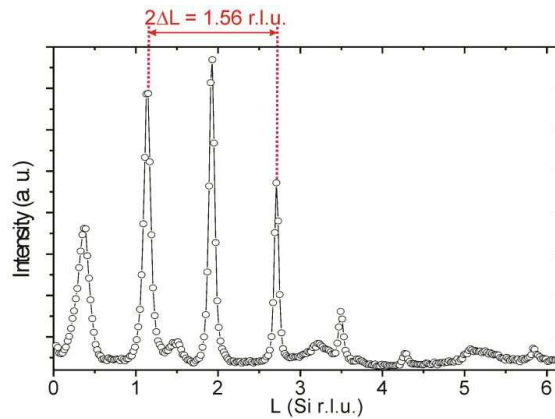


Figure 4.13: L scan along the (2.765 0 L) rod in Si reciprocal lattice unit (r.l.u.). Peak intensities are presented in linear scale.

observations we can deduce the  $a$  and  $b$  lattice constant values of the film using the peak spacings  $\Delta H$  and  $\Delta K$  (see Eq. 2.14), which correspond to 0.422 nm in real space. The  $c$  lattice constant is determined from scans performed along the L direction, with the in-plane (H,K) values corresponding to the incommensurate reflections. Fig. 4.13 shows such a scan along the (2.765 0) rod. The peak spacing  $\Delta L$  suggests a unit cell dimension of 0.696 nm in the real space along the  $c$  axis.

The  $a$ ,  $b$  and  $c$  parameters measured from the three last scans have been compared with those of different Pr inorganic compound containing also Si and/or O that can be found in the [131], a powder diffraction database giving bulk lattice parameters. Since forbidden or weak reflections may exist but cannot be revealed by the scans in Figs. 4.12 and 4.13, the lattice constants should correspond to a multiple of 0.422 nm for  $a$  and  $b$  and 0.696 nm for  $c$ , with  $\alpha = \beta = \gamma = 90^\circ$ . The only candidate that has unit cell dimensions consistent with the measured ones is the tetragonal phase of Pr-disilicide ( $\text{PrSi}_2$ ), the listed bulk lattice constants of which are  $a = b = 0.421$  nm and  $c = 1.373$  nm ( $= 2 \times 0.6865$ ) [132].

### Off-specular rod scans

#### a) Confirmation of $\text{PrSi}_2$ structure

In order to confirm this structure assignment, the structure factors along several rods of this incommensurate phase were measured. Fig. 4.14 shows both the measured (data points)

and calculated (gray columns) intensity distributions for the different reflections along four rods, namely (20L), (30L), (40L), and (50L), of the incommensurate oxide phase. The two top plots are in linear scale while the two bottom ones are in Log scale. The (30L) PrSi<sub>2</sub> rod in Fig. 4.14, for example, corresponds to the (2.765 0 L) rod in Si r.l.u. in Fig. 4.13. For the

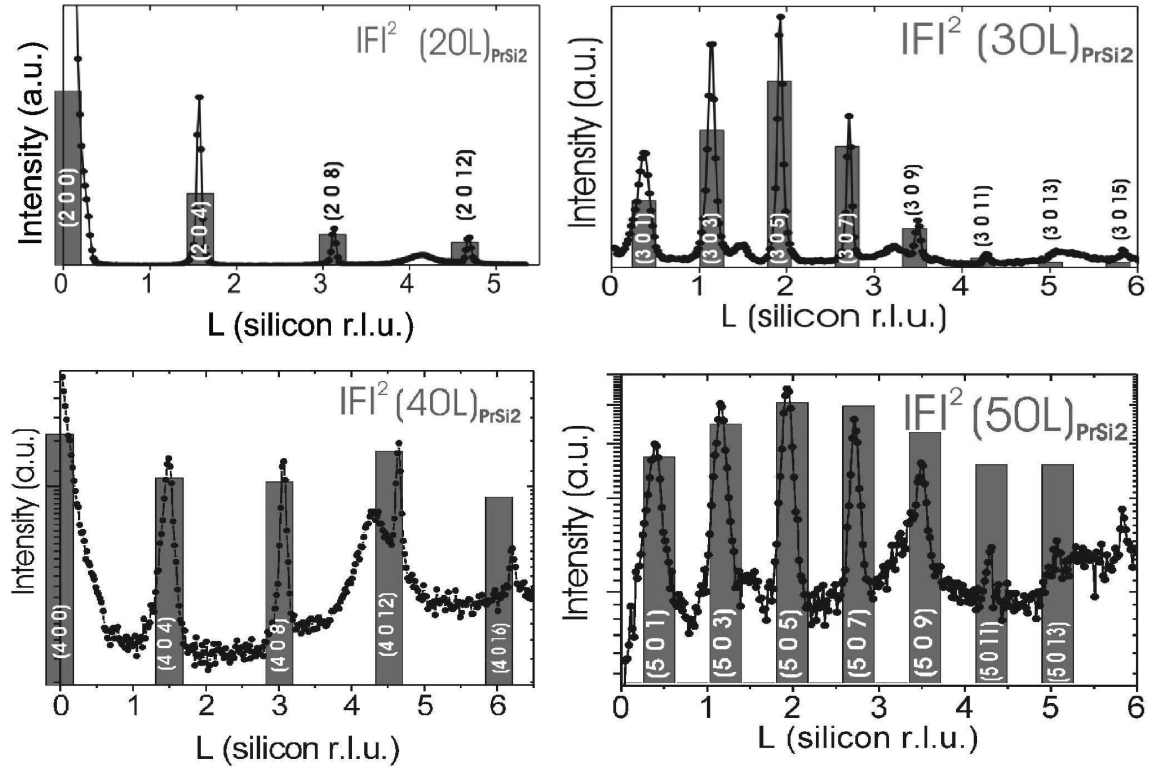


Figure 4.14: (a) Comparison between measured (data points) and calculated (gray columns) peak intensity distribution for the incommensurate oxide phase. The two top plots are in linear scale while the two bottom ones are in Log scale. The scans are plotted in Si reciprocal lattice unit (r.l.u.)

calculated intensity, we used the atomic coordinates determined previously by Lambert-Andron *et al.* [132] for PrSi<sub>2</sub> powder using neutron diffraction to calculate the square of the structure factors for the different reflections. The tetragonal unit cell contains 4 Pr and 8 Si atoms with atomic coordinates Pr = (0, 0, 0) and Si = (0, 0, 0.416) and space group 141 (*I*<sub>41</sub>/*amd*). The crystal structure is plotted in Fig. 4.15. The qualitative agreement between the measured intensities and the calculated ones confirms the formation of the tetragonal PrSi<sub>2</sub> phase. As the experimental raw data are not corrected in intensity by the correction factors presented in Chapter 2, minor deviations for the calculations can be observed.

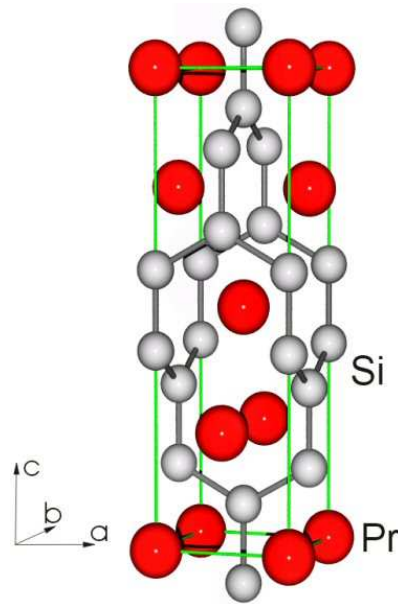


Figure 4.15:  $\text{PrSi}_2$  tetragonal structure. Lattice parameters from [132]:  $a = b = 0.421$  nm and  $c = 1.373$  nm.

#### b) Thickness of the $\text{PrSi}_2$ structure

We have used the intensities of the  $\text{PrSi}_2$  Bragg peaks along the off specular  $\text{PrSi}_2$  rods to identify the atomic structure. The FWHM of the Bragg peaks along the L direction gives additional information on the thickness of the  $\text{PrSi}_2$  structure. Fig. 4.16 presents a L scan of the  $\text{PrSi}_2$  (204) reflection. The experimental data points are fitted with a Lorentzian function. From the FWHM of the peak ( $\Delta L = 0.054$  r.l.u.) the average height of the  $\text{PrSi}_2$  structure can be estimated to be around 10 nm (Eq. 2.6). This result is in good agreement with the island height revealed by the STM line profile presented in Fig. 4.5(f2). However the fact that the regularly spaced oscillations (Laue oscillations), which may occur due to interference between the diffracted x-rays from the substrate and overlayer, were not observed for any of the L scans along the  $\text{PrSi}_2$  rods suggests that the height of the  $\text{PrSi}_2$  structure has a broad distribution around 10 nm. This broad height distribution also prevents the specular reflectivity measurement (Fig. 4.10) from revealing this 10 nm length scale. For the islands shorter than 5 nm in the STM images in Figs. 4.5(f), the lateral dimensions of the islands appear to be also smaller than those of the 10 nm thick ones. Since the Bragg peak intensity scattered from an island is proportional to the square of its volume, those small islands do not contribute very much to the Bragg peak intensity in Fig. 4.16 and thus only the average dimension of the large islands can be deduced from the peak width.

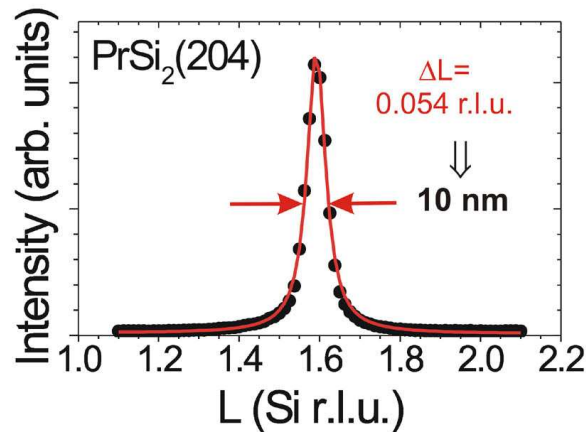


Figure 4.16: 3D island height estimation from the (204)  $\text{PrSi}_2$  reflection. The peak intensity is presented in linear scale and the L scan is plotted in Si reciprocal lattice unit (r.l.u.).

A remaining question is the nature of the 2D layer visible between the  $\text{PrSi}_2$  3D islands in Figs. 4.5(e) and (f) as well as in Fig. 4.6(c). The diffraction data did not give apparent information on other phases than the two ones mentioned above. Therefore XPS measurements were performed.

#### 4.4.2 XPS results

Fig. 4.17 shows the Si2p (a) and O1s (b) core level spectra recorded at an emission angle of  $45^\circ$  on a 2.5 nm thick film grown at  $550^\circ\text{C}$  under UHV condition. The dashed lines mark the respective positions of the indicated chemical bonds, as reported in the literature ([48, 58, 122]). Regarding the Si2p spectrum in Fig. 4.17(a) it exhibits a main component around 100 eV, which splits into two contributions. These contributions are separated by 600 meV and correspond to the spin-orbital split Si2p<sub>1/2</sub> (at  $\approx 100.4$  eV) and Si2p<sub>3/2</sub> (at  $\approx 99.8$  eV) from the Si substrate. A much weaker second component at 102.8 eV can be observed. Its binding energy is different from the one that would reveal Si-O bonds formation (see the dashed line indicating SiO<sub>2</sub> contribution on the Si2p spectrum). This contribution corresponds to the chemical state of Si in a Pr-O-Si bond and can be associated with the formation of Pr-silicate, as explained by Schmeisser *et al.* [58]. Indeed, Si atoms in SiO<sub>2</sub> have four neighbors resulting in a Si2p shift of 4 eV while in a Pr-silicate the four O neighbors of Si have Pr neighbors. Since Pr is more electropositive than Si, electron transfer from Pr in Si-O-Pr competes with the electron transfer from Si, reducing the positive charge of Si and the Si2p binding energy is decreased.

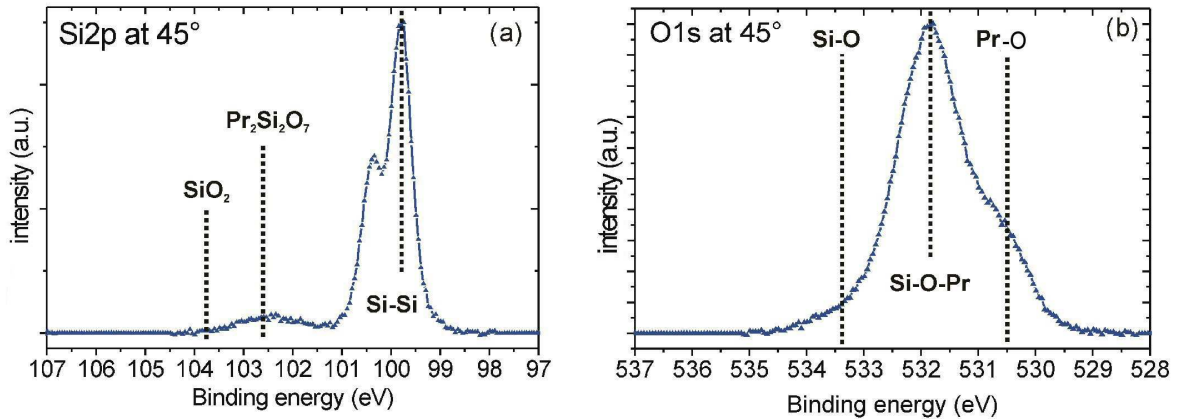


Figure 4.17: Si2p and O1s spectra recorded of a sample with a 2.5 nm thick film grown at 550 °C under UHV condition. Spectra recorded at an emission angle of 45 °. Dashed lines show the respective positions of the indicated chemical bonds, as reported in the literature ([48, 58, 122]).

The O1s spectrum in Fig. 4.17(b) shows a prominent feature at 531.8 eV that can be assigned to the emission from Pr-silicate (Pr<sub>2</sub>Si<sub>2</sub>O<sub>7</sub>) [58,122]. This result can be explained by the increase of the negative charges on O from SiO<sub>2</sub> to Pr<sub>2</sub>Si<sub>2</sub>O<sub>7</sub>, as Pr is more electropositive than Si [58]. One additional component can be observed at ≈ 530.5 eV. It is attributed to the presence of Pr-O bonds and suggests the formation of Pr<sub>2</sub>O<sub>3</sub> compound [48,58,122].

X-ray diffraction measurements on the other hand did not show any trace of a either Pr<sub>2</sub>Si<sub>2</sub>O<sub>7</sub> phase or Pr<sub>2</sub>O<sub>3</sub> phase, suggesting two disordered phases. Correlated to the STM analysis, the disordered silicate, which is visible in the Si2p spectrum and predominates in the O1s spectrum, might correspond to the 2 nm thick 2D layer between the Pr-silicide 3D islands in Fig. 4.5(f2).

In this study, Pr-silicide is expected to form, based on the SXRD results (see § 4.3.3). However, no clear evidence of Pr-silicide was observed in the Si2p spectrum. In principle a new Si2p component, corresponding to Pr-silicide, should have been visible in the binding energy range about 1 eV lower than the one arising from the bulk Si [133]. The absence of this contribution may be the result of small Pr-silicide contribution to the Si2p spectra, since the PrSi<sub>2</sub> forms high islands with a comparably small surface area.

However the corresponding Si KLL lines in the AES spectra of a 2.5 nm thick film grown at 550 °C under UHV seem to detect such a contribution, as visible in Fig. 4.18 with a shoulder between 1615 and 1616 eV, which is pointed out by the arrow. The 1608 eV component on the spectrum of the 2.5 nm thick film grown at 550 °C under UHV condition

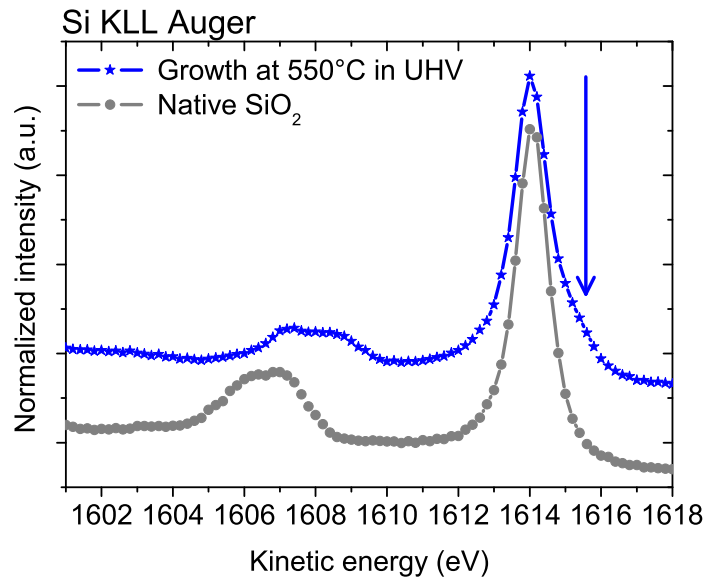


Figure 4.18: SiKLL spectrum of a sample with a 2.5 nm thick film grown at 550 °C under UHV condition, plotted together with the one of SiO<sub>2</sub> native oxide (as a reference). The arrow points on a shoulder of the 1614 eV peak attributed to Pr-silicide formation.

is 2 eV shifted toward higher kinetic energy with respect to the corresponding component in the case of a Si substrate with a SiO<sub>2</sub> layer. This is consistent with the formation of a Pr-silicate (Pr is more electropositive than Si).

The fact that Pr-silicide cannot be observed on the Si2p core level spectra while it contributes to the Si KLL lines in the AES spectra is most likely due to a corresponding chemical shift that is rather small and only Auger spectroscopy, more sensitive since it involves three electronic states, can see it. This is demonstrated by comparing Fig. 4.17(a) and Fig. 4.18. In Fig. 4.17(a) the energy offset between the SiO<sub>2</sub> and the Pr<sub>2</sub>Si<sub>2</sub>O<sub>7</sub> contributions to the Si2p core level spectrum is of  $\approx 1$  eV. In Fig. 4.18 the energy offset between these two contributions is of 2 eV. Fig. 4.19 shows the valence band (VB) spectrum for a 2.5 nm thick film together with the VB spectra of both pure Si and SiO<sub>2</sub>, all scaled to the same integrated area. As previously explained (Chapter 2) the binding energy was calibrated by the Fermi edge of a gold foil and like the previous XPS spectra a Shirley function was subtracted from the data to remove the background due to the contribution of photoelectrons with energy loss. The VB spectra of both pure Si and native SiO<sub>2</sub> show that the valence band maxima are  $\approx 1$  eV below the Fermi edge. The spectrum of the

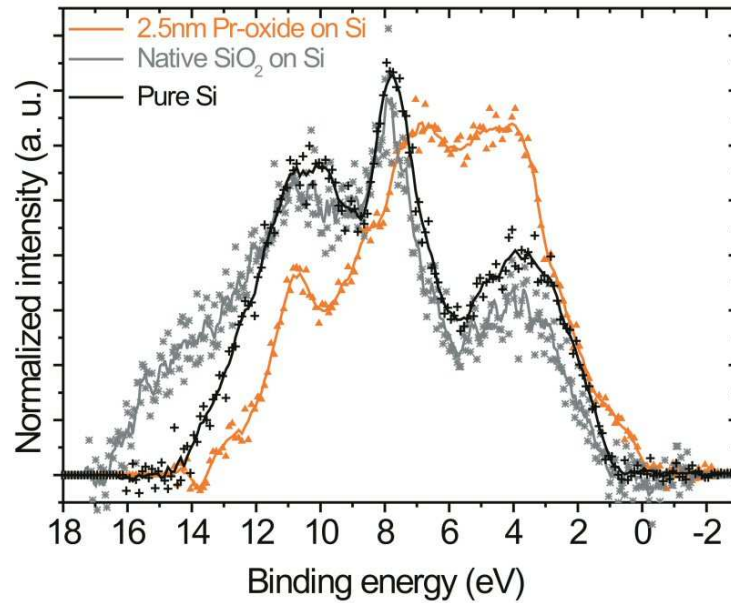


Figure 4.19: Valence band spectra. See the information in the figure for more detail.

2.5 nm Pr-oxide film exhibits a much higher density of states near the Fermi edge, suggesting a metallic nature for the films prepared under UHV conditions. This finding is consistent with the formation of a metallic Pr-silicide phase revealed by SXRD and STM.

### 4.4.3 Summary

Thanks to the combination of XRD and XPS measurements Pr-O films grown at 550 °C under UHV conditions were identified as consisting of three different phases. XRD revealed on one hand a commensurated  $3 \times 1$  ordered layer present at submonolayer coverages and stable with subsequent growth. On the other hand the presence of a relaxed tetragonal  $\text{PrSi}_2$  phase was demonstrated and could be correlated to the 3D islands observed with STM.

The XPS core level study has shown the presence of Pr-silicate. This silicate phase could not be evidenced by XRD. Therefore it is a disordered phase attributed to the 2D wetting layer between the 3D Pr-silicide islands, as observed in Fig. 4.5(f2).

## 4.5 Room temperature grown samples subsequently post-annealed in different (P,T) conditions

In this section the results collected on 2.5 nm films grown at room temperature under UHV conditions are presented (an AES spectrum of a 1 nm thick film is also displayed for comparison). These films were subsequently post-anneal under different (P,T) conditions. The aim of these measurements was to investigate

1. The composition differences with the sample grown at 550 °C and in particular whether silicide forms at room temperature under UHV
2. The film evolution/stability with subsequent post-annealing treatments.

For this study only XPS and AES results are examined. Indeed, samples grown at room temperature did not exhibit any LEED pattern, suggesting disordered overlayer, and therefore no XRD data were recorded on these samples.

For comparison the results obtained on the 2.5 nm thick film grown at 550 °C and presented in the previous section are recalled. When relevant the corresponding results recorded from a clean Si substrate and/or on a substrate with its native oxide are plotted together with the new results.

### 4.5.1 XPS and Auger findings at the beamline

The XPS study was performed on a 2.5 nm film grown at room temperature and subsequently post-annealed several times at different temperatures under UHV or with additional oxygen. Fig. 4.20 summarizes the results of this study. Figs. 4.20 (a) and (b) show each five O1s spectra and Figs. 4.20 (c) and (d) show each five Si2p spectra. The O1s and Si2p spectra are normalized to the peak heights of the O1s component at 531.8 eV and Si2p<sub>3/2</sub> component appearing at 99.8 eV, respectively, once a Shirley function has been applied to the data to remove the background. The spectra presented in Figs. 4.20 (a) and (c) were recorded at an emission angle of 45° with respect to the surface and are thus more bulk sensitive compared with the ones in Figs. 4.20(b) and (d), which were recorded at an emission angle of 12°. The first spectrum in each of the plots shows a reference scan

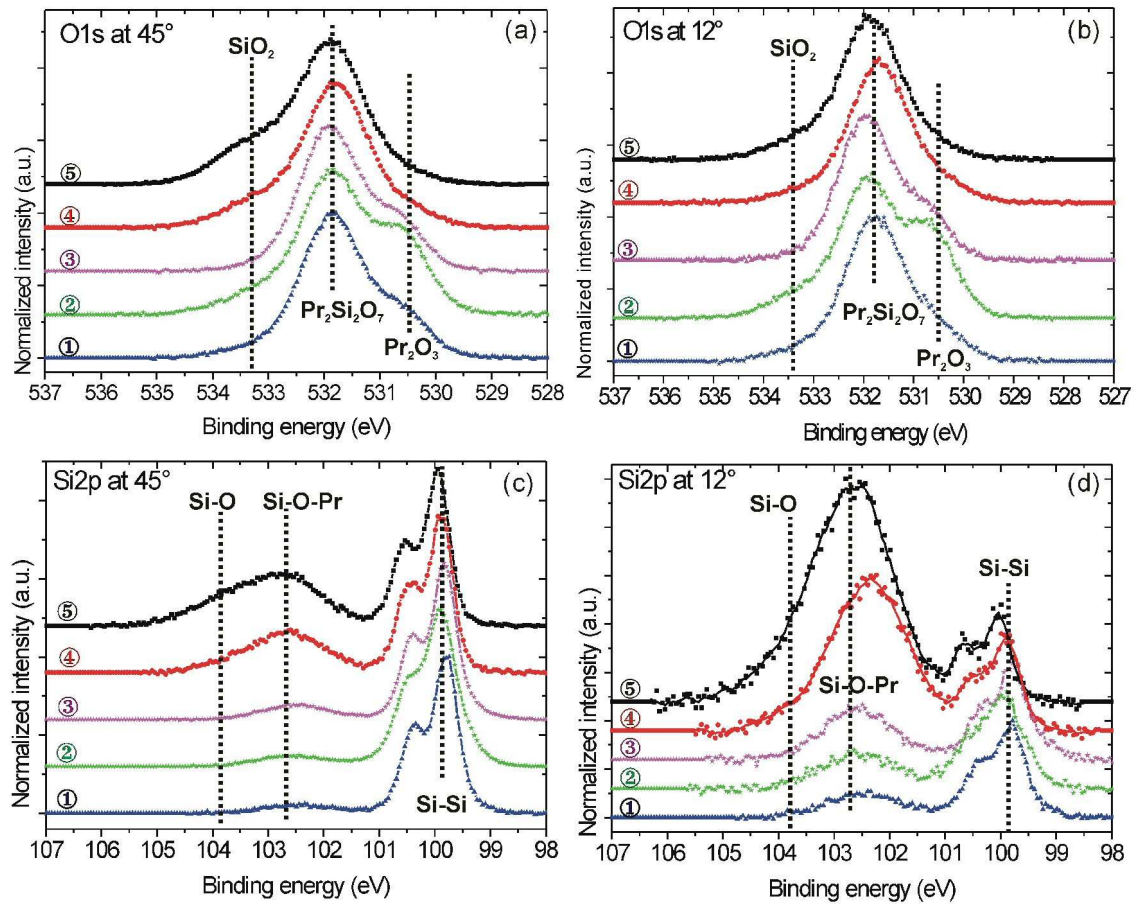


Figure 4.20: XPS results. Evolution of Si2p (c) and (d) and O1s (a) and (b) spectra with subsequent post-annealing treatments on a 2.5 nm film grown at room temperature for both emission angles  $12^\circ$  (b) and (d) and  $45^\circ$  (a) and (c). The O1s spectra are normalized to the 531.8 eV main component while all the Si2p spectra are normalized to the pure silicon Si2p<sub>3/2</sub> component. 1: reference scan. As grown sample at  $550^\circ\text{C}$  under UHV; 2: room T growth; 3: step 2 + 30 min at  $550^\circ\text{C}$  under UHV; 4: step 3 + 20 min at  $550^\circ\text{C}$  in  $5 \times 10^{-8}$  mbar; 5: step 4 + 20 min at  $550^\circ\text{C}$  in  $10^{-7}$  mbar. Dashed lines show the respective positions of the indicated chemical bonds, as reported in the literature ([48, 58, 122])

of a 2.5 nm film, grown at  $550^\circ\text{C}$  under UHV; the second spectrum was measured from the room-temperature grown film of the same thickness; the third one shows the spectrum after half an hour post-annealing treatment at  $550^\circ\text{C}$  under UHV of the room temperature grown sample; the fourth spectrum corresponds to a second post-annealing treatment of 20 min at  $550^\circ\text{C}$  in  $5 \times 10^{-8}$  mbar O<sub>2</sub> of the same sample; the fifth one shows the spectrum after an additional 20 min post-annealing treatment at  $550^\circ\text{C}$  under an oxygen partial pressure of  $10^{-7}$  mbar. The dashed lines mark the respective O1s and Si2p binding energies

corresponding to the relevant chemical states, as reported in the literature [48, 58, 122].

The O1s spectra in Figs. 4.20 (a) and (b) exhibit a prominent feature at 531.8 eV that can be assigned to the emission from Pr-silicate ( $\text{Pr}_2\text{Si}_2\text{O}_7$ ) [122]. Compared with the O1s spectrum for a  $\text{SiO}_2$  native oxide layer, presented in Fig. 5.3 (b), here we observe a chemical shift towards lower binding energy. As previously discussed this result can be explained by the increase of the negative charges on O from  $\text{SiO}_2$  to  $\text{Pr}_2\text{Si}_2\text{O}_7$ , as Pr is more electropositive than Si [58]. Two additional components can be observed in the spectra, with intensities depending on the preparation conditions. Comparison of spectra 1 and 2 in Fig. 4.20 (a) reveals a more intense component at  $\approx 530.5$  eV for the room temperature grown sample. It is attributed to the presence of Pr-O bonds and suggests the formation of  $\text{Pr}_2\text{O}_3$  compound [48, 58, 122]. In addition, a weak contribution at higher binding energy seems to be present at 533.3 eV. It corresponds to the chemical state of oxygen in a Si-O bond and indicates the presence of a  $\text{SiO}_x$  phase in the film. A post-annealing in UHV conditions at 550 °C (step 3) eliminates this latter component from the O1s lines, while the 530.5 eV component remains, although the intensity also decreases. An additional slightly shorter post-annealing treatment at the same temperature but under  $5 \times 10^{-8}$  mbar  $\text{O}_2$  (step 4) gives rise again to the 533.3 eV component ( $\text{SiO}_2$ ), while the  $\text{Pr}_2\text{O}_3$  contribution further decreases. This latter contribution is almost completely removed by the last post-annealing treatment (step 5) carried out at the same temperature with an oxygen partial pressure of  $10^{-7}$  mbar. Another significant effect of this post-annealing step is the increase of the  $\text{SiO}_x$  contribution in the Si2p spectrum. Similar evolutions can be observed in Fig. 4.20 (b). An interesting feature to underline for these series of spectra is that the  $\text{SiO}_x$  contributions in the O1s lines after the last two post-annealing treatments (step 5) are less pronounced in Fig. 4.20 (b) than that in Fig. 4.20 (a). Since Fig. 4.20 (a) was measured with higher bulk sensitivity than Fig. 4.20 (b), this result suggests that Si-O bonds are buried close to the film/substrate interface.

Fig. 4.20 (c) shows the Si2p spectra measured at 45° emission angle. In all the spectra the  $\text{Si}2p_{1/2}$  and  $\text{Si}2p_{3/2}$  components from the pure Si substrate are present around 100 eV and a second component at 102.7 eV is also visible. This latter contribution corresponds to the chemical state of Si in a Pr-O-Si bond and can be associated with the formation of Pr-silicate. For the two last post-annealing treatments, under increasing oxygen partial pressure, an additional component emerges at 103.8 eV and suggests the formation of Si-O bonds. Similar observations are visible in Fig. 4.20 (d), where the Si2p spectra presented

were recorded at an emission angle of  $12^\circ$  and then correspond to a shallower probing depth. The intensity ratio between the two binding energies characteristic of the Si-O and Pr-O-Si bonds appears lower in Fig. 4.20 (d), indicating that a  $\text{SiO}_x$  phase is confined to the interface while the film is mainly Pr-silicate.

Fig. 4.21 shows the Si KLL spectrum of a room temperature grown 2.5 nm thick film together with the one of a similar sample grown at  $550^\circ\text{C}$ . Interestingly the shoulder that was observed on the latter sample and attributed to Pr-silicide (cf. section 4.3.2.) does not show up on the spectrum of the sample grown at room temperature under the same pressure range. This result suggests that growth at room temperature prevents the phase separation leading to  $\text{PrSi}_2$  3D islands.

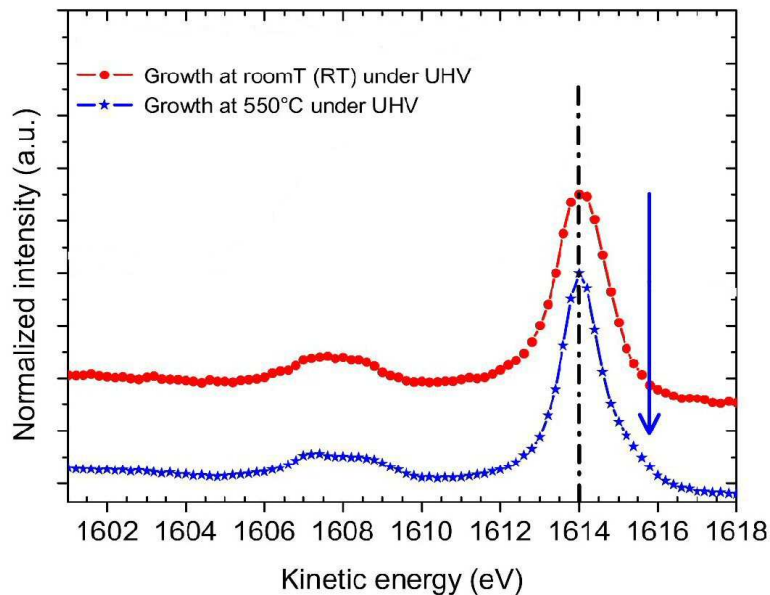


Figure 4.21: Si KLL spectra of three different samples with 2.5 nm thick films. From bottom to top the growth conditions are:  $550^\circ\text{C}$  under UHV; Room temperature deposition under UHV. The dashed line shows the position of the main peak in the case of a pure Si sample. The arrow points on a shouldering of the 1614 eV peak attributed to Pr-silicide formation.

Fig. 4.22 shows the VB spectrum for two 2.5 nm thick films (deposited thickness), one grown at  $550^\circ\text{C}$  and the other one at room temperature, together with the VB spectrum of clean Si as a reference scan, all normalized to their integrated areas.

Compared with the VB spectrum of the film grown at high temperature, the VB spectrum of the room temperature grown film shows slightly less density of states near the Fermi edge, but does not provide sufficient valence band offset with respect to the silicon substrate.

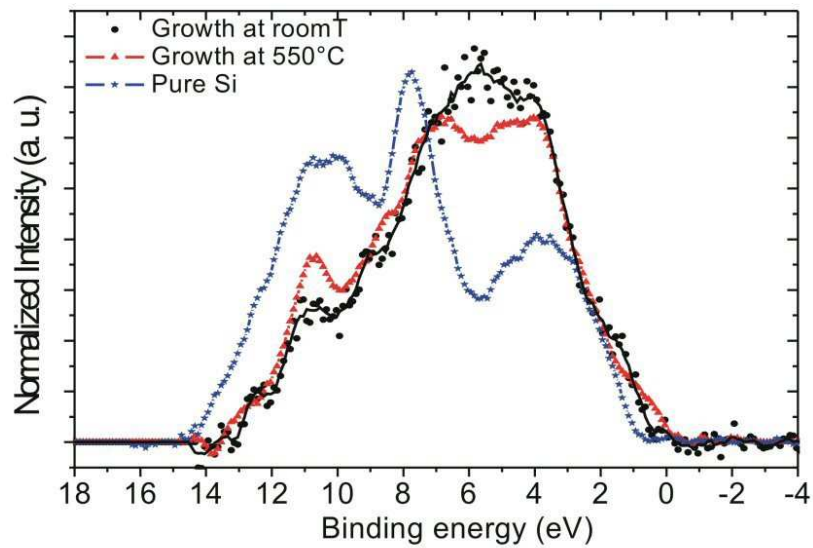


Figure 4.22: Valence band spectra of pure Si and 2 other samples, with a 2.5 nm thick film grown in UHV, one at 550°C, and the other one at room temperature (T).

#### 4.5.2 Complementary AES results from the SCL

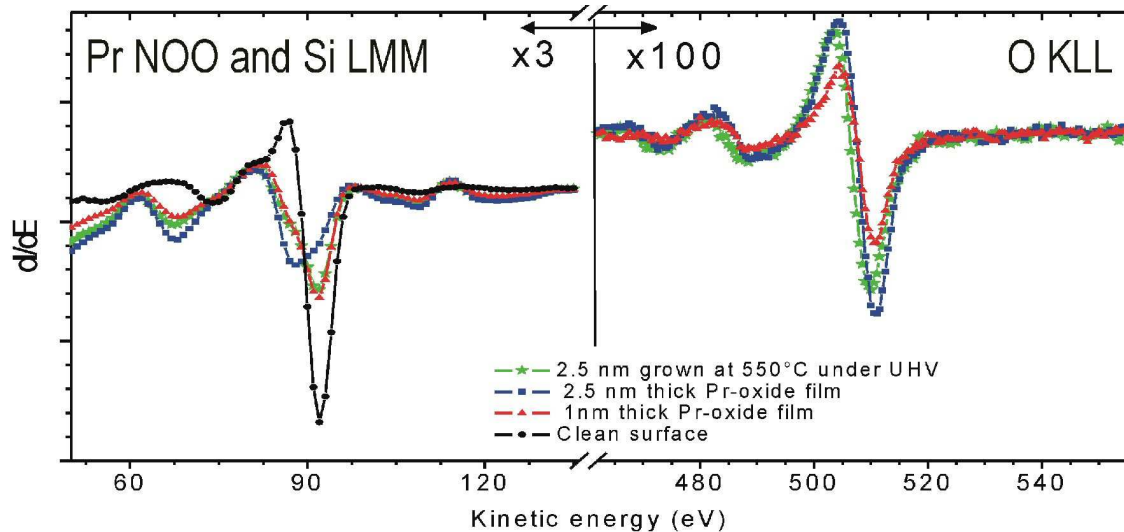


Figure 4.23: Pr NOO and Si LMM (left) and O KLL (right) AES spectra of four samples: clean Si substrate (reference); 1 nm and 2.5 nm thick Pr-oxide films grown at room temperature under UHV; 2.5 nm thick Pr-oxide film grown at 550°C under UHV, for comparison.

An AES study using electron beam excitation was performed on one 2.5 nm thick film grown at room temperature and subsequently post-annealed several times, at different

temperatures, under UHV or under different oxygen partial pressures. For comparison an AES spectrum of a 1 nm thick film also grown at room temperature is displayed, as well as the results collected on the 2.5 nm film grown at 550 °C under UHV (cf. previous section).

The left panel of Fig. 4.23 shows four AES spectra in the kinetic energy region corresponding to the Pr NOO and Si LMM AES peaks. It shows that the AES spectrum of the room temperature grown Pr-oxide film (2.5 nm thick) has a stronger 87 eV component than the 92 eV one, in contrast with the spectrum measured from the sample grown at 550 °C (same thickness). This difference between the two samples can be attributed to the absence of phase separation and PrSi<sub>2</sub> island formation for the room temperature grown sample, since otherwise PrSi<sub>2</sub> island formation, accompanied by the appearance of bare Si, would give rise to a strong 92 eV component due to the Si Auger electrons from the substrate in the depletion areas.

Another interesting feature is the identical shape of the AES spectra of the 1 nm thick film grown at room temperature and the 2.5 nm thick one grown at 550 °C in the energy region [80-130] eV, i.e. where the Pr NOO and Si LMM peaks are. This result indicates that a same amount of Pr and Si is present within the corresponding probing depths for these two elements. The right panel of Fig. 4.23 shows the corresponding O KLL AES spectra for the three samples with Pr-oxide films. It shows that the oxygen content does not depend on the sample temperature as the O KLL peaks of both 2.5 nm films grown under UHV at room temperature and 550 °C are almost identical in shape and amplitude.

Fig. 4.24 shows the evolution of the Pr NOO and Si LMM (left) as well as O KLL (right) AES spectra for the above presented 2.5 nm thick film grown at room temperature after being subsequently post-annealed several times.

The two first post-annealing treatments (steps 2 and 3) shown in Fig. 4.24(a) are carried out under UHV at 460 and 550 °C, respectively. The left panel of Fig. 4.24(a) shows that a first half an hour post-annealing treatment at a temperature below 500 °C and under UHV conditions (step 2) gives rise to an increase of the 92 eV component with a weak shoulder at 87 eV. Since the 92 eV component is contributed mainly by the substrate Si. This suggests that PrSi<sub>2</sub> islands have developed at this stage with the formation of depletion areas. The corresponding O KLL AES spectra presented in the right panel of Fig. 4.24(a) also show that the oxygen content has decreased and support the idea of 3D PrSi<sub>2</sub> island formation.

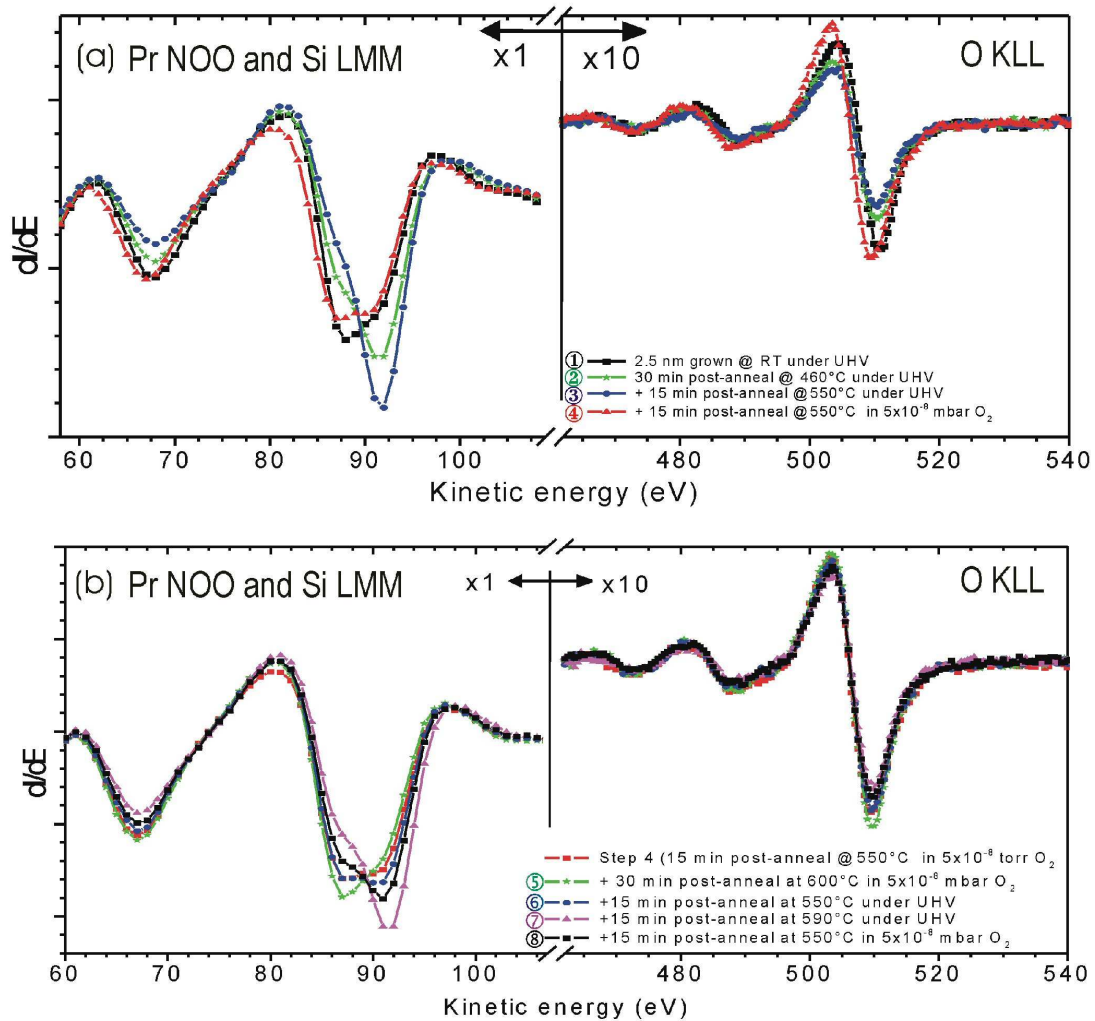


Figure 4.24: Evolution of the Pr NOO and Si LMM (left panels) as well as O KLL (right panels) AES spectra with subsequent post-annealing treatments [from (a) to (b)] on a 2.5 nm film grown at room temperature under UHV.

The second post-annealing treatment under UHV (step 3) was half shorter (15 min) but at higher temperature (550°C). Compared with step 2 the 92 eV component has increased significantly while the 87 eV shoulder becomes even less pronounced.

The third post-annealing treatment was carried out under  $5 \times 10^{-8}$  mbar oxygen (step 4), as long as step 3 (15 min), and also at the same temperature (550°C). This first post-annealing treatment under oxygen has essentially reversed the effects of the first two UHV annealings (steps 2 and 3) and converted the line shape of the spectrum in Fig. 4.24(a) back to the same as the as-grown one (step 1). Since the shift of the spectral weight between

the 87 and 92 eV components is always accompanied by the decrease/increase of the 67 eV component (see Figs. 4.23, 4.24, 5.8(b) and 5.15(a)), which accounts for the metal Pr, the 87 eV component must be also dominated by Pr NOO Auger and the contribution from the oxidized Si to this component can be neglected. Since annealing in oxygen (step 4) recovers the intensity losses of the 67 eV and 87 eV components, UHV annealing (steps 2 and 3) does not cause Pr to desorb. Instead, the intensity reduction of the 67 and 87 eV components during steps 2 and 3 is mainly due to the formation of PrSi<sub>2</sub> islands and the large depletion areas, which reduces the total number of Pr atoms within the probing depth of the Auger electrons (the atomic densities of Pr in PrSi<sub>2</sub> and Pr<sub>2</sub>Si<sub>2</sub>O<sub>7</sub> [tetragonal] are 16.4 and 14.2 e<sup>-</sup>/nm<sup>3</sup>, respectively).

Fig. 4.24(b) displays the evolution of the Pr NOO and Si LMM (left) as well as O KLL (right) AES spectra for four additional post-annealing treatments. Step 4 from Fig. 4.24(a) is plotted as a reference. The left panel of Fig. 4.24(b) shows that further post-annealing of the film in  $5 \times 10^{-8}$  mbar O<sub>2</sub> during half an hour at a slightly higher temperature than step 4 (600 °C instead of 550 °C) leads to a further increase of the 87 eV component and a slight decrease of the 92 eV one. Two additional 15 min post-annealing treatments under UHV, one at 550 °C (step 6) and the other one at 590 °C (step 7) promote the 92 eV component while the 87 eV one decreases in such a way that the spectrum corresponding to step 6 becomes identical to the one of step 4 and on step 7 the 87 eV component only appears as a shoulder of the main 92 eV peak. The last post-annealing treatment (step 8) has the same parameters as step 4: 15 min under  $5 \times 10^{-8}$  mbar at 550 °C. Compared with step 7 the 92 eV component significantly decreases while the 87 eV shoulder becomes stronger.

Our AES study shows a strong dependence of the line shape between 60 and 120 eV on the post-annealing treatments, which is mainly associated with the formation of PrSi<sub>2</sub> and large depletion areas. For the sample grown at room temperature without additional oxygen, the high intensity of the 92 eV component suggests that the PrSi<sub>2</sub> may already form in the film. High temperature post-annealing treatments under UHV are found to promote further the silicide formation. Post-annealing in oxygen partial pressure can reverse this process. However, it does not result in the same AES spectrum as those measured from samples grown in oxygen ambient (e.g. Fig. 5.8(b)).

### 4.5.3 Summary

Growth at room temperature does not form silicide but the Pr-oxide film is disordered and corresponds to a Pr-silicate. These films are very sensitive to post-annealing treatments in the temperature range [550-600]°C. Post-annealing above the mid- $10^{-8}$  mbar range likely develops a  $\text{SiO}_x$  phase and when it is close to  $10^{-7}$  mbar it clearly oxidized the film and gives rise to Si-O bonds and a  $\text{SiO}_2$  layer forms, which apparently located at the film/substrate interface. Furthermore, valence band measurements revealed a valence band maximum that is still close to the Fermi edge even for samples grown at room temperature (cf. Fig. 4.22), indicating conducting samples.

The AES study shows that (i) post-annealing treatments at high temperature under UHV seem to promote the silicide formation, e.g. steps 3 and 7 on Fig. 4.24; (ii) subsequent post-annealing treatments under oxygen seem to make the silicide formation partially reversible.

## 4.6 Discussion on the Pr-O film growth on Si(001) under UHV

The initial stages of the Pr-oxide growth on Si(001) under UHV conditions have been characterized. The formation of elongated oxide line features, commensurated to the underlying silicon substrate, has been identified as growing parallel to the  $\langle 110 \rangle$  directions of the substrate. The oxide overlayer grows on Si(001) as anisotropic islands (long and skinny) that are orthogonal to the underlying Si dimer rows. This shape is most likely due to a diffusional anisotropy on Si adatom covered surface (faster diffusion along the dimer rows vs. perpendicular). The growth of this highly anisotropic phase has been identified by LEED as a  $4 \times 1$  intermediate superstructure, which evolves into continuous streaks in the LEED patterns and elongated stripes following the Si surface dimer bonds in the STM topographs. These results suggest a coherent growth of the film in at least one in-plane direction for subnanometer coverages.

These results can be compared with other STM studies on both  $\text{CaF}_2$  nanostructures [134,135] and other rare-earth silicide nanowires [136,137] grown on Si(001).  $\text{CaF}_2 / \text{Si}(001)$  system can be considered as a prototype for the study of the interaction between a polar

insulator with ionic bonding and a semiconductor with covalent bonding. Its crystalline structure corresponds to the one of  $\text{PrO}_2$  and is the base one of the  $\text{Pr}_2\text{O}_3$  crystal. Sumiya *et al.* found that the morphology of high coverage  $\text{CaF}_2$  room temperature deposits on Si(001) surfaces, and subsequently post annealed, is strongly dependent on the substrate temperature. At high temperature ( $610^\circ\text{C}$ ) long and narrow two-dimensional layers develop.

Pasquali *et al.* in their case focussed on the initial stages of the  $\text{CaF}_2$  growth on Si(001) and monitored the substrate temperature. They have shown a variety of  $\text{CaF}_2$  nanostructures growing on Si(001), including ultrathin two-dimensional layers at  $750^\circ\text{C}$ , quasi-one-dimensional stripes at  $650^\circ\text{C}$  and well-ordered dots at lower growth temperatures.

In the case of rare-earth silicide grown on Si(001), Nogami, Liu *et al.* have revealed that when dysprosium is deposited onto Si(001) surface at  $600^\circ\text{C}$  a network of dysprosium disilicide nanowires is formed, with a width and a density strongly dependent on the deposited coverage. These nanowires grow on a flat terrace, running perpendicular to the Si dimer rows. 3D islands appear with increasing coverages and longer annealing duration.

Therefore, only on the basis of a comparison between these findings and our STM results, we cannot conclude whether the stripes we have observed correspond to a  $\text{CaF}_2$  like structure or to a silicide phase.

Furthermore our STM study revealed small domains formed by the oxide deposits (few nanometers to few tenth of nanometers) while the terrace width of the Si substrate is bigger than  $\approx 500$  nm. This is apparently due to an etching process of the Si surface simultaneously to the oxide growth. Results on Si substrates with a higher miscut seem to indicate the growth of larger domains on that kind of vicinal surfaces. In the case of the growth of  $\text{Gd}_2\text{O}_3$  and  $\text{Y}_2\text{O}_3$  films on Si(001) Kwo *et al.* have already shown that the use of vicinal Si(001) substrates is the key to produce single-domain (110)-oriented epitaxial  $\text{Gd}_2\text{O}_3$  and  $\text{Y}_2\text{O}_3$  films [138]. In our case, we did not investigate in greater detail the effect of the miscut on the Pr-O film growth.

Regarding the XRD measurements collected in this work, they have revealed the formation of a  $3\times 1$  superstructure, which could not be identified with STM and LEED. Müssig *et al.* have already reported, from the observation of STM topographs, a superstructure with a  $3\times 1$  periodicity for the  $\text{Pr}_2\text{O}_3/\text{Si}(001)$  heteroepitaxial system [47], as predicted by theoretical calculations [139]. Later-on, a RHEED study confirmed the  $1/3$  periodicity of

a superstructure present at the initial growth stages [82]. No further experimental results are so far available to elucidate this superstructure. Its nature is the subject of § 5.4 of this report.

Few attempts were made to develop thicker and better ordered  $3\times 1$  layers by varying the growth temperature and/or post-anneal the films under oxygen partial pressure. The collected results suggest that the growth conditions used so far do not seem to be the most appropriate to achieve this goal. Chapter 5 will present further growth parameters investigations together with our results on the determination of the atomic geometry and bonding of the  $(3\times 1)$  2D layer on Si(001).

This chapter has also demonstrated that under UHV conditions the Pr-oxide growth is associated with a silicon diffusion into the film and phase separation giving rise to 3D rectangular (occasionally square) shape Pr-silicide islands. While silicide formation from other RE oxide systems have recently been published [18], Pr-silicide formation, from the deposition of Pr-oxide, has not been reported so far. Dabrowski *et al.* [91] predicted, from ab initio calculations, the formation of Pr-Si bonds when not enough oxygen is available in the growth environment. In Dabrowski's paper the formation and stability of the Pr-silicide phase were discussed as functions of the oxygen chemical potential. Pr-Si bonds become energetically favorable in oxygen deficient growth environment. Indeed, considering the low oxygen partial pressure under UHV conditions (as used in standard MBE growth), the chemical potential of oxygen can be so small that silicide formation can be favored over oxide formation.

Silicide formation is one of the most crucial points for the growth of dielectric layers, because the silicide growth can continue as long as the oxygen content remains low enough or the oxygen chemical potential remains strongly negative. This occurs even faster at a surface or interface region where the energetic equilibrium is out of order, for example due to stress.

The composition of Pr-O film grown under UHV can be discussed as follow. Islands much higher than the amount of evaporated material on the surface (cf. Figs. 4.5(f)) suggest a mass transport, most likely due to the diffusion of Si from the bulk into the islands and due to the incorporation of Pr and Si from the 2D wetting layer identified by XPS as a  $\text{Pr}_2\text{Si}_2\text{O}_7$  phase.

In addition, our SXRD results (cf. Fig. 4.8) reveal that  $\text{PrSi}_2$  tetragonal phase appears on

the surface while the  $3\times 1$  phase has already been developed. Moreover it seems that the  $3\times 1$  superstructure is not affected by this island formation process. Indeed, the diffraction scans in Fig. 4.8 do not support the idea that the  $3\times 1$  interfacial layer is affected by the Pr-silicide island formation. Actually, from the intensity and the FWHM of the  $3\times 1$  peaks, it seems that the  $3\times 1$  superstructure still develops while the Pr-silicide islands form. This discussion about the layer composition of the film is summarized in form of sketches in Fig. 4.25. This figure shows two possible models explaining the layer sequence in the films grown under UHV conditions. For case (a) Si from the substrate diffuses into the layer to form  $\text{PrSi}_2$  (and Pr-silicate), but there is also interdiffusion and the  $\text{PrSi}_2$  islands are directly connected to the Si substrate. Case (b) proposes that the 3D  $\text{PrSi}_2$  islands grow on top of a  $3\times 1$  ordered interfacial layer, with a 2D Pr-silicate wetting layer that surround them. Our XRD data favor case (b), as case (a) would mean that the  $3\times 1$  ordered

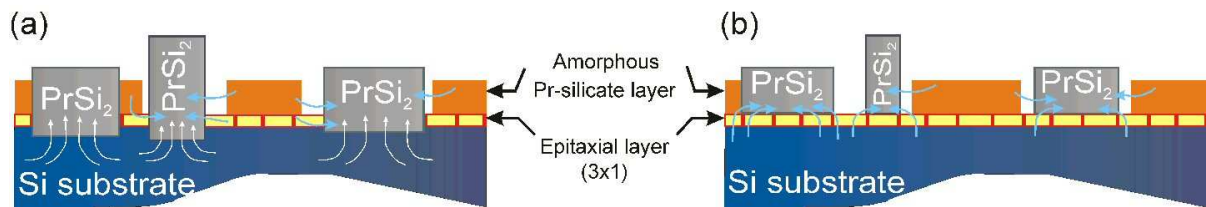


Figure 4.25: sketch of the stacking in UHV growth conditions.

interfacial layer would be affected by the growth of the Pr-silicide islands. In addition the island height estimation from both our STM and XRD data agreed with 10 nm high islands. This agreement does not suggest embedded islands into the Si substrate.

To summarize we have learnt that the film develops first a commensurate interfacial layer and no  $\text{PrSi}_2$  phase are identified for film thicknesses  $< 0.6$  nm. As the film thickness increases  $\text{PrSi}_2$  3D islands appear (see section 4.4).



## Chapter 5

# Pr-oxide thin films on Si(001): The $3\times 1$ phase

---

For any future nano-electronic applications high structural quality of an epitaxial oxide film is of importance. In this chapter the characterization of Pr-oxide thin films grown in oxygen ambient on Si(001) is reported, with a particular focus on the film / substrate interface. As we do not know for very thin oxide layers the influence of (P, T) parameters on the initial stages of the growth and on the interface quality, we invested some effort in fine-tuning the MBE growth conditions. As we could not explore the entire phase diagram of the Pr-oxides, and also as the structural characterization is time intensive (data acquisition and analysis), the temperature range investigated was  $[500-650]^\circ\text{C}$  and the oxidation range stayed below  $10^{-7}$  mbar  $\text{O}_2$ , in order not to develop a  $\text{SiO}_2$  layer. The growth rate was fixed around  $0.2 \text{ \AA}/\text{min}$  of  $\text{Pr}_2\text{O}_3$  molecules. The data shown in this chapter focus on three temperatures: 500, 550 and  $590^\circ\text{C}$  and three pressures:  $2\times 10^{-10}$  mbar (UHV),  $2\times 10^{-8}$  ( $10^{-8}$  for the XPS data) and  $5\times 10^{-8}$  mbar. XRD, XPS and AES measurements were performed. No LEED results will complement them as no LEED patterns could be observed for films thicker than 0.3 nm while prepared under  $P_{\text{O}_2} \geq 2\times 10^{-8}$  mbar. Sections 5.1 and 5.2 report the optimization of the growth conditions for developing the best ordered interfacial  $3\times 1$  layer, and to obtain possibly such ordered layer thicker as the ones described in Chapter 4. The effects of the oxygen partial pressure ( $P_{\text{O}_2}$ ) and of the substrate temperature (T) on the film structures of different thicknesses are described. For comparison, the results obtained under UHV conditions are occasionally presented again together with the new findings. On the sample showing the best interfacial layer quality, a detailed characterization of the film has been carried out. In particular, the atomic

structure of the  $(3\times 1)$  phase is of main interest and its characterization is detailed in section 5.3.

## 5.1 Growth at different oxygen partial pressure at fixed temperature

The results presented in this first section were collected on 1 nm and 2.5 nm thick Pr-oxide films grown at 550 °C in  $2\times 10^{-10}$  mbar (UHV),  $2\times 10^{-8}$  ( $1\times 10^{-8}$  for the XPS data) and  $5\times 10^{-8}$  mbar of  $O_2$ .

### 5.1.1 X-ray structural characterization at ID32

#### In-plane scans

Fig. 5.1 shows the in-plane radial H scans ( $K=0$  ;  $L=0.03$ ) for the three different  $P_{O_2}$  investigated on 1 nm thick films. The comparison of the three scans shows :

1. No signature of  $PrSi_2$  for samples grown in  $2\times 10^{-8}$  and  $5\times 10^{-8}$  mbar of  $O_2$  (the  $PrSi_2$  peaks are indicated in the bottom scan in Fig. 5.1 with arrows).
2. Peaks arising from the  $3\times 1$  superstructure in all three cases, at  $(1.33\ 0\ 0)$  and  $(2.67\ 0\ 0)$ .
3. No significant difference between the results obtained for  $2\times 10^{-8}$  mbar and  $5\times 10^{-8}$  mbar  $O_2$ .

#### Specular reflectivity and off-specular rod scans

The spectra of the specular reflectivity rod  $(00L)$  as well as the ones of the  $(20L)$  and  $(10L)$  off-specular rods have been monitored for different  $P_{O_2}$  on 1 nm thick films. Fig. 5.2 presents the corresponding results and shows the intensity distribution along these three Si rods. Fig. 5.2 (a) displays the  $(00L)$  specular reflectivity results. Compared with the film grown under UHV, the  $(00L)$  rods of the two samples prepared under  $P_{O_2}$  exhibit clear regularly spaced oscillations (Kiessig fringes), indicating smoother surfaces and film / substrate

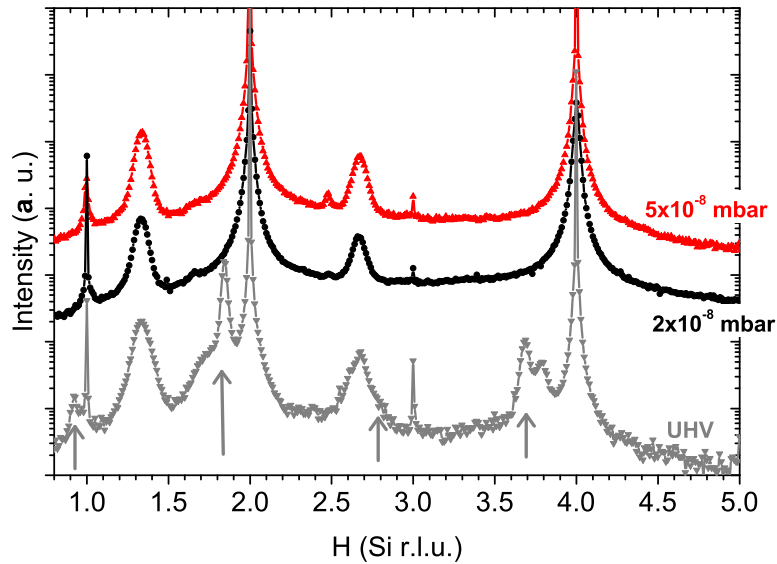


Figure 5.1: Evolution of three in-plane radial H scans ( $K = 0$  ;  $L = 0.03$ ), from UHV to  $5\times 10^{-8}$  mbar  $O_2$  and growth temperature fixed at  $550^\circ C$  on different samples with 1 nm thick Pr-oxide films. Peak intensities are presented in Log scale and the H scans are plotted in Si reciprocal lattice unit (r.l.u.). The background intensities are not removed. The arrows indicate the peaks from the  $PrSi_2$  phase.

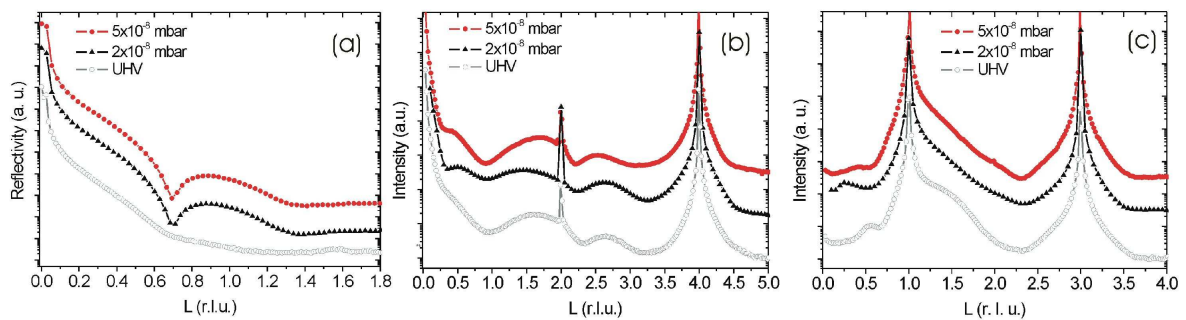


Figure 5.2: Intensity distribution along three Si rods collected from three samples with 1 nm thick Pr-oxide films grown at  $550^\circ C$  and under UHV,  $2\times 10^{-8}$  mbar and  $5\times 10^{-8}$  mbar of  $O_2$ , respectively. Peak intensities are presented in Log scale and the L scans are plotted in Si reciprocal lattice unit (r.l.u.). (a) (00L) Specular reflectivity results. (b) (20L) Si CTRs scans. (c) (10L) Si CTRs scans.

interfaces. For such thin films, the thickness estimation without quantitative modeling of the interference fringes -as previously done for the 2.5 nm thick film- is less reliable due to the difficulties in recognizing the periodicity of such long wavelength oscillations. The result observed for the film grown under UHV, with missing oscillations, can be explained by the Pr-silicide island formation, creating a rougher surface than those grown under  $P_{O_2}$ . However, the interface of the sample prepared under UHV is as smooth as those prepared in  $O_2$ , as evidenced from Figs. 5.2 (b) and (c), where the corresponding (20L) and (10L) Si CTRs, respectively, are presented. The observed intensity oscillations in the off-specular rods indicate the presence of an ordered commensurate interfacial layer, as discussed in Chapter 4. The formation of such a layer appears to be independent of the oxygen partial pressure. The high scattering intensity throughout the CTRs gives the evidence for a smooth Si/Pr-oxide interface over the pressure range of oxygen studied. Although no dramatic changes were observed, the (20L) CTRs do reveal a higher modulation amplitude when  $P_{O_2}$  increases from  $2\times 10^{-8}$  mbar to  $5\times 10^{-8}$  mbar, indicating a better ordering of the structure at the interface.

### 5.1.2 XPS and Auger results obtained at ID32

Fig. 5.3 (a) presents the evolution of the Si2p core level peak as the oxygen pressure varies from UHV to the mid- $10^{-8}$  mbar range. The bottom-most scan corresponds to a Si substrate with a native  $SiO_2$  oxide layer and is plotted as a reference. This scan was recorded at an emission angle of  $20^\circ$  while the other data were collected at an emission angle of  $45^\circ$  from three different samples with 2.5 nm thick Pr-oxide films. In Fig. 5.3 (b) the corresponding evolution of the O1s spectra is displayed.

Regarding the Si2p spectra, a main component at the binding energy around 100 eV contains two contributions corresponding to the spin-orbital split  $Si2p_{1/2}$  and  $Si2p_{3/2}$  from the Si substrate. A second component, shifting from 102.4 eV for the UHV grown sample to 102.8 eV for the sample grown in  $5\times 10^{-8}$  mbar of  $O_2$ , can be distinguished. As previously discussed in Chapter 4, this latter contribution corresponds to the chemical state of Si in a Pr-O-Si bond and can be associated with the formation of Pr-silicate. For the sample grown in  $5\times 10^{-8}$  mbar of  $O_2$  an additional component emerges at 103.8 eV and seems to suggest the formation of Si-O bonds.

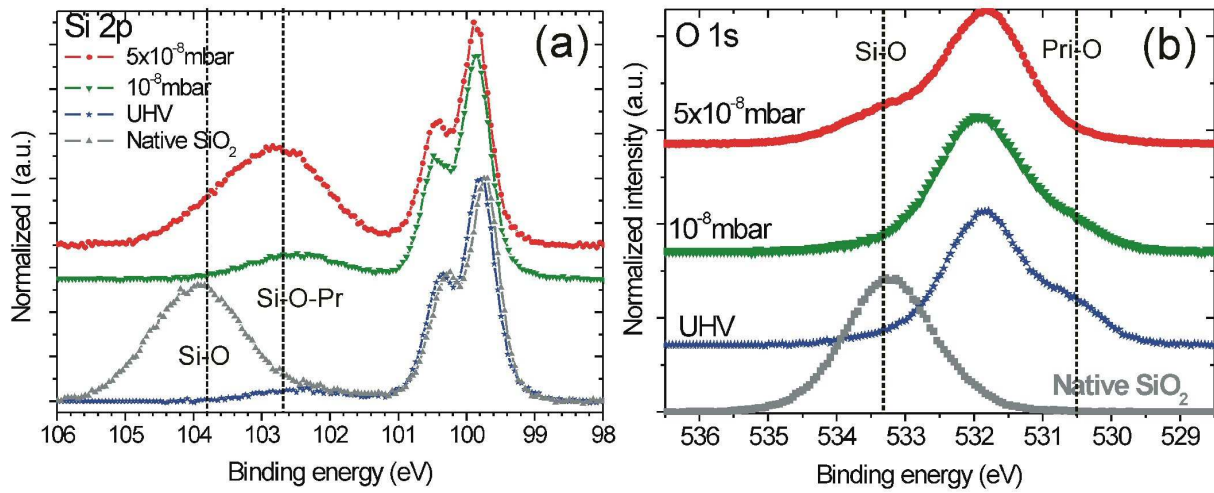


Figure 5.3: Evolution of Si2p (a) and O1s (b) spectra with varying the O<sub>2</sub> pressure from UHV to the mid-10<sup>-8</sup> mbar range. The bottom-most scan, recorded at an emission angle of 20°, corresponds to a Si substrate with a SiO<sub>2</sub> native oxide layer and is plotted as a reference. The other data were collected at an emission angle of 45° on three different samples with 2.5 nm thick Pr-oxide films. Dashed lines show the respective positions of the indicated chemical bonds, as reported in the literature ([48, 58, 122]). The intensity is normalized to the respective main peak intensity in (a) and (b).

The O1s spectra in Fig. 5.3 (b) reveals a prominent feature at 531.8 eV that can be assigned to the emission from Pr-silicate (Pr<sub>2</sub>Si<sub>2</sub>O<sub>7</sub>) [122]. Compared with the reference spectrum obtained from a SiO<sub>2</sub> native oxide layer on Si, we observe a chemical shift towards lower binding energy. As discussed in Chapter 4, this result can be explained by the increase of the negative charges on O from SiO<sub>2</sub> to Pr<sub>2</sub>Si<sub>2</sub>O<sub>7</sub>, as Pr is more electropositive than Si [58]. One additional component at  $\approx 530.5$  eV can be observed in the spectra of the samples grown under UHV and 10<sup>-8</sup> mbar of O<sub>2</sub> and it is stronger in the former case. It is attributed to the presence of Pr-O bonds and suggests the formation of Pr<sub>2</sub>O<sub>3</sub> compound [48, 58, 122]. For the sample grown in 5×10<sup>-8</sup> mbar of O<sub>2</sub> this contribution was much smaller and another weak component at higher binding energy can be observed around 533.3 eV. It corresponds to the chemical state of oxygen in a Si-O bond. This seems to indicate the presence of SiO<sub>x</sub> in the film. However it is noteworthy to underline that this sample remained one week in the UHV chamber before being characterized and on fresher similar samples this latter component was not observed. In addition, Chapter 4 has demonstrated that a post-annealing at 550 °C under UHV can eliminate this latter component.

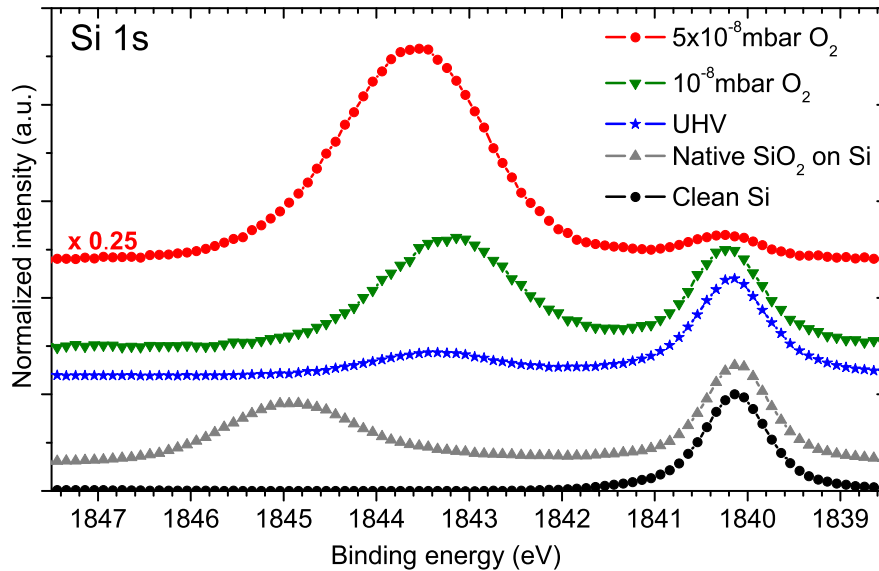


Figure 5.4: Evolution of Si1s core level spectra with varying the pressure from UHV to the mid- $10^{-8}$  mbar range. The bottom-most scan corresponds to a clean Si substrate and the second bottom-most one corresponds to another substrate with a  $\text{SiO}_2$  native oxide layer. They were recorded at an emission angle of  $20^\circ$  and are plotted for reference. The other data were collected at an emission angle of  $45^\circ$  on three different samples with 2.5 nm thick Pr-oxide films.

Since Si1s has a binding energy of 1840.12 eV, the kinetic energy of Si1s ( $\approx 0.8$  KeV) is much smaller than that of Si2p ( $\approx 2.5$  KeV). This makes Si1s much more surface sensitive than Si2p. Due to the high binding energy, Si1s is not accessible with conventional lab XPS sources or at a soft x-ray beamline. It is therefore interesting to record the Si1s spectra. Fig. 5.4 shows the evolution of Si1s core level spectra with the oxygen pressure varying from UHV to the mid- $10^{-8}$  mbar range. The bottom-most scan corresponds to a clean Si substrate and the second bottom-most one corresponds to a substrate with a  $\text{SiO}_2$  native oxide layer. The spectrum of the sample grown under  $5 \times 10^{-8}$  mbar of  $\text{O}_2$  was scaled by a factor of 0.25.

The 1840 eV component arises from the pure Si substrate contribution. Those between 1843.2 and 1843.6 eV correspond to the chemical states of Si in a Pr-O-Si bond and can be associated with the formation of Pr-silicate. Notice that both native  $\text{SiO}_2$  and Pr-silicate have larger binding energy shifts in Si1s than those observed in Si2p.

Figs. 5.5 (a) and (b) present the evolutions of Pr4d and Pr3d spectra, respectively, with the

oxygen pressure varying from UHV to the mid- $10^{-8}$  mbar range. The data were collected at an emission angle of  $45^\circ$  from three different samples with 2.5 nm thick Pr-oxide films.

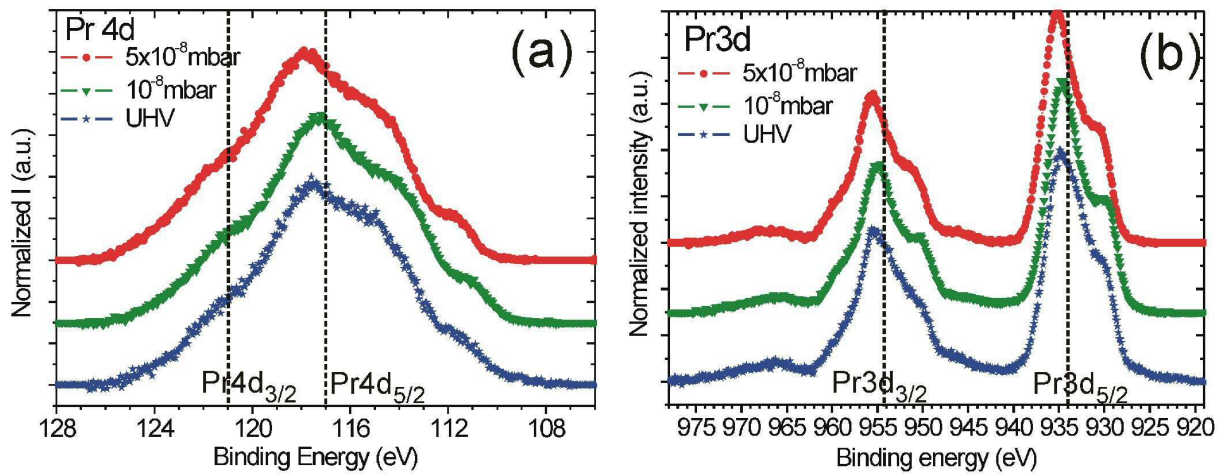


Figure 5.5: Evolution of Pr4d (a) and Pr3d (b) spectra obtained for samples for which the pressure had been varied from UHV to the mid- $10^{-8}$  mbar range. The data were collected at an emission angle of  $45^\circ$  on three different samples with 2.5 nm thick Pr-oxide films. The dashed lines correspond to the tabulated binding energy values as reported in the literature [140]. The intensities are normalized to their peak areas.

In Fig. 5.5 (a), the Pr4d spectra contain one broad component with a maximum at around 117.5 eV. In Fig. 5.5 (b), the Pr3d spectra exhibit two main components, one at around 934.6 eV and the other one at around 955.5 eV, arising from spin orbital split Pr3d<sub>5/2</sub> and Pr3d<sub>3/2</sub>, respectively. Both the Pr3d and Pr4d display very minor modifications of their line shapes when the oxygen pressure changes.

The shape of these peaks can be explained by final state effects, as demonstrated by Kotani and Ogasawara who have studied theoretically in detail the photoemission features of rare-earth oxides [141]. In the case of Pr-oxide, they show that the observed spectral shape of the Pr3d core level is largely due to the effect of hybridization between the 4f and valence states, which is promoted by the presence of a 3d core hole in the photoemission process. This hybridization results in two possible final states, which lead to the main 3d peaks and shoulders at the lower binding energy side. For the Pr4d line shape, Kotani and Ogasawara show that the effect of multiplet coupling plays a more important role. Since the Pr3d and 4d spectra in a Pr-oxide have already been broadened so much by the inter- and intra-atomic effects described by Kotani and Ogasawara, their spectral shapes appear to be insensitive to any further changes in the chemical environment, compared to

Si2p and O1s core levels. They are therefore not helpful in this study for determining the chemical composition of a Pr-oxide film.

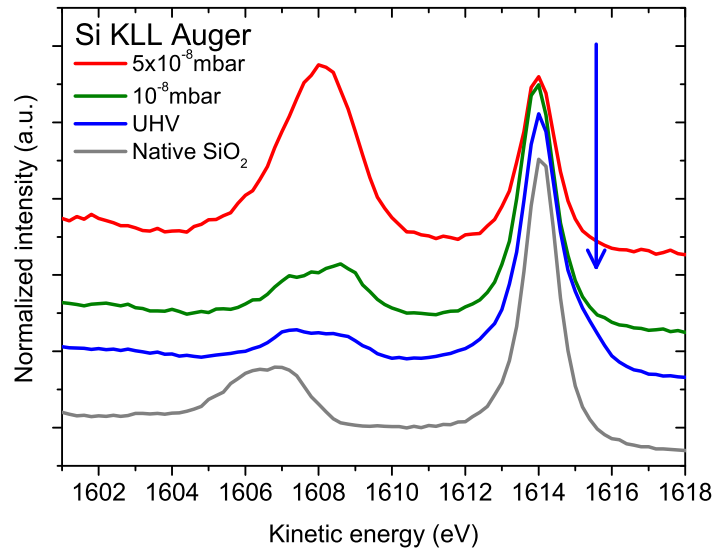


Figure 5.6: Evolution of Si KLL Auger spectra with varying the pressure from UHV to the mid- $10^{-8}$  mbar range. The bottom-most scan, recorded at an emission angle of  $20^\circ$ , corresponds to a Si substrate with a  $\text{SiO}_2$  native oxide layer and is plotted as a reference. The other data were collected at an emission angle of  $45^\circ$  on three different samples with 2.5 nm thick Pr-oxide films. No background subtraction was performed for these scans. The arrow points to a shoulder of the 1614 eV peak attributed to Pr-silicide formation.

Fig. 5.6 shows the evolution of the Si KLL lines in the Auger spectra with the oxygen pressure varying from UHV to the mid- $10^{-8}$  mbar range. The bottom-most scan corresponds to a Si substrate with a  $\text{SiO}_2$  native oxide layer and is plotted as a reference. It was recorded at an emission angle of  $20^\circ$ . The other data were collected at an emission angle of  $45^\circ$  from three different samples with 2.5 nm thick Pr-oxide films. The background intensity is not subtracted for these scans, which are normalized to the intensity of the main component around 1614 eV, for each spectrum. The arrow points to a shoulder of the 1614 eV peak on the spectrum of the sample grown under UHV and can be attributed to Pr-silicide formation, as discussed in Chapter 4. This shoulder cannot be observed for the samples grown under  $10^{-8}$  and  $5\times 10^{-8}$  mbar of  $\text{O}_2$ . Regarding the second component showing up around 1608 eV, it consistently increases with the  $P_{\text{O}_2}$  of the growth. Therefore this component could be attributed to the formation of Pr-silicate phase, which is also

consistent with a 2 eV shift toward higher kinetic energy with respect to the corresponding component in the case of a Si substrate with a SiO<sub>2</sub> layer (cf. § 4.3.2). Notice that the chemical shifts observed here in Si KLL Auger for Pr-silicate and native SiO<sub>2</sub> are nearly twice as large as what we measured in Si2p.

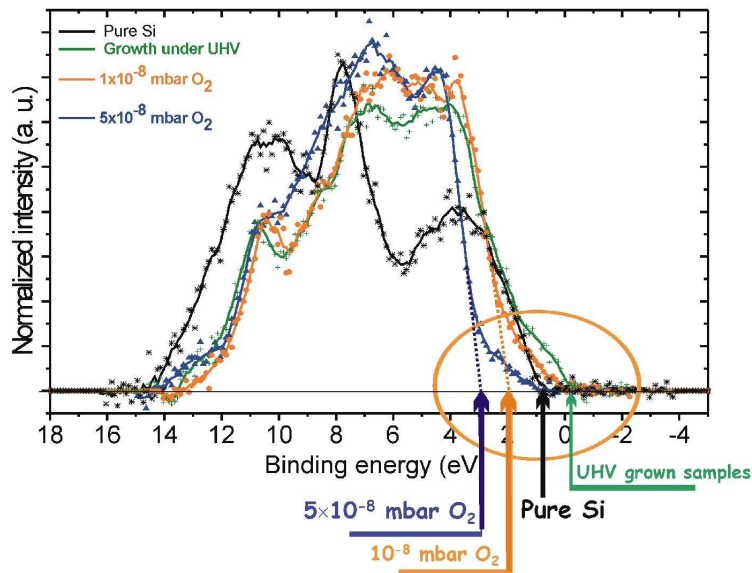


Figure 5.7: Evolution of the valence band spectra with increasing the  $P_{O_2}$ , as specified in the figure. The top-most scan corresponds to a clean Si substrate and is plotted as a reference. The other data were collected at an emission angle of  $45^\circ$  on three different samples with 2.5 nm thick Pr-oxide films.

Fig. 5.7 shows the valence band (VB) spectra for 2.5 nm thick films grown under UHV,  $10^{-8}$  mbar and  $5 \times 10^{-8}$  mbar of O<sub>2</sub>, together with the VB spectrum of pure Si. The VB spectrum of pure Si shows that the valence band maximum is  $\approx 1$  eV below the Fermi edge. As previously discussed in Chapter 4, the spectrum for the 2.5 nm film grown under UHV exhibits a much higher density of states near the Fermi edge, suggesting that the film is metallic. For the films prepared under molecular oxygen flux no density of states can be identified above the edge of the VB maximum. This finding is consistent with the formation of Pr-silicate. The valence-band offset was determined in each case by evaluating the energies of the valence-band maxima, compared with the one of pure Si. These energies were indicated by the intersection of straight lines extrapolated from the sharp rising edges of the VB spectra near the Fermi edge, as pointed out by the dotted lines and the arrows in Fig. 5.7. So the VB offsets of samples prepared in  $10^{-8}$  mbar and  $5 \times 10^{-8}$  mbar of O<sub>2</sub> are about 1 eV and 2 eV, respectively.

### 5.1.3 Characterization by AES

Fig. 5.8 shows Pr NOO, Si LMM, and O KLL lines in the AES spectra for 1 nm and 2.5 nm thick films. For the 1 nm thick samples only a slight amplitude change of the peak derivative of O KLL can be observed in Fig. 5.8(c) when  $P_{O_2}$  increases from UHV to  $5 \times 10^{-8}$  mbar, while the main component around 90 eV shown in Fig. 5.8(a) exhibits a second component at the lower kinetic energy side. For the 2.5 nm thick films (Fig. 5.8(b)), the minimum of the 90 eV component shows a clear shift from 92 to 87 eV for  $P_{O_2} \geq 2 \times 10^{-8}$  mbar. No significant difference is observed for  $P_{O_2} = 2 \times 10^{-8}$  and  $5 \times 10^{-8}$  mbar. In addition, Fig. 5.8(d) shows also clearly an increase of the main component of the O KLL lines in the AES spectrum for the 2.5 nm film when  $P_{O_2}$  increases.

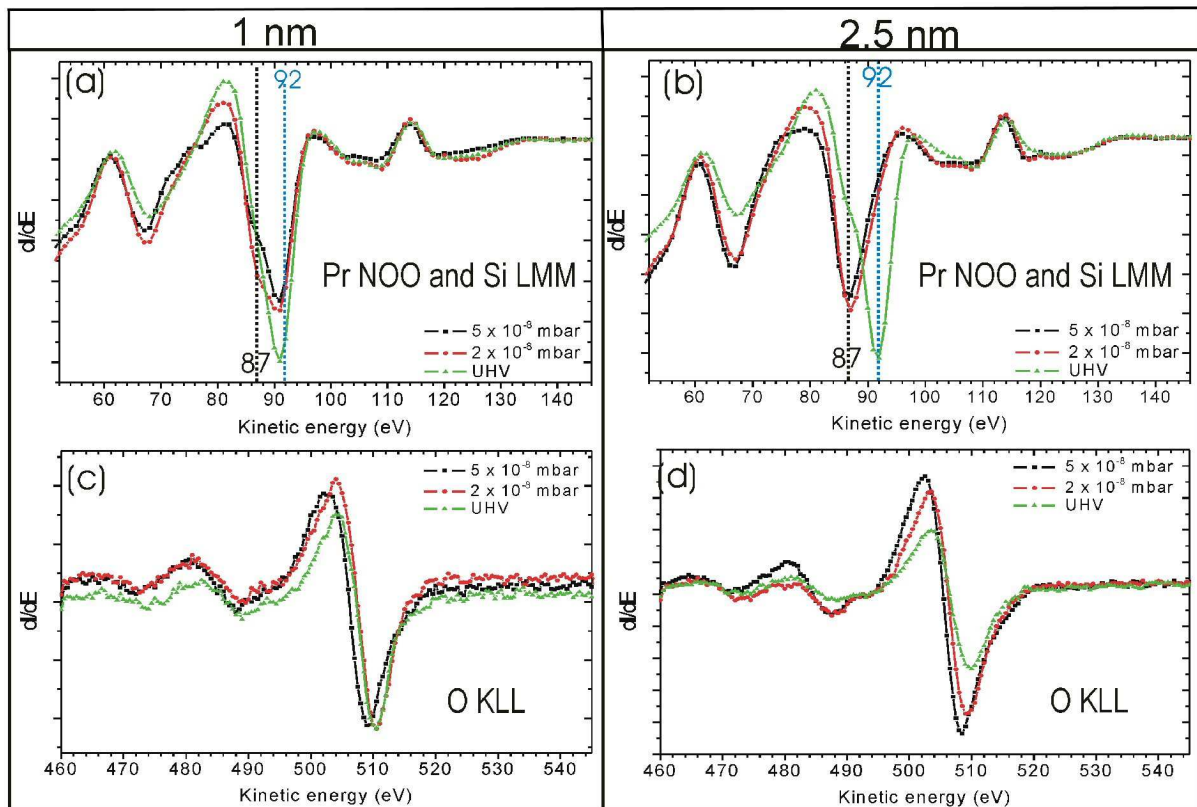


Figure 5.8: AES spectra of the Pr NOO and Si LMM lines (a) and (b) as well as the AES spectra of the O KLL lines (c) and (d), for both 1 nm (a) and (c) and 2.5 nm (b) and (d) thick films, while increasing the oxygen partial pressure for the film growth. The dash lines at 92 eV mark the main component of pure Si while the one at 87 eV indicates the one of pure Pr.

This AES study shows that :

1. The changes of the 90 eV component in the spectrum as a function of  $P_{O_2}$  is less pronounced for the 1 nm thick film than the 2.5 nm thick one. This can be attributed to the large contribution of the substrate to the 92 eV peak for the 1 nm films.
2. Since all the 2.5 nm thick samples should have roughly the same amount of Pr evaporated onto the sample surfaces, they should also show a similar contribution from Pr with the 87 eV minimum. Taking into account the various results collected in Chapter 4, the intensity reduction of the 67 and 87 eV components in the case of the UHV grown sample is due to the formation of  $\text{PrSi}_2$  islands and the large depletion areas, which reduces the total number of Pr atoms within the probing depth of the Auger electrons.
3. Growths under  $P_{O_2}$  give rise to a reduced 92 eV peak in the AES spectra, suggesting that the phase separation and Pr-silicide formation reported in Chapter 4 are largely suppressed by the use of molecular oxygen during the growth.

#### 5.1.4 Summary

The combination of XRD, XPS and AES measurements lead to the following conclusions for the samples grown at 550 °C under various  $O_2$  pressures :

1. Growth under  $P_{O_2} \geq 2\times 10^{-8}$  mbar shows no evidence of Pr-silicide phase
2. Growth under  $P_{O_2} \geq 2\times 10^{-8}$  mbar leads to a smooth film surface
3. Without additional oxygen supply silicide formation cannot be avoided
4. An ordered interfacial layer ( $3\times 1$ ) was found independent of  $P_{O_2}$

## 5.2 Growth at different T with $P_{O_2}$ fixed

To avoid the Pr-silicide formation and to optimize the crystallinity of the interfacial layer, the temperature dependence study was carried out at  $5\times 10^{-8}$  mbar of  $O_2$ . The XRD and AES results presented below were collected from 1 nm and 2.5 nm thick Pr-oxide films for 500, 550 and 590 °C. No XPS studies on growth temperature dependence were carried out for films grown in  $5\times 10^{-8}$  mbar  $O_2$ .

## 5.2.1 XRD results from the beamline

### In-plane scans

Fig. 5.9 (a) shows three in-plane radial scans along the H direction for three samples with 2.5 nm thick Pr-oxide films grown under  $5\times 10^{-8}$  mbar of  $O_2$  at growth temperatures of 500, 550 and 590 °C. The scans for the samples grown at 550 and 590 °C look qualitatively

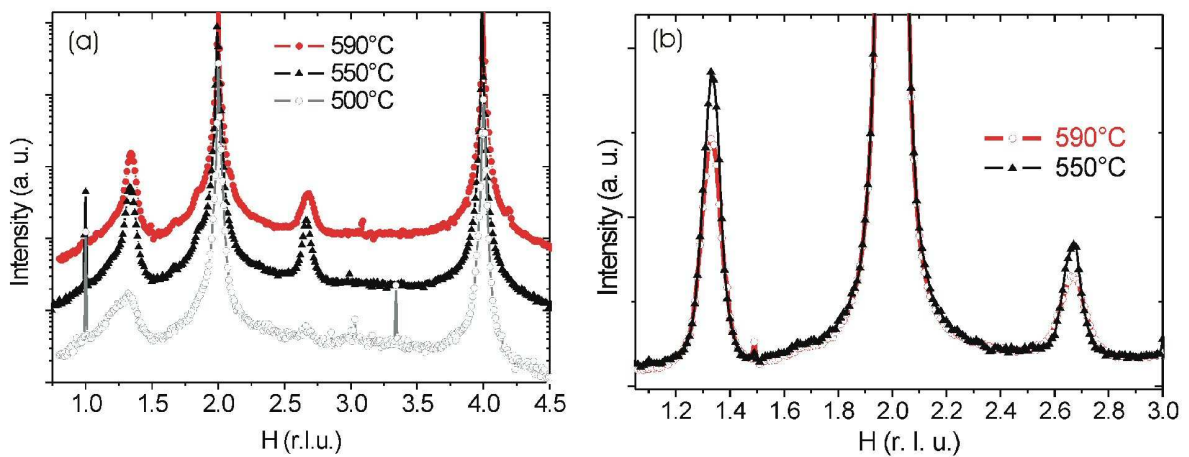


Figure 5.9: In-plane radial scans along the H direction ( $K=0$  and  $L=0.03$ ) from samples grown under  $5\times 10^{-8}$  mbar  $O_2$  and at different temperatures. The scans are in Si reciprocal lattice unit (r.l.u.). (a) Results collected on three samples with 2.5 nm thick Pr-oxide films grown at 500, 550 and 590 °C, respectively. Plot in Log scale. (b) Results collected on two samples with 1 nm thick films grown at 550 and 590 °C, respectively. Plot in linear scale. H units: Si reciprocal lattice unit (r.l.u.)

the same while the one for the sample grown at 500 °C exhibits much weaker and broader diffraction peaks from the  $3\times 1$  superstructure, at  $H \approx 1.33$  and 2.67 r.l.u. Fig. 5.9 (b) presents on a linear scale two in-plane radial scans along the H direction for two samples with 1 nm thick Pr-oxide films. The aim of this figure is to identify whether any difference is visible between 550 and 590 °C regarding the intensity and FWHM of the peaks arising from the  $3\times 1$  superstructure. Both reflections at  $H \approx 1.33$  and 2.67 r.l.u. appear slightly weaker at 590 °C than at 550 °C, while the FWHM remains constant. A similar observation can be made from Fig. 5.9 (a) for the 2.5 nm film. These results seem to suggest that high temperature does not help to promote the development of the  $3\times 1$  superstructure and the domain size does not change as indicated by the constant peak width.

### Specular reflectivity and off-specular rod scans

The evolution of the spectra of the specular reflectivity rod (00L) as well as the ones of the off-specular rods (20L) and (10L) have been monitored as a function of the growth temperature. Fig. 5.10 shows the intensity distribution along these three Si rods when the temperature varies. Fig. 5.10 (a) displays the (00L) specular reflectivity results. The

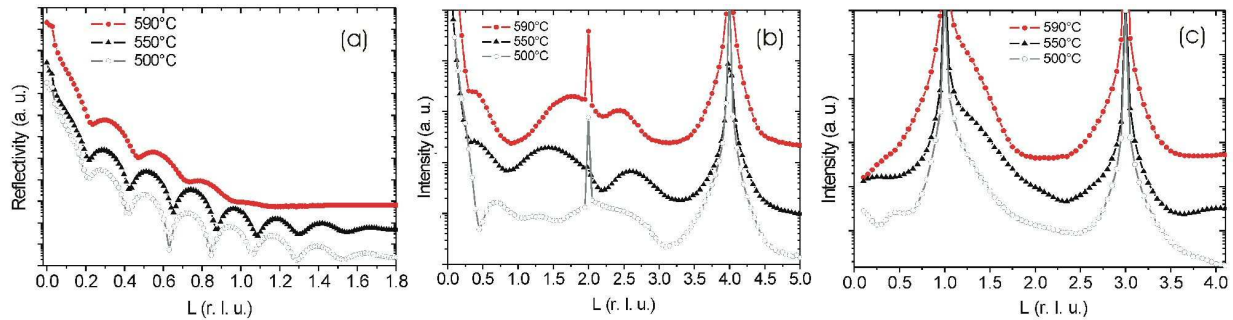


Figure 5.10: Intensity distribution along three Si rods collected from three samples with 2.5 nm thick Pr-oxide films grown under  $5\times 10^{-8}$  mbar  $O_2$  and at 500, 550 and 590 °C, respectively. Peak intensities are presented in Log scale. The L values are in Si reciprocal lattice unit (r.l.u.). (a) (00L) Specular reflectivity results. (b) (20L) Si CTRs scans. (c) (10L) Si CTRs scans.

collected data reveal well developed Kiessig fringes that are visible up to  $L \approx 1.8$  r.l.u. for the films grown at 500 and 550 °C while the scan of the sample prepared at 590 °C exhibits weaker intensity modulations that vanish at  $L \approx 1.2$  r.l.u., pointing to a rougher surface and/or film/substrate interface for the latter. It is interesting to notice that the frequency of the oscillations, and thus the film thickness, decreases systematically as the growth temperature increases, suggesting a lower sticking coefficient for films grown at the higher temperature. Figs. 5.10 (b) and (c) present the corresponding (20L) and (10L) Si CTRs. While Fig. 5.10 (a) has revealed a smooth surface and interface for the film grown at 500 °C, the off-specular rods shown in Figs. 5.10 (b) and (c), which probe the crystalline part of the film, suggest a poorly ordered interfacial layer, as evident from the small modulation amplitudes. This observation can be correlated with the weak in-plane intensity of the  $3\times 1$  peaks shown in Fig. 5.9 (a).

A comparison of the intensity distribution along the (20L) and (10L) rods, e.g. the intensity at  $L \approx 2.3$  r.l.u. in both Figs. 5.10 (b) and (c), for the samples grown at 550 and 590 °C indicates better pronounced oscillation amplitudes for the former sample. This has been confirmed by other samples grown in the same (T, P) conditions.

The corresponding results for samples with 1 nm thick films are reported in Fig. 5.11. This

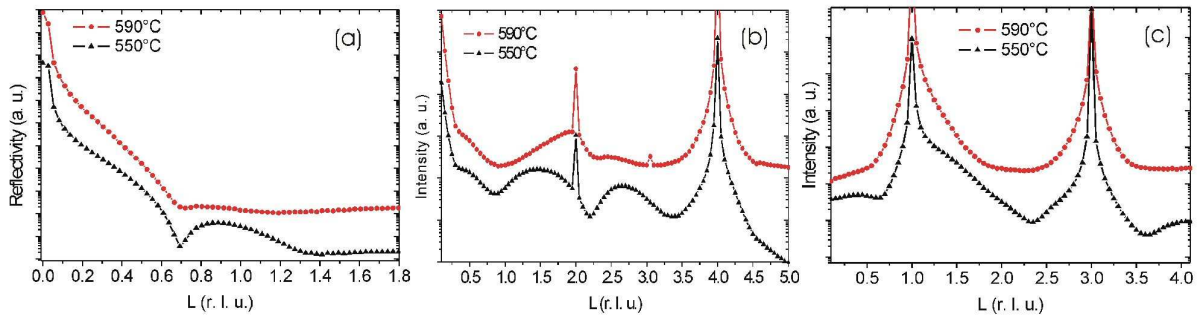


Figure 5.11: Intensity distribution along three Si rods collected from two samples with 1 nm thick Pr-oxide films grown in  $5 \times 10^{-8}$  mbar  $O_2$  at 550 and 590 °C, respectively. Peak intensities are presented in Log scale. The L values are in Si reciprocal lattice unit (r.l.u.). (a) (00L) Specular reflectivity results. (b) (20L) Si CTRs scans. (c) (10L) Si CTRs scans.

figure shows the same types of scans as those shown than in Fig. 5.10 and the observations are similar: growth at 590 °C causes the rod intensity to decrease significantly to nearly the background level at around  $L = 0.8$  and  $L = 3.3$  for the (20L) rods and  $L = 2.3$  for the (10L) one. We can then conclude from Figs. 5.10 and 5.11 that growth at 590 °C creates a much rougher interface than the growth at 550 °C while the growth at 500 °C creates a less crystalline (but still smooth) interface. The plots in Figs. 5.10 and 5.11 suggest that the quality of the interface is quite sensitive to the growth temperature over a narrow window only about 100 °C wide. An optimum growth temperature of 550 °C has been found.

## 5.2.2 Characterization by AES

In this subsection only AES results are reported. No LEED pattern could be observed on all the surfaces prepared under the above described (P, T) conditions. Fig. 5.12 reports the influence of the growth temperature on the Pr NOO, Si LMM and O KLL AES spectra for 1 nm [(a) and (c)] and 2.5 nm [(b) and (d)] thick films, for two different growth temperatures (550 to 590 °C).

It shows that the AES spectra depend much less on temperature than on  $P_{O_2}$  (compared with the spectra in Fig. 5.8). Fig. 5.12 (b) shows that for the 2.5 nm thick films the Pr NOO and Si LMM lines in the AES spectra have their peak intensity maxima all at 87 eV, with a slightly lower intensity for the one grown at 550 °C. This result suggests that

no  $\text{PrSi}_2$  island formation occurs. The disappearance of the 92 eV component for larger film thickness suggests that the 92 eV component appearing in Fig. 5.12 (a) arises from the silicon substrate, and not from Pr-silicide. Fig. 5.12 (d) presents the O KLL AES spectra for the above described samples.

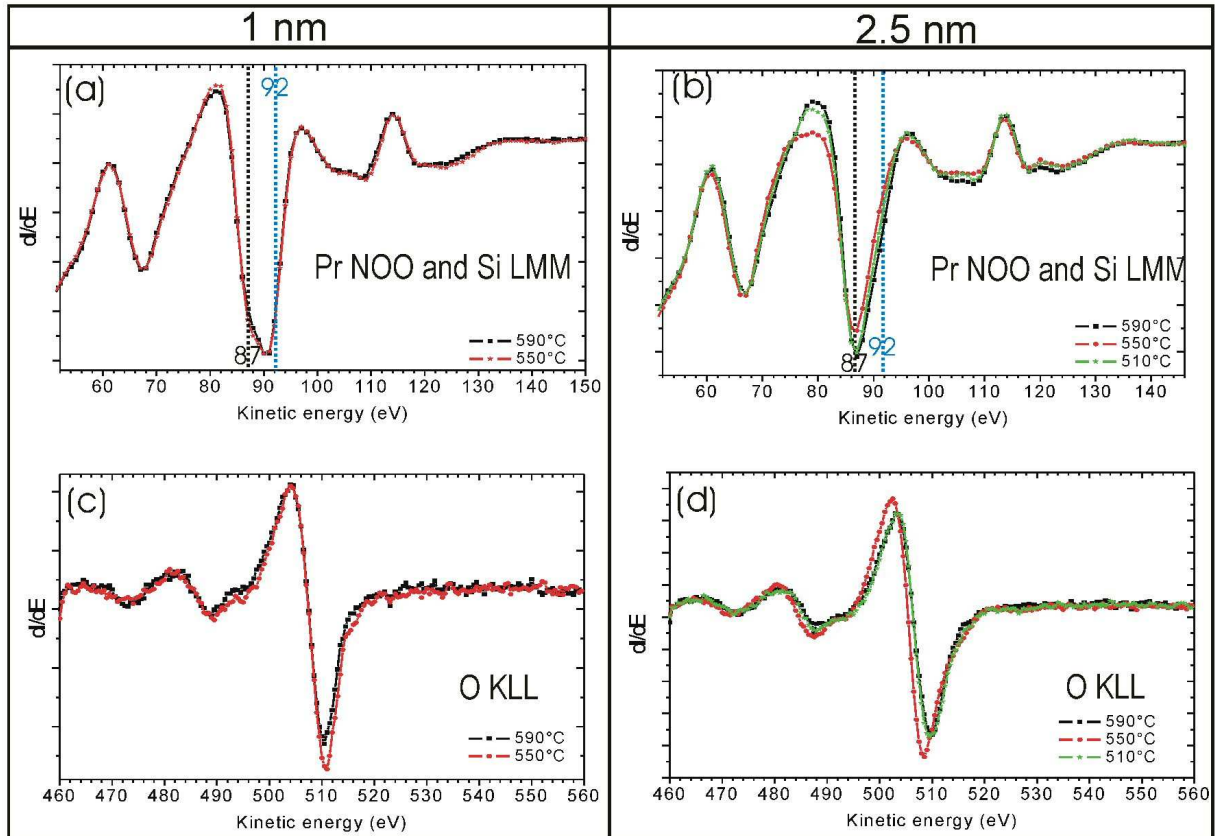


Figure 5.12: Evolution of the Pr NOO and Si LMM (a) and (b) as well as O KLL (c and d) AES spectra, for both 1 nm (a) and (c) and 2.5 nm (b) and (d) thick films with the growth temperature increasing from 510 to 590 °C.  $P_{\text{O}_2}=5\times 10^{-8}$  mbar.

The collected results seem to show that, in the studied temperature range, the oxygen content does not depend on the sample temperature since the different O KLL lines in the AES spectra are almost identical. The AES spectra presented in Fig. 5.12 also confirm the stability of the films over the growth temperature range studied.

### 5.2.3 Summary

The XRD and the AES results presented in this section have shown for samples grown under  $5\times 10^{-8}$  mbar of  $O_2$  at various growth temperatures that:

1. Growth temperature at  $500^\circ\text{C}$  leads to a poorly ordered crystalline interfacial layer
2. Growth temperature  $\geq 590^\circ\text{C}$  results in rougher surface and film / substrate interface
3. Growth temperature at  $550^\circ\text{C}$  provides crystalline and smooth film / substrate interface

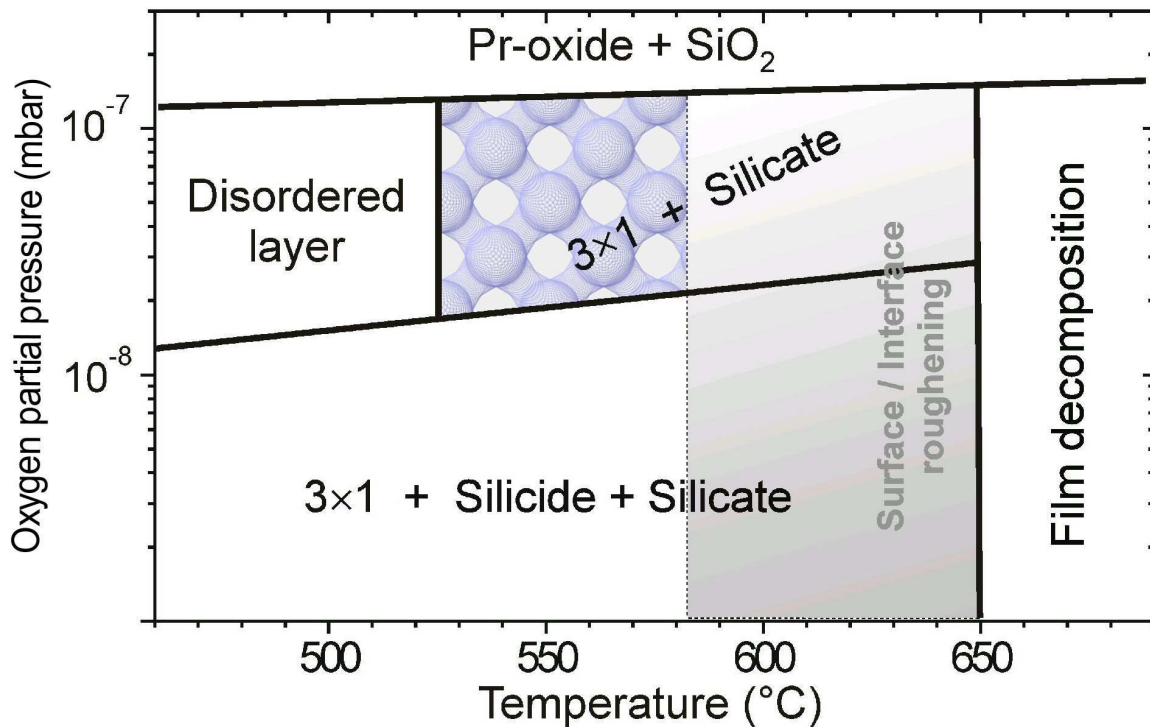


Figure 5.13: Summary of the results in form of a phase diagram plotted in the (P,T) range that was studied. The patterned area corresponds to the optimized parameters to obtain the best crystal interface quality.

Other experiments carried out in the framework of these growth investigations but not reported in this section have indicated that:

1. For growth temperatures above  $650^\circ\text{C}$ , the sticking coefficient of Pr-oxide drops to nearly zero, as the collected results (LEED, AES and XRD mainly) on these samples indicate virtually clean Si surfaces.

2. XRD experiments performed on samples grown at 590 °C in  $2 \times 10^{-8}$  O<sub>2</sub> have revealed the presence of Pr-silicide phase.

Fig. 5.13 presents a summary of the results presented in sections 5.1 and 5.2 in form of a phase diagram plotted over the (P,T) range that we have investigated.

### 5.3 Short summary on the growth optimization

From the results presented in sections 5.1 and 5.2 the required growth conditions to get the best interfacial layer regarding the ordering of the 3×1 phase, the roughness of the surface and interface, and the absence of any silicide phase in the film are (i) a growth temperature of 550 °C and (ii) an oxygen partial pressure of  $5 \times 10^{-8}$  mbar.

Our studies have also shown that the growth conditions that produce such an optimized interfacial layer are limited to a rather narrow (P, T) range. Further experiments, not reported here, were performed to identify for instance (i) the influence of the growth rate on the crystalline quality of the films or (ii) the effect of a pre-oxidized Si(001) surface on the suppression of PrSi<sub>2</sub> phase formation. It was found that (i) an increase of the growth rate (ten times the one used in this study) seemed to lead to rougher interfaces, as deduced from XRD measurements ; (ii) the AES and XRD results collected from samples pre-oxidized with 120 Langmuir of O<sub>2</sub> revealed that these attempts were not successful in preventing the phase separation and PrSi<sub>2</sub> formation.

### 5.4 Characterization of films prepared by optimized growth conditions

In this last section the results of a detailed characterization study of films grown at 550 °C and under  $2 \times 10^{-8}$  and  $5 \times 10^{-8}$  mbar of O<sub>2</sub> is discussed. Our objective is to determine the layer sequence and clarify the nature of the 3×1 superstructure, which is always present at the interface. Finally, the atomic structure identification of the Pr-oxide/Si(001) 3×1-ordered interface are reported.

### 5.4.1 LEED, STM and AES results from the Lab

#### LEED and STM results

A combined LEED and STM study has been performed at different stages on one sample while the oxide coverage increases progressively. The films were grown at  $550^\circ\text{C}$  in  $2\times 10^{-8}$  mbar of  $\text{O}_2$ . Five different coverages have been studied, with film thicknesses ranging from 0.08 nm to about 2 nm, as estimated from the growth rate calibrated by a QCM. The STM and LEED results are reported in Fig. 5.14 and Table 5.1 summarizes the main growth parameters corresponding to each images in Fig. 5.14.

<i>Samples</i>	<i>a1 and a2</i>	<i>b1 and b2</i>	<i>c1 and c2</i>	<i>d</i>	<i>e</i>
Thickness (nm)	0.08	0.16	0.32	1	2
$\text{P}_{\text{O}_2}$ (mbar)	$2 \times 10^{-8}$				
T ( $^\circ\text{C}$ )	550				

Table 5.1: List of samples presented for the LEED and STM study.

The image in Fig. 5.14 (a1) reveals the formation of cluster-like deposits for 0.08 nm of oxide coverage. At such low coverage the LEED pattern (not shown) looks like the one of the clean Si(001) surface, such as the one presented in Fig. 4.2, with slightly higher background intensity. The top inset in Fig. 5.14 (a1) shows a similar scale image and indicates (i) the presence of more or less rectangular dark areas (holes) with an average size of  $15\times 5$  nm<sup>2</sup>; (ii) brighter areas looking cluster-like.

The higher resolution STM topograph presented in Fig. 5.14 (a2) shows in even greater detail the surface morphology of the Si surface after the growth and resolves the dimer rows of the  $2\times 1$  reconstruction of the Si(001) surface between the oxide clusters, which appear brighter in the topograph. The shape of these clusters is not clearly defined.

A typical line profile of such a surface is presented in the bottom inset of Fig. 5.14(a2). The areas marked by the first (left-most) and the third arrows share the same height that corresponds to the silicon dimer rows along the  $[1\bar{1}0]$  direction. The height difference between the areas marked by the left-most and the second arrows corresponds to a Si atomic

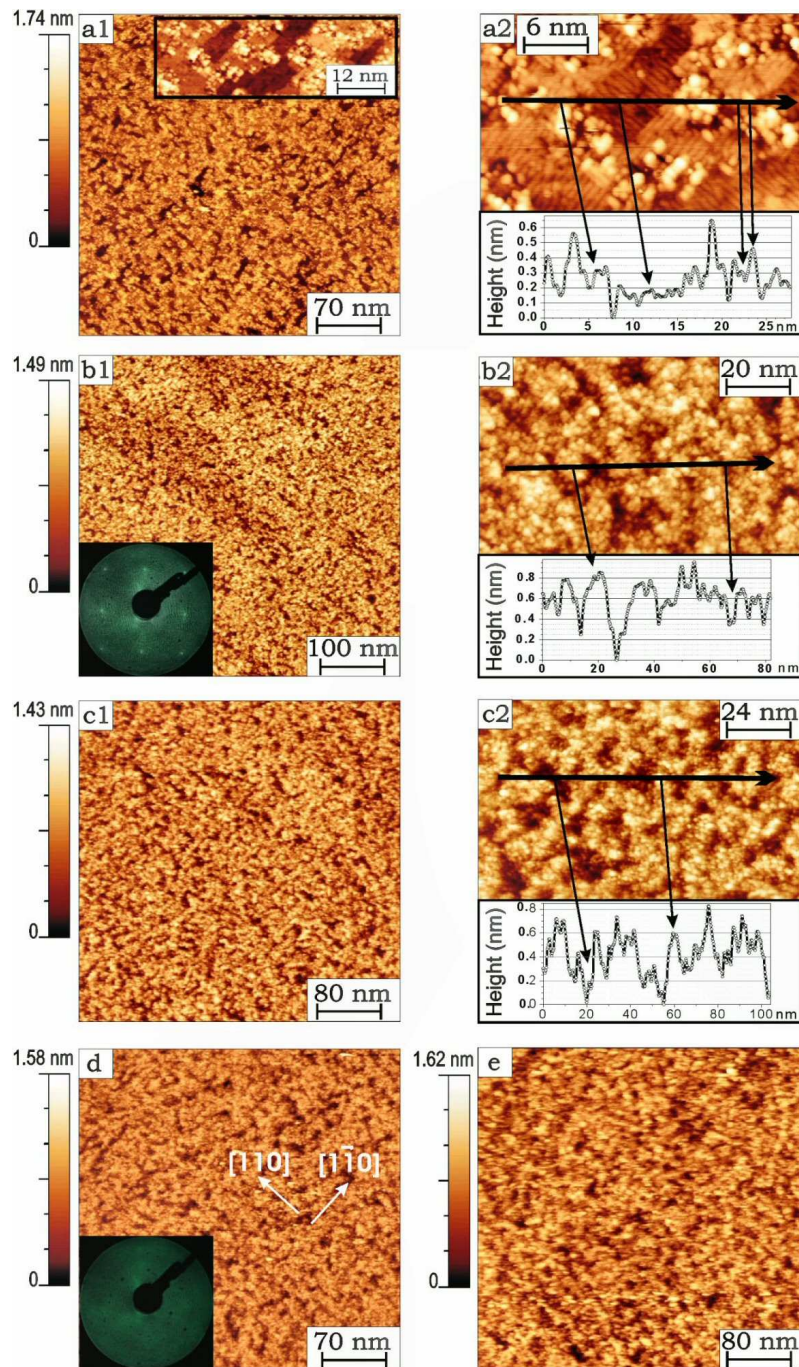


Figure 5.14: High resolution STM topographs of the growth of Pr<sub>2</sub>O<sub>3</sub> on Si(001) at  $2 \times 10^{-8}$  mbar complemented by 2 LEED patterns at 53 eV and line profiles. Measurements performed at room T under UHV. (a1) Deposited thickness: 0.08 nm.  $350 \times 350$  nm<sup>2</sup>,  $U_s = 2.00$  V,  $I = 0.50$  nA. Top insert : Zoom-in on the same surface.  $60 \times 20$  nm<sup>2</sup>,  $U_s = 2.00$  V,  $I = 0.50$  nA; (a2) Same coverage as (a1).  $30 \times 20$  nm<sup>2</sup>,  $U_s = 2.00$  V,  $I = 0.50$  nA. Bottom: line profile across (a2); (b1) Deposited thickness: 0.16 nm.  $500 \times 500$  nm<sup>2</sup>,  $U_s = 2.80$  V,  $I = 0.40$  nA; (b2) Same coverage as (b1).  $100 \times 60$  nm<sup>2</sup>,  $U_s = 2.80$  V,  $I = 0.37$  nA. Bottom: line profile across (b2); (c1) Deposited thickness: 0.32 nm.  $400 \times 400$  nm<sup>2</sup>,  $U_s = 3.00$  V,  $I = 0.50$  nA; (c2) Same coverage as (c1).  $120 \times 75$  nm<sup>2</sup>,  $U_s = 2.00$  V,  $I = 0.50$  nA. Bottom: line profile across (c2); (d) Deposited thickness: 1 nm.  $350 \times 350$  nm<sup>2</sup>,  $U_s = 4.00$  V,  $I = 0.20$  nA; (e) Deposited thickness: 2 nm.  $400 \times 400$  nm<sup>2</sup>,  $U_s = 4.50$  V,  $I = 0.10$  nA.

step ( $\approx 0.14$  nm). The dimer rows visible under the second arrow are indeed aligned along the  $[110]$  direction. As already observed in the UHV growth case (cf. § 5.2.1), the presence of small domains in Fig. 5.14(a2) containing dimer rows aligned in two perpendicular directions indicates that silicon reacts with Pr-oxide. This reaction removes some of the silicon atoms in the topmost layer and leads to small patches of holes separated by atomic steps. The height difference between the areas marked by the third and the right-most arrows corresponds to the height of the oxide species on top of the  $[1\bar{1}0]$  oriented Si dimer rows, i.e.  $\approx 0.17$  nm. No preferential growth orientation can be identified from Fig. 5.14(a2). However, it is interesting to notice that apparently no oxide species can be observed in the depleted dark areas (holes).

Fig. 5.14(b1) shows both a  $500\times 500$  nm<sup>2</sup> STM topograph and the corresponding LEED pattern characterizing a surface covered with a 0.16 nm film. No particular ordering can be identified. Dark and bright areas coexist on the surface and correspond to holes and oxide deposits, respectively. The surface remains smooth and easy to image by STM at this coverage. The corresponding LEED pattern in the inset shows blurred weak  $1\times 1$  spots, which have been broadened by the oxide growth. This indicates a pseudomorphic overlayer but not very well ordered as the intensity of the spots have been damped. A closer look at this surface can be seen in Fig. 5.14(b2). This image shows that the oxide clusters have coalesced with each others. The Si dimer rows cannot be resolved in Fig. 5.14(a2). The line profile in the bottom inset of Fig. 5.14(b2) gives an indication of the roughness level of this surface. The right arrow indicates the height level of the bare Si substrate while the left one indicates the average height of the oxide species at this coverage. The height difference is about 0.4 nm.

Fig. 5.14(c1) presents a  $400\times 400$  nm<sup>2</sup> STM topograph showing the surface morphology of a sample covered with 0.32 nm of Pr-oxide. The morphology looks very similar to the one presented in Fig. 5.14(b1) and no clear evolution of the dark area (hole size) and the oxide clusters can be identified, even the roughness remains to be of the same order of magnitude. A closer look at this surface in Fig. 5.14(c2) reveals the same patches of holes, maybe slightly denser, than on Fig. 5.14(b2). The line profile in the bottom inset of Fig. 5.14(c2) reveals a roughness level on this surface comparable with the one observed in Fig. 5.14(b2). The left arrow indicates a hole while the right one points out the average height of the oxide species at this coverage. The height difference is again about 0.4 nm.

Fig. 5.14(d) shows both the  $350\times 350$  nm<sup>2</sup> large scale STM topograph and the corresponding

LEED pattern of a 1 nm thick Pr-oxide layer. At this coverage it becomes difficult to obtain good tunneling conditions and image the surface properly with the STM, even if the roughness, suggested by the color scale on the left hand side of the image, did not change very much from Fig. 5.14(c1). No spots are visible on the LEED pattern (inset), suggesting a disordered Pr-oxide surface.

A subsequent deposition was carried out on the previous sample in order to double the film thickness (2 nm) and Fig. 5.14(e) presents a  $400\times 400$  nm<sup>2</sup> STM topograph of the corresponding surface. We did not manage to adjust the tunneling conditions (bias and current) to obtain sharper STM topographs. Nevertheless, one can see that the roughness level is similar to that in Fig. 5.14(d).

### AES results

Fig. 5.15 shows the evolution of the electron excited AES spectra with the film thicknesses increasing from 0.16 nm to 2.5 nm. The growth temperature and oxygen pressure were chosen as 550 °C and  $5\times 10^{-8}$  mbar, respectively.

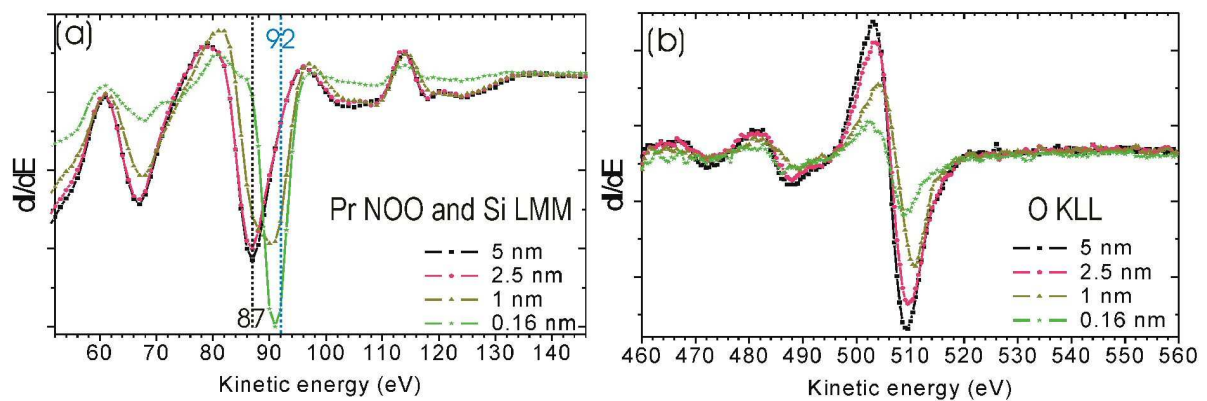


Figure 5.15: Evolution of the Pr NOO and Si LMM (a) as well as O KLL (b) AES spectra, with increasing film thickness from 0.16 nm to 2.5 nm with growth temperature and pressure fixed at 550 °C and  $5\times 10^{-8}$  mbar, respectively. The dashed line at 87 eV marks the energy of the main Pr component and the one at 92 eV indicates the main Si component.

Fig. 5.15(a) presents the Pr NOO and Si LMM AES spectra. For the 0.16 nm thick film the main component in the 85-95 eV energy range is around 91 eV and is attributed to the contribution of the Si substrate, which is dominant for such a low coverage. For the

1 nm thick film the contribution around 91 eV becomes weaker and a shoulder appears at 87 eV, the energy of the main Pr Auger component (position marked with a dashed line).

Unlike the spectra reported for films grown under UHV in Fig. 4.7 (a), where the energy of the main peak shifts back toward 92 eV as the film grows beyond 1 nm, here the minima of the main components for both 2.5 nm and 5 nm thick films appear at 87 eV, which is attributed to Pr in silicate, as discussed in section 4.1.1. These two thickest films show no intensity difference while the film thickness is doubled. As in both cases the measurements are mostly sensitive to the top of the oxide films, due to the limited escape depth of the Auger electrons, this suggests an homogenous and identical composition of the films when the thickness increases from 2.5 to 5 nm.

Fig. 5.15 (b) shows the O KLL AES spectra for the corresponding samples, from 0.16 nm to 5 nm oxide coverage. This figure indicates a continuous increase of the O KLL peak to peak intensity maximum and thus demonstrates the systematic increase of the amount of oxygen for the different samples when the film thickness increases, in strong contrast with the UHV preparation case (see Fig. 4.7 (b)). The larger escape depth of the O KLL AES electrons allows us to detect the increase of the oxygen coverage even for the films thicker than 2.5 nm.

## 5.4.2 XRD characterization at the beamline

This subsection will give results of further investigation of the structure of the stacking in the Pr-oxide film, followed by the discussion of the structure of the ordered Pr-oxide interfacial layer. The structural analysis is based on x-ray specular reflectivity, in-plane scans and a large data set of off-specular CTRs.

### In-plane and off-specular scans

Fig. 5.16 shows two off-specular (20L) CTRs, for a 2.5 and a 1 nm thick films. The intensity modulations between the two main Si Bragg reflections, which are due to the interference between an ordered, commensurate layer and the Si substrate, exhibit the same periodicity for the 1 and the 2.5 nm thick films. This suggests that this ordered layer is confined to the

interface. From the periodicity an average thickness of 0.4 nm is estimated for the ordered interfacial layer (cf. Eq. 2.14).

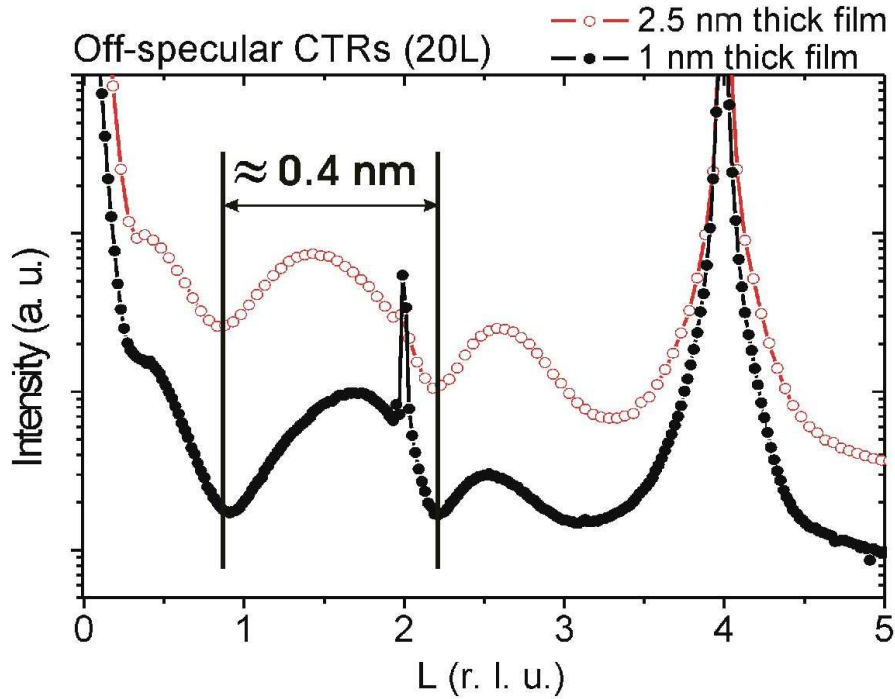


Figure 5.16: Two off-specular (20L) CTRs, for a 2.5 and a 1 nm thick films. Peak intensities are presented in Log scale. The L values are in Si reciprocal lattice unit (r.l.u.).

Fig. 5.17 shows two in-plane radial scans along the H direction for the 1 nm and 2.5 nm thick films. In addition to the two very intense in-plane Bragg peaks from the Si substrate appearing at  $H = 2$  and  $H = 4$ , two  $3\times 1$  reflections are visible in each scan, one at  $H \approx 1.33$  and the other one at  $H \approx 2.67$ . The sharp peak at  $H = 1$  corresponds to the tail of a Si CTR (Bragg reflection at higher L value). Interestingly the intensities of these  $3\times 1$  peaks do not increase when the total oxide film thickness increases. This result is consistent with the data presented in Fig 5.16. Fig 5.16 and 5.17 together suggest that a  $3\times 1$  superstructure exists at the Pr-oxide/Si(001) interface with a layer thickness of 0.4 nm, and beyond this thickness a disordered film develops on top of the interfacial layer.

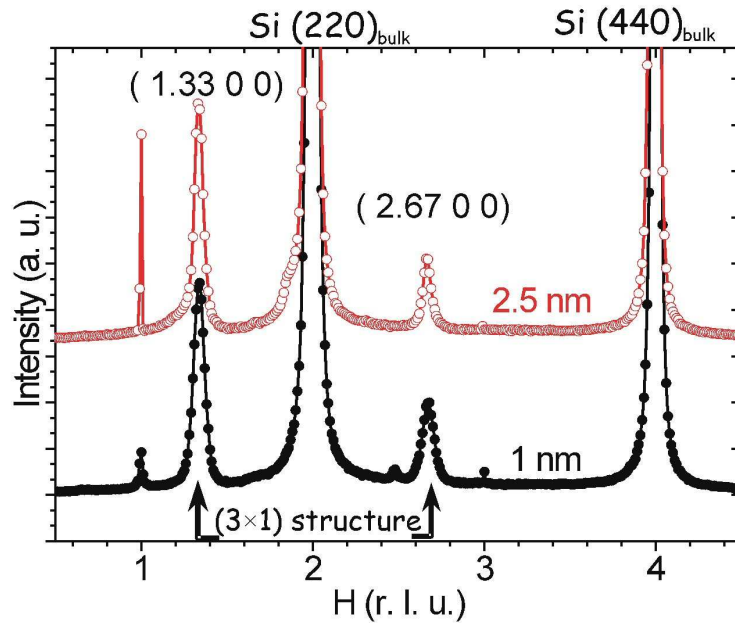


Figure 5.17: Two in-plane radial scans along the H direction, at  $K=0$  and  $L=0.03$ , for a 2.5 and a 1 nm thick films. Peak intensities are presented in linear scale. The H values are in Si reciprocal lattice unit (r.l.u.).

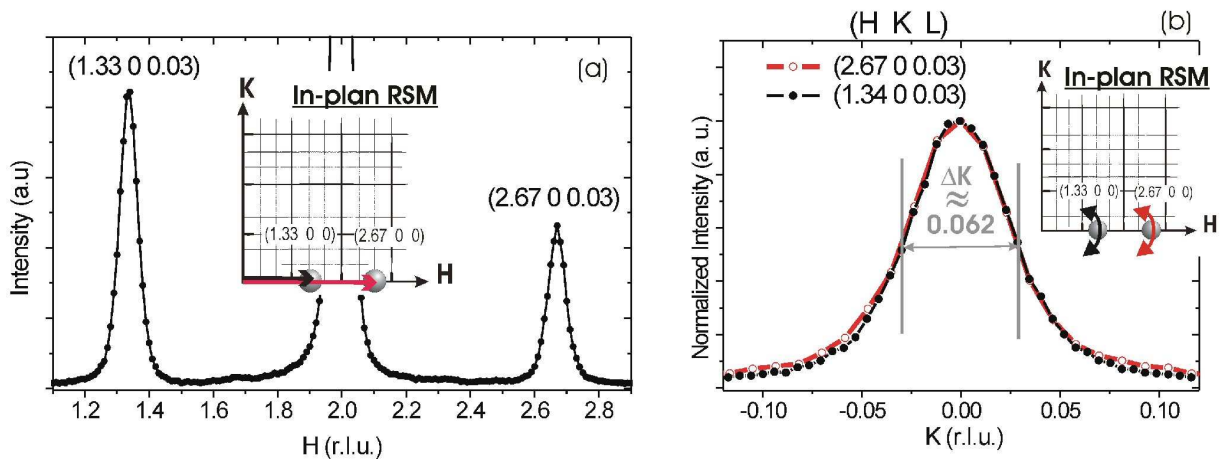


Figure 5.18: (a) In-plane radial scan along the H direction, at  $K=0$  and  $L=0.03$ , for a 1 nm thick film. The sketchy RSM in inset shows only the two  $3 \times 1$  reflections of interest. Peak intensities are presented in linear scale. The H and K values are in Si reciprocal lattice unit (r.l.u.). (b) Rocking scans across the two in-plane  $3 \times 1$  reflections presented in Fig. 5.18 (a), as shown in the top right hand corner inset.

The in-plane domain size of this  $3 \times 1$  superstructure was estimated for the 1 nm thick film by rocking scans across strong in-plane fractional-order reflections that are close to

the origin of the reciprocal space (small H and K). Fig. 5.18 (a) shows an in-plane radial scan along the H direction, at  $K=0$  and  $L=0.03$ , for the 1 nm thick film. The peak widths of the two  $3\times 1$  reflections appearing at  $H\approx 1.33$  and  $H\approx 2.67$  were measured. The corresponding rocking curves versus K are presented in Fig. 5.18 (b). From the FWHM  $\Delta K$  of the  $(1.33\ 0\ 0)$  rocking curve a domain size of about 6.2 nm is estimated, using Eq. 2.13. As the  $(2.67\ 0\ 0)$  rocking curve shows a nearly identical width to the  $(1.33\ 0\ 0)$  one, we can conclude that the measured widths of the  $3\times 1$  reflections are mainly contributed by the domain size of the  $3\times 1$  phase, which has a negligible in-plane mosaicity.

As remarks :

1. Rocking scans across other in-plane  $3\times 1$  reflections along different (H,K) directions have revealed similar domain sizes.
2. The large angular widths of the  $3\times 1$  reflections, which are due to the small domain size of the phase, have made it essentially impossible to collect the integrated intensities along the rods.

### Reflectivity measurements

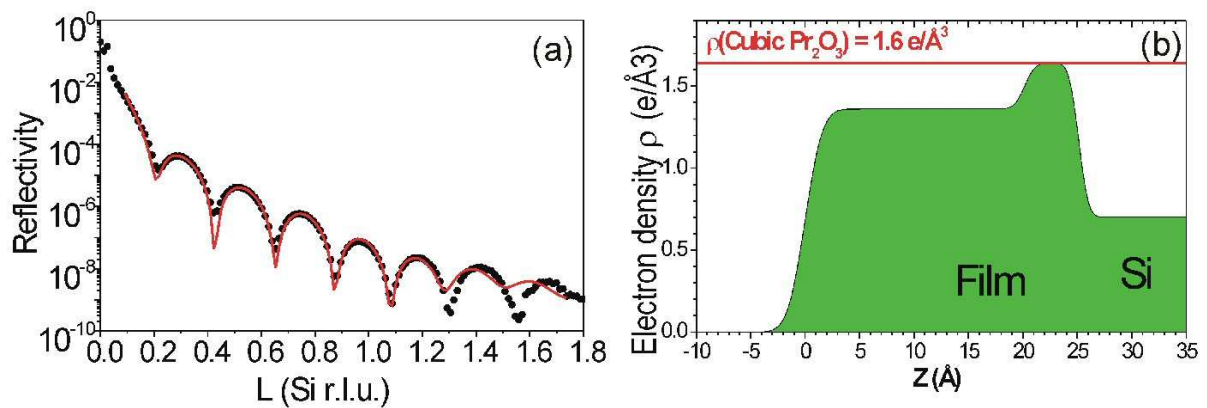


Figure 5.19: Analysis of the reflectivity measurements performed on a 2.5 nm thick sample. (a) The black points are the experimental data and the red curve is the result of the best fit obtained by assuming the electron density profile presented in (b).

Reflectivity measurements were performed on different Pr-oxide films. In the analysis of these measurements only the double-layer model has been considered, as presented in § 2.5.3. From these quantitative analysis, the electronic densities of the layers, their

individual thicknesses, and the roughness of the interfaces were retrieved. In this subsection the results for two films with nominal thicknesses of 2.5 and 1 nm are reported, together with their simulations using Eq. 2.5.

Fig. 5.19 (a) shows the reflectivity measurements performed on a 2.5 nm thick sample. The black points are the experimental data with the background intensities already subtracted. To measure this background intensity we went off the specular rod to both sides by a small in-plane Q vector and then repeated the reflectivity scan. The red curve is the result of the best fit and the deduced electron density profile is presented in Fig. 5.19 (b).

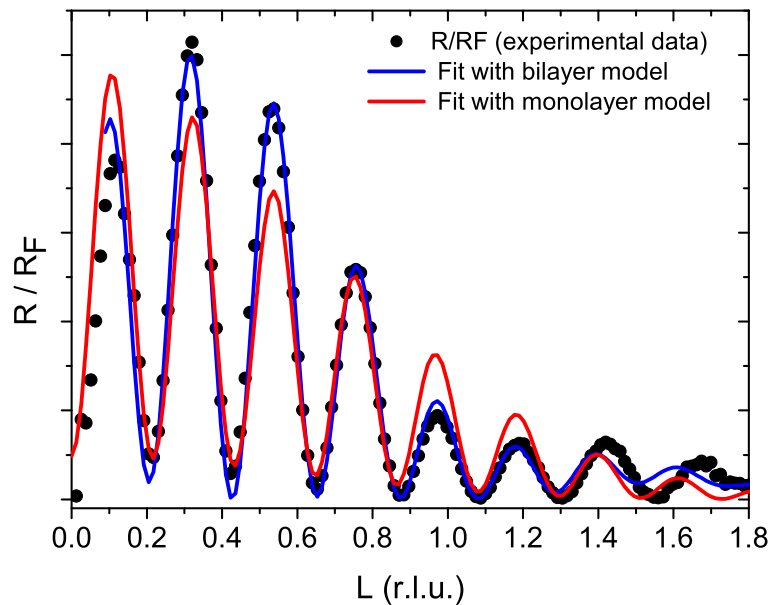


Figure 5.20: Data points of the experimental reflectivity curve ( $R$ ) in Fig. 5.19 (a) divided by the Fresnel reflectivity ( $R_F$ ) together with two fit results assuming either a single layer model (red) or a bilayer one (blue).

To get such a fit a bilayer sequence was assumed. The use of two distinct layers in the simulation was motivated by the presence of two different periodicities in the Kiessig fringes, which can be more easily identified if the Fresnel reflectivity, describing the contribution from the substrate, is removed from the measured reflectivity curve. As presented in Fig. 5.20, it is shown that a monolayer model is not appropriate to fit the  $\frac{R}{R_F}$  data, while a bilayer one agreed much better with the intensity modulations observed.

The parameters optimized by the fitting routine and used to produce Fig. 5.19 (b) are summarized in Table 5.2 (see Fig. 2.17 for the definitions of all the fitting parameters), where  $\sigma$ 's are the roughnesses of the interfaces, the  $\rho$ 's correspond to the electron densities of the layers and  $t$ 's are the thicknesses. The analysis shows that the film has atomically sharp interfaces and a flat surface. The other parameters show that the oxide film consists of:

1. An interfacial thin film, directly on top of the Si substrate, with a thickness around 0.5 nm and an electron density of  $\approx 1.6 \text{ e}^-/\text{\AA}^3$ , close to the one of bulk cubic  $\text{Pr}_2\text{O}_3$ ;
2. Above this first layer, a much thicker one, around 2 nm, with a lower electron density  $\approx 1.4 \text{ e}^-/\text{\AA}^3$ , which is close to the bulk value of  $\text{Pr}_2\text{Si}_2\text{O}_7$ .

Parameters	Bilayer model	Single-layer model
$\sigma_0$ ( $\text{\AA}$ )	$1.26 \pm 0.06$	$0.96 \pm 0.0$
$\sigma_1$ ( $\text{\AA}$ )	$0.75 \pm 0.16$	$0.87 \pm 0.15$
$\sigma_2$ ( $\text{\AA}$ )	$0.69 \pm 0.04$	—
$\rho_1$ ( $\text{e}^-/\text{\AA}^3$ )	$1.36 \pm 0.01$	$1.45 \pm 0.01$
$\rho_2$ ( $\text{e}^-/\text{\AA}^3$ )	$1.64 \pm 0.02$	—
$t_1$ ( $\text{\AA}$ )	$20.17 \pm 0.10$	$25.14 \pm 0.08$
$t_2$ ( $\text{\AA}$ )	$4.96 \pm 0.11$	—

Table 5.2: List of the parameters optimized by the fitting routine for the 2.5 nm thick film.  $\sigma$ 's are the roughness coefficients of the interfaces, the  $\rho$  correspond to the electron densities of the layers and  $t$  are the thicknesses.

Note that by introducing more layers in the simulation a better fit can be obtained. However our goal was to use the simplest model to explain the collected data. A similar analysis was performed on the reflectivity measurement carried out on a 1 nm thick sample.

Fig. 5.21 (a) shows the reflectivity scan for the 1 nm sample together with the best fit to the data. The deduced electron density is presented in Fig. 5.21 (b). For such a thin layer it is not really possible to clearly distinguish the top-most layer. Thus the thickness estimation contains larger uncertainties.

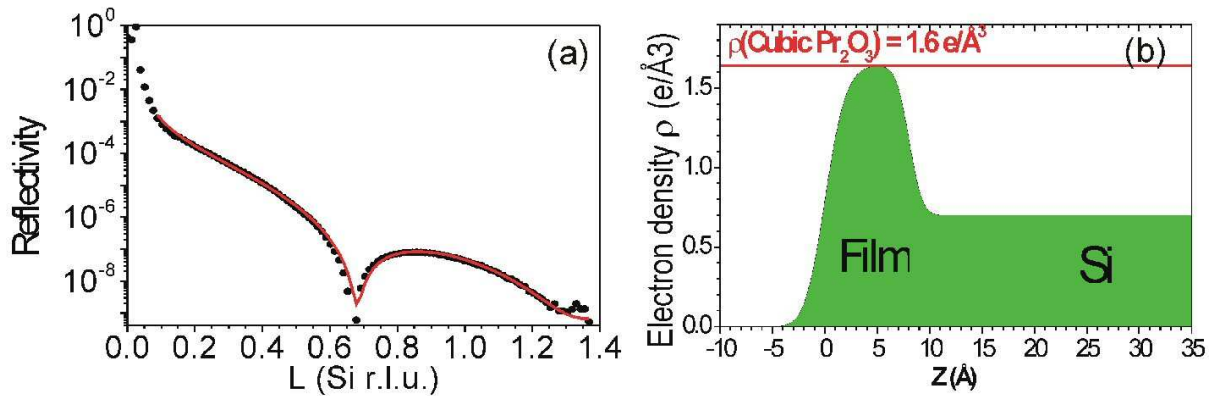


Figure 5.21: Analysis of the reflectivity measurements performed on a 1 nm thick sample. (a) Both experimental (black points) and simulated data (red curve). (b) Electron density profile used to fit the data.

Table 5.3 summarizes the parameters optimized by the fitting routine for this sample. In order to obtain reliable result,  $t_2$  and  $\rho_2$  have been fixed to the values found for the interfacial layer in the case of the 2.5 nm thick film. Therefore the parameters explaining our data are in this case more model dependent. The best fit under this model is described by the parameters in Table 5.3.

Parameters	Bilayer model
$\sigma_0$ ( $\text{\AA}$ )	$1.50 \pm 0.08$
$\sigma_1 = \sigma_2$ ( $\text{\AA}$ )	$0.99 \pm 0.07$
$\rho_1$ ( $e^-/\text{\AA}^3$ )	$1.59 \pm 0.04$
$\rho_2$ ( $e^-/\text{\AA}^3$ )	<i>Fixed at 1.64</i>
$t_1$ ( $\text{\AA}$ )	$3.04 \pm 0.05$
$t_2$ ( $\text{\AA}$ )	<i>Fixed at 5</i>

Table 5.3: List of the parameters optimized by the fitting routine for a 0.8 nm (nominal 1 nm) thick film.

Thus, a total film thickness of 0.8 nm was concluded (nominal film thickness of 1 nm). Regarding the roughnesses they are in the same order of magnitude as in the case of the 2.5 nm thick film. The electron density of the top layer is in this case much closer to the value of the interfacial layer.

### In-plane Patterson map

To study the interfacial layer, ideally it would be very useful to collect a 3D data set based on the  $(3\times 1)$  fractional order rods, which contain the complete structural information of the  $(3\times 1)$  phase without contributions from the Si bulk. Unfortunately such a 3D data set was not accessible due to the large angular widths of the  $(3\times 1)$  rods presented in Fig. 5.18 (b). However, a 2D data set of the in-plane  $(3\times 1)$  reflections is still possible to collect. This allows us to learn more about the  $(3\times 1)$  structure through the in-plane Patterson map. To apply this method we first measured and integrated a large number of the in-plane  $(3\times 1)$  reflections for one of the two rotationally equivalent domains.

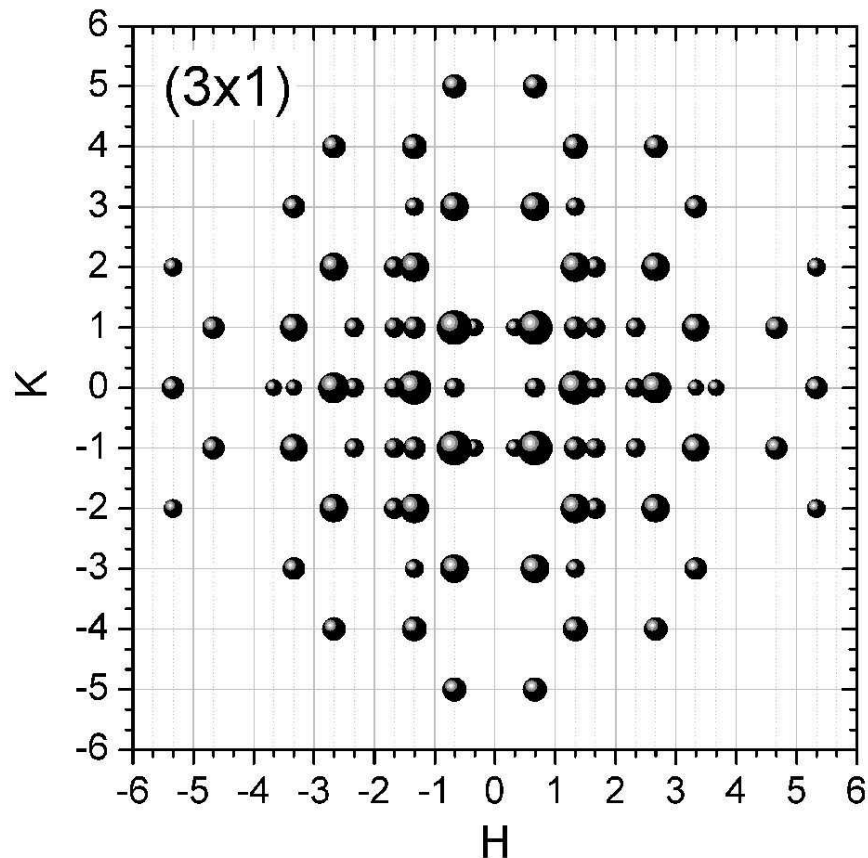


Figure 5.22: Integrated intensities plotted in Log scale of all in-plane peaks ( $L = 0.03$ ) from one type of domains of the  $3\times 1$  superstructure. H and K values are in Si reciprocal lattice unit (r.l.u.).

The result of these measurements is summarized in Fig. 5.22, where the sizes of the symbols

are proportional to the integrated intensities in Log scale of the corresponding (H,K) in-plane peaks recorded at  $L=0.03$ . By performing a Fourier transform of this in-plane  $3\times 1$  data set, the corresponding in-plane Patterson map can be constructed, as explained in Chapter 2. Fig. 5.23 shows such a real space map, which gives information on the interatomic distances for a surface-projected  $3\times 1$  unit cell. As Pr has a much higher electron density than Si and O, the map is expected to show mostly the Pr interatomic distances.

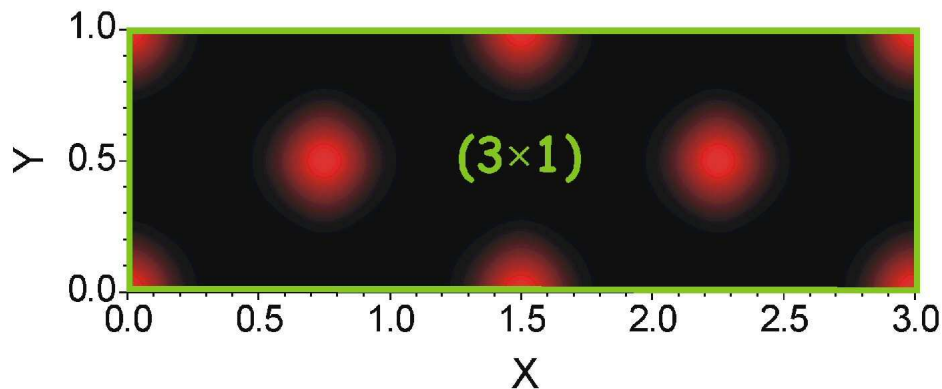


Figure 5.23: In-plane Patterson map of a  $3\times 1$  unit cell of the superstructure from the ordered overlayer.

Since  $\text{Pr}_2\text{O}_3$  has been reported to grow along the [101] direction on the Si(001) surface, in the next step, we compare Fig. 5.23 with the (101) projections of  $\text{PrO}_2$  (left) and  $\text{Pr}_2\text{O}_3$  (right) structures in Fig. 5.24, both of  $\text{CaF}_2$  type - see Chapter 1 for more detail on these two structures. For each structure a  $3\times 1$  unit cell can be defined on the (101) face and a dashed square marks the  $1\times 1$  surface unit cell for the Si(001) substrate.

Although a Patterson map generally can only reveal the interatomic vectors of a structure, not the electron density nor the atomic positions, Fig. 5.23 resembles remarkably well the Pr sublattices associated with the  $3\times 1$  unit cells in Fig. 5.24. This similarity results from the fact that due to the symmetry of the FCC sublattice that is occupied by the Pr cations, the electron density map of the Pr atoms looks identical to their Patterson map. Thus we can conclude that the in-plane structure of the  $3\times 1$  phase looks the same as the (101) projection of a  $\text{CaF}_2$  structure. However, from the Patterson map alone, we can neither conclude whether the interface structure is  $\text{PrO}_2$  or  $\text{Pr}_2\text{O}_3$ , nor identify any structural information for the out of plane direction and, in addition, since Si atoms are not visible in

Fig. 5.23, we do not know at this stage how the  $(3\times 1)$  unit cell is registered to the silicon substrate. To answer these questions, CTR scans need to be performed and analyzed.

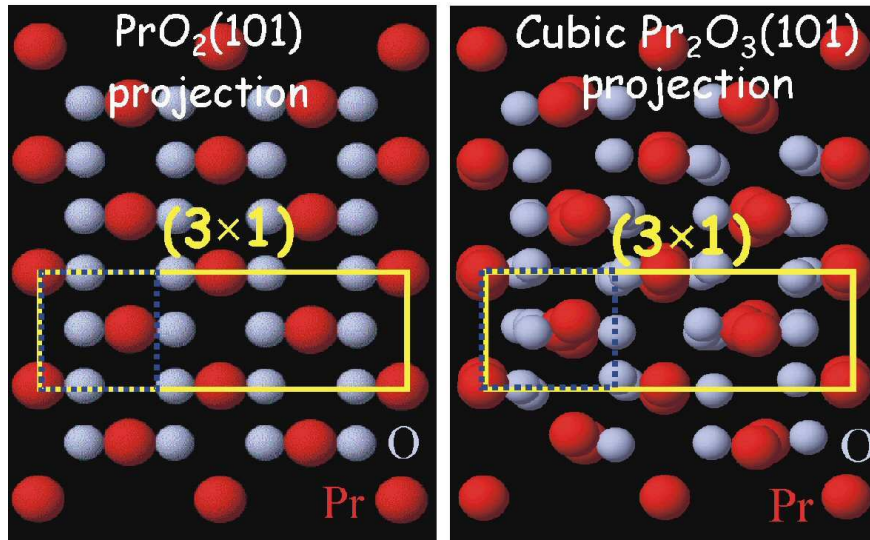


Figure 5.24: (101) projections of both structures  $\text{PrO}_2$  (left) and  $\text{Pr}_2\text{O}_3$  (right). For both structures a  $3\times 1$  unit cell is drawn and a dashed square recall a basic  $1\times 1$  unit cell.

### Off-specular CTRs

To determine the 3D atom structure of the Pr-oxide/Si(001) interface, a large data set of off-specular CTRs was collected from a 1 nm Pr-oxide film grown on Si(001) at  $550^\circ\text{C}$  under  $5\times 10^{-8}$  mbar of molecular oxygen. The x-ray energy was tuned to 17.9 keV for the diffraction experiment. Prior to the CTR measurement, specular reflectivity was measured from this sample to determine the film thickness. A quantitative analysis based on the master equation and two-layer model described in Chapter 2 showed a total film thickness of 0.91 nm for this sample. The analysis also suggested an electron density profile containing an interfacial layer of 0.47 nm with an electron density of  $1.56\text{ e}^-/\text{\AA}^3$ , in good agreement with the earlier results presented in Figs. 5.19 and 5.21.

The incident angle was then fixed to  $0.1^\circ$  for the GIXRD experiment. In-plane scans along the high symmetry directions and L scans confirmed the presence of the  $3\times 1$  superstructure and mirror planes along the H, K and  $H = K$  directions. For the CTR data set totally 20 non-equivalent Si CTRs were recorded by 1350 rocking scans over  $1/8$  of the HK plane. In addition 4 equivalent CTRs were measured in each quadrant for error estimation. The

smoothness and good crystal quality of the interfacial layer allowed us to follow the CTR intensity to as far as  $H = 6$  r.l.u.,  $K = 6$  r.l.u., and  $L = 7$  r.l.u.

After background subtraction, peak integration and intensity correction, as described in Chapter 2, the measured values of  $|F(\mathbf{Q})|^2$  (see Fig. 5.25) were modeled by Tien-Lin Lee using the computer program “FIT” developed by Oliver Bunk for SXRD data analysis. The program minimizes a  $\chi^2$  value, which describes the disagreement between the measured  $|F(\mathbf{Q})|^2$  and those calculated from a model.

As discussed previously in this chapter, the commensurate layer at the interface, which gives rise to the strong intensity modulation in the CTRs, is expected to be also responsible for the  $3\times 1$  superstructure observed in the in-plane scans. Since the in-plane Patterson map has indicated that the  $3\times 1$  phase has a (101)-oriented  $\text{CaF}_2$ - or  $\text{PrO}_2$ -like structure (see Figs. 5.22 and 5.24), we begin our modeling by considering a  $3\times 1$  unit cell that contains three  $\text{PrO}_2(202)$  and more than 10  $\text{Si}(004)$  atomic planes. This results in an interfacial layer thickness of about 0.4 nm, as suggested by the reflectivity measurement and the modulation periodicity in the CTRs. For each  $\text{Si}(001)$  terrace we introduce four equivalent domains to take into account the fact that the bulk-terminated  $\text{Si}(001)$  surface exhibits a  $p2mm$  symmetry. These four domains are linked by two mirror planes that are parallel to the  $a$  and  $b$  axes of the  $\text{Si}(001)$  surface unit cell. In addition, a two-fold rotation axis exists between two neighboring terraces. This doubles the total number of equivalent domains to eight.

To determine the in-plane registration of the  $\text{PrO}_2$  layer with the Si lattice, the oxide layer is allowed to relax from a number of different in-plane positions at the beginning with a reduced number of free positional parameters. This leads to one in-plane registration that has a  $\chi^2$  significantly smaller than all the others. This structure is then allowed to further relax with more positional parameters and the introduction of Debye-Waller factors and occupancies for the individual atoms, all following the symmetry constraints described in the previous paragraph. The final atomic structure obtained from the present analysis is plotted in Fig. 5.26 and the corresponding  $|F(\mathbf{Q})|^2$  values are given as blue curves in Fig. 5.26. The agreement between the measured  $|F(\mathbf{Q})|^2$  and the fit is satisfactory.

Dabrowski and Zavodinsky have performed *ab initio* pseudopotential density functional theory (DFT) calculations on the  $\text{Pr}_2\text{O}_3/\text{Si}(001)$  interface [91]. For comparison the oxygen-enriched interfacial structure concluded by these calculations is reproduced from Ref. [91]

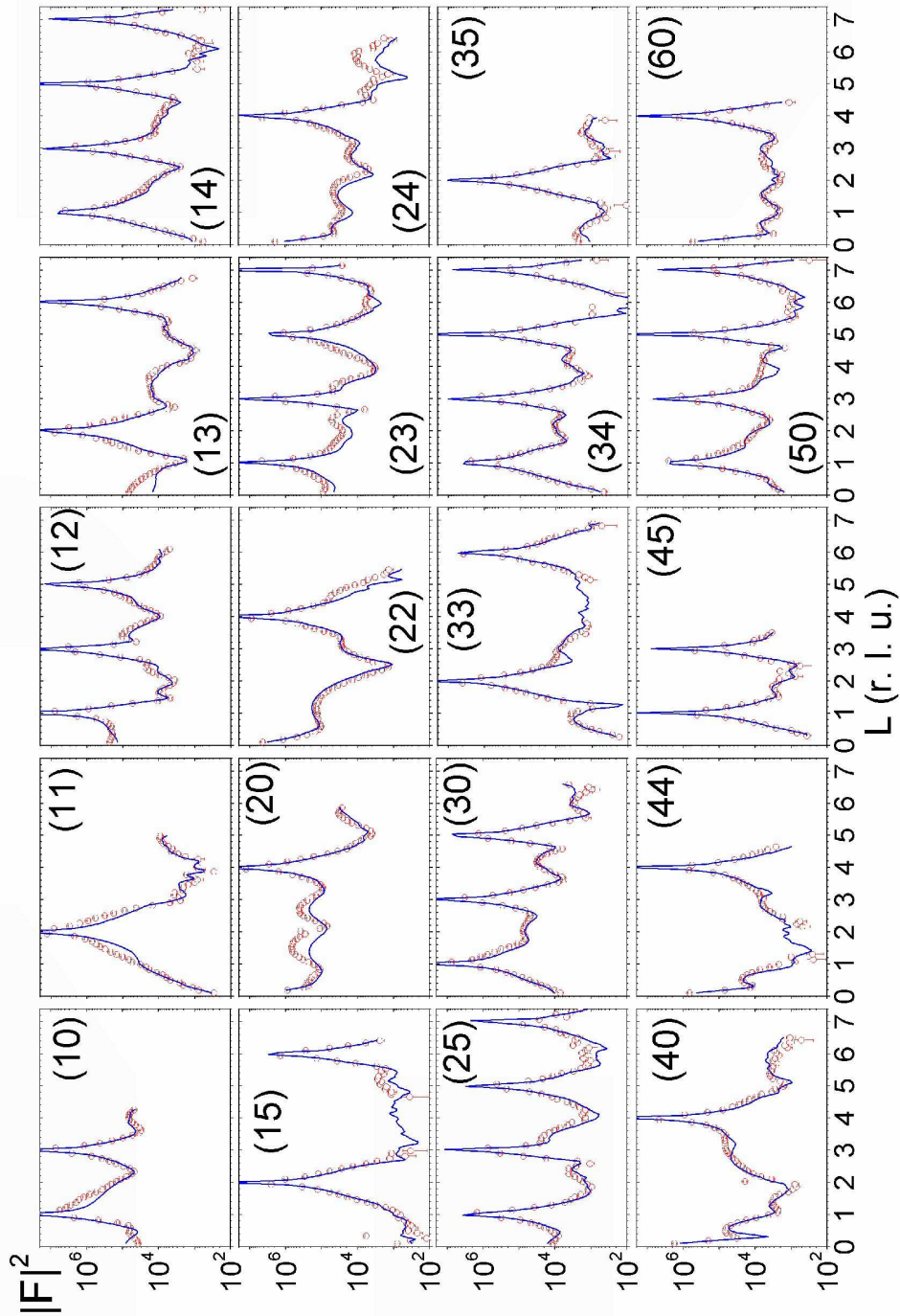


Figure 5.25: 20 Si CTRs measured in the case of a 1 nm thick Pr-oxide film. Each rod is named by its (HK) values. The red points correspond to the integrated intensities extracted from the experimental data and the blue curves correspond to the best fit from structural refinement analysis. The L values are in Si reciprocal lattice unit (r.l.u.).

in Fig. 5.26. The structures deduced from the present SXRD study and the *ab initio* calculations show good agreement in the in-plane registration of Pr-oxide layer with the Si substrate lattice. The Si–Si distances of the first layer Si atoms are found in the present study to be too large ( $> 2.9 \text{ \AA}$ ) to form dimer bonds, suggesting that under our sample preparation conditions the interface may be more oxygen rich than the one considered by the *ab initio* calculations. In addition to the  $\text{Pr}_2\text{O}_3/\text{Si}(001)$  interface, in Ref. [91] the authors also considered the possible structures for partially ordered Pr-silicate forming directly at the interface, which would be also interesting to compare with our SXRD results.

The analysis of this large CTR data set is not finalized while this thesis is being written and its present status is reported in this section. Further work such as to introduce proper constraints on oxygen atoms to stabilize their positions is on the way.

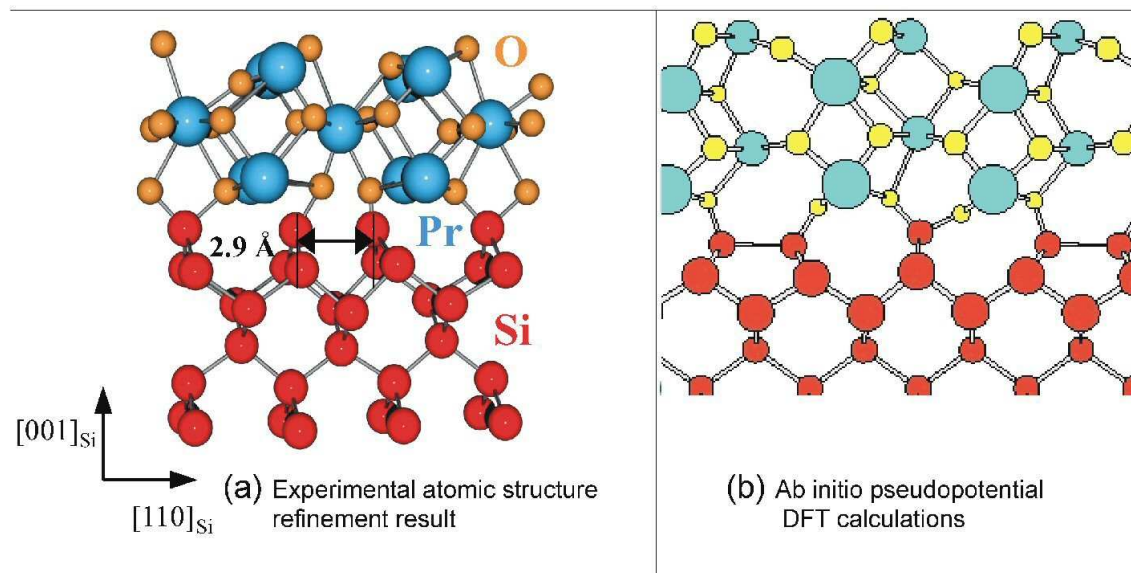


Figure 5.26: (a) Refined atomic structure of the Pr-oxide/Si(001) interface; (b) Dabrowski and Zavodinsky's model obtained by *ab initio* pseudopotential DFT calculations [91].

### 5.4.3 XPS results from the beamline

The first XPS spectra presented in Fig. 5.27 correspond to three overview scans for a pure silicon substrate, Si substrate with  $\text{SiO}_2$  native oxide and another silicon substrate with a 2.5 nm thick film grown at  $550^\circ\text{C}$  in  $5\times 10^{-8}$  mbar of  $\text{O}_2$ . These survey scans are plotted in Log scale versus binding energy between 0 and 2000 eV.

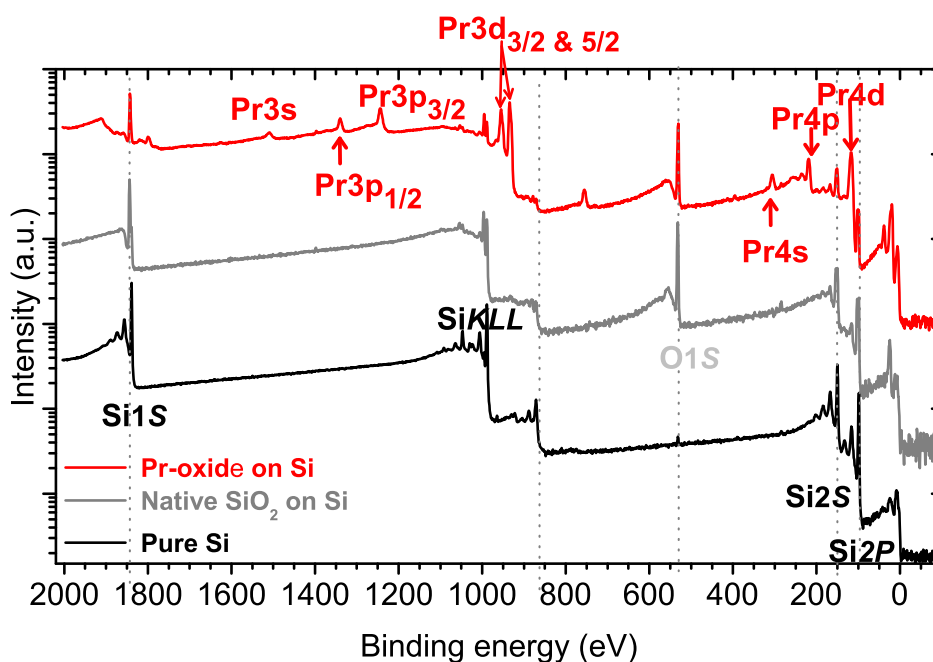


Figure 5.27: Survey spectra of Pr-oxide on Si showing the XPS electronic levels accessible using an incident photon energy of 2.6 KeV. Binding energy range plotted from 0 to 2000 eV for three different samples: Pure silicon substrate, Si substrate with  $\text{SiO}_2$  native oxide and another silicon substrate with a 2.5 nm thick film grown at  $550^\circ\text{C}$  and  $5 \times 10^{-8}$  mbar  $\text{O}_2$ . No background subtraction. The features marked with dotted lines are electron energy loss features due to plasmon excitation.

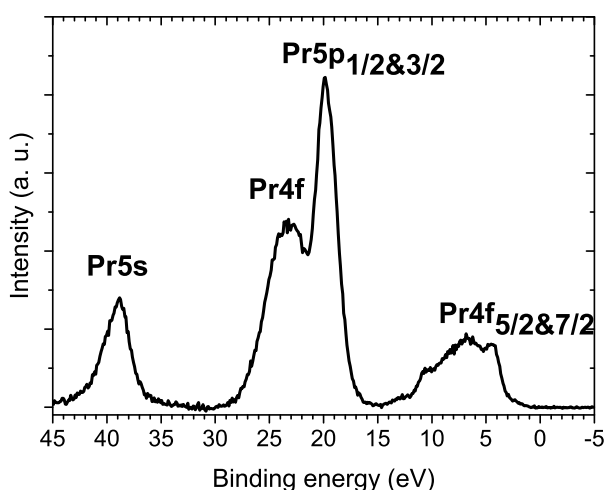


Figure 5.28: Zoom of Fig. 5.27 in the binding energy range below 100 eV for the sample with the 2.5 nm thick Pr-oxide film.

The photoemission peaks with binding energies below 100 eV are identified in Fig. 5.28. Regarding the core level spectroscopy spectra, the results for a 2.5 nm thick Pr-oxide film grown at 550 °C and in  $5\times 10^{-8}$  mbar  $O_2$  was already reported in § 5.1.2. Their evolution with respect to the growth temperature was not studied. Here the valence band (VB) spectrum for such a sample is recalled in Fig. 5.29 (see also Fig. 5.7), together with the VB spectra of both pure Si and  $SiO_2$ . The VB spectra of both pure Si and native  $SiO_2$

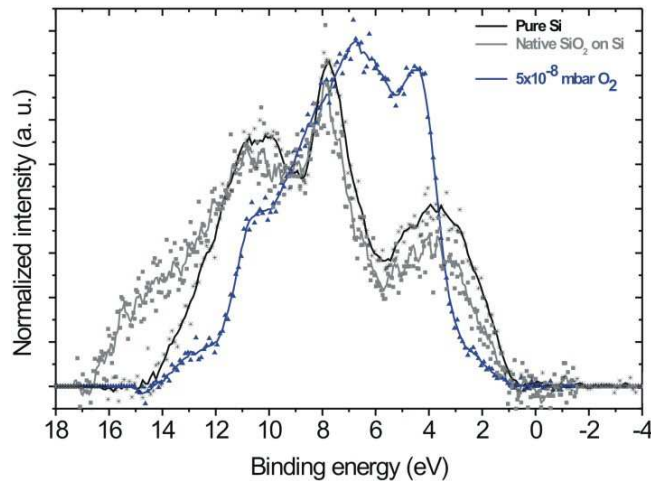


Figure 5.29: Comparison between the valence band spectrum of native  $SiO_2$  and the one of the optimized Pr-oxide stack, both on Si(001). As a reference the valence band spectrum of pure Si is added. Each spectrum is normalized to the integrated peak intensity area in the energy range shown.

show that the valence band maxima are  $\approx 1$  eV below the Fermi edge. The presence of the 2.5 nm Pr-oxide film, prepared at 550 °C and  $5\times 10^{-8}$  mbar  $O_2$ , leads to a 2 eV valence band offset. This finding is consistent with the formation of Pr-silicate [58]. In addition a conduction band offset close to 2.88 eV can be estimated using the experimental band gaps of Si (1.12 eV) and  $Pr_2O_3$  ( $\approx 6$  eV) [3, 63]. Therefore  $Pr_2O_3$ , as a high-K insulator on silicon, can provide sufficiently large tunneling barrier for both holes and electrons.

In the next two subsections we estimate the compositional depth profile of Pr-oxide / Si(001) samples using angle-resolved XPS (ARXPS). The analysis was carried out on two samples of different thicknesses : 2.5 nm and 1 nm.

### Quantitative information on the “Si in silicate vs. Pr4d” ratio versus film depth

Using ARXPS (see also § 2.6.4.) the depth profiles of the Si in silicate were investigated and compared with those of the Pr in the films. To reduce the measurement errors due

to the uncertainties in the electron mean free paths for the outgoing photoelectrons, the comparison was made between the integrated peak intensities of Si2p and Pr4d, which are less than 20 eV apart in binding energy. Fig. 5.30(a) shows both the Pr4d and Si2p core level spectra for a 2.5 nm thick film for four emission angles:  $4^\circ$ ,  $12^\circ$ ,  $37^\circ$  and  $82^\circ$ . All the spectra are background subtracted and normalized to the Pr4d integrated peak

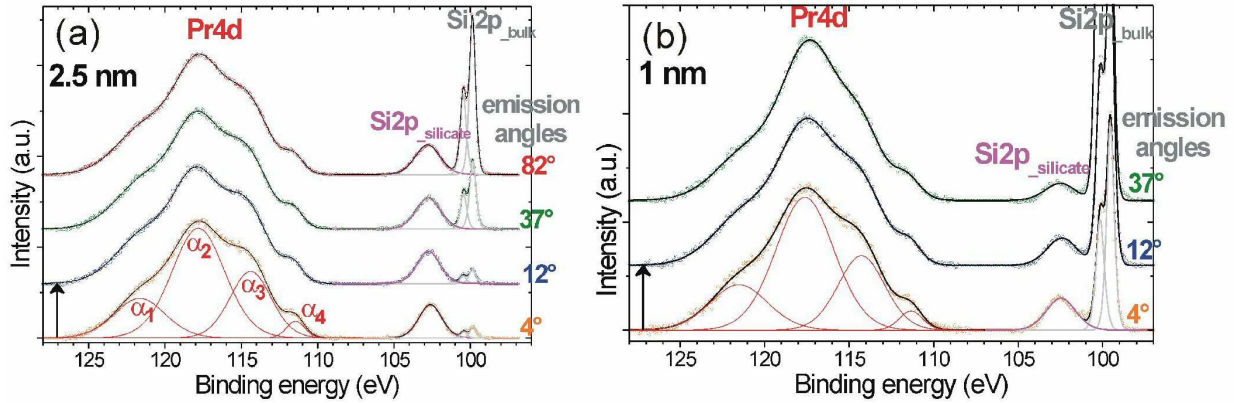


Figure 5.30: Emission patterns from Pr4d and Si2p states collected at different emission angles from a 2.5 nm (a) and a 1 nm (b) thick Pr-oxide films grown at  $550^\circ\text{C}$  under  $5 \times 10^{-8}$  mbar  $\text{O}_2$ . Experimental data points and simulated curves are plotted together to show the evolution of the intensity ratio  $I_{\text{Si}2p_{\text{silicate}}}/I_{\text{Pr}4d}$  versus the emission angle.

intensities, which are estimated from the total peak area of four gaussian components ( $\alpha_1$ ,  $\alpha_2$ ,  $\alpha_3$  and  $\alpha_4$ ) fitted to the Pr4d spectra. The shape of the Pr4d spectrum was already discussed previously. The Si2p component appearing at  $\approx 102.7$  eV corresponds to Si element in a silicate (Si-O-Pr) [58, 122]. Similar measurements were performed on a 1 nm thick Pr-oxide film and are presented in Fig. 5.30(b).

Fig. 5.31 shows the integrated peak intensity ratio  $I_{\text{Si}2p_{\text{silicate}}}/I_{\text{Pr}4d}$ , corrected by their respective photoionization cross section  $\sigma$  (as tabulated in [140, 142]), versus the emission angle  $\alpha$  (see inset in Fig. 5.31) for a 2.5 nm thick film and two other samples with 1 nm thick films. The higher the emission angle, the more bulk sensitive the measurement becomes. The individual points in Fig. 5.31 presents the experimental data for the two film thicknesses together with their arrow bars, accounting for the reproducibility of the measurements and the accuracy of the sample manipulator rotation ( $\pm 5^\circ$ ).

In the case of the 2.5 nm thick film the intensity ratio stays nearly a constant as the emission angle varies, indicating that the chemical composition of the film is homogenous within the probing depth. The measured  $\text{Si}_{\text{silicate}}/\text{Pr}$  atomic ratios, obtained by taking

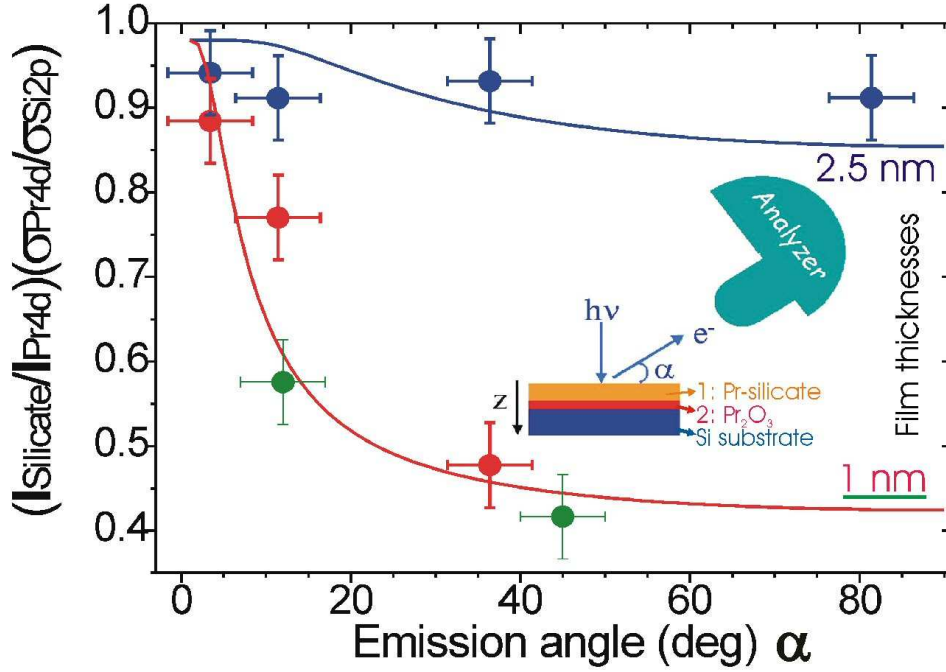


Figure 5.31: Integrated peak intensity area ratio  $I_{Si2p-silicate}/I_{Pr4d}$ , normalized to their respective cross section  $\sigma$  (as tabulated in [140, 142]), versus the emission angle  $\alpha$  (presented in inset) for a 2.5 nm thick film and two other samples with 1 nm thick films.

into account the different photoionization cross sections in the  $I_{Si2p-silicate}/I_{Pr4d}$  ratios, are about 0.93 for all four emission angles, in good agreement with the chemical composition of a thick Pr-silicate ( $Pr_2Si_2O_7$ ) film. For the 1 nm thick sample, the intensity ratio falls sharply as the emission angle increases, suggesting that the interface is much more Pr rich than the Pr-silicate in the film. The presence of such an interface is already evident from the normalized Pr4d and Si2p spectra shown in Fig. 5.31(b), where the silicate peak becomes weaker at larger emission angles. What we have observed from the 1 nm thick sample can be explained by a thin interfacial layer composed of Pr.

To check the validity of the bilayer model, we plot in Fig. 2.29 the simulated intensity ratios for a 2.0 and a 0.5 nm  $Pr_2Si_2O_7$  films with a 0.5 nm buried  $Pr_2O_3$  layer at the interface. The  $I_{Si2p-silicate}$  and Pr4d intensities from such samples can be calculated by

$$\frac{I_{Si_{silicate}}}{\sigma_{Si_{2p}}} \propto \rho_{Si_1} \left( 1 - e^{-\frac{\mu t_1}{\sin \alpha}} \right) \quad (5.1)$$

and

$$\frac{I_{Pr4d}}{\sigma_{Pr4d}} \propto \rho_{Pr_1} \left(1 - e^{-\frac{\mu t_1}{\sin \alpha}}\right) + \rho_{Pr_2} \left(e^{-\frac{\mu t_1}{\sin \alpha}} - e^{-\frac{\mu(t_1+t_2)}{\sin \alpha}}\right) \quad (5.2)$$

where the indices 1 and 2 denoted the top (Pr-silicate) and interfacial (Pr-oxide) layers, respectively.  $\mu$  is the attenuation length determined in § 2.6.4. Notice that the same  $\mu$  is used for both Si2p and Pr4d ;  $\rho$ 's are the atomic densities for the considered elements and  $t$ 's are the thicknesses of the layers. The different constant values are shown in Table 5.4.

$\sigma_{Si2p}$	$\sigma_{Pr4d}$	$\rho_{Si_1} =$ $\rho_{Si_{silicate}}$	$\rho_{Pr_1} =$ $\rho_{Pr_{silicate}}$	$\rho_{Pr_2} =$ $\rho_{Pr_{Pr_2O_3}}$	$\mu$	$t_2 =$ $t_{Pr_2O_3}$
2.08 Kb*	27.34 Kb	0.0142 at./Å <sup>3</sup>	0.0142 at./Å <sup>3</sup>	0.0231 at./Å <sup>3</sup>	0.4 Å <sup>-1</sup>	5 Å

Table 5.4: List of the constant values used in expressions 5.1 and 5.2. The cross sections  $\sigma$  are tabulated in [140, 142], the  $\rho$  have been calculated,  $\mu$  was determined in § 2.6.4., and  $t_{Pr_2O_3}$  value comes from the reflectivity analysis. \* Kb = K barn. 1 K barn =  $10^{-21}$  cm<sup>2</sup>.

The simulation results agree qualitatively with the measurements. In the case of the 2.5 nm thick Pr-oxide film the  $I_{Si2p-silicate}/I_{Pr4d}$  ratio decreases slightly when the emission angle increases. This is due to the fact that the probing depth  $\sin \alpha / \mu$  approaches to 2.5 nm as  $\alpha$  increases to 90°. Therefore the buried interfacial layer can still have some contribution to the intensity ratio at large emission angles for the 2.5 nm film. When the film is 1 nm thick the spectra start getting significant contributions from the interface at the different emission angles. The lack of Si in the interfacial layer leads to a sharp drop in the intensity ratio at high  $\alpha$ . To confirm the above findings and check whether we indeed have the Pr<sub>2</sub>Si<sub>2</sub>O<sub>7</sub> stoichiometry in the films, the same analysis was performed for the O1s and Pr4d spectra. The results are presented in the next subsection.

### Quantitative information on the O1s intensity distribution versus film depth

The O1s core level spectra were compared with the Pr4d ones. Fig. 5.32 shows the integrated peak intensity ratio  $I_{O1s}/I_{Pr4d}$ , normalized to their respective cross section  $\sigma$ , versus the emission angle  $\alpha$  for a 2.5 nm and a 1 nm thick films. The collected data were modeled assuming the same bilayer model. The O1s intensity can be calculated by

$$\frac{I_{O1s}}{\sigma_{O1s}} \propto \rho_{O_1} \left(1 - e^{-\frac{\mu t_1}{\sin \alpha}}\right) + \rho_{O_2} \left(e^{-\frac{\mu t_1}{\sin \alpha}} - e^{-\frac{\mu(t_1+t_2)}{\sin \alpha}}\right) \quad (5.3)$$

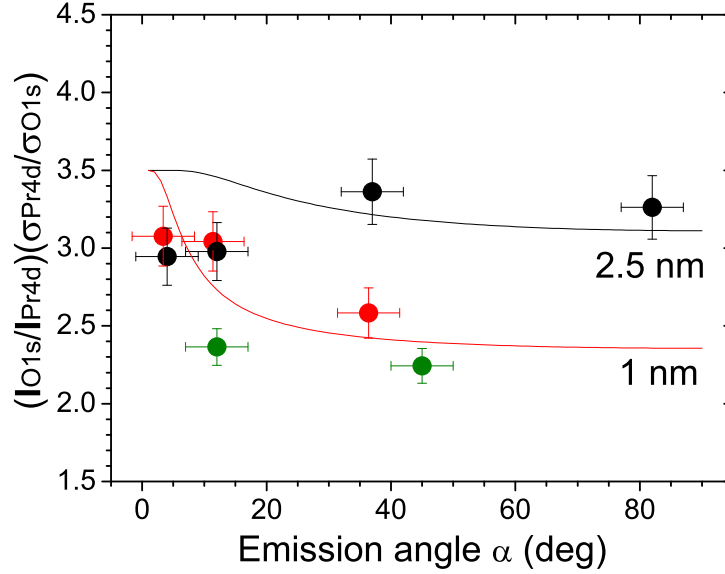


Figure 5.32: Integrated peak intensity area ratio  $I_{O1s}/I_{Pr4d}$ , normalized to their respective cross section  $\sigma$ , versus the emission angle  $\alpha$  for a 2.5 nm and a 1 nm thick films.

where  $\rho_{O_1}$  and  $\rho_{O_2}$  are the atomic densities of oxygen in the Pr-silicate and  $\text{Pr}_2\text{O}_3$  layers, respectively. Notice that here we have made the approximation again that  $\mu = 0.4 \text{ \AA}^{-1}$  for both Si2p and O1s. Qualitative agreement between the measurements and the simulations can be reached if we use in Fig. 5.32 a  $\sigma_{O1s} = 9.73 \text{ Kb}$ , 1.25 times the value listed in Ref. [142].

The different constant values in expression 5.3 are shown in Table 5.5.

$\sigma_{O1s}$	$\rho_{O_1} = \rho_{O_{\text{silicate}}}$	$\rho_{O_2} = \rho_{O_{\text{Pr}_2\text{O}_3}}$	$\mu$	$t_2 = t_{\text{Pr}_2\text{O}_3}$
9.73 Kb	0.0497 at./ $\text{\AA}^3$	0.0346 at./ $\text{\AA}^3$	0.4 $\text{\AA}^{-1}$	5 $\text{\AA}$

Table 5.5: List of the constant values used in expression 5.3. See Table 5.4 caption for more explanations.

The analysis in Fig. 5.32 shows that the O:Pr atomic ratio in a thicker film is close to 3.5:1 (a higher ratio close to 4:1 would be concluded if the  $\sigma_{O1s}$  listed in Ref. [142] is used). The present ARXPS study has therefore determined the chemical composition of our MBE grown Pr-oxide films to be Pr:Si:O  $\approx$  1:1:3.5, same stoichiometry as Pr-silicate. In Fig. 5.32 the presence of an interfacial layer appears to have less effect on the angular

dependence of O1s/Pr4d intensity ratio than the case for the Si2p<sub>silicate</sub>/Pr4d ratio. This is consistent with the fact that Pr<sub>2</sub>O<sub>3</sub> has only 30% less oxygen density than Pr<sub>2</sub>Si<sub>2</sub>O<sub>7</sub>.

#### 5.4.4 Complementary analysis on the optimized films

##### TEM results

Transmission electron microscopy (TEM) enables a quick evaluation, in real space, of the structural quality of the films thanks to “in-plane” and/or “cross-sectional” observations. TEM measurements have been performed at the LMGP (Laboratoire des Matériaux et du Génie Physique - UMR CNRS / INPG ). The TEM device used was a JEOL 2010, at a voltage of 200 kV and a point to point resolution of 1.7 Å. Fig. 5.33 shows a cross sectional

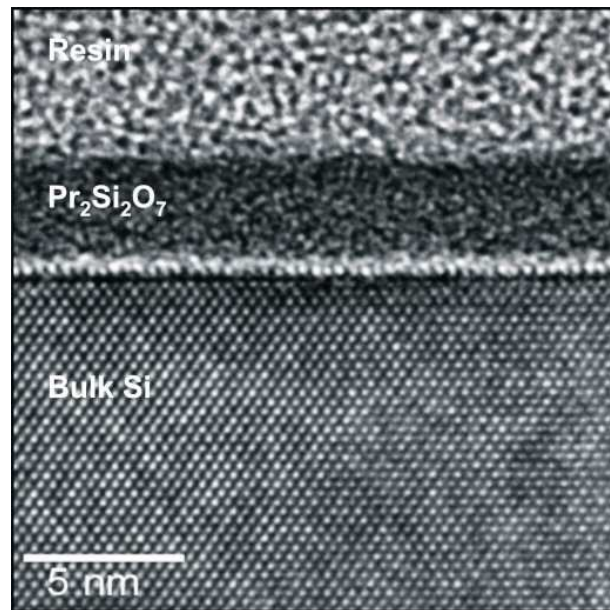


Figure 5.33: Cross sectional TEM picture of a 3 nm thick Pr-oxide film on Si(001), grown at 550 °C and under  $5\times 10^{-8}$  mbar O<sub>2</sub>.

TEM picture performed on a 3 nm thick film. An interfacial layer with a different phase contrast can be observed. Its thickness can be estimated around 0.5 nm but its structure cannot be resolved with this technique. On top of this interfacial layer a 2.5 nm thick featureless layer is observed. Several areas have been probed with this technique and they have all shown a continuous film presenting the same layer sequence as the one presented

in Fig. 5.33. However no conclusions on the ordering of the interfacial layer can be drawn from the obtained results.

### Electrical characterization

The samples were electrically characterized by capacitance-voltage (C-V) and current density - voltage (J-V) measurements. Gold electrodes are made by thermal evaporation through a mask (TEM grid) placed on top of the sample surface, through which electrodes of different sizes can be deposited. The samples are fixed on a test bench under slight pressure created by a vacuum chuck system. The electrical measurements were performed through a conductive tip set-up connected to both the test bench and the samples, via the gold electrodes. These measurements were performed at the CEA / LETI in Grenoble.

Due to technical difficulties in carrying out these measurements on the Si(001) hat-shaped crystals, the measurements presented in this section were achieved on samples grown on commercial p-type Si(001) 350  $\mu\text{m}$  thick wafers with a resistivity estimated between 0.1-1  $\Omega\cdot\text{cm}$  by the supplier. The presented results are for a 5 nm thick Pr-oxide film and were reproducibly collected on several different areas. Fig. 5.34 shows three C-V characteristics : the first one was measured at 0.1 KHz while the two others were recorded two weeks later (the samples stayed in ambient atmosphere) at two different frequencies, i.e. 0.1 KHz and 0.2 KHz, respectively. The goal was to check :

1. The electrical properties of the films
2. The stability of these properties with time
3. The presence of an hysteresis effect, revealed by a frequency dependence of the C-V curves.

The largest capacitance per area measured in the accumulation regime is  $1.23\times 10^{-2}$   $\text{pF}\cdot\mu\text{m}^{-2}$ . The deduced equivalent oxide thickness (EOT) is about 2.7 nm, from which a total effective dielectric constant of 7.2 was estimated. MOCVD grown Pr-silicate films were reported with a dielectric constant of  $\approx 7-8$  and MBE grown Pr-silicate with a K value estimated around 14 [38, 63]. On the other hand  $\text{Pr}_2\text{O}_3$  epitaxial films grown by MBE were found with a dielectric constant  $\approx 30$ . Comparing these results with the K value we found, we can deduce that the overall dielectric constant is dominated by the Pr-silicate layer, which has a much lower k value than  $\text{Pr}_2\text{O}_3$ .

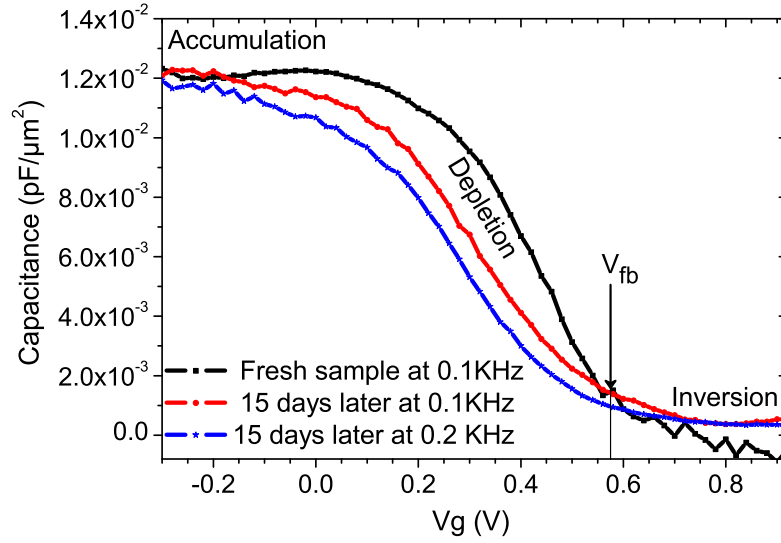


Figure 5.34: Capacitance-voltage (C-V) curves of a MOS structure composed of a 5 nm thick Pr-oxide film with a gold electrode on top. The substrate is a p-type Si(001) wafer. One curve is recorded at 0.1 KHz. The two others are recorded two weeks later at 0.1 KHz and 0.2 KHz

The hysteresis effect observed from the two curves measured at two different frequencies indicates the presence of defects in the film, which may be attributed to the presence of oxygen vacancies [17]. However, the C-V characteristics were measured at low frequencies and the smoothness of the curves attests a low number of interface states at the Pr-oxide / Si interface [143].

From these measurements we can also extract a flat band voltage ( $V_{fb}$ ) of 0.57 eV, as calculated from Maserjian's formula  $y = \frac{dc}{dv} \times \frac{1}{c^3}$ , where  $c$  is the capacitance and  $v$  the voltage [144].  $\frac{y_{min}}{3}$  gives the  $V_{fb}$  value. The theoretical  $V_{fb}$  value can be calculated from:

$$V_{fb} = \phi_{ms} = \phi_m - \left( \chi + \frac{E_g}{2} + E_f \right) \quad (5.4)$$

The terms  $\phi_{ms}$  and  $\phi_m$  in Eq. (5.4) are the metal-semiconductor work function (Au/Si) and the metal work function. For a gold electrode  $\phi_m = 5.1$  eV [145].  $\chi$  is the electronic affinity of Si (4.05 eV) and its gap ( $E_g$ ) is 1.12 eV. The Fermi level ( $E_f$ ) is calculated from :

$$E_f = k.T/q.ln\left(\frac{N_A}{n_i}\right) \quad (5.5)$$

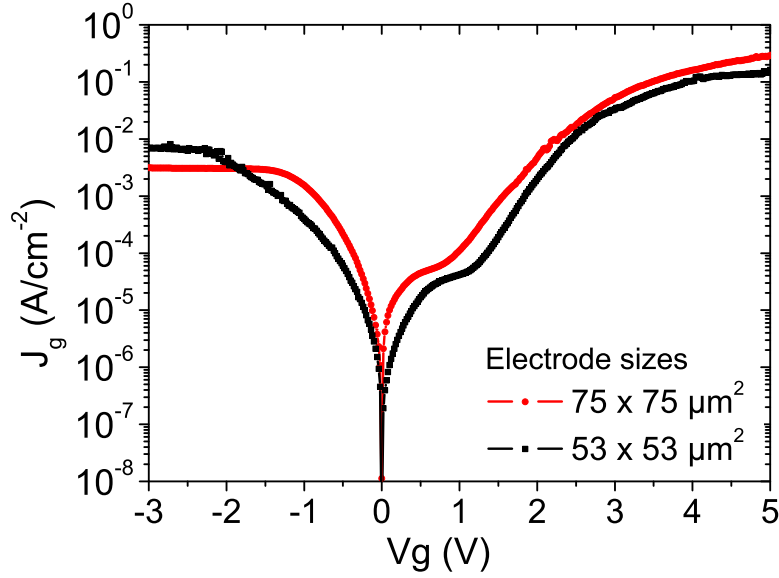


Figure 5.35: Current density-voltage (J-V) curves recorded for the same sample represented on Fig. 5.34. The two curves were collected for two different electrodes of different size, as specified in the figure.

where  $k.T/q$  is a constant (0.0025885),  $N_A$  is the doping concentration of “acceptors” and  $n_i$  is the intrinsic carrier concentration of Si.  $E_f$  depends on the doping level of the substrate. In our case, for a substrate resistivity of around  $0.7 \Omega.cm$ ,  $N_D$  is equal to  $5 \times 10^{15}$ .  $n_i = 1.45 \times 10^{10}$ . Then the theoretical  $V_{fb}$  value deduced from Eq. (5.4) is 0.33 eV. The shift between the experimental and theoretical values could be explained by the presence of negative charges in the oxide film (taking into account the uncertainties of the work function of Au on a  $Pr_2O_3$  surface).

Fig. 5.35 presents two current density-voltage (J-V) characteristics, measured on two electrodes of different sizes, i.e.  $75 \times 75 \mu m^2$  and  $53 \times 53 \mu m^2$ . For the smallest electrode, the leakage current at -1 V is about  $4.2 \times 10^{-4} A.cm^{-2}$  while at +1 V it is about  $4.3 \times 10^{-5} A.cm^{-2}$ . For comparison, a  $SiO_2$  film thickness of 2.7 nm shows a leakage current value at 1 V of  $3 \times 10^{-5} A.cm^{-2}$ . This shows that we did not gain in leakage current by replacing  $SiO_2$  by  $Pr_2O_3$ , for this EOT value.

As a remark we have also tried to perform such measurements on samples with thinner Pr-oxide films but we did not manage to collect reliable and reproducible data. Compared

with other studies [17], we suppose that this was either due to too high leakage currents in those films or due to a bad contact between the gold electrodes and the film, giving rise to fluctuations of the electrical results from one electrode to the other according to the quality of the gold electrode/thin film interface, the quality of the tip/gold electrode contact, etc.

To conclude with, the results presented in this section indicate that the Pr<sub>2</sub>O<sub>3</sub>/Pr<sub>2</sub>Si<sub>2</sub>O<sub>7</sub> stack grown in this study are not interesting for gate oxide applications with EOT < 1nm. This is due to the formation of a disordered Pr-silicate layer with a K value below 10. If by tailoring the growth conditions the Si diffusion can be somehow stop to prevent the formation of this silicate and/or if the interfacial ordered layer, which has a higher dielectric constant, can be grown thicker, the use of Pr-oxide films could be foreseen for CMOS applications.

### 5.4.5 Summary

In this chapter the effects of oxygen partial pressure and growth temperature (P,T) at a low growth rate ( $\approx 0.2 \text{ \AA}/\text{min}$ ) on the crystalline quality of very thin oxide layers have been studied. ( $5 \times 10^{-8}$  mbar O<sub>2</sub>, 550 °C) is the “combination” providing (i) the best crystalline quality of the 3×1 interfacial ordered layer; (ii) a smooth film surface; (iii) a 2 eV valence band offsets.

Film grown under the optimized conditions have been studied *in-situ* by STM, LEED and AES from subnanometer up to few nanometer coverages. The STM / LEED study suggests (i) at the very beginning of the growth a similar surface etching process of the Si substrate than in the case of samples grown under UHV (see Chapter 4); the formation of an ordered layer at the initial stages of the growth; (iii) a smooth film surface up to 2 nm of oxide coverage.

With the diffraction technique, in-plane scans revealed a 3×1 ordered interfacial layer with a domain size of about 6.2 nm when the films are fully developed. Reflectivity analysis indicates that the thickness of this interfacial layer is about 0.5 nm while its electron density is found to be  $1.6 \text{ e}^-/\text{\AA}^3$ . This electron density agrees with the value for bulk Pr<sub>2</sub>O<sub>3</sub>. The in-plane Patterson map deduced from the in-plane reflections of a 3×1 domain reveals a CaF<sub>2</sub> like structure, consistent with the growth of (101) oriented

$\text{Pr}_2\text{O}_3$  at the interface. From the structural refinement of a large Si CTR data set a model could be proposed and explain how this  $3\times 1$  phase, based on the bulk  $\text{Pr}_2\text{O}_3$  structure, is registered to the Si(001) substrate lattice. XPS measurements complement these findings and ARXPS demonstrates a disordered  $\text{Pr}_2\text{Si}_2\text{O}_7$  silicate layer growing above a buried Pr-rich layer. Therefore XPS results are in agreement with the bilayer model proposed from XRD (0.5 nm  $\text{Pr}_2\text{O}_3/\text{Pr}_2\text{Si}_2\text{O}_7$  stack).

TEM results suggest the existence of a distinct interfacial layer, about 0.5 nm thick, at the film/substrate interface. However the resolution is not sufficient to identify the structural arrangement of such a thin interfacial ordered layer.

#### 5.4.6 Pr-oxide films on Si(001) : Discussions

In this section we discuss four different subjects

1. The optimized (P,T) combination and its comparison with other rare-earth oxides grown on Si(001)
2. The disordered Pr-silicate layer, which is the main phase of the Pr-oxide film grown on Si(001) in this study
3. The  $3\times 1$  ordered interfacial layer: its features, origin, and comparison with similar superstructures reported for other deposits on Si(001)
4. We will finally discuss about the question “ How can we have a silicate on top of a silicon free layer? ”

The use of a molecular oxygen flux in the mid- $10^{-8}$  mbar range prevents the Pr-silicide formation. Regarding the influence of the temperature on the film ordering, we have shown evidences that  $T \leq 500^\circ\text{C}$  give rise to disordered films and that for T above  $650^\circ\text{C}$ , the evaporated material does not stick on the surface. Fig. 5.13 summarizes our findings. These results reveal the extreme sensitivity of this system on both the temperature and the oxygen partial pressure applied during the growth. The phase diagram of the Pr-O binary system is indeed very complex, as demonstrated by Eyring *et al.* [65]. The ( $5\times 10^{-8}$  mbar  $\text{O}_2$ ,  $550^\circ\text{C}$ ) optimized combination can be compared with the optimal ones for other rare-earth oxides grown on Si(001). For instance Czernohorsky *et al.* have found

that the optimal ( $5\times 10^{-7}$  mbar  $O_2$ ,  $600^\circ\text{C}$ ) combination in the case of the  $Gd_2O_3$  growth on Si(001) gives the best dielectric layer properties [17].

Papers in the literature published until 2003 reported on epitaxial  $Pr_2O_3$  growth on Si(001) [2, 50, 52, 60]. It is only since 2003 that some groups have evidenced the formation of a Pr-silicate when growing  $Pr_2O_3$  on Si(001) with similar growth procedures [54–59, 62, 63, 87, 88, 146, 147]. However, none of these studies could identify an interfacial transition layer at the film/substrate interface.

The  $3\times 1$  superstructure found at the buried Pr-oxide film/substrate interface can be compared with other superstructures with  $1/3$  periodicities that have recently been reported for other rare-earth oxides grown on Si(001). They were attributed to silicide formation [18], comparing this findings with electronic structure calculations of La adsorption on the Si(001) surface [148]. Our study has experimentally demonstrated that the  $3\times 1$  superstructure observed in these systems does not correspond to a silicide phase but to the (101) plane of a  $CaF_2$  like structure, so that in our case either  $PrO_2$  or  $Pr_2O_3$  could fit with this experimental model. We expect that  $Pr_2O_3$  is most likely growing at the interface since (i) it has a lower oxygen stoichiometry than  $PrO_2$  [Pr:O ratios of (1:1.5) in  $Pr_2O_3$  versus (1:2) in  $PrO_2$ ] and in addition (ii) the electron density of  $Pr_2O_3$  ( $\rho_{Pr_2O_3}$ ) is  $\approx 1.6\text{ e}^-/\text{\AA}^3$ , value in agreement with our reflectivity analysis, while  $\rho_{PrO_2}$  is  $\approx 1.9\text{ e}^-/\text{\AA}^3$ .

So far, there is no information available in the literature for this heteroepitaxial system, regarding the crystalline structure of the very first layers and neither for other rare-earth oxides. From the structural refinement based on the large CTRs data set that was recorded the appearance of a  $3\times 1$  superstructure in the XRD data can be explained by a reconstruction of the  $2\times 1$ -Si(001) surface structure into a  $3\times 1$  one. The corresponding 0.5 nm ordered layer does not contain Si atoms. This is most likely due to an energetically stabilized  $Pr_2O_3$  layer.

A similar study was recently reported by Pasquali *et al.* in the case of the  $CaF_2$  growth on Si(001) substrates [149]. During the bonding process between  $CaF_2$  molecules and Si(001) substrates they found that an uniform wetting layer, bonded with the substrate through Ca atoms, changes the surface periodicity from double domain  $2\times 1 + 1\times 2$  to single domain  $3\times 1$ . In our case we could identify two  $3\times 1$  domains rotated by  $90^\circ$ . This difference could be due to the fact that in their case they have worked with relatively large miscut angle (1 - 3 mrad with respect to the (001) plane) while in our case we worked with miscut free surfaces.

While the CTRs looked sharp and the scattered intensity along them was well above the background, the (3×1) superstructure rods remained too broad to be followed and properly measured. This is due to the fact that in the case of the integer order rods (Si CTRs) the bulk Si substrate and both 3×1 domains [(1×3) and (3×1)] contribute to the intensity modulation in the anti-bragg peak region, while for the 3×1 superstructure rods only the commensurate ordered layer contributes to the intensity modulation and each 3×1 domain is probed individually. This suggests 3×1 domains with a small lateral size (around 6 nm). However, we worked with Si(001) surfaces showing terraces width bigger than 500 nm. The STM topographs collected for both samples grown under UHV and in  $5 \times 10^{-8}$  mbar of O<sub>2</sub> have revealed that these small 3×1 domains are caused by an “etching” of the silicon terrace, which may be due to the oxygen (formation of volatile SiO species?) and the slow growth kinetics in our experiments (0.2 Å/min). In both cases this 3×1 superstructure does not grow thicker than 5 Å, as evidenced with XRR. The large lattice mismatch between the cubic phase of Pr<sub>2</sub>O<sub>3</sub> and Si(001), i.e. 3%, may explain the reason why the interfacial ordered layer can not grow thicker in epitaxy with the underlying Si(001) substrate.

Above this 5 Å critical thickness the formation of a disordered silicate layer Pr<sub>2</sub>Si<sub>2</sub>O<sub>7</sub> occurs (as revealed by our XPS results). Previous studies on this system report that dissolution of Si in Pr<sub>2</sub>O<sub>3</sub> is energetically favorable and Pr-silicate forms [58].

A puzzling question is how can there be a Pr-silicate layer on top of an interfacial silicon free layer (Pr<sub>2</sub>O<sub>3</sub>)?

The absence of Si atoms in a 5 Å thick Pr<sub>2</sub>O<sub>3</sub> interfacial layer suggests that this structure is mostly stabilized by the interfacial energy, i.e., the Si/Pr<sub>2</sub>O<sub>3</sub> interface. However theoretical input would be needed to understand this phenomenon in full detail.

To finally conclude, in our study we have not seen the regrowth of a cubic Pr<sub>2</sub>O<sub>3</sub> phase above the Pr<sub>2</sub>Si<sub>2</sub>O<sub>7</sub> silicate, as reported from Osten [3]. This is due to the fact that we did not grow thick enough layer. Thus, we do not have any information on the film composition when the film thickness is above 10 nm. This subject was beyond the scope of this project and must await further investigations.

# General conclusion and Outlook

---

## General conclusion

This thesis was aimed at shedding light on the interface properties of an oxide on silicon substrates, at the atomic scale. In particular the case of the technologically important Si(001) surface was in the focus.

In chapter 3, the Pr<sub>2</sub>O<sub>3</sub> growth on Si(111) substrates under UHV revealed a pseudomorphic layer, lifting the 7×7 reconstruction of the atomically clean Si(111) surface. 2D equilateral triangular islands with a narrow size distribution were found to grow on terraces with preferential nucleation observed at step edges of the Si(111) surface. One complete layer is about 0.52 nm, as determined by STM. This result is in agreement with the 0.6 nm height of the “hexagonal” Pr<sub>2</sub>O<sub>3</sub> unit cell, considering the fact that the Pr<sub>2</sub>O<sub>3</sub> may offer a smaller density of states than the clean Si surface.

Chapter 4 shows the results of the Pr-oxide growth on Si(001) under UHV. The appearance of a 3×1 superstructure for subnanometer coverages was identified. Beyond ≈ 0.6 nm thickness of the oxide films, 3D-PrSi<sub>2</sub> islands form when the growth is carried out at ≈ 550 °C. These islands have a broad height distribution and are embedded into a 2D Pr-silicate layer, on top of an ordered 0.5 nm 3×1 structure. Room temperature deposition in UHV did not give rise to silicide formation but the Pr-oxide films formed are disordered. Their composition corresponds to a mixture of PrO<sub>x</sub> and Pr<sub>2</sub>Si<sub>2</sub>O<sub>7</sub> silicate. Post annealing treatments of these films demonstrated their high sensitivity to the (P,T) parameters. When oxidized in 10<sup>-7</sup> mbar at 550 °C, a SiO<sub>2</sub> layer is likely to form at the film/substrate interface. Both samples grown under UHV at 550 °C and at room temperature have high densities of electronic states near the Fermi edge.

The very early growth stages of Pr-oxide films on Si(001) under molecular oxygen partial pressure in the  $10^{-8}$  mbar range and the detailed study of the  $3\times 1$  superstructure at the Pr-oxide/Si-substrate interface were the subject of Chapter 5. An optimal condition of  $5\times 10^{-8}$  mbar  $O_2$  and  $550^\circ\text{C}$  was found and a 5 Å thick ordered interfacial layer, with a  $3\times 1$  superstructure, was identified. Its  $\text{CaF}_2$ -like structure and its electron density of about  $1.6\text{ e}^-/\text{Å}^3$  indicate a  $\text{Pr}_2\text{O}_3$  interfacial layer. The atomic structure of this interfacial layer was determined based on a large SXRD dataset. The result shows qualitative agreement with earlier theoretical calculations [91]. On top of this ordered layer a disordered  $\text{Pr}_2\text{Si}_2\text{O}_7$  layer forms. Earlier *ex-situ* studies have shown that this silicate layer represents a transitional film on top of which crystalline cubic  $\text{Pr}_2\text{O}_3$  forms upon growth [51,92].

To conclude, this work has combined several complementary surface science techniques, i.e. SXRD, STM, LEED, AES and XPS, to study the transition between a crystalline substrate and a disordered film (Pr-silicate) which gives rise to a 5 Å thick ordered interfacial transition layer. These are novel results in the area of the study and application of high-K oxides on Si(001) substrates. In particular, the results of the quantitative atomic scale study, which we have performed for the  $\text{Pr}_2\text{O}_3/\text{Si}(001)$  interface, might be used as a model for the case of the growth on Si(001) of other RE oxides exhibiting similar properties than  $\text{Pr}_2\text{O}_3$ , such as  $\text{Gd}_2\text{O}_3$ ,  $\text{Nd}_2\text{O}_3$ ,  $\text{Y}_2\text{O}_3$ , etc.

## Outlook

### Cubic $\text{Pr}_2\text{O}_3$ epitaxy on Si(001)?

As previously mentioned, a remaining question is when and how the cubic  $\text{Pr}_2\text{O}_3$  phase will grow above the silicate layer with subsequent oxide deposition. It would be then interesting to investigate the structural evolution of the oxide films with larger thickness. In particular whether the structure at the interface changes when the cubic  $\text{Pr}_2\text{O}_3$  phase appears is an interesting question, which can be monitored by Si CTRs. Most likely, in order to reduce the Si out-diffusion and to limit the silicate layer thickness, a much higher growth speed than possible with our present growth evaporator is needed.

The differences between the growth parameters used in this study and the ones used by Osten, who obtained a crystalline  $\text{Pr}_2\text{O}_3$  cubic phase on Si(001) [3, 50, 52] (with film

thicknesses thicker than ours), are listed below:

1. Substrate cleaning: UHV high temperature cleaning in our case versus Hf dip to H-terminate the Si surface in Osten's case
2. A Growth rate about at least 100 times higher in Osten's case
3. Pressure range: we can control the oxygen partial pressure down to UHV conditions while Osten has worked with an oxygen residual partial pressure of  $5 \times 10^{-8}$  mbar
4. Our study was carried out on very low miscut surfaces (below  $0.01^\circ$ ) while Osten worked on commercially available 4-inch wafers with a miscut angle about  $0.3^\circ$  [150].

## **Atomic positions in the oxygen subnetwork**

X-ray standing wave measurements combined with XPS could help to gain more information on the position of the oxygen atoms in the  $\text{Pr}_2\text{O}_3$  ordered layer at the interface. As they do scatter much less than Pr, the structural information we have obtained for them with the diffraction experiments is much less reliable than the information obtained for the Pr.

## **Influence of the substrate miscut**

Regarding what was observed in section 4.3.1, we expect that a higher miscut, which will give rise to only one kind of terraces (cf. double height steps), would promote the formation of one single  $3 \times 1$  domain. The influence of the substrate miscut or higher step density on the nucleation process and the growth properties could be an interesting issue to investigate.

## **Influence of the substrate cleaning method on the interfacial properties**

One of the main lessons that was learnt from the studies presented in this thesis regards the necessity of good quality single crystalline substrates and the particular attention that must be devoted to their preparation (height months in the present study). It could be of

interest to study the influence of the substrate cleaning procedure (Hf-determined, HCl passivated, or flash-annealed, for instance) and to look at the film/substrate interfaces in further detail to understand the structural, chemical and electronic modifications occurring together with changes of the sample cleaning method employed. All these different surface preparation procedures may have significant consequences on the electrical performance of the final devices.

# French summary of the thesis

## Résumé:

L'objectif de ce travail a été d'étudier, à l'échelle atomique et depuis les tous premiers stades, la croissance de l'oxyde de praséodyme sur des substrats de silicium orientés (111) et (001). L'étude se focalise sur la caractérisation des propriétés structurales, chimiques, et électroniques de  $\text{Pr}_2\text{O}_3$  déposé sur Si(111) et Si(001), avec un accent plus particulier sur cette dernière surface, importante sur le plan technologique. Cet oxyde de terre-rare a été considéré ces dernières années comme un bon candidat "high-k" pour se substituer à  $\text{SiO}_2$  comme oxyde de grille dans les transistors CMOS, afin de "miniaturiser" davantage les composants électroniques. Dans ce contexte, les propriétés des surfaces et des interfaces commencent à dominer sur les performances des dispositifs à base de silicium, puisque le rapport surface/volume augmente. Comme les basses dimensions de ces structures les rendent difficilement étudiables, la brillance de la radiation synchrotron a été employée pour des analyses de diffraction des rayons X et de spectroscopie de photoélectrons. Les résultats ont été complétés par d'autres techniques de science des surfaces, telles que la microscopie à effet tunnel, la spectroscopie Auger et la diffraction d'électrons à basse énergie. Une couche epitaxiale de  $\text{Pr}_2\text{O}_3$  hexagonal a été trouvée sur Si(111). Sur la surface (001), une couche ordonnée de  $\text{Pr}_2\text{O}_3$  cubique est recouverte par un silicate. Puisque les surfaces atomiquement propres sont le point de départ de la croissance, elles ont également été caractérisées. En particulier, la structure atomique de la surface reconstruite Si(001)- $2 \times 1$  a été analysée.

**MOTS CLÉS :** Couches minces, oxyde de terre-rare, interface, silicium, synchrotron, GIXRD, STM, XPS.

## Introduction générale

L'objectif de cette thèse est l'étude, à l'échelle atomique et depuis les tous premiers stades, de la croissance de l'oxyde de praséodyme sur des substrats de silicium orientés (111) et (001). Cet oxyde de terre rare a été récemment considéré comme un candidat potentiel pour remplacer l'oxyde de grille actuel  $\text{SiO}_2$  dans les transistors CMOS, afin de réduire davantage la taille des dispositifs intégrés sur les substrats de silicium. Cette étude se concentre sur la caractérisation de l'interface entre le film et le substrat via l'association de différentes techniques de science des surfaces. Pour les substrats  $\text{Si}(001)$ , dont le rôle est majeur sur le plan technologique, l'étude de l'influence des paramètres de croissance et la compréhension de la phase formée à l'interface a constitué un aspect important de ce travail.

De manière générale, les matériaux diélectriques jouent un rôle très important dans de multiples applications technologiques, comme le stockage et la transmission des données, les capteurs, et les écrans modernes. La réussite de l'intégration de couches minces diélectriques fonctionnelles innovantes dans la technologie conventionnelle du silicium pourrait permettre la fabrication de nouveaux concepts d'appareils de plus haute performance. Le contrôle de la région interfaciale oxyde/silicium et la compréhension des premiers stades de croissance des couches minces sont des points clés car le rapport surface sur volume augmente dans les petites structures. Ces structures nanométriques sont difficiles à étudier, mais grâce aux techniques basées sur la radiation synchrotron, associées à la microscopie tunnel, des aspects jusqu'à maintenant inexplorés de ces questions ont pu être résolus.

Le contexte de l'étude présentée ici est la nécessité, dans un futur très proche (2008), de remplacer  $\text{SiO}_2$  comme oxyde de grille dans les transistors CMOS. Pour réduire davantage la taille de ces dispositifs, les matériaux diélectriques "High-K" constituent une alternative intéressante. Des oxydes amorphes seront très probablement employés dans une première phase, mais l'industrie micro-électronique souhaite également utiliser des oxydes cristallins avec une interface épitaxiée sur le substrat de silicium d'ici à 2013 [1]. Outre les oxydes perovskites, les films à structures dérivées du fluorure de calcium, tel que  $\text{Pr}_2\text{O}_3$  [2], sont considérés comme des candidats prometteurs pour l'épitaxie sur silicium. Aucune étude à haute résolution de la structure atomique de l'interface formée par ces oxydes de grille avec  $\text{Si}(001)$  n'a été jusqu'ici reportée dans la littérature. Cette étude a également été motivée par le fait que l'interface joue un rôle d'autant plus important que la taille des dispositifs diminue. Par conséquent, pour mieux comprendre les interfaces Pr-oxyde/Si (préparées

selon une méthode de croissance par MBE classique), j'ai étudié les trois systèmes suivant : les tous premiers stades de la croissance de  $\text{Pr}_2\text{O}_3$  sur  $\text{Si}(111)$  par LEED et STM ; la surface propre  $\text{Si}(001)$  reconstruite  $2 \times 1$  par LEED, STM, XPS et SXRD, ainsi que les premiers stades de la croissance de  $\text{Pr}_2\text{O}_3$  sur  $\text{Si}(001)$ , et la phase formée à l'interface film/substrat, par LEED, STM, XPS et SXRD.

Dans ce mémoire, le système modèle  $\text{Pr}_2\text{O}_3/\text{Si}(111)$  a été étudié en raison de la croissance monocristalline de haute qualité de  $\text{Pr}_2\text{O}_3$  sur la surface  $\text{Si}(111)$  [3]. Puis le système  $\text{Pr}_2\text{O}_3/\text{Si}(001)$  a été étudié dans l'optique d'application technologique. Les premiers stades de la croissance de  $\text{Pr}_2\text{O}_3$  sur  $\text{Si}(001)$  pour des épaisseurs de films jusqu'à 3-4 nm ont été étudiés. Notre approche se focalise sur des études à l'échelle atomique de l'interface Pr-oxyde/ $\text{Si}(001)$  par plusieurs techniques complémentaires de surface in-situ (LEED, AES, STM). Le LEED révèle si une surface est ordonnée ou non et donne des informations sur sa symétrie (information macroscopique); l'AES fournit des informations chimiques sur la surface et le STM présente sa morphologie (information nanoscopique). Ces techniques de science des surfaces sont disponibles dans le laboratoire de caractérisation des surfaces (SCL) de la ligne de lumière ID32 à l'installation européenne de radiation synchrotron (ESRF). Associées à ces techniques, la diffraction des rayons X à incidence rasante utilisant la radiation synchrotron sur ID32, a permis de résoudre la structure des dépôts. Un modèle expérimental de l'interface  $\text{Pr}_2\text{O}_3/\text{Si}(001)$  a pu être proposé. Ainsi une précieuse contribution a pu être apportée à la discussion controversée dans la littérature sur l'existence d'une superstructure  $3 \times 1$  à l'interface (siliciure ou Pr-oxyde). Ces résultats ont été également complétés par des mesures XPS qui fournissent des informations chimiques sur les couches d'oxydes (surface et interface avec le substrat).

De plus, l'influence de la pression partielle d'oxygène, ainsi que celle de la température de dépôt et de traitements thermiques post-dépôts, sur la croissance, sont aussi discutés.

En étudiant des phénomènes prenant place à des échelles de quelques nanomètres, nous voulions mieux comprendre les interactions et les modifications de la surface du silicium lors de la formation d'une interface avec une couche d'oxyde. Pour les techniques de rayons X utilisées, une couche d'oxyde ultra mince ( $\approx 1$  nm) est requise afin de maximiser la contribution de l'interface par rapport au signal total. Pour assurer la propreté des surfaces de silicium et donc la qualité des couches minces, les conditions UHV étaient nécessaires et ont été maintenues tout au long de la préparation et de la caractérisation des échantillons. Par ailleurs, il faut souligner que l'oxyde de praséodyme est très instable

à la pression atmosphérique. L'introduction de couches protectrices de silicium sur l'oxyde n'était pas souhaitable pour nos mesures puisqu'elles auraient compliquées l'analyse des données de part leur contribution au signal RX et leur interaction/réaction avec l'oxyde.

Cette thèse s'organise comme suit :

Le Chapitre 1 présente un aperçu de l'état de l'art dans le domaine des oxydes "High-K" ainsi que le contexte et les origines du choix de  $\text{Pr}_2\text{O}_3$ . Ses propriétés en tant que matériau massif sont résumées ainsi que les plus récents et pertinents résultats sur la croissance de cet oxyde sur et Si(111) et Si(001). Les motivations scientifiques ainsi que le but du travail reporté dans cette thèse sont ensuite spécifiés.

Le Chapitre 2 explique les techniques expérimentales utilisées au cours de la thèse et rappelle les principes théoriques fondamentaux utilisés pour l'analyse des résultats présentés dans les chapitres suivant.

Le Chapitre 3 reporte les premiers stades de formation de la couche de Pr-oxyde sur la surface du substrat Si(111), étudiés par LEED et STM. Les résultats sont corrélés avec ceux de Jeutter et Moritz qui ont obtenu un modèle structural à l'échelle atomique de l'interface  $\text{Pr}_2\text{O}_3/\text{Si}(111)$  en utilisant la diffraction de surface (SXRD) [4].

La croissance du Pr-oxyde sur Si(001)- $2\times 1$  est reportée dans les chapitres 4 et 5. Le Chapitre 4 décrit les résultats de la croissance du Pr-oxyde sur Si(001) sous conditions UHV, après avoir donné quelques détails sur la préparation de la surface Si(001)- $2\times 1$ . Sous UHV, une séparation de phase est observée et un Pr-siliciure apparaît au-delà d'une certaine épaisseur critique. L'influence de traitement thermique post-dépôt sous des conditions de température et de pression variées est également reportée dans ce chapitre.

Le Chapitre 5 résume les principaux résultats de différentes tentatives pour optimiser les paramètres de dépôt de  $\text{Pr}_2\text{O}_3$  sur Si(001), dans une étroite fenêtre de température et de pression. De plus, ce chapitre présente une analyse chimique et structurale détaillée des échantillons optimisés et décrit les résultats de la caractérisation d'une phase interfaciale  $3\times 1$ .

La thèse se clôt avec un résumé général et conclut avec quelques suggestions, motivées par les présents résultats, pour de prochaines études du système  $\text{Pr}_2\text{O}_3$  sur silicium.

## Chapitre 1

Notre compréhension des propriétés physiques et chimiques des oxydes demeure loin derrière celle des métaux ou des matériaux semiconducteurs. L'utilisation de la radiation synchrotron a cependant permis des avancées majeures dans l'étude de ces systèmes, en particulier lorsqu'ils sont examinés sous forme de couches minces. L'association de la diffraction de surface et de la spectroscopie avec d'autres techniques de surface, telles que la diffraction à basse énergie (LEED), la spectroscopie Auger (AES) ou encore la microscopie à effet tunnel (STM) peut permettre une analyse très poussée des systèmes complexes que sont les oxydes.

Ce travail de thèse concerne l'étude de l'interface entre l'oxyde de praséodyme  $\text{Pr}_2\text{O}_3$  et des substrats de silicium. Il se place dans le contexte des résultats électriques actuels sur des dispositifs réalisés avec  $\text{Pr}_2\text{O}_3$  comme oxyde de grille, qui révèlent des problèmes associés à la forte densité d'états électroniques à l'interface oxyde/Si [64]. Des études plus fondamentales sur cette interface sont par conséquent nécessaires.

Le système binaire Pr-O présente un diagramme de phase très complexe, avec différentes stœchiométries possibles, allant de la phase  $\text{Pr}_2\text{O}_3$ , la plus pauvre en oxygène, à  $\text{PrO}_2$ , phase la plus riche en oxygène. Les propriétés structurales de  $\text{Pr}_2\text{O}_3$  détaillées dans ce chapitre repose sur l'existence de 2 phases : hexagonale ou cubique.  $\text{Pr}_2\text{O}_3$  hexagonal croit sur Si(111) avec un désaccord de maille de -0.5% et  $\text{Pr}_2\text{O}_3$  cubique croit sur Si(001) selon le plan (101) avec un désaccord de maille de 2% et -3.8% selon respectivement la largeur et la longueur de la maille rectangulaire (101).

Des travaux in situ réalisés par RHEED [3,82,90] sur le système  $\text{Pr}_2\text{O}_3/\text{Si}(001)$  ont montré l'existence d'une superstructure  $3\times 1$  aux premiers stades de la croissance. Cette dernière disparaît au delà d'une épaisseur critique de 0.5 nm. Cependant aucune données quantitatives n'existe à ce jour sur la nature de cette phase interfaciale. Dans notre étude, nous nous sommes notamment intéressés à cette phase ordonnée à l'interface film/substrat, dont la structure atomique a été analysée par diffraction.

## Chapitre 2

La préparation des échantillons a été réalisée sous UHV dans le laboratoire de caractérisation de surface de la ligne de lumière ID32 (SCL). Le SCL est équipé de deux bâtis UHV dont les descriptions sont détaillées dans ce chapitre. Après le dépôt de  $\text{Pr}_2\text{O}_3$  et l'analyse de la surface par STM et LEED, les échantillons sont transférés sous environnement UHV sur les équipements de mesure de la ligne de lumière (mesures de diffraction ou de photoémission) via des chambres UHV portatives communément appelées "baby chambers". Les techniques de caractérisation disponibles dans le SCL (STM, LEED, et AES) sont dans un premier temps décrites. Par la suite, les deux cabines expérimentales d'ID32 sont présentées et les concepts de diffraction de surface et de XPS sont explicités. On pourra retenir que le STM nous apporte une information locale sur la morphologie de surface des échantillons, tandis que le LEED, l'AES, l'XPS et la technique de diffraction en générale permettent de collecter une information moyennée sur toute la surface de l'échantillon. Les concepts fondamentaux relatifs aux expériences de diffraction (mesures de réflectivité, mesures dans le plan (H,K) et long des directions off-spéculaires L) sont détaillés à la fin de ce chapitre.

## Chapitre 3

Les premiers stades de croissance par MBE de  $\text{Pr}_2\text{O}_3$  sur des surfaces Si(111) propre à l'échelle atomique ont été étudiés, depuis les premières étapes de la nucléation jusqu'à la coalescence des premières couches d'oxyde. Les substrats de silicium utilisés ont été prélevés dans des plaquettes de  $350 \mu\text{m}$  d'épaisseur disponibles sur le marché. Le LEED et le STM ont permis la caractérisation de la surface des dépôts d'oxyde.

Pour de très faible taux de couverture, les particules d'oxyde se déposent sur les lignes de dimères de la surface du silicium formant des structures triangulaires ouvertes. Lorsque le taux de couverture augmente, des îlots en forme de triangles équilatéraux 2D sont observés. Ils sont homogènes en épaisseur et leur taille latérale est comprise entre 15 et 20 nm pour un taux de couverture de 0.7 monocouche (1 monocouche correspond à la hauteur de la maille unité de  $\text{Pr}_2\text{O}_3$  hexagonal, i.e. 0.6 nm). Au delà d'une monocouche déposée, la coalescence des îlots forme une couche "plate" à l'échelle atomique et qui est pseudomorphe à la maille unité  $1 \times 1$  du Si(111). Les clichés LEED correspondant sont en accord avec la croissance épitaxiale des plans (001) de la phase "hexagonale" de  $\text{Pr}_2\text{O}_3$ , selon une orientation spécifique. En effet, stricto sensu il s'agit d'un système cristallin trigonal et

par conséquent les plans (001) ont une symétrie d'ordre 3. Grâce aux topographies STM l'épaisseur d'une couche complète d'oxyde est déterminée à 0.52 nm, valeur en accord avec les 0.6 nm de hauteur de la maille unité de  $\text{Pr}_2\text{O}_3$  hexagonal. Ces résultats sont en très bon accord avec ceux de Jeutter et Moritz (mesures de diffraction de surface).

## Chapitre 4

Le but du reste de cette étude est d'établir un modèle structural pour le système  $\text{Pr}_2\text{O}_3/\text{Si}(001)$ . Des films d'oxyde de praséodyme ont été déposés sur des substrats  $\text{Si}(001)$  de très faible miscut ( $0.01^\circ$ ) sous UHV sur le bâti R2P2 décrit dans le Chapitre 2. Les premiers stades de la croissance ont été étudiés in situ par LEED, STM, et AES, afin d'obtenir des informations sur l'arrangement structural, la morphologie de surface et la composition chimique des films d'oxydes. Les résultats présentés par LEED et STM se focalisent sur les premiers stades de croissance et la nucléation du Pr-oxyde sur  $\text{Si}(001)$ . Les échantillons sont ensuite transférés sur la ligne de lumière sous environnement UHV afin de réaliser des mesures de diffraction et de photoémission. La température de dépôt des échantillons étudiés était de  $550^\circ\text{C}$ , température typiquement reportée dans la littérature [3,129]. L'effet du miscut de la surface est également discuté dans ce chapitre, avec à priori des domaines de croissance plus grands lorsque le miscut augmente.

Nous avons montré la nucléation de Pr-oxyde et Pr-silicate sur la surface  $\text{Si}(001)$  et la formation d'une couche 2D, présentant une superstructure  $3\times 1$ , suivie, au delà d'une épaisseur critique de 0.6 nm, par une transition vers une croissance 3D accompagnée d'une séparation de phase et de la formation d'îlots de Pr-siliciure. Étant donné qu'un siliciure n'est pas souhaitable pour les applications précédemment citées, nous avons étudié l'effet de la température en réalisant des dépôts sous UHV à température ambiante, suivis par des recuits thermiques sous différentes conditions de pression partielle d'oxygène et température. Nous avons constaté que les films élaborés dans de telles conditions ne présentent pas de séparation de phase mais sont désordonnés. Les échantillons réalisés sous UHV à  $550^\circ\text{C}$  et ceux réalisés à température ambiante ont de fortes densités d'états électroniques proche du niveau de Fermi, rendant leur application potentielle comme oxyde de grille problématique.

## **Chapitre 5**

L'objet de ce chapitre est la caractérisation de films minces d'oxyde de praséodyme déposés sous pression partielle d'oxygène dans la gamme de  $10^{-8}$  mbar, afin de supprimer la formation de Pr-siliciure. Un intérêt particulier a été porté sur l'interface film/substrat. Une part conséquente de notre étude a consisté à ajuster finement les paramètres de pression (dans une gamme inférieure à  $1 \times 10^{-7}$  mbar, pour ne pas développer une couche de  $\text{SiO}_2$ ) et de température (autour de 500 et 650 °C) pour optimiser les propriétés structurales d'une couche interfaciale ordonnée présentant une superstructure  $3 \times 1$ . Le taux de dépôt a été fixé à 0.02 nm/min. Les résultats présentés dans ce chapitre concernent trois différentes températures (500, 550 et 590 °C) et trois différentes pressions ( $2 \times 10^{-10}$ ,  $2 \times 10^{-8}$  et  $5 \times 10^{-8}$  mbar). Des mesures de diffraction, de photoémission et d'AES ont été réalisées sur ces échantillons. Aucun cliché de diffraction n'a pu être obtenu grâce au LEED pour des épaisseurs déposées supérieures à 0.3 nm et lorsque la pression partielle d'oxygène est supérieure à  $2 \times 10^{-8}$  mbar. Ce résultat témoigne de surfaces désordonnées.

La dernière partie de ce chapitre présente la caractérisation détaillée de la phase interfaciale ordonnée  $3 \times 1$ . Des mesures de réflectivité ont permis d'estimer son épaisseur à 0.5 nm et sa densité électronique à  $1.6 \text{ e}^-/\text{\AA}^3$ . Des mesures de diffraction dans le plan (H,K) ont permis d'identifier sa structure, similaire à celle de  $\text{CaF}_2$ . En corrélant cette identification structurale avec la densité électronique obtenue par réflectivité, nous avons pu déterminer que la phase cubique de  $\text{Pr}_2\text{O}_3$  correspond à la superstructure interfaciale  $3 \times 1$ . La structure atomique de cette couche a été résolue à partir d'une large série de données de diffraction de surface (SXRD). Le modèle atomique trouvé (Fig. 5.26) permet d'expliquer comment les atomes du Pr-oxyde s'agencent sur la surface  $\text{Si}(001)$ . Il est en accord qualitatif avec des calculs théoriques [91]. Des mesures XPS résolues en angle ont permis d'identifier une couche désordonnée de  $\text{Pr}_2\text{Si}_2\text{O}_7$  située au-dessus de cette couche ordonnée de 0.5 nm d'épaisseur.

## **Conclusion Générale et Perspectives**

### **Conclusion Générale**

Le but de cette thèse était d'élucider les propriétés interfaciales de l'oxyde de  $\text{Pr}_2\text{O}_3$  sur des substrats de silicium, à l'échelle atomique, avec un intérêt particulier pour la surface  $\text{Si}(001)$  d'importance technologique.

La croissance de  $\text{Pr}_2\text{O}_3$  sur des substrats  $\text{Si}(111)$ , sous conditions UHV, révèle une couche pseudomorphe, supprimant la reconstruction  $7\times 7$  de la surface  $\text{Si}(111)$  et s'attachant au  $\text{Si } 1\times 1$  massif. La croissance d'îlots 2D, en forme de triangles équilatéraux est observée sur les terraces de cette surface. L'épaisseur d'une couche complète déterminée par le STM est de 0.52 nm, en bon accord avec la hauteur de la cellule unité de  $\text{Pr}_2\text{O}_3$  hexagonal.

L'étude de la croissance de Pr-oxyde sur  $\text{Si}(001)$  sous UHV a montré l'apparition d'une superstructure  $3\times 1$  a été identifiée pour des taux de couverture subnanométriques. Au-delà d'une épaisseur de 0.6 nm pour la couche d'oxyde, des îlots 3D de  $\text{PrSi}_2$  se forment à une température de dépôt de 550 °C. Ces îlots ont une large distribution en hauteur et sont ancrés dans une couche 2D de Pr-silicate, au-dessus de la couche ordonnée  $3\times 1$ . Les dépôts à température ambiante sous UHV conduisent à des couches de Pr-oxyde désordonnées (mélange de  $\text{PrO}_x$  et  $\text{Pr}_2\text{Si}_2\text{O}_7$ ). Des traitements thermiques post-dépôt sous oxygène sur ces films démontrent leur forte sensibilité aux paramètres de température et de pression. Lorsqu'ils sont oxydés sous  $10^{-7}$  mbar à 550 °C, la formation d'une couche de  $\text{SiO}_2$  est probable à l'interface film/substrat.

Nous avons analysés les tous premiers stades de croissance des films de Pr-oxyde sur  $\text{Si}(001)$  sous pression partielle d'oxygène dans la gamme de  $10^{-8}$  mbar ainsi que la superstructure  $3\times 1$  formée à l'interface Pr-oxyde/Si. Pour une condition optimale de  $5\times 10^{-8}$  mbar  $\text{O}_2$  et 550 °C, une couche interfaciale ordonnée de  $\text{Pr}_2\text{O}_3$  de 0.5 nm d'épaisseur présente une superstructure  $3\times 1$ . La structure atomique de cette couche interfaciale a été déterminée à partir d'une large série de données de diffraction de surface (SXRD). Une couche désordonnée de  $\text{Pr}_2\text{Si}_2\text{O}_7$  se forme au-dessus de cette couche ordonnée. Des études ex-situ reportées dans la littérature ont montré qu'un tel silicate constitue une couche transitoire au-dessus de laquelle la croissance d'une phase cristalline de  $\text{Pr}_2\text{O}_3$  cubique se forme [51,92].

Pour conclure, ce travail a combiné plusieurs techniques complémentaires de science de surface, i.e. SXRD, STM, LEED, AES et XPS, pour étudier la transition entre un substrat cristallin et une couche désordonnée (Pr-silicate) par l'intermédiaire d'une couche interfaciale ordonnée de 0.5 nm d'épaisseur. Ces résultats sont originaux dans le domaine d'étude et pour l'application d'oxydes "High-K" sur des substrats  $\text{Si}(001)$ . En particulier, les résultats quantitatifs de l'étude à l'échelle atomique de l'interface de  $\text{Pr}_2\text{O}_3/\text{Si}(001)$  pourraient être utilisés comme modèle pour le cas de la croissance sur  $\text{Si}(001)$  d'autres oxydes de terres rares présentant des propriétés similaires à celles de  $\text{Pr}_2\text{O}_3$ , tels que  $\text{Gd}_2\text{O}_3$ ,  $\text{Nd}_2\text{O}_3$ ,  $\text{Y}_2\text{O}_3$ , etc.

## Perspectives

### Pr<sub>2</sub>O<sub>3</sub> cubique épitaxié sur Si(001)?

Comme précédemment mentionné, une question qui persiste au-delà de cette étude est le point et le mode d'apparition de la phase Pr<sub>2</sub>O<sub>3</sub> cubique au-dessus de la couche de silicate, lorsqu'on poursuit le dépôt. Il serait ainsi intéressant d'examiner l'évolution structurale de couches d'oxyde plus épaisses. En particulier, une question intéressante, qui peut être résolue par des mesures de diffraction de surface, est de savoir si la structure à l'interface change quand la phase cubique du Pr<sub>2</sub>O<sub>3</sub> apparaît. Une vitesse de dépôt beaucoup plus grande que celle possible avec l'évaporateur utilisé dans cette étude serait très probablement nécessaire, afin de réduire la diffusion du silicium vers la surface et limiter l'épaisseur de la couche de silicate.

Les différences entre les paramètres de dépôts utilisés dans cette étude et ceux utilisés par Osten, qui a obtenu une couche épitaxiée de Pr<sub>2</sub>O<sub>3</sub> cubique sur Si(001) [3, 50, 52] (avec des films bien plus épais que les nôtres), sont les suivantes :

1. Nettoyage du substrat : nous avons utilisé le recuit à haute température sous UHV alors que Osten a travaillé sur des substrats avec des terminaisons d'hydrogène (obtenues par trempage dans une solution d'acide fluoridrique).
2. Taux de dépôt : au moins 100 fois supérieur dans le cas de Osten par rapport à nos conditions de dépôt.
3. Gamme de pression : nous pouvons contrôler la pression partielle d'oxygène jusqu'aux conditions UHV tandis que Osten a travaillé sous des pressions partielles d'oxygène résiduel de l'ordre de  $5 \times 10^{-8}$  mbar.
4. Notre étude a été menée sur des surfaces de très faible miscut (en dessous de  $0.1^\circ$ ) tandis que Osten a travaillé sur des plaquettes de silicium de quatre pouces, disponibles sur le marché, et présentant un miscut de  $0.3^\circ$  [?].

### Les positions atomiques dans le sous réseau d'oxygène

Des mesures d'ondes stationnaires RX combinées avec des mesures de XPS pourraient aider à collecter plus d'information sur la position des atomes d'oxygène dans la couche interfaciale de Pr<sub>2</sub>O<sub>3</sub> ordonnée. Comme ces atomes diffusent beaucoup moins que les atomes de

Pr, l'information structurale que nous avons obtenues avec les mesures de diffraction sur les atomes d'oxygène est beaucoup moins fiable que celle obtenue pour les atomes de Pr.

#### L'influence du miscut du substrat

Par rapport aux observations reportées dans la section 4.3.1, nous supposons qu'un plus grand miscut, conduisant à la présence d'un seul type de terrasses sur Si(001), i.e. des marches d'hauteur atomique double, favoriserait la formation d'un seul domaine  $3 \times 1$ . Une autre question intéressante à examiner serait l'influence du miscut du substrat ou de la plus forte densité de marches de la surface du substrat sur le processus de nucléation et les propriétés de la croissance.

#### L'influence de la méthode de nettoyage du substrat sur les propriétés interfaciales

Une des principales leçons que nous avons apprises au fils des études présentées dans cette thèse concerne la nécessité d'avoir des substrats monocristallin de bonne qualité et une attention particulière doit être consacrée à leur préparation (huit mois de la thèse). Il pourrait être intéressant d'étudier l'influence de la procédure de nettoyage des substrats (terminaisons-Hf, passivation HCl, recuit thermique rapide à haute température, par exemple) sur les interfaces film/substrat de manière à comprendre les modifications structurales, chimiques et électroniques liées à la méthode de nettoyage employée. Toutes ces procédures de préparation de la surface pourraient avoir des conséquences majeures sur les performances électriques des dispositifs finaux.



# List of Acronyms

AES	Auger Electron Spectroscopy
ARXPS	Angle-resolved X-Ray Photoelectron Spectroscopy
BG	Band Gap
CMOS	Complementary Metal Oxide Semiconductor
CTR	Crystal Truncation Rod
EOT	Equivalent Oxide Thickness
ESRF	European Synchrotron Radiation Facility
FT	Fourier Transformation
FWHM	Full Width at Half Maximum
GIXRD	Grazing Incidence X-Ray Diffraction
LEED	Low Energy Electron Diffraction
MBE	Molecular Beam Epitaxy
MFP	Mean Free Path
MIM	Metal Insulator Metal
ML	MonoLayer
MOCVD	Metal Organic Chemical Vapor Deposition
MOSFET	Metal Oxide Semiconductor Field Effect Transistor
PLD	Pulse Laser Deposition

QCM	Quartz Crystal Microbalance
RE	Rare Earth
RHEED	Reflection High Energy Electron Diffraction
r.l.u.	Reciprocal Lattice Unit
RGA	Residual Gas Analyzer
RSM	Reciprocal Space Map
SCL	Surface Characterization Laboratory
SEM	Scanning Electron Microscopy
SPM	Scanning Probe Microscope
STM	Scanning Tunneling Microscope
SXRD	Surface X-Ray Diffraction
TEM	Transmission Electron Microscopy
UHV	Ultra High Vacuum
XPS	X-Ray Photoelectron Spectroscopy
XRD	X-Ray Diffraction
XRR	X-Ray Reflectivity
XSW	X-Ray Standing Wave

# Appendix A:

## The Si(001)- $2\times 1$ reconstructed surface

SXRD results collected on a Si(001)- $2\times 1$  reconstructed surface are summarized in this appendix. Our results of the investigation on the atomic structure of the Si(001)- $2\times 1$  reconstructed surface favors a nearly symmetry dimer model over an highly asymmetry one. The symmetry or asymmetry of the dimers on this surface is a subject still under discussion in the literature, as reviewed in the scientific background session below.

In addition, the initial stages of the oxidation of the Si(001)- $2\times 1$  reconstructed surface with molecular oxygen was studied. The idea was to grow a template SiO<sub>x</sub> layer prior to the Pr-oxide growth. In this context we took the opportunity to investigate the Si surface behavior at the very beginning of the oxidation. Preliminary results of this study are presented in the last section of this appendix.

### Scientific background

The surface truncation of a Si bulk crystal along a (001) plane gives rise to two dangling bonds per surface atom. The surface energy can be lowered down by joining two neighboring Si atoms to form dimers. This process leads to a  $2\times 1$  unit cell and an energy reduction of about 2 eV/dimer [151]. Although the dimerization already reduces the total number of dangling bonds by half, there is still one dangling bond left per surface atom. If the two dangling bonds of each dimer are both half filled, the dimer stays symmetric and the surface is metallic. Such a metallic behavior is energetically unstable [152] for semiconductor

surfaces in general. The surface energy can be minimized further by making one of the two dangling bonds unfilled and the other one completely filled, which leads to buckled dimers and a semiconducting surface. The energy reduction here is about 0.1 eV/dimer for the Si(001) surface [151].

This small gain in energy makes difficult any theoretical prediction in determining whether the Si dimers are buckled or not, in particular for the room temperature case [153]. This difficulty does not exist for Ge and diamond (001) surfaces as the corresponding energy changes are relatively big. Many theoretical calculations have been carried out to study whether the Si dimers are symmetric or asymmetric [151, 153–157]. Most of them agree with an asymmetric model. However, calculations supporting symmetric model can be found, for instance, in Refs. [153, 155, 157].

Several groups have studied the Si(001)- $2\times 1$  reconstructed surface by XPS. For example Uhrberg *et al.* [158] analyzed the Si2p core level spectrum, which shows multiple features, with at least five different chemical components, including the contribution from the bulk, Si dimers and the second silicon layer. The interpretation of their results led to the conclusion of asymmetric dimers. However, due to the complexity of the Si2p spectrum, the interpretation is less convincing. Room temperature STM has observed the Si dimer structure [159, 160] that appears to be symmetric. This observation has been interpreted as the result of thermal flipping of asymmetric dimers at room temperature [161].

Based on diffraction techniques, the Si(001)- $2\times 1$  surface has been investigated by Jayaram *et al.* [162] using transmission electron diffraction, by Over *et al.* [163] using LEED I-V, and by Takahasi *et al.* [164] and Felici *et al.* [165] using SXRD. All of these studies concluded with an asymmetric dimer. However, for the previous SXRD work, the quality of the data is rather poor in terms of the size of the data set (number of rods) and how far in the L direction those rods have been measured. We will show with our study that without the use of a large data set the result of a SXRD modeling can be inconclusive.

## **SXRD measurements and data analysis**

The Si(001)- $2\times 1$  surface was prepared in the SCL, as described in section 4.1, and measured *in situ* by SXRD using a UHV baby chamber (cf. section 2.5.1). The x-ray energy used for

this experiment was 17.9 keV and the incident angle was  $0.1^\circ$ . Totally 24 fractional order rods, consisting of 1550 non-equivalent structure factors, were recorded by rocking scans at room temperature for one of the two  $90^\circ$  rotational domains. In addition, four symmetry equivalent fractional order rods were measured for error estimation. The surface quality was monitored using the peak width  $\Delta k$  of the in-plane reflection  $(1/2\ 0\ 0.03)$ . As shown in Fig. 36, the peak intensities and widths of this reflection were measured to be identical before and after the 43 hour data collection for the fractional order rods, demonstrating the cleanness of the sample environment maintained by the baby chamber. The peak width corresponds to a coherently scattering domain of  $\approx 1.3\ \mu\text{m}$ , which can be only achieved with a high quality surface.

For the data analysis, the structure factors  $|F(\mathbf{Q})|^2$  were first retrieved from the rocking scans after peak integration and intensity corrections, following the procedures described in the end of section 5.4.2. A  $\chi^2$  fitting to the measured values of  $|F(\mathbf{Q})|^2$  using the computer program “FIT” developed by Oliver Bunk for SXRD data analysis was then performed to determine the surface structure.

The model used in the  $\chi^2$  fitting has a  $2\times 1$  unit cell that contains 32 Si atoms in 16 layers. In the initial model all the atoms were placed at their bulk positions except the top two Si atoms, which were brought closer together to form a symmetric dimer. During relaxation of the structure, the movements of the top 10 Si layers (Si 1 - 20) and the bottom 6 Si layers (Si 21 - 32) were restricted by  $pm$  and  $p2mm$  symmetries, respectively. The former permitted the dimer to tilt along the dimerization direction. To allow the dimer to tilt in either way, a second  $2\times 1$  unit cell, which is the mirror image of the first one with respect to the  $\times 1$  direction, was introduced and the diffraction contributions from these two unit cells were added coherently. Note that all the Y coordinates were fixed as a result of the symmetry constraints.

In the final refinement, performed by Tien-Lin LEE, in-plane and out-of-plane Debye-Waller B factors and a scale factor were also included, in addition to the positional parameters. Fig. 37 shows the best fit of such a model to the data and Table 6 lists the values of the fitting parameters. The corresponding structure is depicted in Fig. 38(a). The  $\chi^2$  of the best fit is 2.94 and very good agreement between the fit and the data can be seen in Fig. 37. This analysis shows a dimer tilt angle of only  $0.8^\circ$ , which is much smaller than the tilt angles measured previously ( $\approx 20^\circ$ ) by SXRD [164, 165] and LEED I-V [166] and suggests an nearly symmetric dimer. Our measured dimer bond length (0.2407 nm) is

about 2.4% longer than the natural Si-Si bond length (0.235 nm).

To test the asymmetric dimer models reported previously, we repeated the  $\chi^2$  fitting with the only change that introduces and fixes a height difference ( $Z1 - Z2$ ) of 0.065 nm between the two dimer atoms, which forces the dimer to be asymmetry and is very close to the values reported by other measurements [164–166]. The best fit to the data and the corresponding structure based on this asymmetric dimer are plotted in Fig. 39 and Fig. 38(b), respectively. The values of the fitting parameters are given in Table 7. The dimer tilt angle in this case is  $15.3^\circ$  and the dimer bond length is 0.2457 nm. The  $\chi^2$  of the best fit increases significantly to 14.72, indicating a much poorer agreement, which is already evident in Fig. 39. Our SXRD analysis therefore strongly favors a nearly symmetric dimer structure for the Si(001)- $2\times 1$  surface. Further experiments are under way to make sure that this low asymmetry of the Si dimers we have observed did not result from a particular sample preparation.

It can be seen from Fig. 37 and 39 that if much fewer rods are considered with data points measured only at low L included in the fitting, good fit can be achieved with an either symmetric or asymmetric dimer model. For conclusive determination of the Si(001)- $2\times 1$  surface structure, a large data set is therefore mandatory for a SXRD analysis.

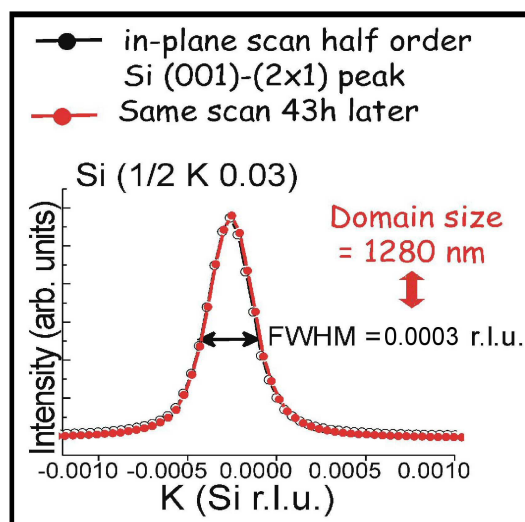


Figure 36: Two in-plane K scans of the Si(1/2 0 0.03) reflection measured in a baby chamber. The second scan was recorded 43 hours after the first one.

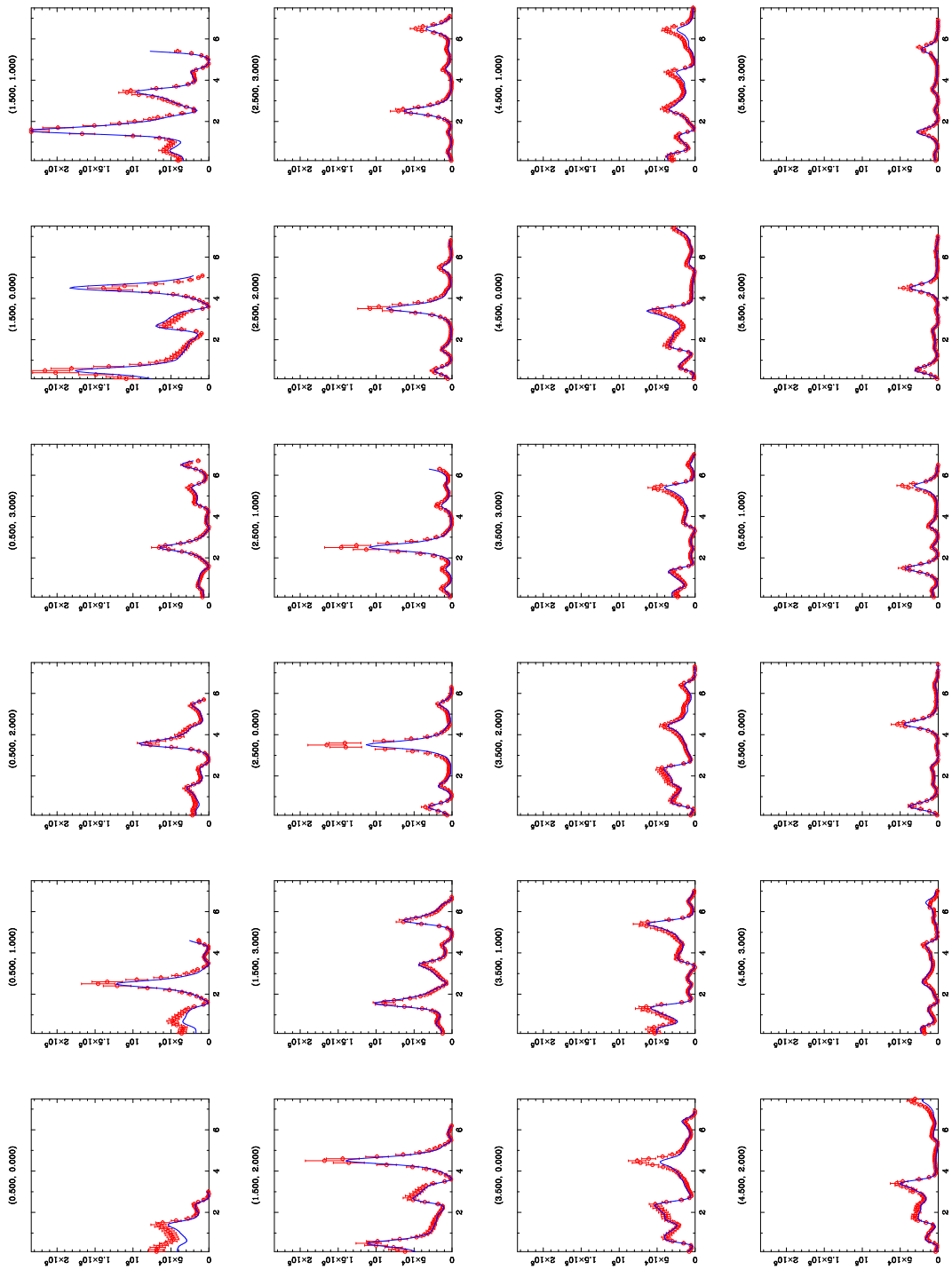


Figure 37: 24 Fractional order rods measured from a Si(001)- $2 \times 1$  surface and the best fit of an asymmetric dimer model to the data without constraints on the height difference between Si1 and Si2.

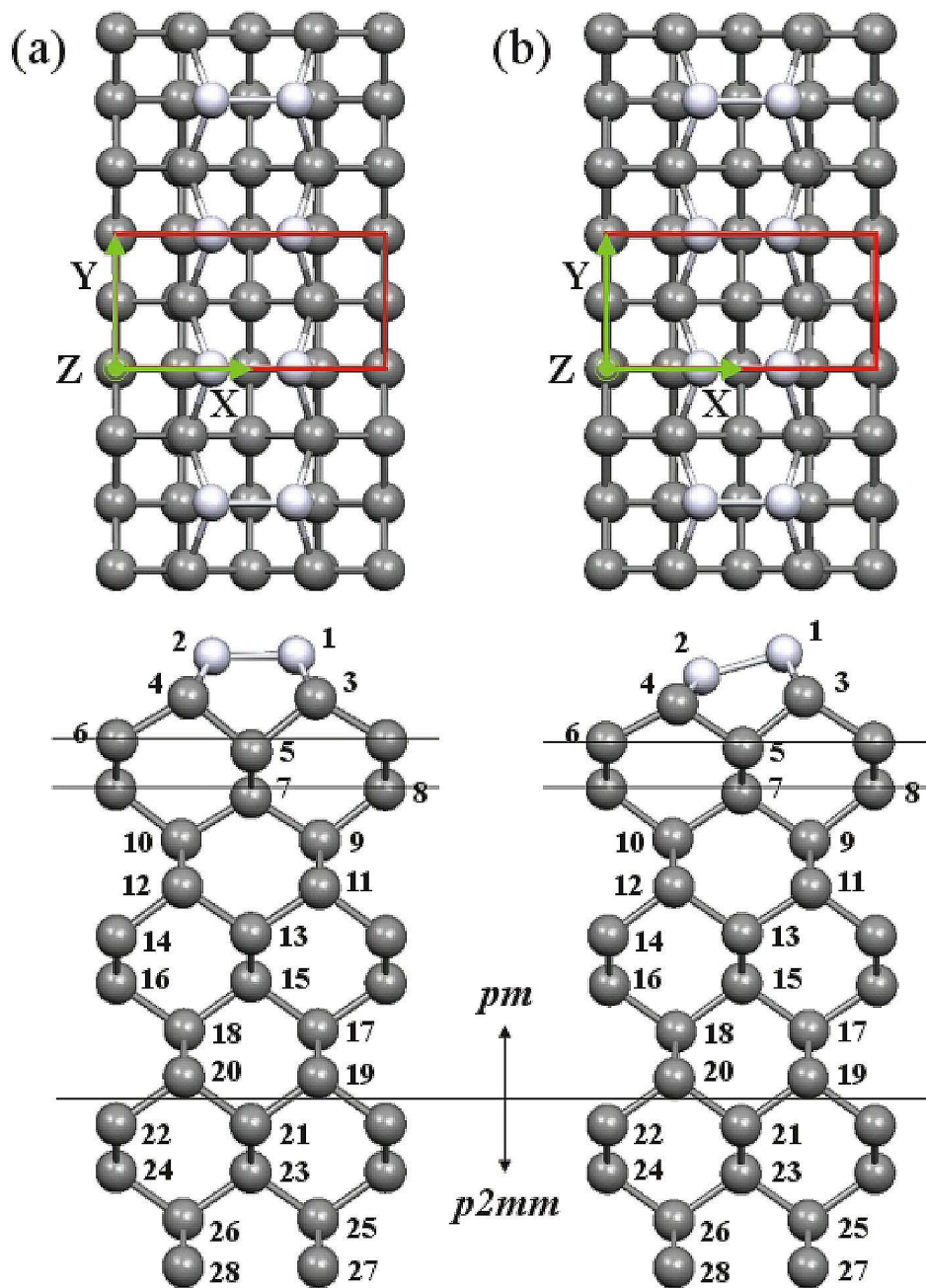


Figure 38: Si(001)-2x1 surface structures determined by the best fits to the SXRD data without (a) and with (b) fixing the height difference between Si1 and Si2 to 0.065 nm.

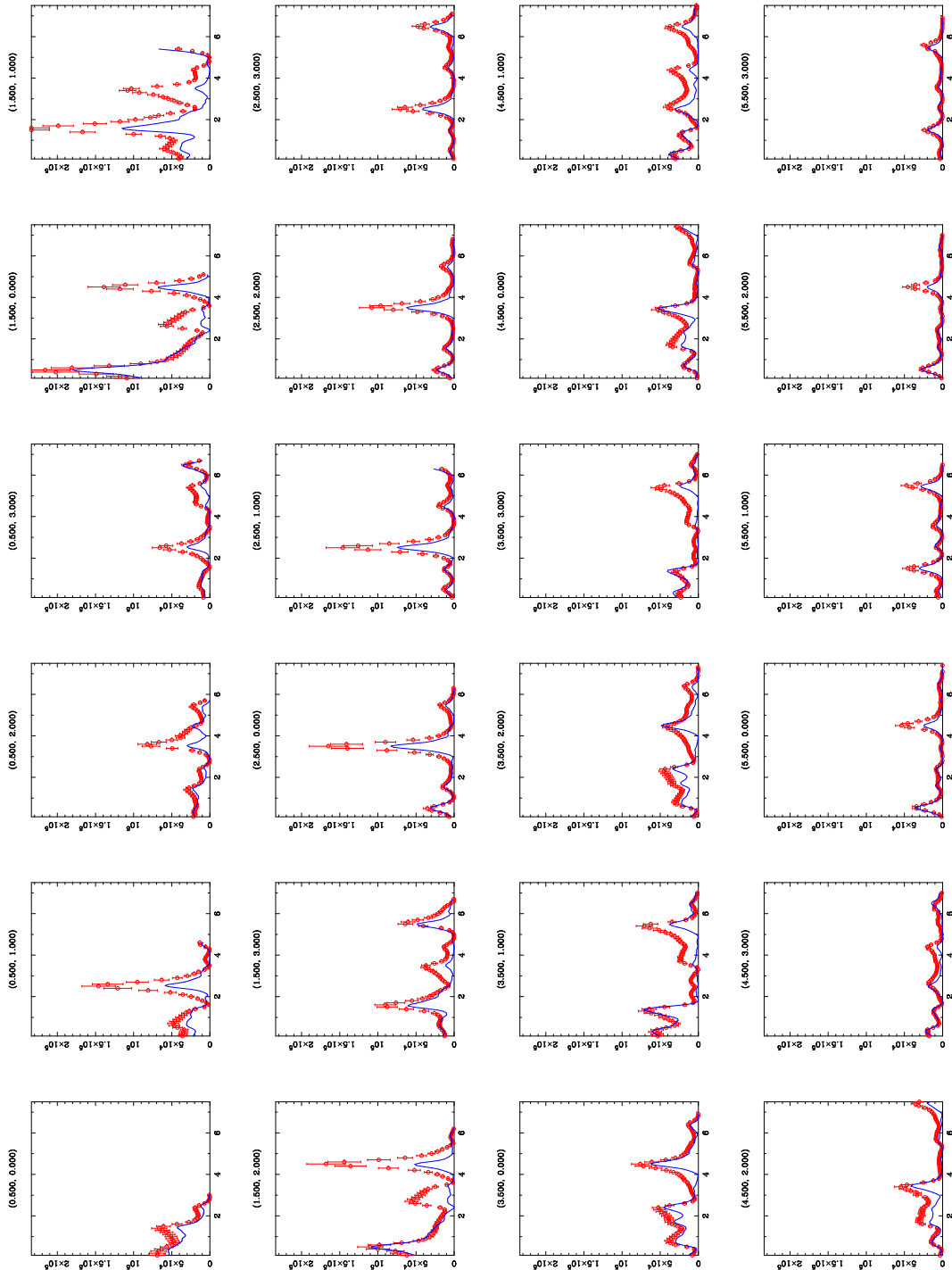


Figure 39: 24 Fractional order rods measured from a Si(001)-2 $\times$ 1 surface and the best fit of an asymmetric dimer model to the data with the height difference between Si1 and Si2 fixed to 0.065 nm.

Si	$\Delta X$	$\delta X$	$\Delta Y$	$\Delta Z$	$\delta Z$
1	-0.166	0.0003	0.000	-0.019	0.0003
2	0.207	0.0003	0.000	-0.025	0.0004
3	-0.023	0.0002	0.000	0.003	0.0006
4	0.032	0.0003	0.000	0.005	0.0005
5	0.002	0.0006	0.000	-0.026	0.0002
6	0.003	0.0006	0.000	0.029	0.0002
7	-0.002	0.0006	0.000	-0.020	0.0002
8	-0.007	0.0006	0.000	0.022	0.0002
9	0.011	0.0002	0.000	0.001	0.0011
10	-0.019	0.0002	0.000	0.005	0.0007
11	0.009	0.0002	0.000	0.002	0.0013
12	-0.011	0.0002	0.000	0.005	0.0011
13	-0.001	0.0006	0.000	0.009	0.0002
14	0.001	0.0007	0.000	-0.006	0.0002
15	0.000	0.0006	0.000	0.007	0.0002
16	0.001	0.0006	0.000	-0.003	0.0002
17	-0.003	0.0002	0.000	0.002	0.0049
18	0.004	0.0002	0.000	0.001	0.0034
19	-0.002	0.0002	0.000	0.001	0.0050
20	0.003	0.0002	0.000	0.001	0.0047
21	0.000	0.0000	0.000	-0.001	0.0002
22	0.000	0.0000	0.000	0.002	0.0002
23	0.000	0.0000	0.000	-0.002	0.0002
24	0.000	0.0000	0.000	0.001	0.0002
25	0.001	0.0001	0.000	0.000	0.0062
26	-0.001	0.0001	0.000	0.000	0.0062
27	0.001	0.0001	0.000	-0.001	0.0085
28	-0.001	0.0001	0.000	-0.001	0.0085
29	0.000	0.0000	0.000	0.000	0.0002
30	0.000	0.0000	0.000	-0.001	0.0002
31	0.000	0.0000	0.000	-0.001	0.0002
32	0.000	0.0000	0.000	-0.001	0.0002

Table 6: Positional parameters for the best fit of an asymmetric dimer model to the SXRD data without constraints on the height difference between Si1 and Si2.  $\Delta X$ ,  $\Delta Y$  and  $\Delta Z$  are the deviation of the atomic coordinates from the original bulk positions in units of the corresponding lattice constants of the Si(001) surface unit cell ( $a = b = 0.384$  nm,  $c = 0.543$  nm). All the Y coordinates are fixed by the symmetry constraints.  $\delta X$  and  $\delta Z$  are the error bars of X and Z.

Si	$\Delta X$	$\delta X$	$\Delta Y$	$\Delta Z$	$\delta Z$
1	-0.183	0.0003	0.000	-0.010	0.0003
2	0.200	0.0003	0.000	-0.130	0.0003
3	-0.035	0.0003	0.000	0.011	0.0005
4	0.021	0.0003	0.000	-0.028	0.0010
5	0.012	0.0004	0.000	-0.008	0.0002
6	-0.011	0.0004	0.000	0.019	0.0002
7	0.002	0.0006	0.000	0.000	0.0002
8	-0.010	0.0005	0.000	0.025	0.0002
9	0.010	0.0002	0.000	0.003	0.0012
10	-0.012	0.0002	0.000	0.012	0.0011
11	0.019	0.0002	0.000	0.001	0.0007
12	-0.004	0.0002	0.000	0.008	0.0030
13	0.007	0.0006	0.000	0.011	0.0002
14	0.007	0.0005	0.000	-0.001	0.0002
15	0.005	0.0006	0.000	-0.001	0.0002
16	0.014	0.0004	0.000	-0.012	0.0002
17	0.005	0.0002	0.000	-0.001	0.0034
18	0.012	0.0002	0.000	-0.006	0.0010
19	-0.002	0.0002	0.000	-0.001	0.0070
20	0.001	0.0002	0.000	-0.004	0.0001
21	0.000	0.0000	0.000	-0.003	0.0002
22	0.000	0.0000	0.000	-0.001	0.0002
23	0.000	0.0000	0.000	-0.005	0.0002
24	0.000	0.0000	0.000	-0.002	0.0002
25	0.001	0.0001	0.000	-0.003	0.0050
26	-0.001	0.0001	0.000	-0.003	0.0050
27	0.001	0.0001	0.000	-0.001	0.0001
28	-0.001	0.0001	0.000	-0.001	0.0001
29	0.000	0.0000	0.000	0.000	0.0002
30	0.000	0.0000	0.000	-0.002	0.0002
31	0.000	0.0000	0.000	-0.001	0.0002
32	0.000	0.0000	0.000	-0.002	0.0002

Table 7: Positional parameters for the best fit of an asymmetric dimer model to the SXRD data. The height difference between Si1 and Si2 are fixed to 0.065 nm.  $\Delta X$ ,  $\Delta Y$  and  $\Delta Z$  are the deviation of the atomic coordinates from the original bulk positions in units of the corresponding lattice constants of the Si(001) surface unit cell ( $a = b = 0.384$  nm,  $c = 0.543$  nm). All the Y coordinates are fixed by the symmetry constraints.  $\delta X$  and  $\delta Z$  are the error bars of X and Z.

## Oxidation of the Si(001)- $2 \times 1$ reconstructed surface

This study aimed at growing a Si-oxide template layer as a buffer for the Pr-oxide film (in order to prevent from Si diffusion through it).

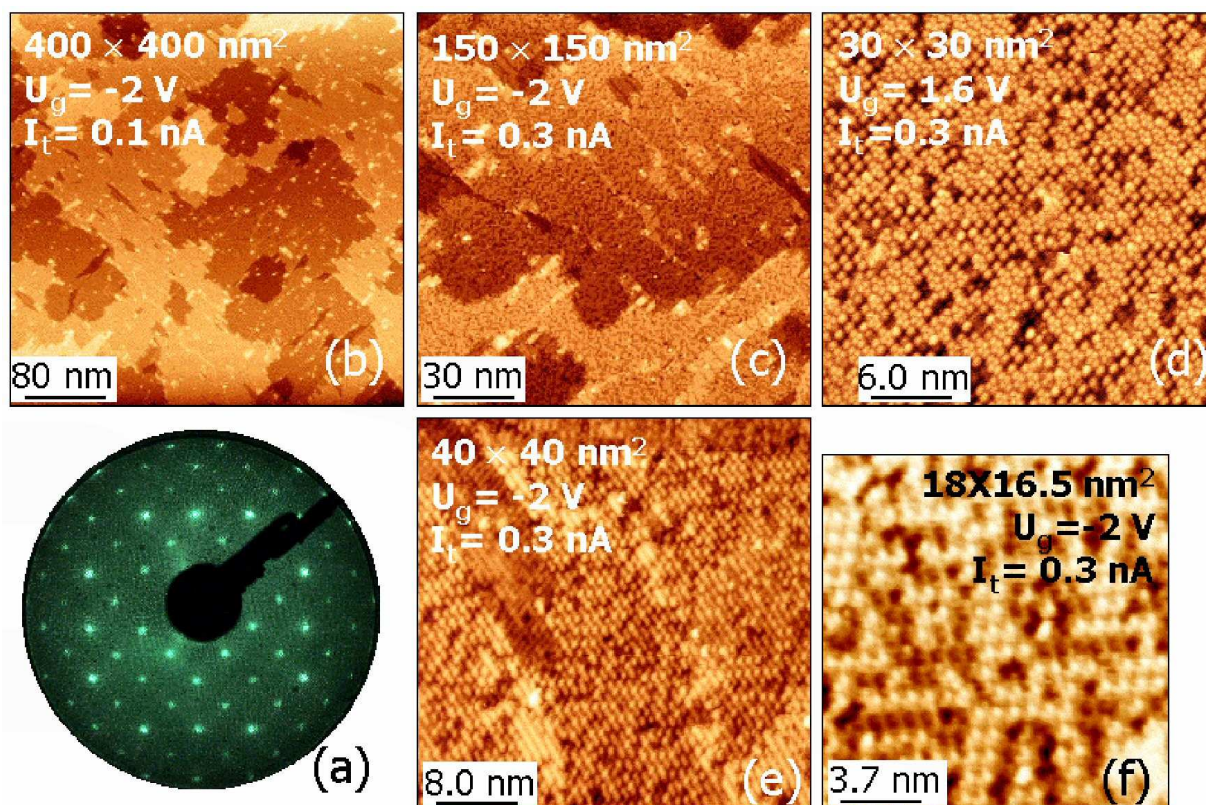


Figure 40: LEED and STM results obtained on a Si(001)-2×1 surface exposed to 18 L of O<sub>2</sub> (30 min at 1×10<sup>-8</sup> mbar). (a) LEED pattern of a c(4×4) reconstructed surface. (b-f) Four different STM images. Their individual size as well as the parameters used to record them are mentioned on the images.

The previous studies of the initial oxidation of the Si(001) surface were briefly discussed in section 1.5. For the present study, the LEED and STM results collected on a Si(001)-2×1 surface exposed to 18 L of O<sub>2</sub> (30 min at 1×10<sup>-8</sup> mbar) are reported in Fig. 40. The LEED pattern in Fig. 40(a) shows a c(4×4) reconstructed surface. Figs. 40(b-f) present four different STM topographs recorded on such a surface. A SXRD data set of was collected but not yet analyzed. The structures of the SiO<sub>x</sub> layer and the SiO<sub>x</sub>/Si(001) interface would need more investigations in order to draw any further conclusion on the observations described above.

# Appendix B

---

List of publications and communications

---



**Publications in journals**

- [1] **L. Libralesso**, T. Schroeder, T.-L. Lee, Z. Zegenhagen, "Initial stages of the epitaxial growth of  $Pr_2O_3$  on Si(111) studied by LEED and STM", Surface Science Letters, 2005, 598, L347-L354.
- [2] T. Schroeder, T.-L. Lee, **L. Libralesso**, I. Joumard, Z. Zegenhagen, P. Zaumseil, C. Wenger, G. Lupina, G. Lippert, J. Dabrowski, H.-J. Müssig, "Structure and strain relaxation mechanisms of ultrathin epitaxial  $Pr_2O_3$  films on Si(111)", Journal of Applied Physics, 2005, 97, 074906.

N.B.: 4 other publications in preparation.

**Publications in conference proceedings**

- [1] **L. Libralesso**, T. Schroeder, T.-L. Lee, J. Zegenhagen, "Initial stages of the epitaxial growth of  $Pr_2O_3$  oxide layers on silicon substrates", acte du workshop "Nouveaux oxydes à forte permittivité dans l'intégration des semi-conducteurs", Autrans (Isère), 30/01 – 02/02/2005, p.119-123.

**Communications in international meetings (the presenting author is underlined)**

- [1] **L. Libralesso**, T.-L. Lee, J. Zegenhagen, "The growth of high-k praseodymium oxide on Si(001)", EMRS IUMRS ICEM Spring Meeting 2006, May 29 – June 2, 2006, Nice (France), **oral communication**.
- [2] T.-L. Lee, **L. Libralesso**, J. Zegenhagen, "Atomic-scale structural characterization of high-k praseodymium oxide on Si(001)", EMRS IUMRS ICEM Spring Meeting 2006, May 29 – June 2, 2006, Nice (France), **oral communication**.
- [3] J. Zegenhagen, **L. Libralesso**, T.-L. Lee, "Epitaxial growth and structure of the high-k dielectric  $Pr_2O_3$  on Si(001) and Si(111)", APS March meeting 2006, March 13-17, 2006, Baltimore, MD (USA), **oral communication**.
- [4] **L. Libralesso**, T.-L. Lee, J. Zegenhagen, "Structure of high-k Praseodymium oxide on Si(001)", ESRF Experiment Division Student Day, 7<sup>th</sup> October 2005, Grenoble (France), **oral communication**.
- [5] T. Schroeder, P. Zaumseil, C. Wenger, G. Lippert, G. Lupina, H.-J. Müssig, **L. Libralesso**, J. Zegenhagen, "Heteroepitaxial silicon /  $Pr_2O_3$  / silicon structures for nanoelectronics applications", DPG Spring Meeting 2005, 4-9 March 2005, Berlin (Germany), **oral communication**.
- [6] **L. Libralesso**, T. Schroeder, T.-L. Lee, J. Zegenhagen, "Initial growth of the  $Pr_2O_3$  epitaxial layers on silicon substrates", DPG Spring Meeting 2005, 4-9 March 2005, Berlin (Germany), **oral communication**.
- [7] **L. Libralesso**, T. Schroeder, T.-L. Lee, I. Joumard, J. Zegenhagen, G. Lippert, C. Wenger, P. Zaumseil, and H.-J. Müssig, "Structural properties of ultra-thin  $Pr_2O_3$  oxide layers on Si(111)", ESRF Experiment Division Student Day, 5<sup>th</sup> October 2004, Grenoble (France), **poster**.
- [8] T. Schroeder, T.-L. Lee, **L. Libralesso**, J. Zegenhagen, "A grazing incidence x-ray diffraction study of ultra-thin praseodymium oxide layers on Si(001): from pseudomorphism to bulk behaviour", European Material Research Society Meeting, 24-28 May 2004, Strasbourg (France), **oral communication**.
- [9] **L. Libralesso**, T. Schroeder, T.-L. Lee, I. Joumard, J. Zegenhagen, "A combined synchrotron x-ray diffraction and STM study of the structural properties of ultra-thin praseodymium oxide layers on Si(111)", European Material Research Society Meeting, 24-28 May 2004, Strasbourg (France), **poster**.
- [10] **L. Libralesso**, T. Schroeder, T.-L. Lee, J. Zegenhagen, "High-k dielectrics for Microelectronics", ESRF Experiment Division Student Day, 20<sup>th</sup> October 2003, Grenoble (France), **poster**.

**Communications in French meetings (the presenting author is underlined)**

- [1] **L. Libralesso**, T. Schroeder, T.-L. Lee, J. Zegenhagen, "Etude des premiers stades de croissance épitaxiale de  $Pr_2O_3$  sur substrats de silicium", Workshop "Nouveaux oxydes à forte permittivité dans l'intégration des semi-conducteurs", 30 Jan.- 2 Feb. 2005, Autrans (France), **oral communication**.
- [2] **L. Libralesso**, T. Schroeder, T.-L. Lee, J. Zegenhagen, "Etude des premiers stades de croissance épitaxiale de  $Pr_2O_3$  sur substrats de silicium", Physique en clips "Jean Souletie", 19 January 2005, Grenoble (France), **oral communication** (4min, 3 slides).



# Bibliography

- [1] *International Technology Roadmap for Semiconductors* (2005).  
URL <http://public.itrs.net>
- [2] H. J. Osten, E. Bugiel, J. Dabrowski, A. Fissel, T. Guminskaya, J. P. Liu, H. J. Müssig, P. Zaumseil, *Epitaxial Praseodymium Oxide: A new High-K Dielectric*, IWGI 2001, Tokyo .
- [3] H. J. Osten, J. Dabrowski, H. J. Müssig, A. Fissel, V. Zavodinski, *Predictive Simulation of Semiconductor Processing*, pp 259-293, Springer-Verlag, 2004.
- [4] N. M. Jeutter, A. Sidorenko, A. Stierle, W. Moritz, *Crystalline Pr<sub>2</sub>O<sub>3</sub> monolayers on Si(111)*, Appl. Phys. Lett. (2006) submitted.
- [5] C. Noguera, *Physics and chemistry at oxide surfaces*, Cambridge University Press, 1996.
- [6] G. Renauld, *Oxide Surfaces and metal/oxide interfaces studied by grazing incidence X-ray scattering*, Surf. Sci. Rep. 32 (1998) 1.
- [7] S. Ferrer, Y. Petroff, *Surface Science done at third generation synchrotron radiation facilities*, Surf. Sci. 500 (2002) 605.
- [8] T. Hori, *Gate Dielectrics and MOS ULSIs*, Vol. 34, Springer Series in Electronics and Physics, 1996.
- [9] G. D. Wilk, R. M. Wallace, J. M. Anthony, *High-k gate dielectrics: Current status and materials properties considerations*, J. Appl. Phys. 89 (2001) 5243.
- [10] K. J. Hubbard, D. G. Schlom, *Thermodynamic stability of binary oxides in contact with silicon*, J. Mater. Res. 11 (1996) 2757.

- [11] J. Robertson, *High dielectric constant gate oxides for metal oxide Si transistors*, Rep. Prog. Phys. 69 (2006) 327.
- [12] Y. Tu, J. Tersoff, *Structure and Energetics of the Si-SiO<sub>2</sub> Interface*, Phys. Rev. B 84 (2000) 4393.
- [13] P. W. Peacock, J. Robertson, *Bonding, Energies, and Band Offsets of Si-ZrO<sub>2</sub> and HfO<sub>2</sub> Gate Oxide Interfaces*, Phys. Rev. B 92 (2004) 057601–1.
- [14] K. Khare, *et al.*, *Ultra-thin Silicon Nitride Gate Dielectric for Deep-Sub-Micron CMOS Devices*, VLSI Tech, Dig. Tech., 1997.
- [15] A. Chin, Y. H. Wu, S. B. Chen, C. C. Liao, W. J. Chen, *High quality La<sub>2</sub>O<sub>3</sub> and Al<sub>2</sub>O<sub>3</sub> gate dielectrics with equivalent oxide thickness 5-10 Å, pp 16-17*, VLSI Tech, Dig. Tech., 2000.
- [16] H. Iwai, K. Kakushima, P. Ahmet, K. Tsutsui, N. Sugii, T. Hattori, *La<sub>2</sub>O<sub>3</sub> gate oxide technology for MOSFETs*, in: EMRS IUMRS ICEM 2006 Spring Meeting, symposium L, 2006.
- [17] M. Czernohorsky, E. Bugiel, H. J. Osten, A. Fissel, O. Kirfel, *Impact of oxygen supply during growth on the electrical properties of crystalline Gd<sub>2</sub>O<sub>3</sub> thin films on Si(001)*, Appl. Phys. Lett. 88 (2006) 152905.
- [18] A. Fissel, Z. Elassar, O. Kirfel, E. Bugiel, M. Czernohorsky, O. H. J., *Interface formation during molecular beam epitaxial growth of neodymium oxide on silicon*, J. Appl. Phys. 99 (2006) 074105.
- [19] A. Fissel, D. Kühne, E. Bugiel, H. J. Osten, *Cooperative solid-vapor-phase epitaxy: An approach for fabrication of single-crystalline insulator/Si/insulator nanostructures*, Appl. Phys. Lett. 88 (2006) 153105.
- [20] A. Laha, E. Bugiel, H. J. Osten, A. Fissel, *Crystalline ternary rare-earth oxide with capacitance equivalent thickness below 1 nm for high-k application*, Appl. Phys. Lett. 88 (2006) 172107.
- [21] D. J. Lichtenwalner, J. S. Jur, A. I. Kingon, M. P. Agustin, Y. Yang, S. Stemmer, L. V. Goncharova, T. Gustafsson, E. Garfunkel, *Lanthanum silicate gate dielectric stacks with subnanometer equivalent oxide thickness utilizing an interfacial silica consumption reaction*, J. Appl. Phys. 98 (2005) 024314.

- [22] Y. Kim, K. Miyauchi, S.-I. Ohmi, K. Tsutsui, H. Iwai, *Electrical properties of vacuum annealed  $La_2O_3$  thin films grown by E-beam evaporation*, Microelec. J. 36 (2005) 41.
- [23] F. Paumier, *Réalisation et étude de films d'oxyde d'yttrium,  $Y_2O_3$ : Relations nanostructure - propriétés physiques*, Ph.D. thesis, Université de Poitiers, Faculté des Sciences Fondamentales et Appliquées (2003).
- [24] F. Pailloux, M. Jublot, R. J. Gaboriaud, M. Jaouen, F. Paumier, D. Imhoff, *Interfacial phases in epitaxial growth of  $Y_2O_3$  on MgO studied via combining electron energy-loss spectroscopy and real-space self-consistent full multiple scattering calculations*, Phys. Rev. B 72 (2005) 125425.
- [25] V. Blech, *Analyse corrélée du plasma de pulvérisation et des films minces de  $La_2O_3$  et de  $RuO_2$  pour les futurs transistors MOSFET*, Ph.D. thesis, Université Paris XI - UFR scientifique d'Orsay (2004).
- [26] C. Bedoya, G. G. Condorelli, S. T. Finocchiaro, A. Di Mauro, D. Atanasio, I. L. Fragalà, L. Cattaneo, S. Carella, *MOCVD of Lanthanum Oxides from  $La(tmhd)_3$  and  $La(tmod)_3$  Precursors: A Thermal and Kinetic Investigation*, Chemical vapor deposition 12 (2006) 46.
- [27] K. Fröhlich, R. Luptak, K. Husekova, M. Lukosius, A. Abrutis, M. Jergel, *Characterization of rare-earth oxides based MOSFET gate stacks prepared by metal-organic chemical vapor deposition*, in: EMRS IUMRS ICEM 2006 Spring Meeting, symposium L, 2006.
- [28] C. Durand, *Elaboration par PE-MOCVD à injection de couches minces d'oxyde d'yttrium pour les applications en microélectronique avancée*, Ph.D. thesis, Université Joseph Fourier - Grenoble I (2004).
- [29] G. Scarel, E. Bonera, C. Wiemer, G. Tallarida, S. Spiga, F. M., I. L. Fedushkin, H. Schumann, Y. Lebedinskii, A. Zenkevich, *Atomic-layer deposition of  $Lu_2O_3$* , Appl. Phys. Lett. 85 (2004) 630.
- [30] M. Malvestuto, G. Scarel, C. Wiemer, M. Fanciulli, F. D'Acapito F., Boscherini, *X-ray absorption spectroscopy study of  $Yb_2O_3$  and  $Lu_2O_3$  thin films deposited on  $Si(100)$  by atomic layer deposition*, Nuclear instruments & methods in physics research section b-beam interactions with materials and atoms 246 (2006) 90.

- [31] A. C. Jones, H. C. Aspinall, P. R. Chalker, R. J. Potter, K. Kukli, A. Rahtu, M. Ritala, M. Leskelä, *Recent developments in MOCVD and ALD of rare-earth oxides and silicates*, Mat. Sci. and Eng. B 118 (2005) 97.
- [32] A. C. Jones, H. C. Aspinall, P. R. Chalker, R. J. Potter, K. Kukli, A. Rahtu, M. Ritala, M. Leskelä, *Some recent developments in MOCVD and ALD of high-k dielectric oxides*, J. Mat. Chem. 14 (2004) 3101.
- [33] R. A. McKee, F. J. Walker, M. F. Chisholm, *Crystalline Oxides on Silicon: The First Five Monolayers*, Phys. Rev. Lett. 81 (1998) 3014.
- [34] S. Gaillard, *Elaboration d'oxydes à forte constante diélectrique sur silicium par épitaxie par jets moléculaires*, Ph.D. thesis, Ecole centrale de Lyon (2005).
- [35] V. Edon, M. C. Hugon, B. Agius, L. Miotti, C. Radtke, F. Tatsch, J. Ganem, I. Triaille, I. J. R. Baumvol, *Effects of sputter deposition parameters and post-deposition annealing on the electrical characteristics of LaAlO<sub>3</sub> dielectric films on Si*, Appl. Phys. A - Mat. Sci. & Proc. 83 (2006) 289.
- [36] H. Nohira, T. Yoshida, H. Okamoto, S. Shinagawa, W. Sakai, K. Nakajima, M. Suzuki, K. Kimura, N. J. Aun, Y. Kabayashi, S. Ohmi, H. Iwai, E. Ikenaga, Y. Takata, K. Kobayashi, T. Hattori, *Thermal stability of Gd<sub>2</sub>O<sub>3</sub>/Si(001) interfacial transition layer*, J. Phys. IV France 132 (2006) 273.
- [37] R. Lo Nigro, V. Raineri, B. C., R. G. Toro, G. Malandrino, I. L. Fragalà, *Dielectric properties of Pr<sub>2</sub>O<sub>3</sub> high-k films grown by metalorganic chemical vapor deposition on silicon*, Appl. Phys. Lett. 83 (2003) 129.
- [38] R. Lo Nigro, R. G. Toro, G. Malandrino, G. G. Condorelli, V. Raineri, I. L. Fragalà, *Praseodymium Silicate as a High-k Dielectric Candidate: An insight into the Pr<sub>2</sub>O<sub>3</sub>-Film/Si-Substrate Interface Fabricated Through a Metal-Organic Chemical Vapor Deposition Process*, Adv. Funct. Mater. 15 (2005) 838.
- [39] R. Lo Nigro, R. G. Toro, G. Malandrino, et al., *Effects of deposition temperature on the microstructural and electrical properties of praseodymium oxide-based films*, Mat. Sci. and Eng. B 118 (2005) 117.

- [40] R. Lo Nigro, R. G. Toro, G. Malandrino, et al., *Effects of the thermal annealing processes on praseodymium oxide based films grown on silicon substrates*, Mat. Sci. and Eng. B 118 (2005) 192.
- [41] R. J. Potter, P. R. Chalker, T. D. Manning, H. C. Aspinall, Y. F. Loo, A. C. Jones, L. M. Smith, G. W. Critchlow, M. Schumacher, *Deposition of HfO<sub>2</sub>, Gd<sub>2</sub>O<sub>3</sub> and PrO<sub>x</sub> by liquid injection ALD techniques*, Chemical vapor deposition 11 (2005) 159.
- [42] J. Päiväsääri, *ATOMIC LAYER DEPOSITION OF LANTHANIDE OXIDE THIN FILMS*, Ph.D. thesis, Helsinki University of Technology (2006).
- [43] E. Tarsa, J. Speck, M. Robinson, *Pulsed laser deposition of epitaxial silicon/h-Pr<sub>2</sub>O<sub>3</sub>/silicon heterostructures*, Appl. Phys. Lett. 63 (1993) 539.
- [44] S. Kitai, O. Maida, T. Kanashima, M. Okuyama, *Preparation and characterization of High-k praseodymium and Lanthanoid oxide thin films prepared by pulsed laser deposition*, Jpn. J. Appl. Phys. 42 (2003) 247.
- [45] K. Ariyoshi, M. Sakashita, A. Sakai, M. Ogawa, S. Zaima, *Film Structures and Electrical Properties of Pr Silicate Formed by Pulsed Laser Deposition*, Jpn. J. Appl. Phys. 45 (2006) 2903.
- [46] D. Wolfram, M. Ratzke, M. Kappa, M. Montenegro, M. Döbeli, T. Lippert, J. Reif, *Pulsed laser deposition of thin Pr<sub>x</sub>O<sub>y</sub> films on Si(001)*, Mat. Sci. and Eng. B 109 (2004) 24.
- [47] H. J. Müssig, J. Dabrowski, K. Ignatovich, J. P. Liu, V. Zavodinsky, H. J. Osten, *Initial stages of praseodymium oxide film formation on Si(001)*, Surf. Sci. 504 (2002) 159.
- [48] H. J. Müssig, J. Dabrowski, C. Wenger, G. Lupina, R. Sorge, P. Formanek, P. Zaumseil, D. Schmeisser, *Ultrathin dielectric films grown by solid phase reaction of Pr with SiO<sub>2</sub>*, Mat. Res. Soc. Symp. Proc. 811 (2004) D7.10.1.
- [49] H. J. Müssig, et al., *Workshop, USA - Final Report*, Tech. rep., IEEE International Integrated Reliability (2001).
- [50] H. J. Osten, E. Bugiel, A. Fissel, *Epitaxial praseodymium oxide: a new high-k dielectric*, Solid State Electronics 47 (2003) 2161.

- [51] H. J. Osten, J. P. Liu, E. Bugiel, H. J. Müssig, P. Zaumseil, *Growth of crystalline praseodymium oxide on silicon*, J. of Cryst. Growth 235 (2002) 229.
- [52] H. J. Osten, J. P. Liu, E. Bugiel, H. J. Müssig, P. Zaumseil, *Epitaxial growth of praseodymium oxide on silicon*, Mat. Sci. and Eng. B 87 (2001) 297.
- [53] H. J. Osten, J. P. Liu, P. Gaworzewski, E. Bugiel, P. Zaumseil, *High-K Gate Dielectrics with Ultra-low Leakage Current Based on Praseodymium Oxide*, Techn. Digest IEDM (IEEE, Piscataway, NJ) (2000) 653.
- [54] D. Schmeisser, *The Pr<sub>2</sub>O<sub>3</sub>/Si(001) interface*, Mat. Sci. in Semiconductor Processing 6 (2003) 59.
- [55] D. Schmeisser, H.-J. Müssig, *Covalent and localized contributions of Pr4f states at the interface of Pr<sub>2</sub>O<sub>3</sub> to Si(001)*, Mat. Sci. in Semiconductor Processing 7 (2004) 221.
- [56] D. Schmeisser, H.-J. Müssig, *Stability and electronic properties of silicates in the system SiO<sub>2</sub>-Pr<sub>2</sub>O<sub>3</sub>-Si(001)*, J. Phys.: Condens. Matter 16 (2004) S153.
- [57] D. Schmeisser, H.-J. Müssig, *The Pr<sub>2</sub>O<sub>3</sub>/Si(001) interface studied by synchrotron radiation photo-electron spectroscopy*, Solid State Electronics 47 (2003) 1607.
- [58] D. Schmeisser, H.-J. Müssig, J. Dabrowski, *Silicate layer formation at Pr<sub>2</sub>O<sub>3</sub> / Si(001) interfaces*, Appl. Phys. Lett. 85 (2004) 88.
- [59] D. Schmeisser, F. Zheng, V. Perez-Dieste, F. Himpsel, R. LoNigro, R. Toro, G. Mandrino, I. Fragala, *Silicate formation at the interface of Pr-oxide as a high-K dielectric and Si(001) surfaces*, Mat. Sci. and Eng. C 26 (2006) 1122.
- [60] A. Fissel, J. Dabrowski, H. J. Osten, *Photoemission and ab initio theoretical study of interface and film formation during epitaxial growth and annealing of praseodymium oxide on Si(001)*, J. Appl. Phys. 91 (2002) 8986.
- [61] D. Schmeisser, H.-J. Müssig, *Pr4f occupancy and VB/CB band offsets of Pr<sub>2</sub>O<sub>3</sub> at the interface to Si(001) and SiC(0001) surfaces*, Mat. Res. Soc. Symp. Proc. 811 (2004) D6.7.1.

- [62] G. Lupina, T. Schroeder, J. Dabrowski, C. Wenger, A. U. Mane, H.-J. Müssig, P. Hoffmann, D. Schmeisser, *Praseodymium silicate films on Si(001) for gate dielectric applications: Physical and electrical characterization*, J. Appl. Phys. 99 (2006) 114109.
- [63] A. Sakai, S. Sakashita, M. Sakashita, Y. Yasuda, *Praseodymium silicate formed by postdeposition high-temperature annealing*, Appl. Phys. Lett. 85 (2004) 5322.
- [64] U. Schwalke, Y. Stefanov, *Process integration and nanometer-scale electrical characterization of crystalline high-k gate dielectrics*, Microelectronics Reliability 45 (2005) 790.
- [65] R. Haire, L. Eyring, *Handbook on the Physics and chemistry of Rare Earths*, Vol. 18, Elsevier Science, 1994.
- [66] B. Hyde, D. Bevan, L. Eyring, *On the praseodymium+oxygen system*, *Philosophical Transactions of the Royal Society of London, Series A*, Mathematical and Physical Sciences 259 (1966) 583.
- [67] G.-Y. Adachi, N. Imanaka, *The Binary Rare Earth Oxides*, Chem. Rev. 98 (1998) 1479.
- [68] P. Villars, L. Calvert, *Pearson's Handbook of Crystallographic Data for Intermetallic Phases, 2nd edition*, ASM International, Materials Park, OH., 1991.
- [69] J. Liu, P. Zaumseil, E. Bugiel, H. Osten, *Epitaxial growth of Pr<sub>2</sub>O<sub>3</sub> on Si(111) and the observation of a hexagonal to cubic phase transition during postgrowth N<sub>2</sub> annealing*, Appl. Phys. Lett. 79 (2001) 671.
- [70] H. S. Momose, T. Ohguro, S.-I. Nakamura, Y. Toyoshima, H. Ishiuchi, H. Iwai, *Ultra-thin Gate Oxide CMOS on (111) Surface-Oriented Si Substrate*, IEEE Transactions on electron devices 49 (2002) 1597.
- [71] M. Fanciulli, *High-K dielectrics on high mobility substrates: interface properties*, in: EMRS IUMRS ICEM 2006 Spring Meeting, symposium L, 2006.
- [72] M. Heyns, M. Meuris, M. Caymax, *Ge, an enabling material for future high-performance CMOS technologies*, in: EMRS IUMRS ICEM 2006 Spring Meeting, symposium L, 2006.

- [73] W. B. Pearson, *A Handbook of LATTICE SPACINGS OF METALS AND ALLOYS*, Vol. 2, Pergamon Press, 1967.
- [74] T. Schroeder, T.-L. Lee, L. Libralesso, I. Joumard, J. Zegenhagen, P. Zaumseil, C. Wenger, H.-J. Müssig, *Structure and strain relaxation mechanisms of ultrathin epitaxial Pr<sub>2</sub>O<sub>3</sub> films on Si(111)*, J. Appl. Phys. 97 (2005) 074906.
- [75] T. Schroeder, P. Zaumseil, G. Weidner, C. Wenger, J. Dabrowski, H.-J. Müssig, P. Storck, *On the epitaxy of twin-free cubic (111) praseodymium sesquioxide films on Si(111)*, J. Appl. Phys. 99 (2006) 014101.
- [76] T. Schroeder, P. Zaumseil, G. Weidner, G. Lupina, C. Wenger, H.-J. Müssig, P. Storck, *Structure, twinning behavior, and interface composition of epitaxial Si(111) films on hex-Pr<sub>2</sub>O<sub>3</sub>(0001)/Si(111) support systems*, J. Appl. Phys. 98 (2005) 123513.
- [77] R. W. Fathauer, L. J. Schowalter, *Surface morphology of epitaxial CaF<sub>2</sub> films on Si substrates*, Appl. Phys. Lett. 45 (1984) 519.
- [78] R. M. Tromp, M. C. Reuter, *Structure of the Si(111)-CaF<sub>2</sub> Interface*, Phys. Rev. Lett. 61 (1988) 1756.
- [79] C. A. Lucas, G. C. L. Wong, D. Loretto, *Structural Transition of the CaF<sub>2</sub>/Si(111) Interface*, Phys. Rev. Lett. 70 (1993) 1826.
- [80] M. A. Olmstead, *Thin Films: Heteroepitaxial Systems*, World Scientific, 1999.
- [81] C. Wang, B. Müller, K. Hofmann, *Epitaxy of atomically flat CaF<sub>2</sub> films on Si(111) substrates*, Thin Solid Films 410 (2002) 72.
- [82] X. Guo, W. Braun, B. Jenichen, K. Ploog, *Reflection high-energy electron diffraction study of molecular beam epitaxy growth of Pr<sub>2</sub>O<sub>3</sub> on Si(001)*, J. of Cryst. Growth 290 (2006) 73.
- [83] B. Swartzentruber, Y.-W. Mo, M. Webb, M. Lagally, *Scanning tunneling microscopy studies of the structural disorder and steps on Si surfaces*, J. Vac. Sci. Technol. A 7 (1989) 2901.
- [84] K. Arima, K. Endo, T. Kataoka, Y. Oshikane, H. Inoue, Y. Mori, *Scanning tunneling microscopy study of hydrogen-terminated Si(001) surfaces after wet cleaning*, Surf. Sci. 446 (2000) 128.

- [85] G. Pietsch, U. Kohler, M. Henzler, *Chemistry of silicon surfaces after wet chemical preparation - a thermodesorption spectroscopy study*, J. Vac. Sci. Technol. B 12 (1994) 78.
- [86] G. Lupina, J. Dabrowski, P. Formanek, D. Schmeisser, R. Sorge, C. Wenger, P. Zaumseil, H.-J. Müssig, *Solid-state reaction between Pr and SiO<sub>2</sub> studied by photoelectron spectroscopy and ab initio calculations*, Mat. Sci. in Semiconductor Processing 7 (2004) 215.
- [87] Z. Wang, J. Wu, M. Ma, W. Chen, Q. Fang, J.-Y. Zhang, *Photoemission study of the interaction of a Pr<sub>2</sub>O<sub>3</sub> overlayer with Si(100) as a function of annealing temperature*, Microelectronic Engineering 66 (2003) 608.
- [88] J. X. Wu, Z. M. Wang, M. S. Ma, S. Li, *X-ray photoemission studies of praseodymium thin films on SiO<sub>2</sub>/Si(001)*, J. Phys.: Condens. Matter 15 (2003) 5857.
- [89] G. Lupina, T. Schroeder, J. Dabrowski, C. Wenger, A. U. Mane, G. Lippert, H.-J. Müssig, P. Hoffmann, D. Schmeisser, *Praseodymium silicate layers with atomically abrupt interface on Si(001)*, Appl. Phys. Lett. 87 (2005) 092901.
- [90] A. Fissel, H. J. Osten, E. Bugiel, *Towards understanding epitaxial growth of alternative high-K dielectrics on Si(001): Application to praseodymium oxide*, J. Vac. Sci. Technol. B 21 (2003) 1765.
- [91] J. Dabrowski, V. Zavodinsky, *Ab Initio Study of Pr Oxides for CMOS Technology*, NIC Series, ISBN 3-00-012372-5 20 (2003) 171.
- [92] T. Schroeder, T.-L. Lee, J. Zegenhagen, C. Wenger, P. Zaumseil, H.-J. Müssig, *Structure and thickness-dependent lattice parameters of ultra-thin epitaxial Pr<sub>2</sub>O<sub>3</sub> films on Si(001)*, Appl. Phys. Lett. 85 (2004) 1229.
- [93] C. J. Först, C. R. Ashman, K. Schwarz, P. E. Blöchl, *The interface between silicon and a high-k oxide*, Nature 427 (2004) 53.
- [94] C. J. Först, K. Schwarz, P. E. Blöchl, *Structural and Electronic Properties of the Interface between the High-K Oxide LaAlO<sub>3</sub> and Si(001)*, Phys. Rev. Lett. 95 (2005) 137602.
- [95] A. Ourmazd, D. W. Taylor, J. A. Rentschler, *Si → SiO<sub>2</sub> Transformation: Interfacial Structure and Mechanism*, Phys. Rev. Lett. 59 (1987) 213.

- [96] F. J. Himpsel, G. Hollinger, F. R. McFeely, A. Taleb-Ibrahimi, J. A. Yarmoff, *Microscopic structure of the SiO<sub>2</sub>/Si interface*, Phys. Rev. B 38 (1988) 6084.
- [97] A. Munkholm, S. Brennan, F. Comin, L. Ortega, *Observation of a Distributed Epitaxial Oxide in Thermally Grown SiO<sub>2</sub> on Si(001)*, Phys. Rev. Lett. 75 (1995) 4254.
- [98] T. Shimura, M. Umeno, I. Takahashi, J. Harada, *Comments on "Observation of a Distributed Epitaxial Oxide in Thermally Grown SiO<sub>2</sub> on Si(001)"*, Phys. Rev. Lett. 79 (1997) 4932.
- [99] A. Munkholm, S. Brennan, F. Comin, L. Ortega, *Munkholm et al. Reply to the Comment by Takayoshi Shimura, et al.*, Phys. Rev. Lett. 79 (1997) 4933.
- [100] A. Pasquarello, M. Hybertsen, R. Car, *Interface structure between silicon and its oxide by first-principles molecular dynamics*, Nature 396 (1998) 58.
- [101] T. Yamasaki, C. Kaneta, T. Uchiyama, T. Uda, K. Terakura, *Geometric and electronic structures of SiO<sub>2</sub>/Si(001) interfaces*, Phys. Rev. B 63 (2001) 115314.
- [102] H. Kageshima, K. Shiraishi, *First-Principles Study of Oxide Growth on Si(100) Surfaces and at SiO<sub>2</sub>/Si(100) Interfaces*, Phys. Rev. Lett. 81 (1998) 5936.
- [103] A. I. Kingon, J.-P. Maria, S. K. Streiffer, *Alternative dielectrics to silicon dioxide for memory and logic devices*, Nature (London) 406 (2000) 1032.
- [104] D.-L. Kwong, *Silicon Devices, structures and processing*, WILEY-VCH Verlag GmbH, 1998.
- [105] E. B. Graper, *Handbook of Thin Film Process Technology, Physical Deposition Techniques, Thermal Evaporation, Introduction and general discussion.*, IOP Publishing Ltd, 1995.
- [106] G. Binnig, H. Rohrer, C. Gerber, E. Weibel, *Surface Studies by Scanning Tunneling Microscopy*, Phys. Rev. Lett. 49 (1982) 57.
- [107] J. P. Ibe, P. P. Bey, S. L. Brandow, R. A. Brizzolara, N. A. Burnham, D. P. DiLella, K. P. Lee, C. R. K. Marrian, R. J. Colton, *On the electrochemical etching of tips for scanning tunneling microscopy*, J. Vac. Sci. Technol. A 8 (1990) 3570.

- [108] C. J. Chen, *Introduction to Scanning Tunneling Microscopy*, Oxford University Press, 1993.
- [109] R. Wiesendanger, *Scanning Probe Microscopy and Spectroscopy: Methods and Applications*, Cambridge University Press, 1994.
- [110] J. F. Watts, J. Wolstenholme, *An introduction to Surface Analysis by XPS and AES*, John Wiley and sons, 2003.
- [111] C. Dallera, L. Duò, L. Braicovich, G. Panaccione, G. Paolicelli, B. Cowie, J. Zegenhagen, *Looking at 100 Å deep into spatially inhomogeneous dilute systems with hard X-ray photoemission*, Appl. Phys. Lett. 85 (2004) 4532.
- [112] J. Als-Nielsen, *Topics in Current Physics, p.181*, Springer-Verlag, Berlin, 1986.
- [113] R. Feidenhans'l, *Surface structure determination by X-ray diffraction*, Surf. Sci. Rep. 10 (1989) 105.
- [114] I. W. Hamley, J. S. Pedersen, *Analysis of Neutron and X-ray Reflectivity Data. I. Theory*, J. Appl. Phys. 27 (1994) 29.
- [115] H. Kiessig, *Interferenz von Röntgenstrahlen an dünnen Schichten*, Ann. Phys. Leipzig 10 (1931) 769.
- [116] B. E. Warren, *X-ray diffraction*, Dover publications, 1990.
- [117] E. N. Maslen, A. G. Fox, M. A. O'Keefe, *Section 6.1.1 of International Tables for Crystallography, Volume C: Mathematical, physical and chemical states*, International Union of Crystallograph. 3rd edition, 2004.
- [118] C. Flensburg, R. F. Stewart, *Lattice dynamical Debye-Waller factor for silicon*, Phys. Rev. B 60 (1999) 284.
- [119] I. K. Robinson, D. J. Tweet, *Surface x-ray diffraction*, Rep. Prog. Phys. 55 (1992) 599.
- [120] E. Vlieg, *Integrated intensities using a six-circle surface x-ray diffractometer*, J. Appl. Cryst. 30 (1997) 532.
- [121] I. Robinson, *Handbook on synchrotron radiation*, Vol. 3, North-Holland, Amsterdam, 1994, Chap. 7, *Surface crystallography*, p. 221.

- [122] C. D. Wagner, W. M. Riggs, L. E. Davis, J. F. Moulder, *Handbook of the X-ray photoelectron spectroscopy*, Eden Prairie, 1978.
- [123] P. Bagus, F. Illas, G. Paccioni, F. Parmigiani, *Mechanisms responsible for chemical shifts of core-level binding energies and their relationship to chemical bonding*, J. Electron. Spectrosc. relat. Phenom. 100 (1999) 215.
- [124] K. Takayanagi, Y. Tanishiro, S. Takahashi, M. Takahashi, *Structure analysis of Si(111)- $7\times 7$  reconstructed surface by transmission electron diffraction*, Surf. Sci. 164 (1985) 367.
- [125] E. Schweda, L. Eyring, D. Smith, *Structural transformation and chemical reduction of Pr<sub>24</sub>O<sub>44</sub> induced by the electron beam during microscopical examination*, Ultramicroscopy 23 (1987) 443.
- [126] R. Schwoebel, E. Shipsey, *Step Motion on Crystal Surfaces*, J. Appl. Phys. 37 (1966) 3682.
- [127] G.-X. Qian, D. Chadi, *Si(111)- $7\times 7$  surface: Energy-minimization calculation for the dimer-atom-stacking-fault model*, Phys. Rev. B 35 (1987) 1288.
- [128] T. Nakayama, M. Katayama, G. Selva, M. Aono, *Mechanism of epitaxial growth of monolayer CaF on Si(111)-( $7\times 7$ )*, Phys. Rev. Lett. 72 (1994) 1718.
- [129] N. M. Jeutter, *private discussion* (2004).
- [130] J. Dabrowski, H. J. Müssig, *Silicon surfaces and formation of interfaces*, World Scientific Publishing Co. Pte. Ltd., 2000, S<sub>A</sub> and S<sub>B</sub> steps (p.173).
- [131] *Inorganic Crystal Structure Database* (2006).  
URL <http://icsdweb.fiz-karlsruhe.de>
- [132] B. Lambert-Andron, F. Sayetat, S. Auffret, J. Pierre, R. Madar, *Phase separation and magnetic structure in praseodymium disilicide*, J. Phys.: Condens. Matter 3 (1991) 3113.
- [133] R. Hofmann, W. Henle, H. Ofner, M. Ramsey, F. Netzer, W. Braun, K. Horn, *Physical and chemical effects at rare-earth-metal-SiO<sub>2</sub>-Si structures*, Phys. Rev. B 47 (1993) 10407.

- [134] L. Pasquali, S. D'Addato, G. Selvaggi, S. Nannarone, N. Sokolov, S. Suturin, H. Zogg, *Formation of CaF<sub>2</sub> nanostructures on Si(001)*, Nanotechnology 12 (2001) 403.
- [135] T. Sumiya, T. Miura, H. Fujinuma, S.-I. Tanaka, *Surface reconstruction in CaF<sub>2</sub>/Si(001) investigated by scanning tunneling microscopy*, Surf. Sci. 376 (1997) 192.
- [136] B. Z. Liu, J. Nogami, *A scanning tunneling microscopy study of dysprosium silicide nanowire growth on Si(001)*, J. Appl. Phys. 93 (2003) 593.
- [137] J. Nogami, B. Z. Liu, M. V. Katkov, C. Ohbuchi, *Self-assembled rare-earth silicide nanowires on Si(001)*, Phys. Rev. B 63 (2001) 233305.
- [138] J. Kwo, M. Hong, A. R. Kortan, K. T. Queeney, Y. J. Chabal, J. P. Mannaerts, T. Boone, J. J. Krajewski, A. M. Sergent, J. M. Rosamilia, *High- $\epsilon$  gate dielectrics Gd<sub>2</sub>O<sub>3</sub> and Y<sub>2</sub>O<sub>3</sub> for silicon*, Appl. Phys. Lett. 77 (2000) 130.
- [139] J. Dabrowski, V. Zavodinsky, A. Fleszar, *Pseudopotential study of PrO<sub>2</sub> and HfO<sub>2</sub> in fluorite phase*, Microelectronics Reliability 41 (2001) 1093.
- [140] M. Trzhaskovskaya, V. Nefedov, V. Yarzhemsky, *Photoelectron angular distribution parameters for elements Z=55 to Z=100 in the photoelectron energy range 100-5000 eV*, Atomic Data and Nuclear Data Tables 82 (2002) 257.
- [141] A. Kotani, H. Ogasawara, *Theory of core-level spectroscopy of rare-earth oxides*, J. of Electron Spectroscopy and Related Phenomena 60 (1992) 257.
- [142] M. Trzhaskovskaya, V. Nefedov, V. Yarzhemsky, *Photoelectron angular distribution parameters for elements Z=1 to Z=54 in the photoelectron energy range 100-5000 eV*, Atomic Data and Nuclear Data Tables 77 (2001) 109.
- [143] E. Nicollian, J. Brews, *MOS (metal oxide semiconductor) physics and technology*, John Wiley and sons, 1992.
- [144] J. Maserjian, G. Peterson, C. Svensson, *Saturation capacitance of thin oxide MOS structures and the effective surface density of states of silicon*, Solid State Electron. 17 (1974) 335.
- [145] H. B. Michaelson, *The work function of the elements and its periodicity*, J. Appl. Phys. 48 (1977) 4729.

- [146] Z. Wang, J. Wu, Q. Fang, J.-Y. Zhang, *Photoemission study of high-k praseodymium silicates formed by annealing of ultrathin Pr<sub>2</sub>O<sub>3</sub> on SiO<sub>2</sub>/Si*, Thin Solid Films 462-463 (2004) 118.
- [147] J. X. Wu, Z. M. Wang, S. Li, M. S. Ma, *Photoemission study of the oxidation and the post-annealing behaviors of a Pr-covered Si(100) surface*, Applied Surface Science 225 (2004) 229.
- [148] C. Ashman, K. Först, J. and Schwarz, P. E. Blöchl, *Chemistry of La on the Si(001) surface from first principles*, Phys. Rev. B 70 (2004) 155330.
- [149] L. Pasquali, M. Suturin, S., V. Ulin, N. Sokolov, G. Selvaggi, N. Giglia, A. Mahne, M. Pedio, N. S., *Calcium fluoride on Si(001): Adsorption mechanisms and epitaxial growth modes*, Phys. Rev. B 72 (2005) 045448.
- [150] T. Schroeder, *private discussion* (2006).
- [151] A. Ramstad, G. Brocks, P. J. Kelly, *Theoretical study of the Si(100) surface reconstruction*, Phys. Rev. B 51 (1995) 14504.
- [152] C. B. Duke, *Semiconductor Surface Reconstruction: The Structural Chemistry of Two-Dimensional Surface Compounds*, Chem. Rev. 96 (1996) 1237.
- [153] P. Bokes, I. Stich, L. Mitas, *Ground-state reconstruction of the Si(001) surface: symmetric versus buckled dimers*, Chem. Phys. Lett. 362 (2002) 559.
- [154] P. Krüger, J. Pollmann, *Dimer Reconstruction of Diamond, Si, and Ge (001) Surfaces*, Phys. Rev. Lett. 74 (1995) 1155.
- [155] B. Paulus, *Correlation calculations for the reconstruction of the Si(100) surface*, Surf. Sci. 408 (1998) 195.
- [156] D. J. Chadi, *Atomic and Electronic Structures of Reconstructed Si(100) Surfaces*, Phys. Rev. Lett. 43 (1979) 43.
- [157] E. Artacho, F. Ynduráin, *Proposal for Symmetric Dimers at the Si(100)-2×1 Surface*, Phys. Rev. Lett. 62 (1989) 2491.
- [158] R. Uhrberg, E. Landemark, Y.-C. Chao, *High-resolution core-level studies of silicon surfaces*, J. of Electron Spectroscopy and Related Phenomena 75 (1995) 197.

- [159] R. M. Tromp, R. J. Hamers, J. E. Demuth, *Si(001) Dimer Structure Observed with Scanning Tunneling Microscopy*, Phys. Rev. Lett. 55 (1985) 1303.
- [160] R. J. Hamers, R. M. Tromp, J. E. Demuth, *Scanning tunneling microscopy of Si(001)*, Phys. Rev. B 34 (1986) 5343.
- [161] J. Dabrowski, M. Scheffler, *Self-consistent study of the electronic and structural properties of the clean Si(001)(2×1) surface*, Appl. Surf. Sci. 56 (1992) 15.
- [162] G. Jayaram, P. Xu, L. D. Marks, *Structure of Si(001)-2×1 Surface Using UHV Transmission Electron Diffraction*, Phys. Rev. Lett. 71 (1993) 3489.
- [163] H. Over, J. Wasserfall, W. Ranke, C. Ambiatello, R. Sawitzki, D. Wolf, W. Moritz, *Surface atomic geometry of Si(001)-2×1: A low-energy electron-diffraction structure analysis*, Phys. Rev. B 55 (1997) 4731.
- [164] M. Takahashi, S. Nakatani, Y. Ito, T. Takahashi, X. Zhang, M. Ando, *Surface x-ray diffraction study on the Si(001)-2×1 structure*, Surf. Sci. Lett. 338 (1995) L846.
- [165] R. Felici, I. Robinson, C. Ottaviani, P. Imperatori, P. Eng, P. Perfetti, *Room temperature Si(001)-2×1 reconstruction solved by X-ray diffraction*, Surf. Sci. 375 (1997) 55.
- [166] H. Over, J. Wasserfall, W. Ranke, C. Ambiatello, R. Sawitzki, D. Wolf, W. Moritz, *Surface atomic geometry of Si(001)-2×1 : A low-energy electron-diffraction structure analysis*, Phys. Rev. B 55 (1997) 4731.





## **Résumé:**

L'objectif de ce travail a été d'étudier, à l'échelle atomique et depuis les tous premiers stades, la croissance de l'oxyde de praséodyme sur des substrats de silicium orientés (111) et (001). L'étude se focalise sur la caractérisation des propriétés structurales, chimiques, et électroniques de  $\text{Pr}_2\text{O}_3$  déposé sur Si(111) et Si(001), avec un accent plus particulier sur cette dernière surface, importante sur le plan technologique. Cet oxyde de terre-rare a été considéré ces dernières années comme un bon candidat "high-k" pour se substituer à  $\text{SiO}_2$  comme oxyde de grille dans les transistors CMOS, afin de "miniaturiser" davantage les composants électroniques. Dans ce contexte, les propriétés des surfaces et des interfaces commencent à dominer sur les performances des dispositifs à base de silicium, puisque le rapport surface/volume augmente. Comme les basses dimensions de ces structures les rendent difficilement étudiables, la brillance de la radiation synchrotron a été employée pour des analyses de diffraction des rayons X et de spectroscopie de photoélectrons. Les résultats ont été complétés par d'autres techniques de science des surfaces, telles que la microscopie à effet tunnel, la spectroscopie Auger et la diffraction d'électrons à basse énergie. Une couche épitaxiale de  $\text{Pr}_2\text{O}_3$  hexagonal a été trouvée sur Si(111). Sur la surface (001), une couche ordonnée de  $\text{Pr}_2\text{O}_3$  cubique est recouverte par un silicate. Puisque les surfaces atomiquement propres sont le point de départ de la croissance, elles ont également été caractérisées. En particulier, la structure atomique de la surface reconstruite Si(001)- $2\times 1$  a été analysée.

**MOTS CLES :** Couches minces, oxyde de terre-rare, interface, silicium, synchrotron, GIXRD, STM, XPS.

## **Abstract :**

The goal of this project has been to investigate, at the atomic scale and from the very early stage, the growth of praseodymium oxide on silicon (111) and (001) oriented substrates. The study focuses on characterizing the structural, chemical, and electronic properties of  $\text{Pr}_2\text{O}_3$  deposited on both Si(111) and Si(001) substrates, with emphasis on the latter, which is of more technological importance. This rare-earth oxide has been considered recently as a good "high-k" candidate to substitute  $\text{SiO}_2$  as a gate oxide in CMOS transistors for further down scaling of devices. In this process, surfaces and interfaces begin to dominate the silicon device performances, due to the large surface to volume ratio. While the surfaces and interfaces are of increasing importance for electronic devices, such low-dimensional structures are difficult to study. In this context, brilliant synchrotron radiation is a valuable tool, which we employed here for X-ray diffraction and photoelectron spectroscopy analysis. The obtained results are complemented by other surface science techniques such as scanning tunneling microscopy, Auger electron spectroscopy, and low energy electron diffraction. It is found that an epitaxial hexagonal  $\text{Pr}_2\text{O}_3$  layer can be grown on the (111) surface. On the (001) surface, an ultra thin layer of cubic  $\text{Pr}_2\text{O}_3$  is covered by Pr-silicate upon further growth. Since the atomically clean surfaces are the starting point for the growth, they have been characterized as well. In particular, the atomic structure of the Si(001)- $2\times 1$  reconstructed surface has been analyzed.

**KEY WORDS:** Thin films, rare-earth oxide, interface, silicon, synchrotron, GIXRD, STM, XPS.